Studies On Ultrafast Dynamics And Spectroscopic Investigations On Fluorescent Probes In Bimolecular And Biomimetic Recognition

A thesis submitted for the award of the degree of

Doctor of Philosophy (Science)

in

Chemistry (Physical)

by

Sk Imadul Islam

Department of Chemistry

University of Calcutta

July 2021

Dedicated to

My beloved Parents &

the Supervisor.

DECLARATION

I hereby announce that the works manifested in the thesis "Studies On Ultrafast Dynamics And Spectroscopic Investigations On Fluorescent Probes In Bimolecular And Biomimetic Recognition" are original. I conduct experiments and set up instruments during my Ph.D. work at the Satyendra Nath Bose National Centre for Basic Sciences, Salt Lake, Kolkata, under the supervision of Prof. Rajib Kumar Mitra. I also declare that these findings have not been used to award any university or institute a degree diploma.

Sk Imadul Islam

Sk Imadul Islam (E-mail: ***skimadulislam1993@gmail.com)***
Senior Research Fellow
S. N. Bose National Centre for Basic Sciences
Block JD, Sector III, Salt Lake, Kolkata-700106

Abstract

This dissertation is focused on the study of the photo-physical properties of fluorescence/laser dyes in embodied in various biological and biomimetic systems (e.g. model proteins, micelles, reverse micelles (RM), RMs made up of mixture of surfactants, pure solvents, binary mixtures etc.) in different environments using various steady state and time-resolved experimental techniques. An essential part of this thesis concerns the systematic study of various bimolecular and biomimetic recognition compounds (e.g., fluorescence probes which act as organic ligands/dyes) at the excited states. For such systems, the change in the photo-physical parameters of the fluorescence probes are tracked using time-resolved fluorescence spectroscopy on a timescale spanning from nanosecond (ns) to sub-picosecond (ps). Dimension (hydrodynamic diameter) of the RMs used (d_H) has been measured using dynamic light scattering (DLS) spectroscopy. Structure of water encapsulated in the RMs (in terms of hydrogen bonding in the mid-infrared region (2200-2800 cm^{-1})) has been investigated using Fourier transform infrared spectroscopy (FTIR). *This dissertation covers two broad aspects: (a)* ESPT (intermolecular "excited-state proton transfer", a phenomenon in which photo-excited molecules transfer protons to the neighbouring solvents to relax their energy) dynamics of D-luciferin in various micro-heterogeneous environments (such as RMs, mixed RMs, binary mixture etc.): the possible role of hydration dynamics on controlling the ESPT dynamics and (b) probing two-photon induced emission of a dye to extract information on the local environment of aggregated systems using 2-photon absorption spectroscopy (2PAS). *In the first part of the dissertation,* we intend to observe the effect of mixing of surfactants; we have investigated the ESPT reaction of D-luciferin in mixed RM systems composed of non-ionic polyoxyethylene (5) nonylphenylether (Igepal CO-520) with cationic di-dodecyl dimethyl ammonium bromide (DDAB) and anionic sodium bis-(2-ethylhexyl) sulfosuccinate (AOT) in cyclohexane at different mole fractions of Ig (X_{Ig}) and at a fixed hydration (w_0=[H_2O]/[surfactant]=10). It has been observed that the maximum water solubilization capacity of the RMs mostly displays synergistic effects whereas various physical and chemical properties of the mixed RMs follow an overall linear trend with X_{Ig}. Also, the addition of Ig is observed to monotonically facilitate ESPT in AOT RM, while in DDAB it shows a synergistic effect. According to our findings, the ESPT rate inside a RM water pool can be regulated by blending surfactants with differing charge types while

keeping all other parameters unchanged. We have also investigated the ESPT process of D-luciferin in AOT, Ig and DDAB RMs at different temperatures (from 293K to 315 K) to identify the specific role of solvation during the ESPT process. We found that solvation precedes ESPT in the charged RMs (DDAB, AOT), however, in Ig they co-occur. Our study has established the pivotal role of solvation to be considered to explain ESPT process, specially in constrained environments like in RMs. Finally, to identify how micro-heterogeneity in aqueous environment affects the ESPT process, we investigate ESPT of D-luciferin in aqueous mixtures of water-ethanol and water-trifluoroethanol (TFE). We have found that ESPT kinetics of D-luciferin in EtOH-water is faster than that in TFE-water mixture. It increases near-linearly with water content in the mixtures in EtOH while in TFE the change is not linear. Our study showed that ESPT occurs after solvation in TFE-water (up to 0.6 water mole fraction (X_w)) whereas in EtOH-water, they occur simultaneously at each X_w. *In the second part of the dissertation,* we have used an otherwise unique spectroscopic technique, 2PAS, which can probe the specific binding of probes (Rhodamine 6G (R6G) and Rhodamine B) to proteins (bovine serum albumin (BSA)), and we have investigated whether this could be exploited to understand site-specific binding as well as conformational changes of proteins during thermal/chemical denaturation. 2PAS measurements have clearly demonstrated site-specific binding between the probes and the protein, and could be used to track protein (un)folding pathways induced by temperature changes. In a connected study, the effect of charge on the interaction of a cationic dye R6G with surfactants of different charge types: sodium dodecylsulfate (SDS, negatively charged), cetyltrimethylammonium bromide (CTAB, cationic charged), and Titron X100 (Tx 100, uncharged) was measured, and these interactions have been corroborated by classical MD simulation studies. In order to determine if the hydrophobicity of the surfactant influences the complex formation process, we altered the chain length of anionic surfactants (sodium octylsulfate (SOS), sodium decylsulfate (SDeS), SDS and sodium tetradecylsulfate (TSDS)) while keeping the cationic dye constant. We observed that monomeric anionic surfactants solubilize in cationic dye dimers at pre-micellar concentrations, distorting the dyes' parallel orientation. This distorted geometry has a positive impact on the dipolar orientation of the R6G molecules in the SDS-R6G complex and change in the dipole moment of the complex at pre-micellar aggregates as compared to pure water and it is also dependent on the surfactant hydrophobicity, which is intriguing provided that the interaction is predominantly electrostatic in nature.

List of Publications

The following publications and manuscripts are based on this thesis:

1. Das, A., **Islam, S. I**., Das, D. K. and Mitra, R. K. (2017) "Modulation of the Excited-State Proton Transfer Rate of D-luciferin in Mixed Reverse Micellar Systems", *ACS omega* 3, 5715-5724. (*Joint first author*)

2. **Islam, S. I**, Das, A. and Mitra, R. K. (2021) "Excited-state proton transfer in reverse micelles: Effect of temperature and a possible interplay with solvation", *J. Photochem. Photobiol. A* 404, 112928.

3. **Islam, S. I.**, Pyne, S., Mahanta, D. D., Palit, D. K., and Mitra, R. K., "Role of Micro-Heterogeneity in the H-bonded Network on the ESPT Mechanisms of D-Luciferin". (*To be submitted*)

4. Das, D. K., **Islam, S. I.**, Samanta, N., Yadav, Y., Goswami, D. and Mitra, R.K. (2017) "Two-Photon Spectroscopy Can Serve as a Marker of Protein Denaturation Pathway", *J. Fluoresc*, 28, 855-862.

5. **Islam, S. I.**, Pyne, P., Das, D. K., Mukherjee, S., Chakrabarty, S., and Mitra, R. K., "Molecular Insight onto Dye-Surfactant Interaction at pre-micellar Concentrations: A Combined two-photon Absorption and MD Simulation Study". (*Submitted*)

.

I have also contributed to the publications below (not included in this thesis):

1. Mahanta, D. D., **Islam, S. I.**, Choudhury, S., Das, D. K., Mitra, R. K. and Barman, A. (2019) "Contrasting hydration dynamics in DME and DMSO aqueous solutions: A combined optical pump-probe and GHz-THz dielectric relaxation investigation", *J. Mol. Liq*., 290, 111194.

Acknowledgements

So far, it's been an incredible journey that began in a small village called Tarachand Bar, P.S+P.O.-Nandigram, East Medinipur district, 721631, West Bengal, India. For the past five years, I have lived and worked at the S. N. Bose National Centre for Basic Sciences as a research scholar in the Department of Chemical, Biological, and Macromolecular Sciences (CBMS). To be honest, all of the people who have helped me along the way (including my dissertation) cannot be named individually and writing my dissertation without acknowledging certain people would be incomplete. However, I will do my best to express my gratitude to everyone who has assisted me in any way, both scientifically and emotionally, through my dissertation.

First and foremost, I want to express my deepest gratitude and admiration for my very first teachers, (Sk Ruhul Amin) & Maa (Komerun Bibi)" (my parents). Because of their unconditional love, affection, encouragement, philosophy, and guidance, I am here today. They continually urge me to strive to be a wonderful man who is kind and loving. Since early childhood, they have been planting moral seeds, in my opinion. It appears to be my most significant source of inspiration. From the beginning of my life to now, they have made many sacrifices for me. My wonderful childhood memories would live on in my heart forever.

It is my pleasure to express my cordial gratitude and humble gratitude to my supervisor, Professor Rajib Kumar Mitra, for his continued support and encouragement. Throughout my Ph.D. and

writing this dissertation, his constant encouragement, support, inspiration, and expertise helped me and I feel very lucky to have him as my guide in my work as well. It's a life lesson to be trained under his guidance, and he gave me the opportunity to think and work independently. I've learned some very basic things from him, such as preparing presentable graphs, presenting posters, and writing manuscripts in the right way. I would like to express my gratitude to him for all the suggestions and advice that helped to improve my Ph.D. works and knowledge. He also taught me how to think of the problem from every perspective, and the extensive knowledge, the extreme dedication to work, and the immense enthusiasm to study new things will remain the inspiration of my life. His kind and loving attitude towards me is worth cherishing for an entire life. I still think I was fortunate enough to have a chance to work with kindness, welcoming attitudes, and a good sense of humour under the guidance of such a man.

Besides my supervisor, I would also like to express my sincere gratitude to Prof. Dipak Kumar Palit (UM, Mumbai), my collaborator, for his valuable advice and encouragement and for giving me the opportunity to work with him. I want to express my sincere appreciation to Prof. Debabrata Goswami (IIT Kanpur), Prof. Anjan Barman (SNBNCBS, Kolkata) and Dr. Suman Chakrabarty (SNBNCBS, Kolkata) for giving me the opportunity to access their laboratories and research facilities. I would also like to thank my other collaborator, Yogendra Yadav (IIT Kanpur), Shounak Mukherjee (SNBNCBS, Kolkata) for their helpful advice and support.

I would like to thank my former (THz Spectroscopy Lab) and current (Bio-photonics Lab) lab mates: Dr. Animesh Patra, Dr. Arindam Das, Dr. Nirnay Samanta, Dr. Debasish Das Mahanta, Dr. Dipak Kumar Das, Dr. Debanjan Polley, Dr. Chaitrali Sengupta, Dr. Bibhab Majumdar, Anulekha De, Amit Barh, Debkumar Rana, Partha Pyne, Saikat Pal, Sayantan Adak, Sudip Majumder, Didhiti Bhattacharya, Sumana Pyne, Ria Saha, Shubhajit Singha and Dr. Subhadip Chakraborty for working together in a fun atmosphere, for stimulating discussions, for all the fun we've had in the last five years.

First of all, I would like to thank Arindam Da, from whom I learned many things, such as experimental techniques, analysis of data, etc. Thanks to Dipak Da for thoroughly helping to build up two-photon absorption spectroscopy and also thanks for providing tips and suggestions on understanding some basic instruments and optical alignment techniques. A very sincere thanks to Nirnay Da and Animesh Da for helping a lot (like lab attitude, data analysis, and experimental techniques, etc.). I express my admiration and special thanks to Debasish Da, from whom I have learned so many things, and for all the support during my Ph.D. work. I would like to thank Partha for all the help and support I have received throughout my Ph.D. work. In addition, my seniors have taught me a lot of technical skills (such as word processing software, MS PowerPoint, Igor, Origin, SigmaPlot, and many more) about how to use the software with some helpful tips. Once again, I thank all lab members "Bio-photonics" for always helping me in a different way, in the lab as well as outside the lab. For the final proof corrections of my thesis, I thank Ria, Partha, Sumana, Subhadip da, Shubhajit and Debasish da. The help and

cooperation of each and every one abounds in my research work, and I have to say that this is the best laboratory in the world.

We, the members of the lab, spent some lovely evenings in the sweet home of our Sir and Madam (Dr. Sukanya Chakrabarty). Thank you, Madam, and thank you, Sir, again, for those happy moments and memorable dinners. I would also like to thank Sonali di, Animesh da, and Nirnay da for the in-room dinner parties. I do love to taste the mouth-watering divine foods prepare by Nirnay da, Dipak da, Animesh da, Sonali Di, and Sumana.

Besides my parents, I would like to extend my sincere thanks to everyone in my family. My four elder brothers, Sk Manjurul Islam (Vaijan) and his two children; Sajjad & Sadika, Sk Hapijul Islam (Maina) and his two children; Mubaina & Mariyam, Sk Moidul Islam (Sege dada) and his two children; Sohana & Mujahid, and Sk Tafijul Islam (Choto dada) and his two children; Mahir & Tanisha and their (four elder brothers) spouses (Mustari khatun (Boro vabi), Nuriman Yeasmin (Bujan), Afsana Parvin (sona vabi), and Khansatun Nesha (choto vabi) "one-to-one" guided and loved me. I'd often liked to study since I was a child, but I wasn't especially skilled. Of course, the love of family made me proud; once again, many thanks to my family for their unwavering support and unconditional love. I'd like to express my affection for my grandfather (Late Sk Mamtaj Uddin, dadu), grandmother (Arjan Bibi, thakuma), Uncle (Sk Khasiar Rahaman) and his mother Subeda bibi (younger grandmother), Aunty (Aspiyari Khatun). Also, I'd like to express my love and concern for my uncle's sons (Aslam & Arfan) and daughters Parul (and her husband Kamal), & Payel), as well as the sons and daughters of my four elder brothers.

The unwavering support and unconditional love of my younger aunt (Amina Khatun, Mamima), Mujibur Rahaman (uncle, Mama), Late Usaron Bibi (grandmother, Nanima), Halima (auntie), Kolima (auntie), Momtaz Begum (younger grandmother, Nanima), Ibrahim (uncle, mama) are greatly appreciated.

Quite apart from my studies, my friends, colleagues, and beloved seniors at the S. N. Bose Centre have all played an important role in this journey. They are my families. In my hostel room, we used to treasure the occasional get-togethers, gossips, and enjoying food, which made this place a home away from home. Though it is difficult to name all of them, some that come close are Dr. Debasish Das Mahanta (and his spouse Anamika Patra (boudi)), Dr. Subrata Dev, Dr. Sarowar Hossain (and his spouse Sanjeda Afrin (vabi)), Dr. Vinood Kumar, Dr. Subhadip Chakraborti, Dr. Rakesh Das, Ananda, Amit, Sourav, Subhasree di, Arunava, Dr. Sudiptto Pattanayak, Indranil da, Dr. Arindam Das, Dr. Kartik Samanta, Dr. Krishnendu Pal, Dr. Souvanik Talukdar. From the SNB family, special thanks to Deba da, Ananda, Sourav, Amit & Sarowar da for their support (including physically, mentally, and emotionally) until the end of my thesis work. Also thanks to Balwant Sing Bisth, Anupam Gorai, Dhimadri da, Sasthi, Sayan, Edwin, Samir, Dr. Poulomi Chakraborty, Anirban. I am grateful to Dr. Aslam Parvej, Dr. Sarowar Hossain, Ejaj Tarif, Mehbub Alam, Nur Islam, Rafikul, Mudasir, and Saniur for all the enjoyable and great moments; we spent together during Ramadan, including the "Sehri and Iftar party". I am grateful to them for providing such a welcoming atmosphere. At lunch and dinner, I enjoy the company of my co-workers and the SNB mess cooking team (Kajal, Ramu, Ganesh, Rajib, and Shamal). I would like to thank

Vidyasagar da and Haripoda da for their affection and support, as well as the entire canteen staff. I spent most of my evenings playing football or carrom, and the afternoons of weekend days playing cricket. These games are my everyday refreshment, so I enjoy playing them. I learn the value of teamwork and appreciate the competitive spirit of the games. I had the opportunity to indulge in some great fitness activities through the platform of different sports competitions which creates a great friendly environment inside the campus. I'd want to express my gratitude to "SNB Muktangan" (all committee members, sports activity) for offering a platform on which I was able to collaborate and develop my persona. I was the coordinator of Muktangan's sports activity group from 2017 to 2021 (a formal Bose Centre Recreation Club (BCRC)). We held tournaments among ourselves as well as among other institutes on a regular basis. We host an inter-institutional badminton tournament in 2017 and 2019. The Muktangan working committee was a great experience. Aside from these daily events, the "Muktangan Sports Activity Group" has arranged a "Bose-125 Marathon" (5km Marathon) to celebrate Prof. Satyendra Nath Bose's 125th birthday on December 31, 2018. I'd also like to thank all members of the "SNB Khaja Team" musical community (international musical band). For the tea shop, I also thank the late Horen da, Dulal da, and Laksman da. Almost every day, I stop by their tea shop for tea and evening snacks. I had the opportunity to participate in some great responsible activities (COVID volunteers (Co-V) & COVID Task Force (Co-TF)) which helped me to be responsible. My deepest gratitude is to my sir (prof. RKM and his Co-V & Co-TF teams) for including me in his team in such a trifling way.

I'd like to express my gratitude to home town friends Israfil, Sarifur, Saddam, Saddam (vaipo), Bappa, Bodruddoza, Mujibur, Sabir da, Asraf, Kalam and others for their motivation and amusement. It is with great gratitude that I extend my deepest thanks to Ayesha (friend), Rubi Kakima (Mom of Rejaul) and Rejaul (friend) for all their unending support and encouragement.

I'd like to express my gratitude to my best friend Nazma Khatun (would be better half) for her unwavering love and encouragement, for always being there for me through the roller coaster ride of my life, for all of our wonderful battles, and for loving me in all of my craziness. This innocent soul is one of the major pillars of my life. I would like to thank (her) entire family for their unwavering support.

I give a debt of gratitude to my beloved teachers, whose constant encouragement motivates me to keep moving forward. I am grateful to my all college teachers Dr. Animesh Patra, Dr. Jayasree Laha, Dr. Anup Kumar Das Mahapatra, Dr. Nilkamal Maity, Dr. Gobinda Prasad Sahoo, Dr. Tridib Tripathy, Dr. Koushik Chandra, Sri. Subhabrata Mabhai, Dr. Pradip Patra, Sri. Tarapada Midya and laboratory assistant are Sri Haradhan Kolya, Sri Tarun Kumar Bhattacharya and Amit da for enlightening me during my "Post-Under" Graduate days.

I express my gratitude to Prof. Samir Kumar Pal, Prof. PKM, Mr. Sanjoy Choudhury and Prof. RKM for teaching during Ph. D. coursework program. I am also grateful to the reviewers for their judicial comments from various journals, as well as the thesis committee.

I also gratefully acknowledge some frequently visited websites such as YouTube, Google, ResearchGate (RG), Google Scholar, Sci-Finder, Sci-Hub, and some social networking sites such as Whatsapp, Facebook, and others.

I am grateful to all of the faculty members, research scholars, academic staff, and non-academic staff at SNBNCBS for their kind help and cooperation. Words cannot express how grateful I am for your support. I want to thank the SNBNCBS centre for providing me a friendly environment, experimental and other facilities. I thankfully acknowledge to UGC (the University Grants Commission), India, for a research grant (Sr. no. 2061510232; Ref. no. 21/06/2015(i) EU-V; Roll no. 129597) and my centre SNBNCBS, Department of Science & Technology (DST, India) for financial assistance.

Signature: ***Date: 28.07.2021***

SK IMADUL ISLAM
E-mail: **skimadulislam1993@gmail.com**
imadulislam@bose.res.in
S. N. Bose National Centre for Basic Sciences
Department of Chemical, Biological & Macro-Molecular Sciences
Block JD, Sector III, Salt Lake, Kolkata-700106 (W.B.), INDIA.

Acronyms

"1 or S" PAS	"One or single"-Photon Absorption Spectroscopy
1PEF	One-Photon Excitation Fluorescence
2PAS or TPAS	Two-Photon Absorption Spectroscopy
2PEF	Two-Photon Excitation Fluorescence
BSA	Bovine Serum Albumin
BTW	Biological Transference Window
CD	Circular Dichroism
CMC	Critical Micelle Concentration
DLS	Dynamic Light Scattering
ESPT	Excited-state Proton Transfer
fs	Femtosecond
FTIR	Fourier Transform Infrared Spectroscopy
GM	Göppert Mayer
IEP	Iso-emissive Point
IRF	Instruments Response Function
MIR-FTIR	Mid-Infrared Fourier Transform Infrared Spectroscopy
MD	Molecular Dynamics
NIR	Near-Infrared
ps	Picosecond
PT	Proton Transfer
QY (ϕ)	Quantum Yield
R.I.	Relative Intensity
RM	Reverse Micelle
R_c	Critical Radius
SC	Solubilization Capacity
SS	Stoke Shift
SSS	Steady State Spectra
TCSPC	Time Correlated Single Photon Counting
TPACS	Two-Photon Absorption Cross-Section
TPM	Two-Photon Microscopy
TRANES	Time-resolved Area Normalized Emission Spectra
TRES	Time-resolved Emission Spectra
TRFS	Time-resolved Fluorescence Spectroscopy
UV	Ultra Violet

List of Tables

List of Figures

List of Schemes

Table of Contents

Chapter 1

1.1 Introduction

Researchers had to concentrate on the kinetics of reactions for many years, by only monitoring the relevant rates. However, with the evolution of ultrafast spectroscopy, it became feasible to focus extensively on the real-time investigation of how the molecules approach, collide, transfer energy, break or form bonds, and deform into products. Initial events in many biomolecular processes occur on a very short time scale (pico second (ps) to sub ps), which determines the final performance or output in many cases. Research on ultrafast science finds utmost importance in this context and has gained profound attention from both fundamental as well as applied perspectives. In this scenario, ultrafast spectroscopy has emerged as a potential tool to probe the underlying physical properties and reaction mechanisms of biomolecular systems also. Several decades ago ultrafast methods were used to be described in short timescale regime where ns (nanosecond) light pulses were the state of the art technology. The short time "fs" period light pulses are now being considered to be ultrafast by the majority of the research community. Perhaps the most notable advancement has been achieved in the field of fluorescence spectroscopy. Fluorescent probes can be used to observe biomolecular interaction[1], catalytic reaction[2], structural/conformational changes[3] as well as an understanding of several ultrafast processes (e.g. electron/proton transfer) occurring in real life. Fluorescent probes (often referred to as 'ligand' or 'drug' from a biological perspective) have become very apparent in biophysical research in recent years, and their use has gradually increased due to their sensitivity, versatility, quantitative abilities, and industrial applications. Fluorescence probes are the most rapidly developing molecules in fluorescence spectroscopy during the recent years, and their various interactions with light have been vastly investigated. A fluorophore is a fluorescent compounds that absorbs energy from a particular wavelength and then emits energy at a different but equally specific wavelength, and both the fluorophore and the chemical environment govern the emitted

energy. Fluorophores, more specifically, the portion or entity responsible for the color of a molecule are also referred to as chromophores. Furthermore, the characteristics of the probes decide the knowledge available from the experiments. Fluorescence spectroscopy has been widely used in studies of the dynamics and structure of molecules in complex methods.[4, 5] Since kinetic methods that influence fluorescence, such as collisional quenching, transfer of energy, solvent relaxation, and rotational reorientation, occurs on the timescale of the fluorescence probe lifetime (10^{-9} s), time-resolved fluorescence observations are more precise about the fluorescence probe molecular atmosphere than steady-state fluorescence measurements. In order to exploit non-zero anisotropic probes to test rotational diffusion, the fluorophore's lifetime must be equal to the time scale of attention of the experiment and pH-sensitive fluorophore's should be used to measure pH. A huge number of fluorescent probes are known, and explaining them all is not realistic. This study offers a summary of the different forms of fluorophores, their spectral properties, and their applications.

Time-resolved fluorescence spectroscopy has evolved as a significant instrument for the investigation of biomolecular interactions and structures.[6, 7] Over the past few decades, it has been observed that the application of fluorescent probes in bio-oriented researches is increasing and so is the subsequent usage of fluorophores as markers in photophysical and photochemical processes.[8] The specific interactions between small molecules (ligands) and biomolecules often serve as a signature of biomolecular recognition. In real systems, often such small molecules (ligands/drugs) bare spectroscopic signature and monitoring the changes in their spectroscopic signature (both in steady-state as well as with time) provides a clear avenue to understand the changes in biomolecular recognition.[9] This dissertation covers a wide variety of complex structures and phenomena that can be studied using ultrafast spectroscopy, with a focus on the methods and experiments described in chapters 2 and 3.

Surfactant is a type of molecule that has surface-active properties. Surfactant molecules naturally self-aggregate in solvents to construct micelles (M), reverse micelles (RM), various forms of amorphous structures, and vesicles, among other structured assemblies.[10] Surfactants spontaneously aggregate to form micelles (M) in aqueous solutions, which is in contrast to their aggregation to form inverted or reverse micelles in organic solvents. Standard micelles (M) are described as aggregates of surfactant molecules with dispersing solvent-oriented hydrophilic heads (usually water) and hydrophobic tails oriented towards the inside of the assembly (the micellar core). Micelles appear as the principal form "at and above" the so-called critical micelle concentration (CMC) in the system where free

surfactants are also present as monomers in the system. The aggregate number (average quantity of surfactant molecules in a micelle) depends on the type of surfactant and its concentration. When the solvent is changed from aqueous to a nonpolar medium, the representation of micelles is reversed. To minimize their contact with non-polar solvents in bulk, the head groups of surfactants are linked to water molecules, which extend its hydrophobic tails into the non-polar medium. RM may also be produced with materials that have reasonably high dielectric constants, including other non-aqueous polar solvents (such as glycerol, ethylene glycol, formamide etc.) that are immiscible with hydrocarbon solvents.[11] With its water content, the aggregation number of RMs increases, typically described in terms of the RM hydration level, w_0= [H_2O]/[surfactant].[12] It has been shown from both thermodynamic model and molecular simulation studies that the development of large permanent aggregates of surfactants is triggered by a limited number of polar solvent molecules.[13]

Often complex biomolecular systems are viewed as a simplistic model in the form of self-aggregated systems (M, RM, vesicles, etc.). In many areas, ranging from basic sciences to the relevant technical aspects, RMs are of particular interest and have various applications, such as models for biological systems, for the extraction and purification of biomolecules such as food additives or medicinal substances in biologically compatible systems, in the delivery of medicinal products and as enzymatic reaction media etc.[14-18] Studying ligand-surfactant (in aggregated and/or monomeric form) interaction, as well as ultrafast processes in such systems, leads towards a platform for understanding the mechanism of such interactions. This property of the self-aggregated systems has made them a useful biomimetic analogue of in-vivo systems. These bio-mimicking systems (RM) are less complex than the corresponding biomolecules and easy to plan for the benefit of real biological systems and have been recognized as an ideal medium for the past few decades to research the properties of confined/restricted water.[19-25] Several techniques, including scattering techniques such as small-angle neutron scattering (SANS)[26], small-angle X-ray scattering (SAXS)[27, 28], and both dynamic and static light scattering[29], have defined reverse micelle shape and size which can be experimentally varied from 0.3 - 20 nm by changing the w_0.[20, 30]

Micro-heterogeneity in complex solutions (like RMs) have been investigated thoroughly as a result of recent developments in ultrafast laser technology. Water present in RMs has been studied previously, providing distinct variations in physical and chemical properties compared to its bulk counterpart.[19, 20, 31-36] *What kind of water is in the RMs water*

pool? is one of the utmost significant queries raised by those reviewing RMs. However, the origin of these variations (due to confinement or contacts with the frequently highly charged interfacial layer) is still a point of contention. Many previous experiments using vibrational spectroscopy showed that water in RMs behaves differently than bulk water.[37-39] The slow dynamics within the RMs interface strongly interact with the water molecules, making them 'highly organized'[20, 25, 40] and relatively faster dynamics within RM water pools[41], such water dynamics restriction within RM can be described by the most commonly used "*Core-Shell"* model.[20, 42-44] The core-shell model (scheme 1.1) uses bulk water values to model the core properties, while the shell is modelled from the $w_0 = 2$ RMs response, which includes no core water meanwhile all water molecules would be associated with the surfactant head groups.[31] It is observed that the steady-state spectra of shell water tend to shift to a higher frequency than bulk water, due to reorientation of molecules, and reduction in vibrational lifetimes, and reduction in spectral diffusion, among the other factors. Time-resolved vibrational spectroscopy has recently been used to investigate the dynamics and hydration in RM systems.[33, 34, 45, 46] Compared to that of 'core water' (1.7 ps)[20], the vibrational relaxation time of 'shell water' (~5.2 ps) is significantly slower and, interestingly, the shell water shows a strong dependence on the nature of the RM polar interface. Various experimental methods have been used to investigate the dynamics of bulk and confined water in constrained media.[19, 25, 31, 36, 42, 47-49] Results from molecular dynamic (MD) simulation also show that the core and shell water are not static (scheme 1.1) and there is a sluggish inter-conversion between them.[50] This altered retarded dynamics within RM, therefore, focus on many factors such as interface polarity, w_0, nonpolar solvent, etc.[19, 24, 33, 50-55], which can be changed by replacing a single surfactant with a blend of different surfactants. Surfactant mixtures are often preferred in commercial, pharmaceutical, and technical formulations over the consistent single surfactant(s) for their greater presentation and cost-effectiveness in various aspects, including solubilization, dispersion, suspension, etc.[56-62] It was found that solubilization ability of RM and the physicochemical properties of the trapped water are heavily dependent on the chemical composition of the oil, surfactant charge type and w_0.[63] Several explanations have been suggested for the synergistic solubilization activity observed, often based on either the interaction between the curvatures of the surfactant monolayer or the interaction of the inter-droplet or the formation of an optimum hydrophilic-lipophilic balance (HLB) or both.[64-67] Numerous studies of RM systems involving more than one surfactant using solubilization[66-68], conductivity[63, 68], interfacial composition[69], viscosity[70], spectroscopy[71-73], SANS[74, 75], FTIR and NMR[76, 77] have reported major improvements in the mechanical

characteristics of the interface and subsequently, in the water structure of the RMs compared to the corresponding single surfactant systems. The properties of water (or any different polar solvents) in the vicinity of such aggregates are distinctly different than those of the bulk. Accordingly, the molecular interaction pattern changes as most of those are solvation mediated. Monitoring the spectroscopic response (fluorescence) of the ligands thus invokes information on the altered hydration dynamics also.

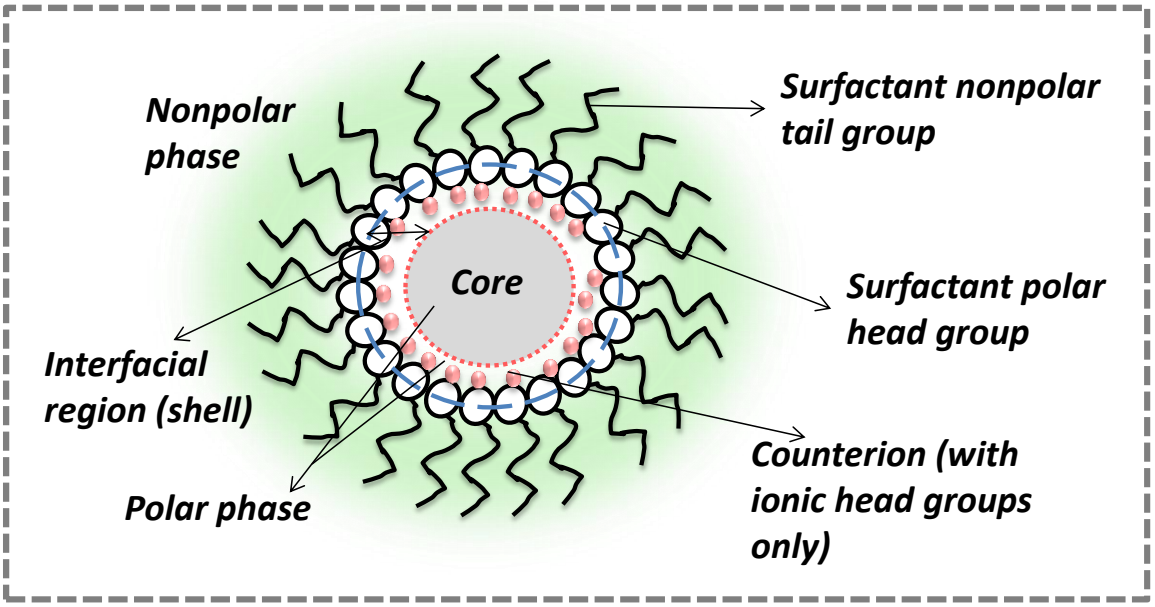

Scheme 1.1.: Pictorial overview of the core and shell regions, as well as a schematic illustration of the various regions in a reverse micelle.[31]

Proton transfer (PT) in an aqueous medium is a fundamental route for several chemical and biological methods ranging from enzyme catalysis to acid reactions and has received much attention in chemistry and biology.[78-83] In organic-inorganic and biochemical systems, isolated hydrogen (H) is needed to create covalent and "H" bonds. It is known that there are four variants of H, such as solvated or free proton (H^+), "H" atom, hydride anion (H^-), and often as a wave of quantum mechanical elements. PT is amongst the most basic measures in many areas of chemistry and biology. A lot of mechanistic research has also been done on this subject. There are three types of proton and electron transfer chemical reaction system, such as (i) the transfer of a proton (Brønsted acid-base reaction), (ii) the transfer of a proton and an electron, and (iii) the transfer of a proton and two electrons (H^- transfer). The key emphasis of this study will be the transfer of photochemical protons involved in reactions of interest in different media. One of the most universal and simplest chemical reactions appears to be the method of proton transfer (PT).[84] A proton is transferred from a proton

donor molecule to a proton acceptor in these reactions. PT reactions are one of the humblest chemical revolutions since they involve the movement of a hydrogen atom, it is ultrafast and happens in the sub-picosecond time scale.[85] While molecular level understanding of PT mechanisms still remains not clearly established, gaining more knowledge from these processes about ultrafast dynamics will allow us to understand the behavior of PT comprehensively. Biological PT reactions often take place at interfaces that provide additional complexity in the PT mechanism and dynamics as opposed to that in bulk solvents owing to modified solute-solvent interactions.[86, 87] There are two broad categories of PT reactions; such as, ground-state proton transfer (GSPT) and excited-state proton transfer (ESPT) (scheme 1.2). GSPT is one of the most common chemical reactions and it has been found to play an important role in various chemical and biological processes. There are two different GSPT sets, such as the ground state intramolecular proton transfer (GSIPT) and the ground state intermolecular proton transfer. Examples of GSIPT include keto-enol tautomerization in pyruvic acid, a key component of carbohydrate metabolism.[88, 89] In ground-level intermolecular proton transfer occurs in the acid-base reaction ($ROH + H_2O + B^- = RO^- + HB$), e.g. the proton shuttles between various types of green fluorescent protein (GFP).[90] ESPT reactions are broadly categorized into four different classes: (i) Photo-acids, from their electronically excited-states, transfer H^+ to nearby solvent molecules through intermolecular H-bonded bridges.[87, 91, 92] (ii) Excited-state intramolecular protons transfer (ESIPT) processes, where PT takes place in the same molecule via its constituent donor (hydroxyl group) and accepter (heterocyclic nitrogen atom or a carbonyl group) moiety.[93] (iii) Some molecules, known as photo-base (such as 7-hydroxy-coumarin, 1-naphthol etc.) can accept an excess proton from the solvent or the solution. (iv) In bi-functional compounds (e.g. 1-ammonium-2-naphthol) PT occurs in the presence of H^+ donor (photo-acidic) and accepter (photo-basic) when these groups are near to each other.[94, 95] Experimental studies on PT reactions get complicated by the presence of dynamic nature of the dissociation-association equilibrium.

ES acid (photoacids) are organic compounds that gain acidity (lower pK_a value) when excited to a higher electronic state, allowing for detailed time-resolved studies of the dissociation mechanism. Excitation with a laser pulse will thus start the dissociation process of photoacids. Weber published the first experimental evidence of ESPT in 1931, when he reported a pH-dependent steady-state fluorescence spectrum of 1-naphthylamine-4-sulfonate, although the absorption spectrum remained constant in that pH range.[96] Just single protons

are displaced as ESPT occurs, but what causes them to shift is a major change in the molecule's electronic structure. This change has been described by chemists as "an increase in proton donor acidity and proton acceptor basicity (change in pK_a value)"[97, 98], and "a start changing in aromatic character".[99, 100] In hydroxyl-substituted aromatic compounds, Weller was the first to propose that photo acidity is induced by an intramolecular charge transfer (ICT) from the hydroxyl oxygen to the aromatic system.[101] Several studies have looked into the ESPT reaction pathways of various excited-state photo-acids, as well as the role of the environment in proton transfer dynamics.[78, 102, 103] After excitation of the photo-acid, a proton is transferred to the solvent, which serves as the rate-determining step, and therefore, the local concentration of water molecules around the photo-acid and solvent reorganization is the primary factor to govern the ESPT.[104] The presence of an additional proton acceptor, usually the solvent, is needed for intermolecular ESPT. Among the various types of photochemical reactions, the ESPT process has received a lot of attention due to its importance in photochemistry and photobiology.[105, 106] The ultrafast dynamics of excited-state photophysical processes (such as ESPT) in bimolecular and biomimetic recognition (reverse micelle, binary mixtures, etc.) can be understood in this dissertation.

There are numerous techniques for biomimetic systems, which also include mimicking the nanostructures/architecture of a biological compartment or surface, as well as the surface of a bio-receptor that comes into contact with target molecules. Biomimicry, one of the utmost distinctive approaches for understanding the principles of biological systems, takes information from the design of nature and uses this data to construct incredibly challenging and difficult production systems at various length scales to resolve critical problems.[107] *Why is it important to have biomimetic systems?* Since biomimicry is a motivated type of science, especially a natural entity that uses nature to improve human lives[108], biomimicry can be commonly mentioned as a proof of concept, used to embrace and adapt the tried-and-tested principles of nature to handle problems.[109] The key structural and dynamic characteristics of RMs is the water solubilization capacity along with the opportunity of modulating this parameters in a regulated manner which makes them a potential biomimetic solvent. ESPT provides useful information about the dynamical nature of water in RM systems.[110-115] ESPT reaction in RMs is not very straightforward due to the solvent micro-heterogeneity in the water pool, and therefore, has paved way for a fascinating area of research with a broad variety of applications in chemistry and biology.[116,106] Because of the diverse physical nature of the water encapsulated in the RM water-pool, as well as the

additional control of regulating the physical characteristics of water by adjusting the head group charge, diffusing solvent, and w_0, the ESPT reaction of numerous photoacids in RM systems has received a lot of attention recently.[105, 110, 113, 115, 117-121]

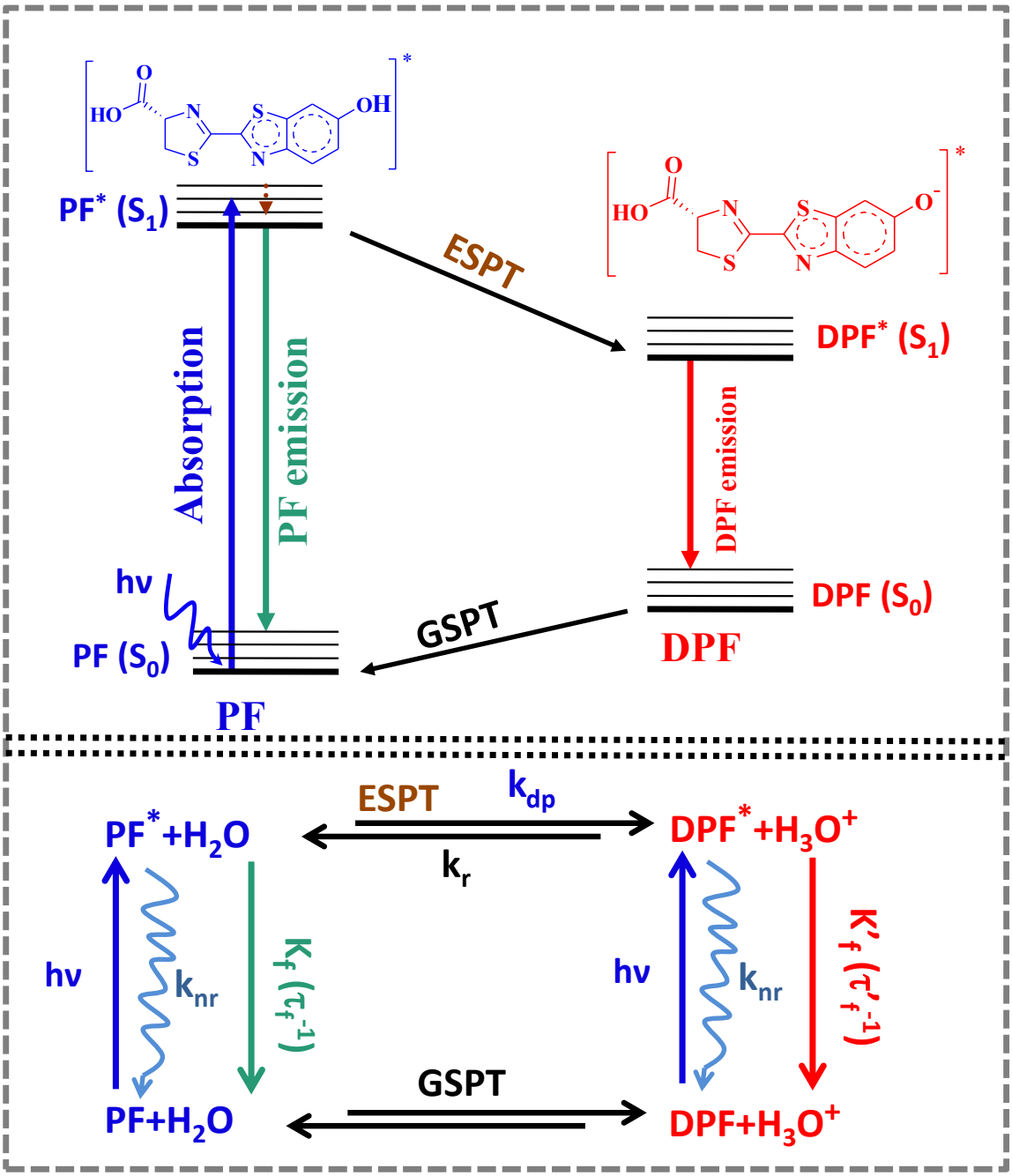

Scheme 1.2.: Diagrammatic explanation of the GSPT and ESPT process. K_{nr}, K_r, K_f, k'_f, PF, DPF signify the non-radiative, radiative, fluorescence emission rate constant of protonated form, fluorescence emission rate constant of deprotonated form, protonated form, deprotonated form, and "*" stands for excited-state respectively.

The nature of the surfactant charge has a significant impact on the position of the probe and the ESPT dynamics within RM[111, 122], pH and dielectric constant of water inside the RM

environment[105], the environment's polarity, and the screening effects of counter-ions present at the interface.[123] The role of the interface in determining the rate of the ESPT reaction is useful in this stage, and the ESPT dynamics modulate with the charge type of the RM head groups. For example, in anionic sodium bis-(2-ethylhexyl)sulfosuccinate (AOT) RMs the rate of ESPT growths with an increase in the water content (w_0)[111,113] while in cationic RMs, interface-localized probe offers only subtle changes with w_0.[122,124,110] Lawler et al. demonstrated in a seminal paper that in AOT RM, photoacid ESPT kinetics resemble those of bulk water, implying a diffusion-controlled power-law time-dependent method, whereas in non-ionic Ig-520 RM, ESPT rate exhibits slow, two-component kinetics with one relatively bulk water-like population and a second surface-bound population with a slower lifetime.[111] Few other research studies have linked the ESPT probe's solvation dynamics to its intramolecular proton transfer dynamics.[114, 115, 125] Surfactant Mixtures are frequently preferred over single surfactant(s) related to industrial, pharmaceutical, and technical formulas due to its excellent performance and cost-effectiveness in a variety of fields, including solubility, dispersion, suspension, etc.[56-62] Ionic/nonionic mixed surfactants are often used in many biophysical applications because they provide more flexible physicochemical properties for synergistic monitoring in RMs.[126] In addition to the significant changes in the doping interfacial properties of nonionic surfactants in the interface of ionic surfactants of RM, it also changes the water structure inside the water pool of RMs.

ESPT process is widely studied from the acid group of excited photoacids to the nearby solvent (aqueous, non-aqueous, binary mixtures, etc.) of two molecules (one is a proton donor and another is a proton acceptor). The proton is transferred from neutral photo acids in ES (ROH^*) to a neighbouring water molecule and forms a $RO^{-*}\cdots H_3O^+$ contact ion pair (CIP^*) which successively dissociates by proton transfer to another water molecule next to the H_3O^+.[127, 128] It is well understood that protons move inside the water-hydrogen-bound network. Over the last few decades, ESPT dynamics within a wide range of water solvent mixtures have been extensively investigated.[129-131] In the ground state, such a fluorophore (or photoacid) is usually weakly acidic, but due to unexpected redistribution of electronic charges, it unexpectedly transforms to a strong acid in the excited-state. The driving force of the reaction has a big impact on how different photoacids behave. Weaker photoacids in ES cannot undergo ESPT in non-aqueous environments, and deprotonation is relatively slow, even in water, and contests with excited-state decay. In other protic solvents and some organic solvents, stronger photoacids will deprotonate.[132] The firefly photoacid (D-luciferin)

chemiluminescence, which has been thoroughly studied in the literature for decades[81, 82, 133], has a moderate pK_a of 8.7[134] in the GS and a remarkably low pK_a* of 0.5[135] in the ES. Again, HPTS (8-Hydroxypyrene-1,3,6-trisulfonic acid tri-sodium salt) is another standard photoacid that has been thoroughly studied in the literature for decades[136, 137] and has a moderate pK_a in the GS of 7.2-7.7[138, 139] and a remarkably low pK_a* in an ES of 0.5-1.4.[139, 140] In most cases, the reaction continues as a standard over-the-barrier mechanism after solvent relaxation.[132] Numerous studies have previously been performed on the ESPT process in different neat solvent and solvent mixtures.[82, 91, 141, 142]

In addition, this dissertation explores how probing two-photon mediated emission of a dye provides information on the local environment of aggregated structures, using home-built two-photon absorption (TPA or 2PA) spectroscopy (Chapter 3). The 2PA is a nonlinear optical phenomenon of the third order[143], in which a molecule absorbs two photons at the same time.[144, 145] This system's transition energy is equal to the sum of the energies of the two absorbed photons. The 2PA processes, as predicted by Maria Göppert-Mayer in 1931, are one of the most sensitive methods[146] and the first experimental evidence was predicted by the Kaiser and Garret group for this phenomenon.[147] The 2PA technique has successfully been applied in various research fields including fluorescence microscopy[148], nanofabrication[149], up-converted lasing[150], localized release of bio-active species[151], 3D optical memory[152, 153], optical power limiting[154] protein (un)folding[155, 156] and photodynamic therapy[157, 158]. The main advantage of 2PA spectroscopy is its low energy which leaves biomolecules unharmed, high penetration depth, and the 2PA process occurs only at the focal point (within a very small volume element). Currently, 2PA of fluorescent lase dyes is a rapidly expanding research field, as tunable femtosecond lasers are accessible to provide a high-intensity light source ideal for 2PA observation and analysis. In this dissertation, a higher amplifier controllable femtosecond laser is used for quantitative 2PA spectroscopy of fluorescent laser dyes. The performance of 2PA tends to vary with wavelength and is characteristic of a specific laser dye or chromophore, similar to traditional linear absorption spectra. However, the rate of a 2PA transition increases as the square of the number of photons incident on the sample for every unit area per unit time increases, i.e. when the laser source is narrowly focused, 2PA happens predominantly at the focal volume, in which the intensity is highest. The wavelength and concentration dependence of spectroscopy studies using linear (one-photon) absorption (1PA) and 2PA spectroscopy studies are both the same. This technique enables one to measure absorption cross-section (TPACS, σ_2 as discussed in chapter 2) of dye

molecules bound to biomolecules or macromolecules, which is typically expressed in terms of Göppert-Mayer units (1 GM= 10^{-50} cm^4 s $photon^{-1}$) and provides a unique opportunity to confer on the probe environment in various environments. To create structure-property relationships for different organic and inorganic chromophores, quantitative 2PA spectroscopy is used and is a key to the design of newly efficient 2PA materials. Previously, intermolecular interactions with elongated π-conjugation and multi-branched moieties have significant molecular nonlinear absorptivity[159] and researchers have also shown that multi-branched chromophore structures (such as tri-substituted systems) have large nonlinear optical properties in the near-infrared (NIR) environment. Another major aspect of 2PA is in the field of microscopy and has the potential to perform detailed imaging of cells and tissues in greater detail and over a longer time. In 1990, the high-resolution two-photon microscopy (2PM) was developed by Denk et al.[160] Due to the problems presented by scattering effects, this 2PM was limited to thin-section preparations and can reduce the scattering effect via this technique. Fluorescence microscopy is so precise that the background of several fluorescent molecules can only detect such fluorescent molecules. The technique will also notify the distribution of fluorophore-labeled molecules, cells, or tissues to assist in their imaging. The 2PM is the favored imaging technique by far and provides 2PA materials labeled on cells or two-photon laser excitation issues.[161, 162] The primary distinction between one-photon excitation fluorescence and two-photon excitation fluorescence (1PEF & 2PEF) is that the fluorescence (2PA) collected is proportional to the square of incident light intensity (2PEF ~ I^2). Fluorescence is collected from a tiny volume (<1 μm^3) at the focus of the highly localized excitation beam during two-photon excitation. Therefore, the use of two-photons in the near-IR range, which corresponds to an 'optical window' for biological tissue, would be an appropriate alternative.[163]

Previous studies have shown that the 2PA spectrum suffers solvent effect in both neutral and ionic chromophores.[164] 2PA cross-sections of popular organic dyes including anthracene, fluorescein, and some rhodamines have also been documented in the literature at specific wavelengths.[165-167] The transition dipole moment and the fluctuation in the dipole moment after excitation have a big impact on the 2PACS of chromophores. Such compounds typically provide higher load-separation, transition dipole moment, and shift in dipole moment after excitation, which is very crucial for improving the 2PACS. The ultimate aim of previously designing new molecules for the significant predictors is to produce a good separation of the charge in ES, which affects the shift in the dipole moment to increase the

2PA cross-sections. To improve the 2PACS, several organic and inorganic materials were previously designed.[166-171] The change in the 2PACS was examined before determining the binding mode based on the DNA electric field-induced perturbation of the transition dipole of the dye. The local electrical fields have been shown to affect the 2PACS.[172-174] Researchers have reported the effect of fluorophore molecules in aqueous micellar solutions[175], and enhancement of σ_2 value in cyclodextrin systems.[176]

The primary goal of this dissertation is to comprehend the changes in the physical properties of fluorescence/laser dyes in presence of different biological and biomimetic systems (e.g. model proteins, micelles, reverse micelles, mixtures of RM, pure solvents, binary mixtures, etc.) in presence of varied environments (temperature, pH, concentration, etc.) using different experimental techniques, such as dynamic light scattering (DLS), Fourier transform infrared (FTIR) spectroscopy, time-resolved fluorescence spectroscopy (TRFS), circular dichroism (CD) spectroscopy and two-photon absorption spectroscopy (TPAS). DLS is used to measure the hydrodynamic diameter (d_H) of RM droplets. FTIR is used to investigate the hydrogen bonding in water in the mid-infrared (MIR) region[47, 177-181], by deconvolution of water spectrum into three distinct types of hydrogen bonding environments, namely, multimer or isolated water (MW, water molecule which is not hydrogen-bonded to any neighbouring molecule), intermediate water (IW, unable to develop fully hydrogen-bonded structure) and hydrogen-bonded water (HW, tetrahedrally hydrogen-bonded water).[20, 182] Fluorescence spectroscopy is a flexible tool for representing the polarity and microenvironment around the molecule of a probe.[23, 183, 184] To provide adequate information and geometry of the desired interface and to investigate the hydration dynamics in biomolecules, supramolecular assemblies such as protein[6, 185, 186], DNA[187-190], micelle[166, 169-171], RM[191-194], etc, TRFS has been used for years. TRFS has revealed at least two types of water species in these restricted systems, namely 'bound' water molecules associated at the surfactant interface offering slower dynamics than that of pure water (timescale from hundreds of ps to few ns) and 'bulk-type' water molecules.[186, 195] This slow relaxation mechanism, which is effectively a coupled rotational-translational orientation of water molecules, has recently emerged as a potential method for realizing the interaction of restricted water molecules with the interface. Solvent relaxation for water is well known to be orders of magnitude slower in the vicinity of the interface compared to that in pure water. TRFS study of bulk water yields two-time scales: ~100 fs and ~1 ps.[19, 196] In restricted systems, however, two kinds of water coexist, firstly the water molecules with faster

dynamics (~ few ps) and the other is slower in dynamics with a time scale of hundreds of ps to several ns.[191, 197-200] The root of this bimodal water distribution can be recognized as 'bound' water molecules that are bound to the polar interface providing significantly slower dynamics than that of pure and 'free-type' water molecules that are not bound to the interface by hydrogen but remain in the hydration layer.[201]

The dissertation's main objective is to investigate the photophysical processes of the excited-state in a variety of bimolecular and biomimetic recognitions. The thesis also covers two large categories, such as (a) ESPT dynamics of D-luciferin in various micro-heterogeneous environments (such as RMs, mixed RMs, binary mixture): the possible role of hydration dynamics on controlling the ESPT dynamics and (b) probing two-photon induced emission of a dye to extract information on the local environment of aggregated systems using 2-photon absorption spectroscopy.

Summary of Dissertation

This dissertation contains 9 chapters (Ch). The remaining of the dissertation is formulated in the following manner, apart from this chapter:

Chapter 2 describes the main concepts of some of the relevant basic theories, information, and experimental methods that we have used. In this chapter, the chemical structure of the samples used is also given.

Chapter 3 briefly describes the experimental setup and the basic working principle used throughout the dissertation.

ESPT Studies (Ch. 4, 5 & 6)

Chapter 4 presents the effect of the mixing of surfactants as we have investigated the ESPT reaction of D-luciferin in mixed RM systems composed of non-ionic polyoxyethylene (5) nonylphenylether (Igepal CO-520) with cationic di-dodecyl dimethyl ammonium bromide (DDAB) and anionic sodium bis-(2-ethylhexyl) sulfosuccinate (AOT) in cyclohexane (Cy) at different mole fractions of Ig (X_{Ig}) and fixed hydration (w_0=10). This section is published in *Journal of American Chemical Society Omega 2018, 3, 5715−5724.*

Chapter 5 analyzed the ESPT process in AOT, Ig, and DDAB RMs at different temperatures, also to identify the specific role of solvation during the ESPT process. This section is published in *Journal of Photochemistry & Photobiology, A: Chemistry 404 (2021) 112928.*

Chapter 6 identifies how micro-heterogeneity in the aqueous environment affects the ESPT process; we investigate the ESPT of D-luciferin in aqueous mixtures of water-ethanol and water-TFE.

Two-Photon Spectroscopy Studies (Ch. 7 & 8)

Chapter 7 addressed the specific binding of probes with protein, and we investigated whether this could be exploited by using the unique spectroscopic technique, 2-photon absorption spectroscopy, to understand site-specific binding as well as conformational changes of proteins during thermal/chemical denaturation. This section is published in *Journal of Fluorescence, 2017, 28 (3), 855-862.*

Chapter 8 demonstrated that the 2PAS could be used to investigate the molecular basis of cationic dye-surfactant (anionic) interactions, which were verified by classical simulation studies. To see if the hydrophobicity of the surfactant influences complex formation, we altered the chain length of anionic surfactants while keeping the cationic dye constant.

Chapter 9 provides, along with some future plans, a concluding remark on the work carried out in the dissertation.

1.2: References

1. Zhang, T.-H.; Luo, J.; Zhou, J.-M., Conformational changes at the active site of adenylate kinase detected using a fluorescent probe and monoclonal antibody binding. *Biochimie* **2002,** *84* (4), 335-339.
2. Bautista-Gomez, J.; Usman, A.; Zhang, M.; Rafferty, R. J.; Bossmann, S. H.; Hohn, K. L.; Higgins, D. A., Fluorescence spectroscopy studies of crossed aldol reactions: a reactive Nile red dye reveals catalyst-dependent product formation. *Catalysis Science & Technology* **2020,** *10* (16), 5579-5592.
3. Flora, K.; Brennan, J. D.; Baker, G. A.; Doody, M. A.; Bright, F. V., Unfolding of acrylodan-labeled human serum albumin probed by steady-state and time-resolved fluorescence methods. *Biophysical journal* **1998,** *75* (2), 1084-1096.
4. Lakowicz, J. R., *Principles of fluorescence spectroscopy*. Springer science & business media: 2013.
5. Fleming, G., Chemical applications of ultrafast spectroscopy. **1986**.
6. Pal, S. K.; Peon, J.; Zewail, A. H., Biological water at the protein surface: Dynamical solvation probed directly with femtosecond resolution. *Proceedings of the National Academy of Sciences* **2002,** *99* (4), 1763-1768.
7. Bhattacharyya, K., Nature of biological water: a femtosecond study. *Chem. Commun.* **2008,** *44*, 2848-2857.
8. Stennett, E. M.; Ciuba, M. A.; Levitus, M., Photophysical processes in single molecule organic fluorescent probes. *Chemical Society Reviews* **2014,** *43* (4), 1057-1075.

9. Rossi, A. M.; Taylor, C. W., Analysis of protein-ligand interactions by fluorescence polarization. *Nature Protocols* **2011,** *6*, 365–387.
10. Paul, B. K.; Moulik, S. P., Microemulsions: an overview. *Journal of Dispersion science and Technology* **1997,** *18* (4), 301-367.
11. Silber, J. J.; Falcone, R. D.; Correa, N. M.; Biasutti, M. A.; Abuin, E.; Lissi, E.; Campodonico, P., Exploratory study of the effect of polar solvents upon the partitioning of solutes in nonaqueous reverse micellar solutions. *Langmuir* **2003,** *19* (6), 2067-2071.
12. Luisi, P. L.; Straub, B., *Reverse Micelles: Biological and Technological Relevance of Amphiphilic Structures in Apolar Media*. Plenum Pub Corp: 1984.
13. Khoshnood, A.; Firoozabadi, A., Polar solvents trigger formation of reverse micelles. *Langmuir* **2015,** *31* (22), 5982-5991.
14. Furusaki, S.; Ichikawa, S.; Goto, M., Recent advances in reversed micellar techniques for bioseparation. *Progress in Biotechnology* **2000,** *16*, 133-136.
15. Carvalho, C. M.; Cabral, J. M., Reverse micelles as reaction media for lipases. *Biochimie* **2000,** *82* (11), 1063-1085.
16. Luisi, P.; Giomini, M.; Pileni, M.; Robinson, B., Reverse micelles as hosts for proteins and small molecules. *Biochimica et Biophysica Acta (BBA)-Reviews on Biomembranes* **1988,** *947* (1), 209-246.
17. Melo, E.; Aires-Barros, M.; Cabral, J., Reverse micelles and protein biotechnology. *Biotechnology annual review* **2001,** *7*, 87-129.
18. Mathew, D. S.; Juang, R.-S., Role of alcohols in the formation of inverse microemulsions and back extraction of proteins/enzymes in a reverse micellar system. *Separation and purification technology* **2007,** *53* (3), 199-215.
19. Fayer, M. D.; Levinger, N. E., Analysis of water in confined geometries and at interfaces. *Annual Review of Analytical Chemistry* **2010,** *3*, 89-107.
20. Moilanen, D. E.; Levinger, N. E.; Spry, D.; Fayer, M., Confinement or the nature of the interface? Dynamics of nanoscopic water. *Journal of the American Chemical Society* **2007,** *129* (46), 14311-14318.
21. Bakulin, A. A.; Cringus, D.; Pieniazek, P. A.; Skinner, J. L.; Jansen, T. L. C.; Pshenichnikov, M. S., Dynamics of Water Confined in Reversed Micelles: Multidimensional Vibrational Spectroscopy Study. *The Journal of Physical Chemistry B* **2013,** *117* (49), 15545-15558.
22. Costard, R.; Levinger, N. E.; Nibbering, E. T. J.; Elsaesser, T., Ultrafast Vibrational Dynamics of Water Confined in Phospholipid Reverse Micelles. *The Journal of Physical Chemistry B* **2012,** *116* (19), 5752-5759.
23. Bhattacharyya, K., Solvation dynamics and proton transfer in supramolecular assemblies. *Accounts of chemical research* **2003,** *36* (2), 95-101.
24. Bhattacharyya, K.; Bagchi, B., Slow dynamics of constrained water in complex geometries. *The Journal of Physical Chemistry A* **2000,** *104* (46), 10603-10613.
25. Nandi, N.; Bhattacharyya, K.; Bagchi, B., Dielectric relaxation and solvation dynamics of water in complex chemical and biological systems. *Chemical Reviews* **2000,** *100* (6), 2013-2046.
26. Svensson, B.; Olsson, U.; Alexandridis, P.; Mortensen, K., A SANS investigation of reverse (water-in-oil) micelles of amphiphilic block copolymers. *Macromolecules* **1999,** *32* (20), 6725-6733.
27. Shrestha, L. K.; Sato, T.; Aramaki, K., Intrinsic parameters for structural variation of reverse micelles in nonionic surfactant (glycerol α-monolaurate)/oil systems: a SAXS study. *Physical Chemistry Chemical Physics* **2009,** *11* (21), 4251-4259.
28. Simmons, B. A.; Taylor, C. E.; Landis, F. A.; John, V. T.; McPherson, G. L.; Schwartz, D. K.; Moore, R., Microstructure determination of AOT+ phenol organogels

utilizing small-angle X-ray scattering and atomic force microscopy. *Journal of the American Chemical Society* **2001,** *123* (10), 2414-2421.
29. Vasquez, V.; Williams, B.; Graeve, O., Stability and comparative analysis of AOT/water/isooctane reverse micelle system using dynamic light scattering and molecular dynamics. *The Journal of Physical Chemistry B* **2011,** *115* (12), 2979-2987.
30. Rosenfeld, D. E.; Schmuttenmaer, C. A., Dynamics of Water Confined Within Reverse Micelles. *The Journal of Physical Chemistry B* **2006,** *110*, 14304-14312
31. Levinger, N. E.; Swafford, L. A., Ultrafast Dynamics in Reverse Micelles. *Annual Review of Physical Chemistry* **2009,** *60*, 385-406.
32. Levinger, N. E., Water in confinement *Science* **2002,** *298*, 1722-1723.
33. Dokter, A. M.; Woutersen, S.; Bakker, H. J., Inhomogeneous dynamics in confined water nanodroplets. *Proceedings of the National Academy of Sciences* **2006,** *103* (42), 15355-15358.
34. Moilanen, D. E.; Fenn, E. E.; Wong, D.; Fayer, M. D., Water dynamics in large and small reverse micelles: From two ensembles to collective behavior. *The Journal of chemical physics* **2009,** *131* (1), 014704.
35. Fayer, M. D., Water in a Crowd. *Physiology* **2011,** *26*, 381-392.
36. Bagchi, B., Water Dynamics in the Hydration Layer around Proteins and Micelles. *Chemical Reviews* **2005,** *105* (9), 3197-3219.
37. Valero, M.; Sanchez, F.; Gomez-Herrera, C.; Lopez-Cornejo, P., Study of water solubilized in AOT/n-decane/water microemulsions. *Chemical Physics* **2008,** *345* (1), 65-72.
38. Moran, P. D.; Bowmaker, G. A.; Cooney, R. P.; Bartlett, J. R.; Woolfrey, J. L., Vibrational spectroscopic study of the structure of sodium bis (2-ethylhexyl) sulfosuccinate reverse micelles and water-in-oil microemulsions. *Langmuir* **1995,** *11* (3), 738-743.
39. Christopher, D. J.; Yarwood, J.; Belton, P. S.; Hills, B. P., A Fourier transform infrared study of water—head group interactions in reversed micelles containing sodium bis (2-ethylhexyl) sulfosuccinate (AOT). *Journal of colloid and interface science* **1992,** *152* (2), 465-472.
40. El Seoud, O. A., Use of NMR to probe the structure of water at interfaces of organized assemblies. *Journal of Molecular Liquids* **1997,** *72* (1–3), 85-103.
41. Correa, N. M.; Silber, J. J.; Riter, R. E.; Levinger, N. E., Nonaqueous polar solvents in reverse micelle systems. *Chemical reviews* **2012,** *112* (8), 4569-4602.
42. Piletic, I. R.; Moilanen, D. E.; Spry, D. B.; Levinger, N. E.; Fayer, M. D., Testing the Core/Shell Model of Nanoconfined Water in Reverse Micelles Using Linear and Nonlinear IR Spectroscopy. *The Journal of Physical Chemistry A* **2006,** *110* (15), 4985-4999.
43. Dokter, A. M.; Woutersen, S.; Bakker, H. J., Ultrafast dynamics of water in cationic micelles. *The Journal of Chemical Physics* **2007,** *126* (12), 124507.
44. Biswas, R.; Furtado, J.; Bagchi, B., Layerwise decomposition of water dynamics in reverse micelles: A simulation study of two-dimensional infrared spectrum. *The Journal of Chemical Physics* **2013,** *139* (14), 144906.
45. Fenn, E. E.; Wong, D. B.; Fayer, M. D., Water dynamics at neutral and ionic interfaces. *P Natl Acad Sci USA* **2009,** *106* (36), 15243-15248.
46. Dokter, A. M.; Woutersen, S.; Bakker, H. J., Anomalous slowing down of the vibrational relaxation of liquid water upon nanoscale confinement. *Physical review letters* **2005,** *94* (17), 178301.
47. Fayer, M. D., Dynamics of Water Interacting with Interfaces, Molecules, and Ions. *Accounts of Chemical Research* **2012,** *45*, 3-14.
48. Tan, H.-S.; Piletic, I. R.; Fayer, M. D., Orientational dynamics of water confined on a nanometer length scale in reverse micelles. *The Journal of Chemical Physics* **2005,** *122*, 174501.

49. Levinger, N. E., Ultrafast dynamics in reverse micelles, microemulsions, and vesicles. *Current Opinion in Colloid & Interface Science* **2000,** *5*, 118-124.
50. Faeder, J.; Ladanyi, B. M., Molecular Dynamics Simulations of the Interior of Aqueous Reverse Micelles. *The Journal of Physical Chemistry B* **2000,** *104*, 1033-1046.
51. Sarkar, N.; Das, K.; Datta, A.; Das, S.; Bhattacharyya, K., Solvation dynamics of coumarin 480 in reverse micelles. Slow relaxation of water molecules. *The Journal of Physical Chemistry* **1996,** *100* (25), 10523-10527.
52. Harpham, M. R.; Ladanyi, B. M.; Levinger, N. E.; Herwig, K. W., Water motion in reverse micelles studied by quasielastic neutron scattering and molecular dynamics simulations. *The Journal of chemical physics* **2004,** *121* (16), 7855-7868.
53. Chattopadhyay, A.; Mukherjee, S.; Raghuraman, H., Reverse micellar organization and dynamics: a wavelength-selective fluorescence approach. *The Journal of Physical Chemistry B* **2002,** *106* (50), 13002-13009.
54. Cringus, D.; Lindner, J.; Milder, M. T.; Pshenichnikov, M. S.; Vöhringer, P.; Wiersma, D. A., Femtosecond water dynamics in reverse-micellar nanodroplets. *Chemical physics letters* **2005,** *408* (1), 162-168.
55. Pieniazek, P. A.; Lin, Y.-S.; Chowdhary, J.; Ladanyi, B. M.; Skinner, J., Vibrational spectroscopy and dynamics of water confined inside reverse micelles. *The Journal of Physical Chemistry B* **2009,** *113* (45), 15017-15028.
56. Zhang, S., Fabrication of novel biomaterials through molecular self-assembly. *Nature biotechnology* **2003,** *21* (10), 1171-1178.
57. Bumajdad, A.; Eastoe, J.; Nave, S.; Steytler, D. C.; Heenan, R. K.; Grillo, I., Compositions of mixed surfactant layers in microemulsions determined by small-angle neutron scattering. *Langmuir* **2003,** *19* (7), 2560-2567.
58. Lisiecki, I.; Pileni, M. P., Synthesis of copper metallic clusters using reverse micelles as microreactors. *Journal of the American Chemical Society* **1993,** *115* (10), 3887-3896.
59. Simmons, B. A.; Li, S.; John, V. T.; McPherson, G. L.; Bose, A.; Zhou, W.; He, J., Morphology of CdS nanocrystals synthesized in a mixed surfactant system. *Nano Letters* **2002,** *2* (4), 263-268.
60. Shi, H.; Qi, L.; Ma, J.; Wu, N., Architectural control of hierarchical nanobelt superstructures in catanionic reverse micelles. *Advanced Functional Materials* **2005,** *15* (3), 442-450.
61. Alexandridis, P.; Olsson, U.; Lindman, B., A record nine different phases (four cubic, two hexagonal, and one lamellar lyotropic liquid crystalline and two micellar solutions) in a ternary isothermal system of an amphiphilic block copolymer and selective solvents (water and oil). *Langmuir* **1998,** *14* (10), 2627-2638.
62. Pandalai, S. G., Recent Research Developments in Physical Chemistry. *Research Signpost* **2000,** *8* (4(Pt. 2)), 337.
63. Paul, B. K.; Mitra, R. K., Water solubilization capacity of mixed reverse micelles: effect of surfactant component, the nature of the oil, and electrolyte concentration. *Journal of colloid and interface science* **2005,** *288* (1), 261-279.
64. Kunieda, H.; Yamagata, M., Mixing of nonionic surfactants at water-oil interfaces in microemulsions. *Langmuir* **1993,** *9* 3345-3351.
65. Pes, M. A.; Kunieda, H., Surfactant distribution in mixed surfactant microemulsions. *Trends Phys. Chem.* **1995,** *5*, 75-89.
66. Hou, M. J.; Shah, D. O., Effects of the molecular structure of the interface and continuous phase on solubilization of water in water/oil microemulsions. *Langmuir* **1987,** *3*, 1086-1096.

67. Huibers, P. D. T.; Shah, D. O., Evidence for Synergism in Nonionic Surfactant Mixtures: Enhancement of Solubilization in Water-in-Oil Microemulsions. *Langmuir* **1997,** *13*, 5762 - 5765.
68. Mitra, R. K.; Paul, B. K., Effect of NaCl and temperature on the water solubilization behavior of AOT/nonionics mixed reverse micellar systems stabilized in IPM oil. *Colloids and Surfaces A* **2005,** *255*, 165-180.
69. Mitra, R. K.; Paul, B. K.; Moulik, S. P., Phase behavior, interfacial composition and thermodynamic properties of mixed surfactant (CTAB and Brij-58) derived w/o microemulsions with 1-butanol and 1-pentanol as cosurfactants and n-heptane and n-decane as oils. *J. Colloid Interface Sci.* **2006,** *300*, 755-764.
70. Kinugasa, T.; Kondo, A.; Nishimura, S.; Miyauchi, Y.; Nishii, Y.; Watanabe, K.; Takeuchi, H., Estimation for size of reverse micelles formed by AOT and SDEHP based on viscosity measurement. *Colloids and Surfaces, A: Physicochemical and Engineering Aspects* **2002,** *204*, 193-199.
71. Liu, D.; Ma, J.; Cheng, H.; Zhao, Z., Fluorescence probing of mixed reverse micelles formed with AOT and nonionic surfactants in n-heptane. *Colloids and Surfaces A: Physicochemical and Engineering Aspects* **1998,** *139*, 21-26.
72. Chatterjee, S.; Mitra, R. K.; Paul, B. K.; Bhattacharya, S. C., Interface of AOT/Brij mixed reverse micellar systems: Conductometric and spectrophotometric investigations. *J. Colloid Interface Sci.* **2006,** *298*, 935-941.
73. Chatterjee, S.; Nandi, S.; Bhattacharya, S. C., Interface of AOT/Igepal CO720/cyclohexane/water mixed reverse micelle by spectroscopic approach. *Colloids and Surfaces A: Physicochemical and Engineering Aspects* **2006,** *279*, 58-63.
74. Bumajdad, A.; Eastoe, J.; Heenan, R. K.; Lu, R. J.; Steytler, D. C. S.; Egelhaaf, S., E., Mixing in cationic surfactant films studied by small-angle neutron scattering. *J. Chem. Soc., Faraday Trans.* **1998,** *94*, 2143-2150.
75. Bumajdad, A.; Eastoe, J.; Griffiths, P.; Steytler, D. C.; Heenan, R. K.; Lu, J. R.; Timmins, P., Interfacial Compositions and Phase Structures in Mixed Surfactant Microemulsions. *Langmuir* **1999,** *15*, 5271-5278.
76. Sarkar, M.; Poddar, S., Studies on the interaction of surfactants with cationic dye by absorption spectroscopy. *J. Colloid Interface Sci.* **2000,** *221*, 181-185.
77. Brubach, J.-B.; Mermet, A.; Filabozzi, A.; Gerschel, A.; Lairez, D.; Krafft, M.; Roy, P., Dependence of water dynamics upon confinement size. *The Journal of Physical Chemistry B* **2001,** *105* (2), 430-435.
78. Lawler, C.; Fayer, M. D., Proton Transfer in Ionic and Neutral Reverse Micelles. *The Journal of Physical Chemistry B* **2015,** *119* (19), 6024-6034.
79. Mitra, R. K.; Sinha, S. S.; Pal, S. K., Temperature-Dependent Solvation Dynamics of Water in Sodium Bis(2-ethylhexyl)sulfosuccinate/Isooctane Reverse Micelles. *Langmuir* **2008,** *24* (1), 49-56.
80. Singh, S.; Koley, S.; Mishra, K.; Ghosh, S., An Approach to a Model Free Analysis of Excited-State Proton Transfer Kinetics in a Reverse Micelle. *The Journal of Physical Chemistry C* **2018,** *122* (1), 732-740.
81. Kuchlyan, J.; Banik, D.; Roy, A.; Kundu, N.; Sarkar, N., Excited-State Proton Transfer Dynamics of Firefly's Chromophore D-Luciferin in DMSO–Water Binary Mixture. *The Journal of Physical Chemistry B* **2014,** *118* (48), 13946-13953.
82. Presiado, I.; Erez, Y.; Huppert, D., Excited-State Intermolecular Proton Transfer of the Firefly's Chromophore d-Luciferin. 2. Water− Methanol Mixtures. *The Journal of Physical Chemistry A* **2010,** *114* (35), 9471-9479.

83. Matsugami, M.; Yamamoto, R.; Kumai, T.; Tanaka, M.; Umecky, T.; Takamuku, T., Hydrogen bonding in ethanol–water and trifluoroethanol–water mixtures studied by NMR and molecular dynamics simulation. *Journal of Molecular Liquids* **2016,** *217*, 3-11.
84. Marcus, R. A., Theoretical relations among rate constants, barriers, and Broensted slopes of chemical reactions. *The Journal of Physical Chemistry* **1968,** *72* (3), 891-899.
85. Douhal, A.; Lahmani, F.; Zehnacker-Rentien, A.; Amat-Guerri, F., Excited-State Proton (or Hydrogen Atom) Transfer in Jet-Cooled 2-(2'-Hydroxyphenyl-5-phenyloxazole. *The Journal of Physical Chemistry* **1994,** *98* (47), 12198-12205.
86. Cohen, B.; Martin Álvarez, C.; Alarcos Carmona, N.; Organero, J. A.; Douhal, A., Proton-Transfer Reaction Dynamics within the Human Serum Albumin Protein. *The Journal of Physical Chemistry B* **2011,** *115* (23), 7637-7647.
87. Wilson, T.; Hastings, J. W., Bioluminescence. *Annual review of cell and developmental biology* **1998,** *14* (1), 197-230.
88. Tautomerism; Sciacovelli, O.; Dell 'atti, A.; De Giglio, A.; Cassidei, L.; Tautomerism, I. K.-E., Studies on Phenylpyruvic Acid. *Zeitschrift für Naturforschung C* **1976,** *31* (1-2), 5-11.
89. Valadbeigi, Y.; Farrokhpour, H., Theoretical study on keto–enol tautomerism and isomerization in pyruvic acid. *International Journal of Quantum Chemistry* **2013,** *113* (21), 2372-2378.
90. Tansila, N.; Tantimongcolwat, T.; Isarankura-Na-Ayudhya, C.; Nantasenamat, C.; Prachayasittikul, V., Rational design of analyte channels of the green fluorescent protein for biosensor applications. *Int J Biol Sci* **2007,** *3*, 463-470.
91. Erez, Y.; Huppert, D., Excited-State Intermolecular Proton Transfer of the Firefly's Chromophore d-Luciferin. *The Journal of Physical Chemistry A* **2010,** *114* (31), 8075-8082.
92. Presiado, I.; Erez, Y.; Huppert, D., Excited-state intermolecular proton transfer of firefly luciferin III. Proton transfer to a mild base. *The Journal of Physical Chemistry A* **2010,** *114* (51), 13337-13346.
93. Takeuchi, S.; Tahara, T., Coherent Nuclear Wavepacket Motions in Ultrafast Excited-State Intramolecular Proton Transfer: Sub-30-fs Resolved Pump− Probe Absorption Spectroscopy of 10-Hydroxybenzo [h] quinoline in Solution. *The Journal of Physical Chemistry A* **2005,** *109* (45), 10199-10207.
94. Simkovitch, R.; Huppert, D., Photoprotolytic processes of umbelliferone and proposed function in resistance to fungal infection. *The Journal of Physical Chemistry B* **2015,** *119* (46), 14683-14696.
95. Nelson, K. J.; Brown, P. J.; Rudel, H. E.; Takematsu, K., Divergent excited state proton transfer reactions of bifunctional photoacids 1-ammonium-2-naphthol and 3-ammonium-2-naphthol in water and methanol. *Physical Chemistry Chemical Physics* **2019,** *21* (44), 24383-24392.
96. Weber, K., The close relationship of fluorescence obliteration to the inhibition of photochemical reactions. *Z. Phys. Chem., Abt. B* **1931,** *15*, 18-44.
97. Kwon, J. E.; Park, S. Y., Advanced organic optoelectronic materials: Harnessing excited- state intramolecular proton transfer (ESIPT) process. *Advanced Materials* **2011,** *23* (32), 3615-3642.
98. Stasyuk, A. J.; Chen, Y.-T.; Chen, C.-L.; Wu, P.-J.; Chou, P.-T., A new class of N–H excited-state intramolecular proton transfer (ESIPT) molecules bearing localized zwitterionic tautomers. *Physical Chemistry Chemical Physics* **2016,** *18* (35), 24428-24436.
99. Forés, M.; Duran, M.; Solà, M.; Adamowicz, L., Excited-State Intramolecular Proton Transfer and Rotamerism of 2-(2 '-hydroxyvinyl) benzimidazole and 2-(2 '-hydroxyphenyl) imidazole. *The Journal of Physical Chemistry A* **1999,** *103* (22), 4413-4420.

100. Nishina, N.; Mutai, T.; Aihara, J.-i., Excited-state intramolecular proton transfer and global aromaticity. *The Journal of Physical Chemistry A* **2017,** *121* (1), 151-161.
101. Weller, A., Quantitative untersuchungen der fluoreszenzumwandlung bei naphtholen. *Zeitschrift für Elektrochemie, Berichte der Bunsengesellschaft für physikalische Chemie* **1952,** *56* (7), 662-668.
102. Phukon, A.; Ray, S.; Sahu, K., Effect of cosurfactants on the interfacial hydration of CTAB quaternary reverse micelle probed using excited state proton transfer. *Langmuir* **2016,** *32* (41), 10659-10667.
103. Phukon, A.; Ray, S.; Sahu, K., How does interfacial hydration alter during rod to sphere transition in DDAB/water/cyclohexane reverse micelles? Insights from excited state proton transfer and fluorescence anisotropy. *Langmuir* **2016,** *32* (26), 6656-6665.
104. Rakshit, S.; Saha, R.; Verma, P. K.; Pal, S. K., Role of Solvation Dynamics in Excited State Proton Transfer of 1- Naphthol in Nanoscopic Water Clusters Formed in a Hydrophobic Solvent. *Photochemistry and photobiology* **2012,** *88* (4), 851-859.
105. Cohen, B.; Huppert, D.; Solntsev, K. M.; Tsfadia, Y.; Nachliel, E.; Gutman, M., Excited State Proton Transfer in Reverse Micelles. *J. Am. Chem. Soc.* **2002,** *124*, 7539-7547.
106. Mallick, A.; Purkayastha, P.; Chattopadhyay, N., Photoprocesses of excited molecules in confined liquid environments: An overview. *J. Photochem. Photobiol. C: Photochem. Rev.* **2007,** *8*, 109-127.
107. Singamaneni, R. R. N. a. S., Introduction: Bioinspired and Biomimetic Materials. *Chemical Reviews* **2017,** *117* (20), 12581-12583.
108. Hwang, J.; Jeong, Y.; Park, J. M.; Lee, K. H.; Hong, J. W.; Choi, J., Biomimetics: forecasting the future of science, engineering, and medicine. *Int J Nanomedicine* **2015,** *10*, 5701-5713.
109. Bar-Cohen, Y., *Biomimetics: Nature-Based Innovation*. Taylor & Francis: 2011.
110. Phukon, A.; Ray, S.; Sahu, K., How does interfacial hydration alter during rod to sphere transition in DDAB/water/cyclohexane reverse micelles? Insights from excited state proton transfer and fluorescence anisotropy. *Langmuir* **2016,** *32*, 6656-6665.
111. Lawler, C.; Fayer, M. D., Proton Transfer in Ionic and Neutral Reverse Micelles. *J. Phys. Chem. B* **2015,** *119*, 6024-6034.
112. Choudhury, S. D.; Pal, H., Modulation of Excited-State Proton-Transfer Reactions of 7-Hydroxy-4-methylcoumarin in Ionic and Nonionic Reverse Micelles. *J. Phys. Chem. B* **2009,** *113*, 6736-6744.
113. Kuchlyan, J.; Banik, D.; Kundu, N.; Ghosh, S.; Banerjee, C.; Sarkar, N., Effect of Confinement on Excited-State Proton Transfer of Firefly's Chromophore d-Luciferin in AOT Reverse Micelles. *J. Phys Chem. B* **2014,** *118*, 3401-3408.
114. Ghosh, D.; Batuta, S.; Begum, N. A.; Mandal, D., Proton transfer dynamics in a polar nanodroplet: ESIPT of 4'-n,n-dimethylamino-3-hydroxyflavone in AOT/alkane/water reverse micelles. *J. Lumin.* **2017,** *184*, 64-73.
115. Mukherjee, T. K.; Panda, D.; Datta, A., Excited-State Proton Transfer of 2-(2'-Pyridyl)benzimidazole in Microemulsions: Selective Enhancement and Slow Dynamics in Aerosol OT Reverse Micelles with an Aqueous Core. *J. Phys. Chem. B* **2005,** *109* 18895-18901.
116. Cohen, B.; Huppert, D.; Solntsev, K. M.; Tsfadia, Y.; Nachliel, E.; Gutman, M., Excited State Proton Transfer in Reverse Micelles. *Journal of the American Chemical Society* **2002,** *124* (25), 7539-7547.
117. Khorwal, V.; Sen, P., Ultrafast excited state intermolecular proton transfer dynamics of 2-(4'-Pyridyl)benzimidazole inside the nanocavity of reverse micelles. *J. Photochem. Photobiol. A* **2017,** *347*, 86-92.

118. Choudhury, S. D.; Nath, S.; Pal, H., Excited-State Proton Transfer Behavior of 7-Hydroxy-4-methylcoumarin in AOT Reverse Micelles. *J. Phys. Chem. B* **2008,** *112*, 7748-7753.
119. Spry, D. B.; Goun, A.; Glusac, K.; Moilanen, D. E.; Fayer, M. D., Proton transport and the water environment in nafion fuel cell membranes and AOT reverse micelles. *J. Am. Chem. Soc.* **2007,** *129*, 8122-8130.
120. Das, A.; Islam, S. I.; Das, D. K.; Mitra, R. K., Modulation of the Excited-State Proton Transfer Rate of d-luciferin in Mixed Reverse Micellar Systems. *ACS Omega* **2018,** *3* (5), 5715-5724.
121. Singh, S.; Koley, S.; Mishra, K.; Ghosh, S., An Approach to a Model Free Analysis of Excited-State Proton Transfer Kinetics in a Reverse Micelle. *J. Phys. Chem. C* **2018,** *122* (1), 732-740.
122. Sedgwick, M.; Cole, R. L.; Rithner, C. D.; Crans, D. C.; Levinger, N. E., Correlating proton transfer dynamics to probe location in confined environments. *J. Am. Chem. Soc.* **2012,** *134*, 11904-11907.
123. Koninti, R. K.; Gavvala, K.; Sengupta, A.; Hazra, P., Excited State Proton Transfer Dynamics of Topotecan Inside Biomimicking Nanocavity. *J. Phys. Chem. B* **2015,** *119*, 2363-2371.
124. Phukon, A.; Ray, S.; Sahu, K., Effect of Cosurfactants on the Interfacial Hydration of CTAB Quaternary Reverse Micelle Probed Using Excited State Proton Transfer. *Langmuir* **2016,** *32*, 10659-10667.
125. Rakshit, S.; Saha, R.; Verma, P. K.; Pal, S. K., Role of Solvation Dynamics in Excited State Proton Transfer of 1- Naphthol in Nanoscopic Water Clusters Formed in a Hydrophobic Solvent. *Photochem. Photobiol.* **2012,** *88*, 851-859.
126. Mitra, R. K.; Sinha, S. S.; Verma, P. K.; Pal, S. K., Modulation of dynamics and reactivity of water in reverse micelles of mixed surfactants. *The Journal of Physical Chemistry B* **2008,** *112* (41), 12946-12953.
127. Imadul Islam, S.; Das, A.; Mitra, R. K., Excited state proton transfer in reverse micelles: Effect of temperature and a possible interplay with solvation. *Journal of Photochemistry and Photobiology A: Chemistry* **2021,** *404*, 112928.
128. Kumpulainen, T.; Brouwer, A. M., Excited-state proton transfer and ion pair formation in a Cinchona organocatalyst. *Physical Chemistry Chemical Physics* **2012,** *14* (37), 13019-13026.
129. Agmon, N.; Huppert, D.; Masad, A.; Pines, E., Excited-state proton transfer to methanol-water mixtures. *The Journal of Physical Chemistry* **1991,** *95* (25), 10407-10413.
130. Suwaiyan, A.; Al-Adel, F.; Hamdan, A.; Klein, U. K. A., Dynamics of proton transfer from photon-initiated acids in alcohol/water mixtures. *The Journal of Physical Chemistry* **1990,** *94* (19), 7423-7429.
131. Solntsev, K. M.; Huppert, D.; Agmon, N.; Tolbert, L. M., Photochemistry of "super" photoacids. 2. Excited-state proton transfer in methanol/water mixtures. *The Journal of Physical Chemistry A* **2000,** *104* (19), 4658-4669.
132. Kumpulainen, T.; Lang, B.; Rosspeintner, A.; Vauthey, E., Ultrafast elementary photochemical processes of organic molecules in liquid solution. *Chemical reviews* **2017,** *117* (16), 10826-10939.
133. Presiado, I.; Erez, Y.; Simkovitch, R.; Shomer, S.; Gepshtein, R.; Pinto da Silva, L. s.; Esteves da Silva, J. C.; Huppert, D., Excited-state proton transfer of firefly dehydroluciferin. *The Journal of Physical Chemistry A* **2012,** *116* (44), 10770-10779.
134. Morton, R. A.; Hopkins, T. A.; Seliger, H. H., Spectroscopic properties of firefly luciferin and related compounds; an approach to product emission. *Biochemistry* **1969,** *8* (4), 1598-1607.

135. Erez, Y.; Presiado, I.; Gepshtein, R.; Pinto da Silva, L. s.; Esteves da Silva, J. C.; Huppert, D., Comparative study of the photoprotolytic reactions of D-luciferin and oxyluciferin. *The Journal of Physical Chemistry A* **2012,** *116* (28), 7452-7461.
136. Tran-Thi, T.-H.; Gustavsson, T.; Prayer, C.; Pommeret, S.; Hynes, J. T., Primary ultrafast events preceding the photoinduced proton transfer from pyranine to water. *Chemical Physics Letters* **2000,** *329* (5-6), 421-430.
137. Spry, D.; Goun, A.; Fayer, M. D., Deprotonation dynamics and Stokes shift of pyranine (HPTS). *The Journal of Physical Chemistry A* **2007,** *111* (2), 230-237.
138. Pines, E.; Huppert, D., Observation of geminate recombination in excited state proton transfer. *The Journal of chemical physics* **1986,** *84* (6), 3576-3577.
139. Bardez, E.; Goguillon, B. T.; Keh, E.; Valeur, B., Dynamics of excited-state reactions in reversed micelles. 1. Proton transfer involving a hydrophilic fluorescent probe. *The Journal of Physical Chemistry* **1984,** *88* (9), 1909-1913.
140. Smith, K.; Kaufmann, K.; Huppert, D.; Gutman, M., Picosecond proton ejection: an ultrafast pH jump. *Chemical Physics Letters* **1979,** *64* (3), 522-527.
141. Green, O.; Simkovitch, R.; Pinto da Silva, L. s.; Esteves da Silva, J. C.; Shabat, D.; Huppert, D., Excited-State Proton Transfer and Formation of the Excited Tautomer of 3-Hydroxypyridine-Dipicolinium Cyanine Dye. *The Journal of Physical Chemistry A* **2016,** *120* (31), 6184-6199.
142. Simkovitch, R.; Shomer, S.; Gepshtein, R.; Shabat, D.; Huppert, D., Excited-state proton transfer from quinone-cyanine 9 to protic polar-solvent mixtures. *The Journal of Physical Chemistry A* **2014,** *118* (10), 1832-1840.
143. Vodopyanov, K.; Richard, L. S., Handbook of nonlinear optics. *Opt Photonics News* **1997,** *8*, 54-55.
144. Andrews, D. L., Multiphoton absorption in molecules. In *Molecular Photophysics and Spectroscopy*, Morgan & Claypool Publishers: 2014; pp 14-11-14-17.
145. Rumi, M.; Perry, J. W., Two-photon absorption: an overview of measurements and principles. *Adv. Opt. Photon.* **2010,** *2* (4), 451-518.
146. Göppert-Mayer, M., Über Elementarakte mit zwei Quantensprüngen. *Annalen der Physik* **1931,** *401* (3), 273-294.
147. Kaiser, W.; Garrett, C., Two-photon excitation in Ca F 2: Eu 2+. *Physical review letters* **1961,** *7* (6), 229.
148. Zipfel, W. R.; Williams, R. M.; Webb, W. W., Nonlinear magic: multiphoton microscopy in the biosciences. *Nature biotechnology* **2003,** *21* (11), 1369.
149. Kuebler, S. M.; Cumpston, B. H.; Ananthavel, S.; Barlow, S.; Ehrlich, J. E.; Erskine, L.; Heikal, A. A.; McCord-Maughon, D.; Qin, J.; Roeckel, H. In *Three-dimensional microfabrication using two-photon-activated chemistry*, Micro-and Nano-photonic Materials and Devices, International Society for Optics and Photonics: 2000; pp 97-106.
150. Lin, T.-C.; Chung, S.-J.; Kim, K.-S.; Wang, X.; He, G. S.; Swiatkiewicz, J.; Pudavar, H. E.; Prasad, P. N., Organics and polymers with high two-photon activities and their applications. *Polymers for Photonics Applications II* **2003**, 157-193.
151. Ellis-Davies, G. C., Caged compounds: photorelease technology for control of cellular chemistry and physiology. *Nature methods* **2007,** *4* (8), 619-628.
152. Parthenopoulos, D. A.; Rentzepis, P. M., Three-dimensional optical storage memory. *Science* **1989,** *245* (4920), 843-845.
153. Burr, G., Volumetric storage Encyclopedia of Optical Engineering ed RB Johnson and RG Driggers. New York: Dekker: 2003.
154. Spangler, C., Recent development in the design of organic materials for optical power limiting. *Journal of Materials Chemistry* **1999,** *9* (9), 2013-2020.

155. Wang, Y.; Goodson, T., Early aggregation in prion peptide nanostructures investigated by nonlinear and ultrafast time-resolved fluorescence spectroscopy. *The Journal of Physical Chemistry B* **2007,** *111* (2), 327-330.
156. Cotlet, M.; Goodwin, P. M.; Waldo, G. S.; Werner, J. H., A comparison of the fluorescence dynamics of single molecules of a green fluorescent protein: one- versus two-photon excitation. *ChemPhysChem* **2006,** *7* (1), 250-260.
157. Bhawalkar, J.; Kumar, N.; Zhao, C.-F.; Prasad, P., Two-photon photodynamic therapy. *Journal of clinical laser medicine & surgery* **1997,** *15* (5), 201-204.
158. Liu, J.; Zhao, Y.; Zhao, J.; Xia, A.; Jiang, L.; Wu, S.; Ma, L.; Dong, Y.; Gu, Y., Two-photon excitation studies of hypocrellins for photodynamic therapy. *Journal of Photochemistry and Photobiology B: Biology* **2002,** *68* (2-3), 156-164.
159. Lin, T.-C.; Chen, Y.-F.; Hu, C.-L.; Hsu, C.-S., Two-photon absorption and optical power limiting properties in femtosecond regime of novel multi-branched chromophores based on tri-substituted olefinic scaffolds. *Journal of Materials Chemistry* **2009,** *19* (38), 7075-7080.
160. Denk, W.; Strickler, J. H.; Webb, W. W., Two-photon laser scanning fluorescence microscopy. *Science* **1990,** *248* (4951), 73-76.
161. Piston, D.; Masters, B.; Webb, W., Three- dimensionally resolved NAD (P) H cellular metabolic redox imaging of the in situ cornea with two- photon excitation laser scanning microscopy. *Journal of microscopy* **1995,** *178* (1), 20-27.
162. Shear, J. B.; Xu, C.; Webb, W. W., Multiphoton- excited visible emission by serotonin solutions. *Photochemistry and photobiology* **1997,** *65* (6), 931-936.
163. Alabugin, A., Near-IR Photochemistry for Biology: Exploiting the Optical Window of Tissue. *Photochemistry and Photobiology* **2019,** *95* (3), 722-732.
164. Woo, H. Y.; Liu, B.; Kohler, B.; Korystov, D.; Mikhailovsky, A.; Bazan, G. C., Solvent effects on the two-photon absorption of distyrylbenzene chromophores. *Journal of the American Chemical Society* **2005,** *127* (42), 14721-14729.
165. Peticolas, W. L.; Norris, R.; Rieckhoff, K. E., Polarization Effects in the Two- Photon Excitation of Anthracene Fluorescence. *The Journal of Chemical Physics* **1965,** *42* (12), 4164-4169.
166. Hermann, J.; Ducuing, J., Dispersion of the two-photon cross section in rhodamine dyes. *Optics Communications* **1972,** *6* (2), 101-105.
167. Li, S.; She, C., Two-photon Absorption Cross-section Measurements in Common Laser Dyes at 1· 06 μm. *Optica Acta: International Journal of Optics* **1982,** *29* (3), 281-287.
168. Drobizhev, M.; Tillo, S.; Makarov, N. S.; Hughes, T. E.; Rebane, A., Absolute two-photon absorption spectra and two-photon brightness of orange and red fluorescent proteins. *The journal of physical chemistry. B* **2009,** *113* (4), 855-859.
169. Woo, H. Y.; Hong, J. W.; Liu, B.; Mikhailovsky, A.; Korystov, D.; Bazan, G. C., Water-soluble [2.2] paracyclophane chromophores with large two-photon action cross sections. *Journal of the American Chemical Society* **2005,** *127* (3), 820-821.
170. Wielgus, M.; Michalska, J.; Samoc, M.; Bartkowiak, W., Two-photon solvatochromism III: Experimental study of the solvent effects on two-photon absorption spectrum of p-nitroaniline. *Dyes Pigm* **2015,** *113*, 426-434.
171. Nag, A.; De, A. K.; Goswami, D., Two-photon cross-section measurements using an optical chopper: z-scan and two-photon fluorescence schemes. *J. Phys. B: At. Mol. Opt. Phys.* **2009,** *42*, 065103.
172. Drobizhev, M.; Makarov, N. S.; Tillo, S. E.; Hughes, T. E.; Rebane, A., Two-photon absorption properties of fluorescent proteins. *Nature methods* **2011,** *8* (5), 393-399.

173. Drobizhev, M.; Tillo, S.; Makarov, N. S.; Hughes, T. E.; Rebane, A., Color hues in red fluorescent proteins are due to internal quadratic Stark effect. *The Journal of Physical Chemistry B* **2009,** *113* (39), 12860-12864.
174. Bairu, S.; Ramakrishna, G., Two-Photon Absorption Properties of Chromophores in Micelles: Electrostatic Interactions. *J. Phys Chem. B* **2013,** *117*, 10484-10491.
175. Woo, H. Y.; Korystov, D.; Mikhailovsky, A.; Nguyen, T.-Q.; Bazan, G. C., Two-photon absorption in aqueous micellar solutions. *Journal of the American Chemical Society* **2005,** *127* (40), 13794-13795.
176. Nag, O. K.; Nayak, R. R.; Lim, C. S.; Kim, I. H.; Kyhm, K.; Cho, B. R.; Woo, H. Y., Two-photon absorption properties of cationic 1, 4-Bis (styryl) benzene derivative and its inclusion complexes with cyclodextrins. *The Journal of Physical Chemistry B* **2010,** *114* (29), 9684-9690.
177. Cammarata, L.; Kazarian, S. G.; Salter, P. A.; Welton, T., Molecular states of water in room temperature ionic liquids. *Physical Chemistry Chemical Physics* **2001,** *3* (23), 5192-5200.
178. Jain, T. K.; Varshney, M.; Maitra, A., Structural studies of aerosol OT reverse micellar aggregates by FT-IR spectroscopy. *The Journal of Physical Chemistry* **1989,** *93* (21), 7409-7416.
179. Scatena, L. F.; Brown, M. G.; Richmond, G. L., Water at Hydrophobic Surfaces: Weak Hydrogen Bonding and Strong Orientation Effects. *Science* **2001,** *292*, 908-912.
180. Bakulin, A. A.; Liang, C.; la Cour Jansen, T.; Wiersma, D. A.; Bakker, H. J.; Pshenichnikov, M. S., Hydrophobic Solvation: A 2D IR Spectroscopic Inquest. *Accounts of Chemical Research* **2009,** *42* (9), 1229-1238.
181. Maréchal, Y., HORIZONS IN HYDROGEN BOND RESEARCH 1993 Proceedings of the Xth Workshop \ldHorizons in Hydrogen Bond Research\rd,IR spectroscopy of an exceptional H-bonded liquid: water. *Journal of Molecular Structure* **1994,** *322*, 105-111.
182. Brubach, J.-B.; Mermet, A.; Filabozzi, A.; Gerschel, A.; Lairez, D.; Krafft, M. P.; Roy, P., Dependence of Water Dynamics upon Confinement Size. *J. Phys. Chem. B* **2001,** *105*, 430-435.
183. Bhattacharyya, K., Nature of biological water: a femtosecond study. *Chemical Communications* **2008,** (25), 2848-2857.
184. Bhattacharyya, K., Study of Organized Media Using Time-Resolved Fluorescence Spectroscopy. *Journal of Fluorescence* **2001,** *11* (3), 167-176.
185. Pal, S. K.; Mandal, D.; Sukul, D.; Sen, S.; Bhattacharyya, K., Solvation Dynamics of DCM in Human Serum Albumin. *The Journal of Physical Chemistry B* **2001,** *105* (7), 1438-1441.
186. Pal, S. K.; Peon, J.; Bagchi, B.; Zewail, A. H., Biological Water: Femtosecond Dynamics of Macromolecular Hydration. *The Journal of Physical Chemistry B* **2002,** *106* (48), 12376-12395.
187. Pal, S. K.; Zhao, L.; Zewail, A. H., Water at DNA surfaces: Ultrafast dynamics in minor groove recognition. *Proceedings of the National Academy of Sciences* **2003,** *100* (14), 8113-8118.
188. Verma, S. D.; Pal, N.; Singh, M. K.; Sen, S., Sequence-Dependent Solvation Dynamics of Minor-Groove Bound Ligand Inside Duplex-DNA. *The Journal of Physical Chemistry B* **2015,** *119* (34), 11019-11029.
189. Pal, N.; Shweta, H.; Singh, M. K.; Verma, S. D.; Sen, S., Power-Law Solvation Dynamics in G-Quadruplex DNA: Role of Hydration Dynamics on Ligand Solvation inside DNA. *The Journal of Physical Chemistry Letters* **2015,** *6* (9), 1754-1760.

190. Patra, A.; Hazra, S.; Suresh Kumar, G.; Mitra, R. K., Entropy contribution toward micelle-driven deintercalation of drug–DNA complex. *The Journal of Physical Chemistry B* **2014,** *118* (4), 901-908.
191. Verma, P. K.; Saha, R.; Mitra, R. K.; Pal, S. K., Slow water dynamics at the surface of macromolecular assemblies of different morphologies. *Soft Matter* **2010,** *6*, 5971-5979.
192. Verma, P. K.; Makhal, A.; Mitra, R. K.; Pal, S. K., Role of Solvation Dynamics in the Kinetics of Solvolysis Reactions in Microreactors. *Physical Chemistry Chemical Physics* **2009,** *11*, 8467-8476.
193. Mitra, R. K.; Sinha, S. S.; Verma, P. K.; Pal, S. K., Modulation of Dynamics and Reactivity of Water in Reverse Micelles of Mixed Surfactants *The Journal of Physical Chemistry B* **2008,** *112* (41), 12946-12953.
194. Banerjee, D.; Pal, S. K., Solvation dynamics of LDS 750 in micelles, reverse micelles and proteins. *Chemical Physics Letters* **2008,** *451* (4–6), 237-242.
195. Pal, S. K.; Zewail, A. H., Dynamics of water in biological recognition. *Chemical Reviews* **2004,** *104* (4), 2099-2124.
196. Jimenez, R.; Fleming, G. R.; Kumar, P.; Maroncelli, M., dynamics of water. *Nature* **1994,** *369*, 471-473.
197. Narayanan, S. S.; Sinha, S. S.; Sarkar, R.; Pal, S. K., Picosecond to nanosecond reorganization of water in AOT/lecithin mixed reverse micelles of different morphology. *Chemical Physics Letters* **2008,** *452*, 99-104.
198. Sarkar, R.; Ghosh, M.; Shaw, A. K.; Pal, S. K., Ultrafast surface solvation dynamics and functionality of an enzyme α-chymotrypsin upon interfacial binding to a cationic micelle. *Journal of Photochemistry and Photobiology B: Biology* **2005,** *79* (1), 67-78.
199. Verma, P. K.; Mitra, R. K.; Pal, S. K., A Molecular Picture of Diffusion Controlled Reaction: Role of Microviscosity and Hydration on Hydrolysis of Benzoyl Chloride at a Polymer Hydration Region. *Langmuir* **2009,** *25*, 11336-11343.
200. Mitra, R.; Sinha, S.; Pal, S., Interactions of Nile Blue with Micelles, Reverse Micelles and a Genomic DNA. *Journal of Fluorescence* **2008,** *18* (2), 423-432.
201. Cho, M.; Fleming, G. R.; Saito, S.; Ohmine, I.; Stratt, R. M., Instantaneous normal mode analysis of liquid water. *The Journal of chemical physics* **1994,** *100* (9), 6672-6683.

Chapter 2

2. Summary of Experimental Methods and Basic Theories

This chapter presents some relevant theories, information and experimental methods used in chapters 4, 5, 6, 7 & 8. This chapter also contains the chemicals used in this dissertation work.

Basic Theories

This chapter explains the photophysical principles that underpin the use of fluorescent probes to detect microenvironments and biomolecular interactions. We also identify the experimental techniques used in this Ph.D. dissertation work to examine the environmental effect on the photophysical properties of different probes. Various steady-state and dynamical instruments have been used to investigate the structure, dynamics, and behavior of water in constrained environments. These include the basic theory of photophysics, quantum yield, fluorescence quenching, fluorescence lifetime, solvation dynamics, anisotropy, ESPT and two-photon absorption (by using two-photon absorption spectroscopy) analyses. We have included a brief discussion in this chapter about the dynamical tools and two-photon absorption spectroscopy mentioned above. An overview of the different systems and the fluorescent probes used in the dissertation has also been provided.

2.1. Steady-state (1PA) and Dynamical Tools:

2.1.1. Basic Theory of Photophysics

The definition of spectroscopy, referring to the study of matter through its interaction with light fields (electromagnetic radiation), is among the most important topics in time-dependent quantum mechanics for researchers. To recognize the interaction between light and

matter, it is significant to understand that methods such as scattering or absorption result from accelerating electrical charge. When light strikes an atom or molecule, it disturbs its stationary state, and the system's state can then be represented as a superposition of the ground and excited states, displayed as a linear combination of the basic functions. For example, the change in transition dipole moment is also not zero, and incident light energy coincides with the energy difference between two states (from the ground state to the excited state).[1] The Jablonski[2] diagram typically describes the methods that exist between the absorption and emission of light. Photon absorption (the quickest process), internal conversion (IC), fluorescence emission, intersystem crossing (ISC), and phosphorescence[3] are all possible methods, and the respective processes shown in scheme 2.1 will be implemented shortly. The electronic states singlet ground, first and second are expressed by S_0, S_1, and S_2, respectively.

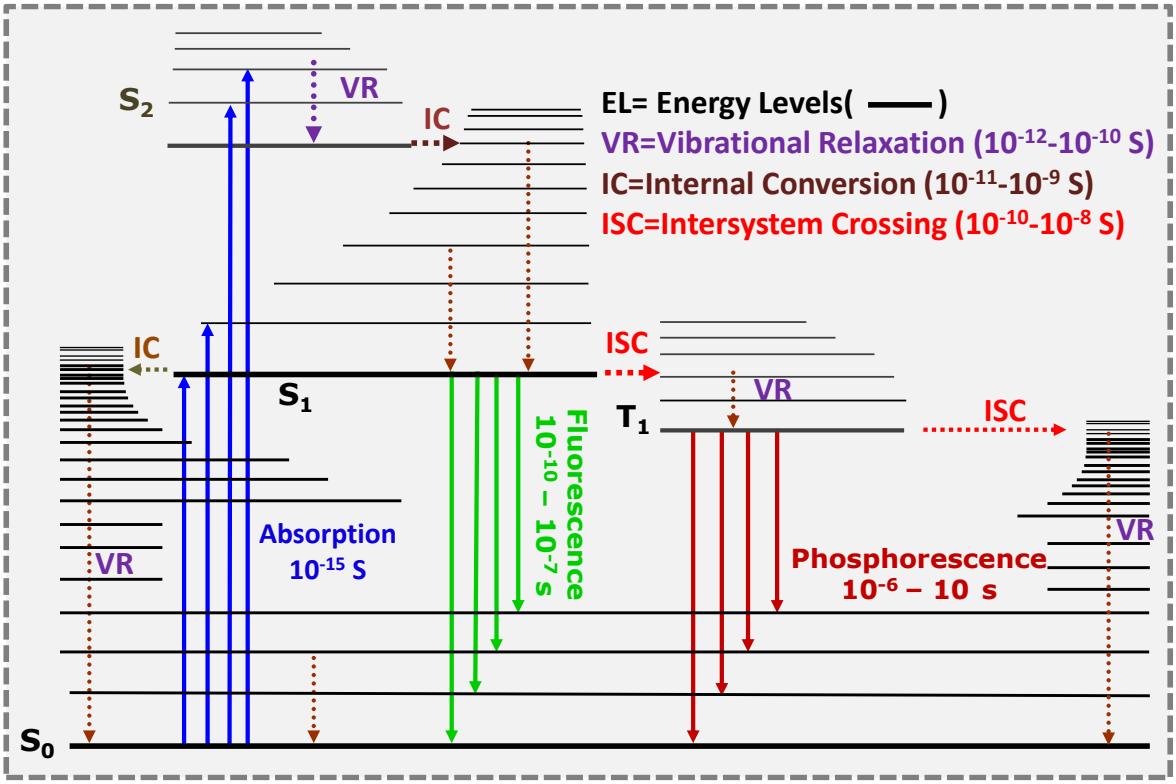

Scheme 2.1: The Jablonski energy diagram[3] represents the transition of a molecule between electronic states. Non-radiative transitions are marked by dotted lines, internal conversion is abbreviated as IC, and intersystem crossing is abbreviated as ISC. The following sections will clarify both of these transitions.

➢ *Absorption of photon*

Absorption of a sample generally follows Beer-Lambert law, which is explained in the next chapter (Ch. 3). Electron movements are quicker than those of nuclei, according to the Born-Oppenheimer approximation (molecular vibrations). When an electron is excited, it

moves to another molecular orbital in about 10^{-15} seconds (the optical period), which is fast in compared to molecular vibrations (10^{-10}-10^{-13} s). This discovery led to the Franck-Condon theory, which states that an electronic transition occurs in the presence of no changes in the nuclei's positions in the molecular entity and its environment and that the resulting state is known as the Franck-Condon (FC) state.

- ***Fluorescence emission***

Fluorescence is the emission of photons from S_1 (higher energetic state) to the S_0 state (lower energetic state) and this phenomenon was first noticed in 1852 by Sir G. G. Stokes.[4] Fluorescence emission occurs at a longer wavelength than the incident light (absorption), following the empirical Stokes law. Accordingly, the change between the absorption and fluorescence spectra to a longer wavelength is called the Stokes shift. To this stage, it must be emphasized that while the emission of a single photon is as rapid as the absorption phase (~10^{-15} s), the steady-state fluorescence emission of a group of molecules remains higher because the excited molecules remain in S_1 over a certain amount of time (from 100s of ps to 100s of ns or, 10^{-10}-10^{-7}s) before emitting a photon. Also recognizable is that the emission of fluorescence reduces exponentially with a characteristic time, which is the average lifetime of the S_1 state.

- ***Vibrational relaxation***

The molecules of interest, followed by a variety of vibrational sub-levels, have a specific number of electronic states.[3, 5] After the molecule is excited, it relaxes to lower vibrational sublevels, normally on sub-ps to a few ps time scale, before returning to higher vibrational sublevels of an electronic state.

- ***Internal Conversion (IC)***

IC[3, 5] is the non-radiative transformation between two electronic states with identical spin multiplicity. Since no photons are released, it is often called "radiationless de-excitation". This process is accompanied by vibrational relaxation to the lowest vibrational stage of the final electronic state. IC from S_2 to S_1 is more efficient due to a smaller energy gap compared to the transition from S_1 to S_0. As a result, the internal conversion from S_2 to S_1 is a process that is likely to compete with fluorescence emission and also with the transformation of the intersystem to a triplet state.

- ***Intersystem crossing (ISC)***

ISC is a non-radiative mechanism between two iso-energy vibrational stages belonging to different multiplicities of electronic states.[3, 5] It is primarily prohibited to cross between states of varying multiplicity. Intersystem crossing probabilities are based specially on the system's singlet and triplet states.

- ***Phosphorescence***

Phosphorescence can happen if an intersystem crossing occurs.[3, 6] It is a radiative process to the singlet ground state S_0 from a triplet or advanced spin multiplicity state and such transitions are, therefore "forbidden" and can happen due to spin-orbit coupling. As a consequence, phosphorescence transition probabilities can be small, resulting in extremely long triplet state lifetimes (until other non-radiative factors, such as ISC to the GS), contribute to a reduction in triplet state lifetimes.

2.1.2. Fluorescence Quantum Yields (QY)

A significant experimental parameter for measuring the fluorescence parameters of a molecule in a given medium is fluorescence quantum yield.[7] The intensity of fluorescence of any molecule depends on that molecule's ability to transform a number of its absorbed photons into emitted photons due to excitation. Fluorescence quantum yield (ϕ) is the ratio of the number of photons released to the number of photons consumed (Equation or Eq. 2.1).[7, 8] Any fluorescent molecule's quantum yield is less than unity and can only be measured experimentally.

$$\phi = \frac{\text{Number of photons released}}{\text{Number of photons consumed}} \qquad \text{(Eq. 2.1)}$$

Any unknown sample's fluorescence quantum yield can be estimated from experimental results of a relative technique. The fluorescence quantum yield is then determined in accordance with equation 2.2, taking into account the absorbance of both the sample and the reference at the respective excitation wavelength from the Beer-Lambert law (see Ch. 3) via the corresponding absorption factor (AF, eq. 2.3).[9] The fluorescence quantum yield of the sample (Φ_s) can be found out for the fluorescence quantum yield of the reference (Φ_r) solution using the following equation.[8]

$$\phi_s = \phi_{ref}\left(\frac{D_s}{D_{ref}}\right)\left(\frac{AF_{ref}}{AF_s}\right)\left(\frac{n_s}{n_{ref}}\right)^2 \qquad \text{(Eq. 2.2)}$$

Where, $AF_{s,ref} = 1 - 10^{-A_{s,ref}}$ (Eq. 2.3)

where, D_s = The sample's integrated field under the emission spectrum

D_{ref} = The reference's integrated field under the emission spectrum

A_s = Absorbance of the sample

A_{ref} = Absorbance of the reference

n_s = The solvent's refractive index, which was used to make the sample

n_{ref} = The solvent's refractive index, which was used as a reference

In dilute solutions, the fluorescence quantum yield of a sample is calculated to avoid scattering effects on absorption and fluorescence measurements. The concentration of the solutions for the quantum yield calculations is diluted so that the optical density or absorption of the solutions does not exceed 0.1 ($A_{s,\text{ or ref}} < 0.1$).

2.1.3. Fluorescence Quenching

Quenching is a broad word that refers to any operation that results in a reduction in fluorescence intensity, lifetime, or quantum yield. Collisions (dynamic quenching) or complex (static quenching) formation may cause molecular contact between the fluorophore and the quencher. The deactivation of an excited fluorophore by interaction with other molecules in the solution, known as quenchers, is referred to as dynamic quenching. The Stern-Volmer equation[10] (eq. 2.4) states that dynamic quenching leads to a reduction in intensity and the equation as follows:

$$\frac{F_M}{F} = 1 + k[M] = 1 + k_M\tau_0[M] \qquad \text{(Eq. 2.4)}$$

Where, the fluorophore strength is denoted by the symbol F, F_M is the fluorescence probe intensity with a quencher present, the quencher concentration is [M], k is the quenching constant of Stern-Volmer, the bimolecular quenching constant is k_M, and the lifetime without the effect of quenching is τ_0.

The famous Stern-Volmer equation, including lifetime and quantum yield, defines the dependency of dynamic quenching upon concentration as follows:

$$\frac{\phi_0}{\phi} = \frac{\tau_0}{\tau} = \frac{I_0}{I} = 1 + k_M \tau_0 [M] \qquad \text{(Eq. 2.5)}$$

Dynamic quenching is an alternate rate method that depopulates the excited-state because, in the absence and presence of the quencher, the ratio of the quantum yield ($\frac{\phi_0}{\phi}$) would've been equal to the ratio of equivalent lifetimes ($\frac{\tau_0}{\tau}$) and the ratio of fluorescence intensities ($\frac{I_0}{I}$). Static quenching results in the formation of a non-fluorescent complex in between fluorophore and the quencher. Because only the fluorescent molecule with its unquenched lifetime can be noticed, static quenching has no effect on lifetime.

2.1.4. Fluorescence Lifetime

Fluorophores are excited to the higher energy states by excitation. The time the fluorophore stays in an ES until returning to its GS is measured in a time-resolved fluorescence technique. In certain situations, lifetime measurements are preferable over steady-state measurements.[3] A time-resolved fluorescence lifetime measurement using pulsed light has been included in the illustrative scheme 2.2, as well as a historical diagram of photon counting.

A fluorophore is excited by a narrow light pulse. If n_0 is the initial excited population of fluorophore molecules, it decays in various ways (radiative, non-radiative, intersystem crossing, photochemistry) with a rate of $k_r+k_{nr}+k_{isc}+k_{pc}$. At time t, the number of molecules excited is given by,

$$-\frac{dn(t)}{dt} = (k_r + k_{nr} + k_{isc} + k_{pc})n(t) \qquad \text{(Eq. 2.6)}$$

On integration,

$$n(t) = n(0)\exp(-kt) = n(0)\exp(-t/\tau) \qquad \text{(Eq. 2.7)}$$

where $k = k_r + k_{nr} + k_{isc} + k_{pc}$ and the lifetime is the reverse of the entire decay rate, $\tau = k^{-1}$.

In terms of intensity,

$$I(t) = I_0 \exp(-t/\tau) \qquad \text{(Eq. 2.8)}$$

This is a single exponential decay. Most of the systems, however, exhibit multi-exponential decay,

$$I(t) = \sum_i a_i \exp(-t/\tau_i) \qquad \text{(Eq. 2.9)}$$

where $\sum_i a_i = 1$ and the average lifetime is determined by the following equation,

$$\langle \tau \rangle = \sum_i a_i \tau_i \qquad \text{(Eq. 2.10)}$$

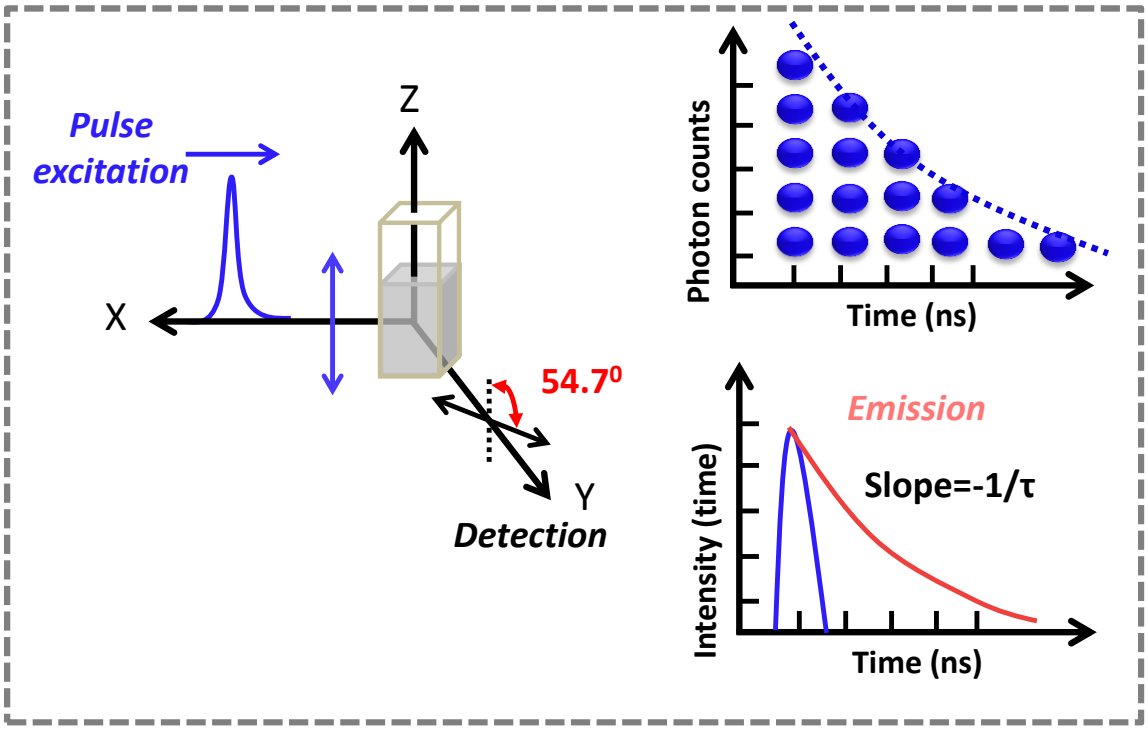

Scheme 2.2.: Time-resolved fluorescence lifetime measurement by exciting with pulsed light.

In our study, we observed the lifetime of the fluorophore dye using a laser diode (LD). From the Raleigh dispersion (using dust in water), the instrument response function (IRF) is determined at the excitation wavelength (wavelength of LD) and then the emission decay (at λ_{max}) of the sample is measured. Both decays are fitted by the process of re-convolution and then the lifetimes are obtained using F900 (Edinburgh) software by fitting in multi-exponential equations.[3]

2.1.5. Solvation Dynamics

Theory:

Solvation dynamics defines how polar solvent molecules are reorganized around an instantaneously generated dipole or a proton/electron unexpectedly plunged into a polar liquid. At time t= 0, a transition in the probe (solute) is made by an ultra-short pulse of excitation that leads to the formation of a dipole. An instantaneous electric field is produced by this dipole on the solvent molecules. The interaction of the solvent's permanent dipoles with the electrical field generated instantaneously changes the solvent's free energy minimum to a non-zero polarization value. Since electronic excitation is much faster (according to the Frank-Condon principle) than the nuclear motion of atoms in molecules, the instantaneously excited probe in the vicinity of solvent molecules is in a relatively high-energy configuration at t=0. As a result, the solvent molecules around the probe continue to shift and relax back to their new positions of equilibrium (scheme 2.3). The nuclear motion involved in the process of rearrangement or relaxation can be narrowly categorized into rotational and translation motions. [11, 12]

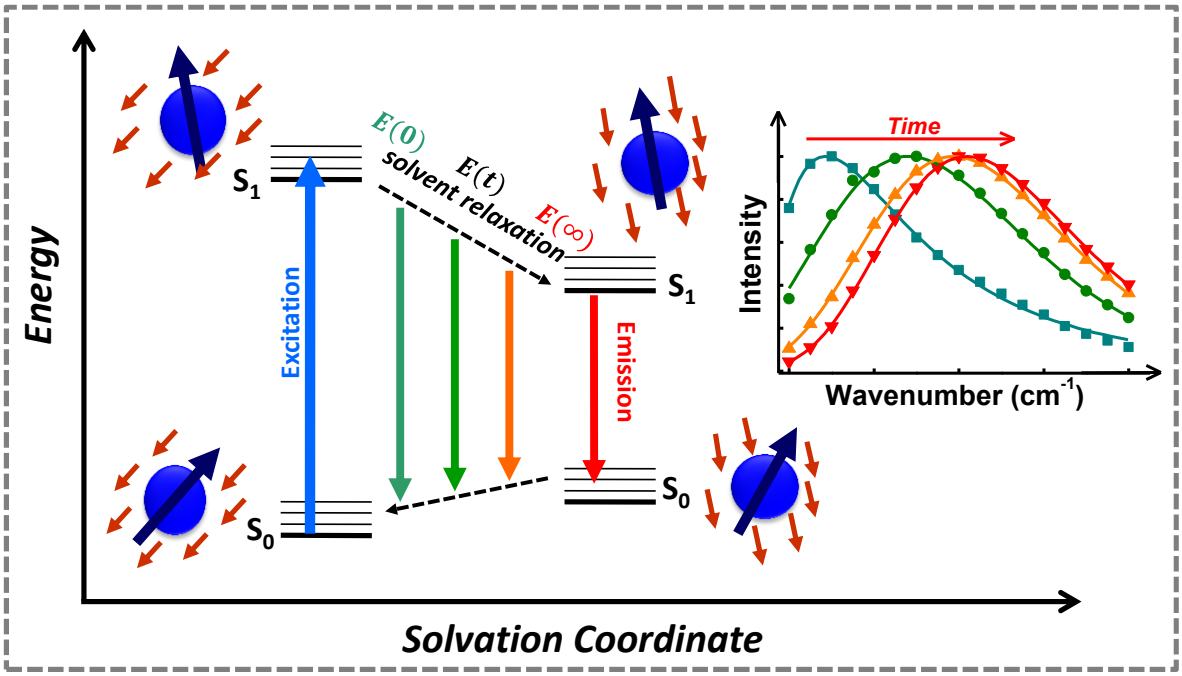

Scheme 2.3: Schematic demonstration of the potential energy surfaces involved in the solvation relaxation process, presentation of the water orientation movements along with the solvation coordinates together with instantaneous excitation. As the solution proceeds, the energy of the solute comes down giving growth to a redshift in the fluorescence spectrum.

According to its extensive hydrogen bonding, the rotational motion of water would also include inhibited rotation and libration, whereas intermolecular vibration would be included in translation. There are two specific types of high-frequency motion: libration and intermolecular vibration, and these are predictable to play a leading part in the faster part of solvent relaxation. Scheme 2.3 depicts the molecular motions that are involved. A standard solvation time correlation function is shown in scheme 2.4a. We estimate the motions responsible for the decay in various regions for clarity's sake.

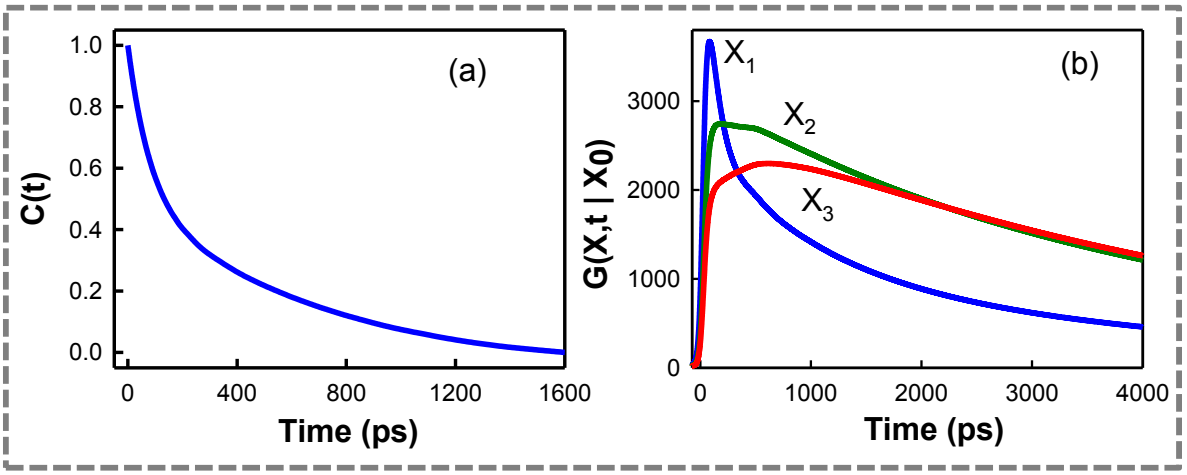

Scheme 2.4: (a) A standard solvation time correlation feature for water in a confined environment. (b) Green's function $G(X,t \mid X_0)$ for population relaxation beside the solvation coordinate (X) is picosecond plotted against time. In G, X_0 is the initial position at t = 0. The location and time dependence of the fluorescence intensity of the population is shown in this figure. There is an ultrafast growth at an early stage (when the population is at X_1), followed by an ultrafast decay. There is a growth followed by a sluggish decay at intermediate times (when the population is at X_2), as shown by the green line. Only a rise is observed during long periods when the population is almost relaxed (position X_3, red line).

The measured solvation correlation function is often bi-exponential. The solvation correlation function is associated with the solvation energy within linear response theory as,

$$C(t) = \frac{\langle E(t)\rangle - \langle E(\infty)\rangle}{\langle E(0)\rangle - \langle E(\infty)\rangle} \qquad \text{(Eq. 2.11)}$$

where, $\langle E(0)\rangle, \langle E(t)\rangle$ and $\langle E(\infty)\rangle$ are energy along the solvation coordinate of the probe at time t=0, t and ∞ respectively.

A graphical representation of the solvation potential and the movements involved in the relaxation method for the water molecules around the instantaneously formed dipole is shown in scheme 2.3. The transient behavior of the population throughout solvation should be a function of decay on the blue edge of the spectrum and a function of increasing on the red edge, as shown in scheme 2.4, based on the shape of the potential.

Experimental Methods:

For the experimental determination of the solvation correlation function of a probe in an atmosphere, numerous fluorescence transients are taken from various wavelengths across the emission spectral range of the probe. All fluorescence transients collected are fitted to a function using a nonlinear least square fitting procedure,

$$\left(X(t) = \int_0^t E(t')R(t-t')dt' \right) \qquad \text{(Eq. 2.12)}$$

including of convolution of the instrument response function (IRF) ($E(t)$) with a sum of exponentials,

$$\left(R(t) = A + \sum_{i=1}^{N} B_i \exp\left(-t/\tau_i\right) \right) \qquad \text{(Eq. 2.13)}$$

where B_i is the pre-exponential component, τ_i is the characteristic lifetime of the i^{th} process, and a background (A). In a multi-exponential decay, relative concentration is eventually represented as:

$$\alpha_n = \frac{B_n}{\sum_{i=1}^{N} B_i}. \qquad \text{(Eq. 2.14)}$$

The significant importance of each decay factor (f_n) to total fluorescence is calculated as follows:

$$f_n = \frac{\tau_n B_n}{\sum_{i=1}^{N} B_i \tau_i} \times 100. \qquad \text{(Eq. 2.15)}$$

Reduced chi-square (0.9-1.1) and residual data control the quality of the curve fitting. In an analytical method appropriate for advanced data processing, the motivation of the fitting is to overcome the decays.

We adopt the technique mentioned in the references to create time-resolved emission spectra (TRES).[8, 13] The multi-exponential model is used to evaluate the emission intensity decays, as defined earlier,

$$I(\lambda,t)=\sum_{i=1}^{N}\alpha_i(\lambda)\exp\left(-t/\tau_i(\lambda)\right) \qquad \text{(Eq. 2.16)}$$

where $\alpha_i(\lambda)$ stand the pre-exponential components, with $\Sigma\alpha_i(\lambda)$ = 1.0. In this study, we calculate a new collection of intensity decays that are normalized such that the time-integrated intensity at every wavelength equals the steady-state intensity at that wavelength. Assuming $F(\lambda)$ seems to be the steady-state emission, we measure a series of $H(\lambda)$ values using,

$$H(\lambda)=\frac{F(\lambda)}{\int_0^{\infty} I(\lambda,t)dt} \qquad \text{(Eq. 2.17)}$$

which becomes, for multi-exponential analysis,

$$\mathrm{H}(\lambda)=\frac{\mathrm{F}(\lambda)}{\sum_i \alpha_i(\lambda)\tau_i(\lambda)} \qquad \text{(Eq. 2.18)}$$

The adequately normalized intensity decay functions are provided by,

$$I'(\lambda,t)=H(\lambda)I(\lambda,t)=\sum_{i=1}^{N}\alpha_i'(\lambda)\exp\left(-t/\tau_i(\lambda)\right) \qquad \text{(Eq. 2.19)}$$

where $\alpha'_i(\lambda) = \mathrm{H}(\lambda)\alpha_i(\lambda)$. The values of $I'(\lambda,t)$ are used to determine the intensity and thus the TRES at any wavelength and time. The nonlinear least-squares fitting of the TRES's spectral shape determines the emission maxima and spectral width values. The spectral shape is expected to be that of a lognormal line,

$$I(\bar{\nu})=I_0\exp\left\{-\left[\ln 2\left(\frac{\ln(\alpha+1)}{b}\right)^2\right]\right\} \qquad \text{(Eq. 2.20)}$$

with $\alpha=\frac{2b(\bar{\nu}-\bar{\nu}_{\max})}{\Delta}-1$ where I_0 is amplitude, $\bar{\nu}_{max}$ is the wavenumber of the emission maximum and the spectral width is given by, $\Gamma=\Delta\left[\frac{\sinh(b)}{b}\right]$. Asymmetry and width parameters are denoted by the terms b and Δ, respectively, and equation (2.19) reductions to a Gaussian function when b = 0. The normalized spectral shift correlation function or the

solvent correlation function *C(t)* is constructed using the time-dependent fluorescence Stokes shifts calculated from TRES and *C(t)* described as,

$$C(t) = \frac{\bar{\nu}(t) - \bar{\nu}(\infty)}{\bar{\nu}(0) - \bar{\nu}(\infty)} \qquad \text{(Eq. 2.21)}$$

where, $\bar{\nu}(0)$, $\bar{\nu}(t)$ and $\bar{\nu}(\infty)$ are the TRES emission maxima (in cm^{-1}) at time zero, *t,* and infinity, respectively. The $\bar{\nu}(\infty)$ value is regarded as the emission frequency beyond which no or unimportant spectral shift is identified. The C(t) function is given the temporal response of the solvent relaxation method as it happens around the probe after photo-excitation and the resulting change in the dipole moment.

We have also used time-resolved area normalized emission spectroscopy (TRANES) to understand the distribution of the probe or any excited-state phenomenon that occurs during excitation, which is a well-known technique[14, 15] and is an improved version of TRES. By normalizing the area of every spectrum in TRES, TRANES is built such that the area of the spectrum at a time "t" is equal to the area of the spectrum at time t = 0.0. A useful aspect of this technique is that the presence of an iso-emissive point in the spectrum distinguishes emissions from two species that are either irreversibly or reversibly kinetically related or not at all combined.

2.1.6. Anisotropy

The degree of polarization of the emission from a chromophore is known as anisotropy. These calculations are focused on the principle of photo-selective excitation for fluorophore molecules with absorption transition dipoles parallel to the polarised excitation light electrical vector. Fluorophores are oriented uniformly in an isotropic solution. However, in the case of selective excitation, the partly oriented population of chromophores with polarized fluorescence emission results. The maximum anisotropy measured is determined by the angle between the absorption and emission transition dipole moments (r_0). Fluorescence anisotropy (r) and polarization (P) are outlined by,

$$r = \frac{I_{II} - I_{\perp}}{I_{II} + 2I_{\perp}} \qquad \text{(Eq. 2. 22)}$$

$$P = \frac{I_{II} - I_{\perp}}{I_{II} + I_{\perp}} \qquad \text{(Eq. 2.23)}$$

When the fluorophore is excited with vertically polarised light, $I_{\parallel}$ and $I_{\perp}$ are the fluorescence intensities of vertically and horizontally polarised emission. Polarization and anisotropy are interconnected as,

$$r = \frac{2P}{3-P} \qquad \text{(Eq. 2.24)}$$

$$P = \frac{3r}{2+r} \qquad \text{(Eq. 2.25)}$$

While polarization and anisotropy deliver the same data, anisotropy is favored because the total fluorescence intensity is normalized by the latter ($I_T = I_{II} + 2I_{\perp}$) and anisotropy is additive in the event of several emissive molecules, while polarization is not. Numerous phenomena, containing rotational diffusion and energy transfer, may cause the calculated anisotropy to be less than the theoretical limit. Following a pulsed excitation the time-resolved fluorescence anisotropy, *r(t)* of a sphere is assumed by,

$$r(t) = r_0 \exp(-t/\tau_{rot}) \qquad \text{(Eq. 2.26)}$$

where r_0 is the anisotropy at time $t = 0$ and τ_{rot} is the rotational correlation time of the sphere.

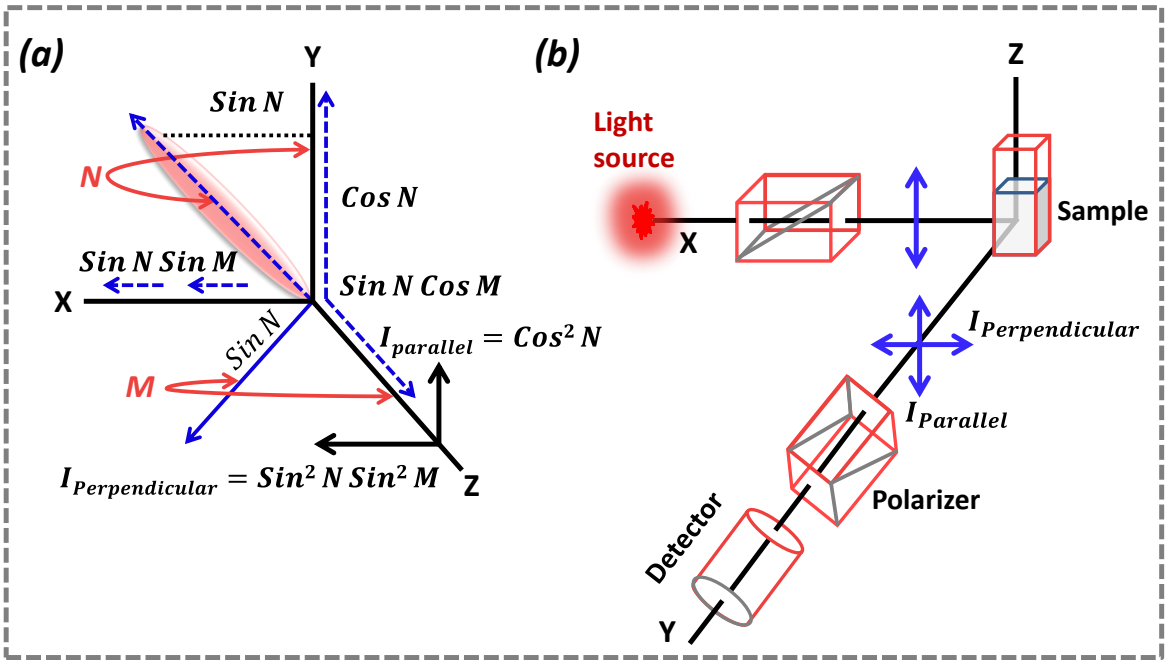

Scheme 2.5: (a) Single fluorophore (pink ellipsoid) emission intensity in the coordinate method. (b) The measurement of fluorescence anisotropy is depicted in this diagram.

Experimental methods:

The emission polarisation is calibrated to be parallel and perpendicular to the excitation polarization for time-resolved anisotropy (*r(t)*) calculations (Scheme 2.5b). Spencer and Weber[16, 17] have derived the relevant equations for the time dependence of $I_{II}(t)$ (equation 2.27) and $I_{\perp}(t)$ (equation 2.28) for single rotational and fluorescence relaxation times, τ_{rot} and τ_f, respectively,

$$I_{II}(t) = \exp\left(-t/\tau_f\right)\left(1+2r_0\exp\left(-t/\tau_{rot}\right)\right) \qquad \text{(Eq. 2.27)}$$

$$I_{\perp}(t) = \exp\left(-t/\tau_f\right)\left(1-r_0\exp\left(-t/\tau_{rot}\right)\right) \qquad \text{(Eq. 2.28)}$$

The total fluorescence is given by,

$$F(t) = I_{II}(t) + 2I_{\perp}(t) = 3\exp\left(-t/\tau_f\right) = F_0\exp\left(-t/\tau_f\right) \qquad \text{(Eq. 2.29)}$$

The time-dependent anisotropy, *r(t)* is given by,

$$r(t) = \frac{I_{II}(t) - I_{\perp}(t)}{I_{II}(t) + 2I_{\perp}(t)} = r_0\exp\left(-t/\tau_{rot}\right) \qquad \text{(Eq. 2.30)}$$

F(t) is dependent on τ_f, while *r(t)* is dependent on τ_{rot}, so these two lifetimes can be distinguished. In steady-state measurements, this distinction is not feasible. It really should be mentioned that the degree of polarization *(P)* is not independent of τ_f and thus is not a convenient quantity to use as a substitute for r. Three restricting cases can be identified for accurate *r(t)* calculation.

(a) If $\tau_f < \tau_{rot}$, only r_0 can be determined since the fluorescence decays even before anisotropy decays.

(b) If $\tau_{rot} < \tau_f$, in comparison to steady-state measurements, τ_{rot} can theoretically be calculated. The equations (2.27) and (2.28) indicate that τ_{rot} is the only factor that affects the decay of parallel and perpendicular components. The only experimental disadvantage, in this case, is that those photons are released after a few times duration of τ_{rot}, so they cannot be used to determine τ_{rot}.

(c) If $\tau_{rot} \approx \tau_f$, it has become the optimal situation because nearly all photons are recorded during the period (equal to the many rotational relaxation times) during which *r(t)* displays observable changes.

When dealing with structures that have several rotational correlation times, *r(t)* is given by,

$$r(t) = r_0 \sum_i \beta_i e^{-t/\tau_i} \qquad \text{(Eq. 2.31)}$$

where $\sum_i \beta_i = 1$. It should have been mentioned that the spectral dispersion feature of the fluorescence monitoring instrument responds differently with different light polarizations, necessitating the use of a correction factor. The use of such diffraction gratings, for example, will result in emission intensities that are highly dependent on the grating plane's orientation. Predictably, it is necessary to correct anisotropy in response when using such instruments. This instrumental anisotropy is commonly referred to as the G-factor (grating factor), and it is characterized as the proportion of vertically polarised light transmission efficiency to horizontally polarised light transmission efficiency ($G = I_{II} + I_{\perp}$). Hence, the values of fluorescence anisotropy, *r(t)* modified for the response of the instrument, would be assumed by[3],

$$r(t) = \frac{I_{II}(t) - GI_{\perp}(t)}{I_{II}(t) + 2GI_{\perp}(t)} \qquad \text{(Eq. 2.32)}$$

Exciting the sample with a horizontally polarised excitation beam and extracting the two polarised fluorescence decays, one parallel and the other perpendicular to the horizontally polarised excitation beam, may be used to calculate the G-factor at a defined wavelength. The long-time tail matching technique can also be used to calculate the G-factor. If $\tau_{rot} < \tau_f$, it is expected that the curves for $I_{II}(t)$ and $I_{\perp}(t)$ would become identical. If they are not in any experiment, it can generally consider being due to a non-unitary G-factor. The G-factor is eliminated in the monitoring of anisotropy by normalizing the two decay curves on the tail of the decay.

The rotational anisotropy decay of the probe can be defined in the light of the '***wobbling-in-cone***' *model.*[18-20] Different types of rotational motions, cone angles, diffusion constants for motion within the cones, and the probe's final diffusion constants can all be used to explain bi-exponential anisotropy decay. This model proposes, the anisotropy decay is a product of three different independent motion :(i) wobbling of the probe $r_w(t)$ with a time constant τ_w, (ii) translation of the probe or lateral diffusion of the monomer $r_D(t)$ over the surface of the environment, with a time constant τ_D, and (iii) rotational motion of the

environment $r_T(t)$, with a time constant of τ_T. Thus, r(t) may be disassembled as a product of three independent motions as,

$$r(t) = r_w(t) r_d(t) r_T(t) \qquad \text{(Eq. 2.33)}$$

Again, in accordance with the two steps model, if the fast and the slow motions are independent

$$r(t) = r_{slow}(t) r_{fast}(t) \qquad \text{(Eq. 2.34)}$$

where, r_{fast}(t) and r_{slow}(t) the respective correlation function of fast motion within the environment or system and to the slow motion of the system.

In this model, the order parameter (P) indicates the average rigidity of the region surrounding which the solvent molecules are more ordered around the probe. P can be related to the recovered decay of anisotropy through

$$r(t) = r_0 \times \left[P^2 + \left\{(1 - P^2)\, e^{-\left(\frac{t}{\tau_{fast}}\right)}\right\}\right]\left[e^{-\left(\frac{t}{\tau_{slow}}\right)}\right] \qquad \text{(Eq. 2.35)}$$

P satisfies the inequality $0 \leq P^2 \leq 1$. If the fast motion or orientational diffusion is not at all restricted, $P = 0$ and if it is completely restricted $|P| = 1$. It can be shown that

$$P^2 = a_{slow} \qquad \text{(Eq. 2.36)}$$

τ_{slow} contains contributions of both τ_T and τ_D as:

$$\frac{1}{\tau_{slow}} = \frac{1}{\tau_T} + \frac{1}{\tau_D} \qquad \text{(Eq. 2.37)}$$

The semi-cone angle(θ) formed by the probe during its rotation at the system interface and the order parameter is given as

$$\theta = Cos^{-1}[0.5\{(1 + 8P)^{0.5} - 1\}] \qquad \text{(Eq. 2.38)}$$

We define the effective correlation time τ_w that is associated with the wobbling rotational motion as,

$$\frac{1}{\tau_w} = \frac{1}{\tau_{fast}} - \frac{1}{\tau_{slow}} \qquad \text{(Eq. 2.39)}$$

The wobbling-in-the-cone diffusion coefficient D_w related to τ_w is given by the following equation for $\theta \leq 30^0$

$$D_w \tau_w \approx \frac{7\theta^2}{24} \qquad \text{(Eq. 2.40)}$$

where θ is expressed in radians.

For $\theta \geq 30^0$ D_w is expressed as:

$$D_w = \{(1-P^2)\tau_w\}^{-1}\left[\left(\frac{y^2(1+y)^2}{2(y-1)}\right)\left\{ln\left(\frac{1+y}{2}\right)+\left(\frac{1-y}{2}\right)\right\}+\left(\frac{1-y}{24}\right)(6+8y-y^2-12y^3-7y^4)\right] \qquad \text{(Eq. 2.41)}$$

where $y = Cos\,\theta$.

2.1.7. Excited-State Proton Transfer (ESPT) Analysis

ESPT is a tautomerization mechanism in which photo-excited molecules relax their energy by transferring protons.[21]

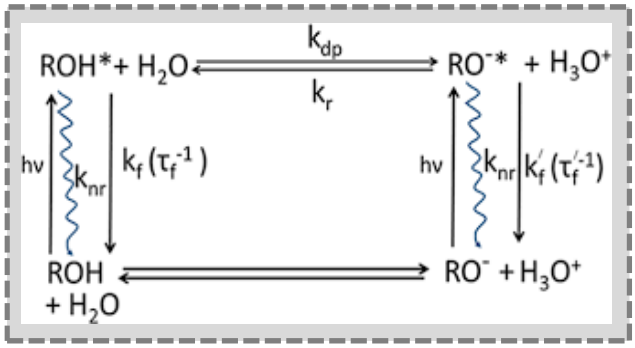

After a quantum of light has been absorbed (hv), the photoacid (ESPT dye molecule) has a neutral ROH^* (protonated form) state followed by solvent relaxation (where "*" stands for excited-state phenomena). Two different routes can be followed by the ROH^* state, either relaxing to the ground ROH state through photon emission (rate k_f) or undergoing ESPT, establishing the excited-state of tautomeric RO^{-*} (deprotonated form). After the transfer of the proton from the ROH^* to the nearby solvent (like water) and the formation of the RO^{-*} in an excited-state, it is called the ESPT process and the rate is k_{dp} (deprotonated rate constant). The probability of diffusion-assisted geminate recombination (rate k_r) between RO^{-*} and H^+ to reform ROH^* opposes this mechanism process (ESPT). The latter subsequently decays by photon emission to the RO^- ground state (rate is $k^/_f$). The RO^- state would eventually relax due to a proton back transition in the ground state, restoring the ROH ground state. It should be emphasized that all four ROH, ROH^*, RO^- and RO^{-*} states have different burden distributions and this indicates different interactions through their micro-environment.

➢ TRANES Decomposition into ROH^* and RO^{-*} Spectra:

All the *TRANES* are can be fitted by *bi-lognormal functions*[22, 23], is given by the following relation:

$$I(\lambda) = I_p \exp\left\{-0.693\left[\frac{\ln\left(1+\frac{2b_p(\lambda-n_p)}{\Delta_p}\right)}{b_p}\right]^2\right\} + I_d \exp\left\{-0.693\left[\frac{\ln\left(1+\frac{2b_d(\lambda-n_d)}{\Delta_d}\right)}{b_d}\right]^2\right\} \qquad \text{(Eq. 2.42)}$$

when both $\frac{2b_p(\lambda-n_p)}{\Delta_p} \leq -1$ and $\frac{2b_d(\lambda-n_d)}{\Delta_d} \leq -1$

Else, $I(\lambda) = 0$

Here, I_i, n_i, Δ_i, b_i denote maximum peak intensity, wavelength maximum, width parameter, and asymmetry factor of each band respectively. The label (p and d) in the subscript denote the ROH^* and RO^{-*} band parameters respectively.

➢ Kinetic Model to Evaluate the Dynamics of Proton Transfer in Various Media (Such as RMs, Binary Solutions etc.):

This model assumes that ROH^* can have two fates: either emitting to the ground state (ROH) with a time constant of τ_f or get converted to RO^{-*} through deprotonation (with a rate constant of $1/\tau_{dp}$). On the other hand, RO^{-*} could also undergo Geminate recombination to form back ROH^* (with a rate constant of $1/\tau_r$) or it can get back to the ground state with a time constant of τ'_f. The corresponding rate equations are:

$$\frac{d}{dt}[ROH^*](t) = -\left(\frac{1}{\tau_f}+\frac{1}{\tau_{dp}}\right)[ROH^*](t)+\frac{1}{\tau_r}[RO^{-*}](t) \qquad \text{(Eq. 2.43)}$$

$$\frac{d}{dt}[RO^{-*}](t) = -\left(\frac{1}{\tau'_f}+\frac{1}{\tau_r}\right)[RO^{-*}](t)+\frac{1}{\tau_{dp}}[ROH^*](t) \qquad \text{(Eq. 2.44)}$$

This model is fitted well to the data, while a small fast component is omitted and only long decay transient is taken for fitting as followed from the method provided by Fayer et al.[24]

For the photoacid (like; D-luciferin) molecules undergoing ESPT (we define those as ROH^*_Y) the rate equation becomes:

$$\frac{d}{dt}[ROH^*]_Y = -\left(\frac{1}{\tau_f}+\frac{1}{\tau_{dp}}\right)[ROH^*]_Y \qquad \text{(Eq. 2.45)}$$

Solving this we get,

$$[ROH^*]_Y = [ROH^*]_{0,Y}\, e^{-\left(\frac{1}{\tau_f}+\frac{1}{\tau_{dp}}\right)} \qquad \text{(Eq. 2.46)}$$

Similarly for those which are not undergoing ESPT the rate equation becomes,

$$\frac{d}{dt}[ROH^*]_N = -\left(\frac{1}{\tau_f}\right)[ROH^*]_N \qquad \text{(Eq. 2.47)}$$

which on solving yields:

$$[ROH^*]_N = [ROH^*]_{0,N}\, e^{-\left(\frac{1}{\tau_f}\right)} \qquad \text{(Eq. 2.48)}$$

Therefore, at any given point of time 't' we can write:

$$[ROH^*] = [ROH^*]_{0,Y} e^{-\left(\frac{1}{\tau_{dp}}+\frac{1}{\tau_f}\right)t} + [ROH^*]_{0,N} e^{-\left(\frac{1}{\tau_f}\right)t} \qquad \text{(Eq. 2.49)}$$

2.2. Two-Photon (2P) Analysis

Fluorescent molecules and ions are useful probes for studying biological processes, and the fluorescence of certain ions and molecules is normally triggered by the absorption of a single photon. However, exciting the molecule by using two or more photons is always preferable. Throughout this chapter, we review the process of two-photon absorption (2PA) and address the benefits it provides for biological system investigation. This chapter aims to clarify some fundamental concepts of nonlinear optics, namely "2PA", and to provide a summary of the applications for 2PA implemented. We also describe the two-photon absorption cross-section (2PACS, σ_2) and explain how it is calculated.

2.2.1. History of 2P

Maria Goeppert-Mayer
Nobel Prize in Physics (1963)
[Picture collected from Wikipedia]

When a ray of light propagates through it, the non-linear optical (NLO) property of a material can be theoretically clarified.[25] Again, the nonlinear properties of materials depend on the incident radiation's intensity or strength of the electric field. In the case of a nonlinear medium, induced polarization is always a nonlinear function of the applied field.[26] The fate of the NLO property of the material can be defined based on the order of nonlinearity exhibited by a material upon contact with incident radiation. The ability of a material to absorb several photons simultaneously is one of the design approaches responsible for the development of NLO materials. A material's simplest multi-photon absorption property is the concurrent absorption of two photons, even if there may be 3 or more cases of photon absorption. Thus, the function that describes the polarization of the displacement of charges within the nonlinear material, P(t), when interacting with the incoming electrical field, can be determined by the power series of the anharmonic oscillator model as follows.[27]

For linear process

$$\text{Polarization } \tilde{P} = \varepsilon_0 \chi \tilde{E} \qquad \text{(Eq. 2.50)}$$

But in general, polarization is a non-linear optical parameter.

$$\tilde{P}(t) = \varepsilon_0\left[\chi^{(1)}\tilde{E}(t) + \chi^{(2)}\tilde{E}(t) + \chi^{(3)}\tilde{E}(t) + \cdots\right] \qquad \text{(Eq. 2.51)}$$

The first term $\chi\tilde{E}(t)$ refers to the induced polarization at the time "t", which is linearly related to the applied electrical field, where χ and E represent the linear susceptibility of the medium and the corresponding electrical field vector, respectively. In this case, the nonlinear susceptibilities of the medium are distinguished as second, third, and fourth orders, respectively. As a result, depending on the order of nonlinearity of the material exhibited, different types of frequencies can be generated which, in turn, provide additional options for studying NLO materials. The emphasis is on the two-photon absorption (2PA) property of materials in this dissertation. Göppert-Mayer suggested in 1931 that a molecule would absorb two photons at the same time if their frequency is exactly equal to the energy difference between two states.[27, 28] The first experimental study by "W. Kaiser and C. G. B. Garrett" on two-photon excitation (TPE) of $CaF_2:Eu^{2+}$ fluorescence was published in 1961.[29] In 1963, the Göppert-Mayer theory was finally verified 32 years later and she was awarded the "Nobel Prize" in Physics.[30]

2.2.2. Fundamental Principles

There are many applications of 2PA, especially in nonlinear optics, resulting from the specific benefits of two-photon excitation (2PE) instead of one-photon excitation (1PE) (scheme 2.6).[31, 32] Excitation with two-photons during the 2PA process of near-infrared wavelength significantly decreases the scattering effect and this effect is also confirmed by Rayleigh's scattering law. According to Rayleigh, scattering and wavelength are mathematically related via[33]:

$$\sigma_{sc} = Scattering\ of\ the\ light\ \propto \frac{1}{\lambda^4} \qquad \text{(Eq. 2.52)}$$

where "σ_{sc}" is the scattering of light and "λ" is the wavelength.

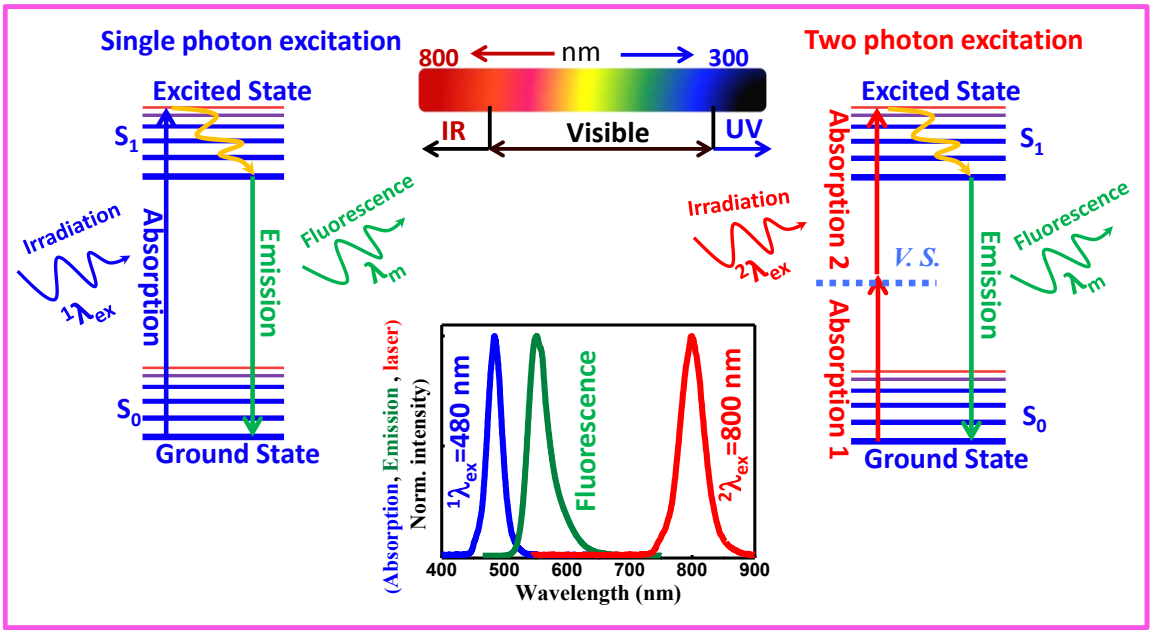

Scheme 2.6: Schematic of "Jablonski Diagram" for one and two-photon process (1PA & 2PA). "V.S." stands for the virtual state. (Modified from the source file: *https://sites.middlebury.edu/durst/research/*)

From the equation (2.51), scattering is reduced by as much as 16 times with a two-fold increase in excitation wavelength. In the 2PA system, after simultaneously absorbing a two-photon via virtual state (VS) in scheme 2.6, the molecule reaches the excited-state. This "VS" is an intermediate state, often represented as 'imaginary' in many quantum processes. A virtual state is a very short-lived (<1 fs) situation in quantum physics.[34] The "lifetime" of the intermediate state, according to the relationship of uncertainty, as[34]:

$$\tau_{virtual} \sim \frac{\hbar}{\frac{E_{gap}}{2}} \sim 0.84 \times 10^{-15} s \qquad \text{(Eq. 2.53)}$$

Where, $\tau_{virtual}$ is the lifetime of the molecule in the virtual state is estimated, E_{gap} is the energy difference or gap between the two-state (GS & ES) and ħ is the plank constant respectively.

2.2.3 The Two-Photon Absorption Cross-section (2PACS,σ_2) Measurement

We are all connected to the absorption coefficients of 1PAS[3], typically expressed in units of M^{-1} cm^{-1} as the molar extinction coefficients. Absorption can be represented in units of cm^2 for a single molecule, which is the effective area over which the incident light is absorbed by a single molecule. The optical cross-sections σ_1 differ from 10^{-15} to 10^{-17} cm^2 for 1PE.[3]

The 2PACS value is highly influenced by the experimental methods used to calculate the activity of the 2PAS. The Z-scan and two-photon excited fluorescence (TPEF) techniques are the two primary and direct ways of measuring the 2PACS.[8, 35] Only the TPEF approach was used in this dissertation (Chapter 3). Again for 2PACS (σ_2) is defined by the area of focal spot (scheme 2.7) of the incident light at the focal point where maximum numbers of photons are absorbed. TPACS (σ_2) was calculated using a two-photon induced fluorescence method. The calculated σ_2 values were obtained by using the following equation,[36, 37, 38]

$$\sigma_2 = \sigma_{\mathrm{ref}} \frac{\phi_{\mathrm{ref}}}{\phi_2} \frac{c_{\mathrm{ref}}}{c_2} \frac{n_{ref}}{n_2} \frac{F_2}{F_{ref}} \qquad \text{(Eq. 2.54)}$$

where 'F' is the two-photon induced fluorescence (TPIF) integrated over the complete fluorescence curve, 'Φ' is the fluorescence quantum yield, 'c' is the concentration and n is the refractive index. Here, the subscript '2' represents for the solution under calculation, and *'ref'* (reference) stands for water, for which the values were derived from earlier published types of literature (e.g. for R6G, σ_2 ~ 10.3 GM and for RhB, σ_2~ 4 GM, where, 1 GM = 10^{-50} cm^4 s $photon^{-1}$).[39]

2.2.4 Unit of the 2PACS

Maria Göppert-Mayer, who established the theory of two-photon absorption processes, is honored with these units.[28] When the explanation for these *units* is considered, it can be shown that the product results in two areas (one for each photon, one in cm^2) and a time (within which the two photons must arrive in order to cooperate). The broad scaling factor is applied to provide convenient values for 2PACS of common dyes. Two-photon absorption is a third-order process, with absorption cross-section usually many orders of magnitude smaller than cross-sectional one-photon absorption.

Some simple considerations can be understood as the physical origin of the 2PACS. The number of photons absorbed per second (N_{1PA}) is given for one-photon absorption by[3],

$$N_{1PA}(photon/s) = \sigma_1(cm^2) I(photon/cm^2 s) \qquad \text{(Eq. 2.55)}$$

where "I" stands for intensity and "σ_1" stands for one-photon absorption cross-section (1PACS). The amount of photons per second absorbed is calculated by multiplying the cross-

section in cm^2 by the number of photons per second passing near to the molecule. To get N_{1PA} in photons per second, the cross-section unit should be in cm^2.

Now consider the absorption of two photons. The number of two-photons (N_{2PA}) absorbed per second is provided by,

$$N_{2PA}(photons/s) = \sigma_2 I^2(photons/cm^2 s)^2 \qquad \text{(Eq. 2.56)}$$

To match the units on both sides of the equation 2.56 and the σ_2 units have to be cm^4 s $photon^{-1}$.

2.2.5: Two-photon absorption identification

Organic molecule excitation (fluorescent dye and numerous bio-molecules) is often the most powerful in the blue and UV areas of the spectrum. Their absorption spectra are distinguished by wide bands that allow a wide range of wavelengths for excitation. After absorption, the molecules fluoresce in the visible or near-infrared, and the emission spectrum is unaffected by the method of excitation. That is, the emission spectrum is usually unchanged, whether such a molecule is excited by a single-photon, two-photon, or several photons. Thus, one is usually unable to determine whether one or numerous photons were used to excite the sample from the emission spectrum. One refers to the fact that fluorescence is proportional to the number of molecules excited to determine the number of photons involved in the excitation process. Under these situations, the luminescence energy from the sample is proportional to the beam intensity of the laser power. A log (fluorescence intensity) plot versus a log (beam intensity) gives a straight line whose slope gives the number of photons involved in the transition information. A slope of 1 means 1PA, a slope of 2 means 2PA, etc., and it is not unusual for more than one kind of absorption process to occur at the same time. "Kaiser and Garrett"[29] reported their 2PA results by monitoring the fluorescence intensity of the $CaF_2:Eu^{2+}$ crystal, as a function of the laser output intensity (power) used for excitation. For power dependency studies, we used a neutral density filter (see chapter 3 for instrument model number) to adjust the laser intensity and reported data at every laser power. The logarithm of fluorescence intensity was then plotted against the logarithm of laser power (intensity) to determine the presence of the two-photon phase, we ensured a slope of 1.92 (~ 2) (scheme 2.7). We can find some examples of two-photon dye fluorescence in the references.[40, 41]

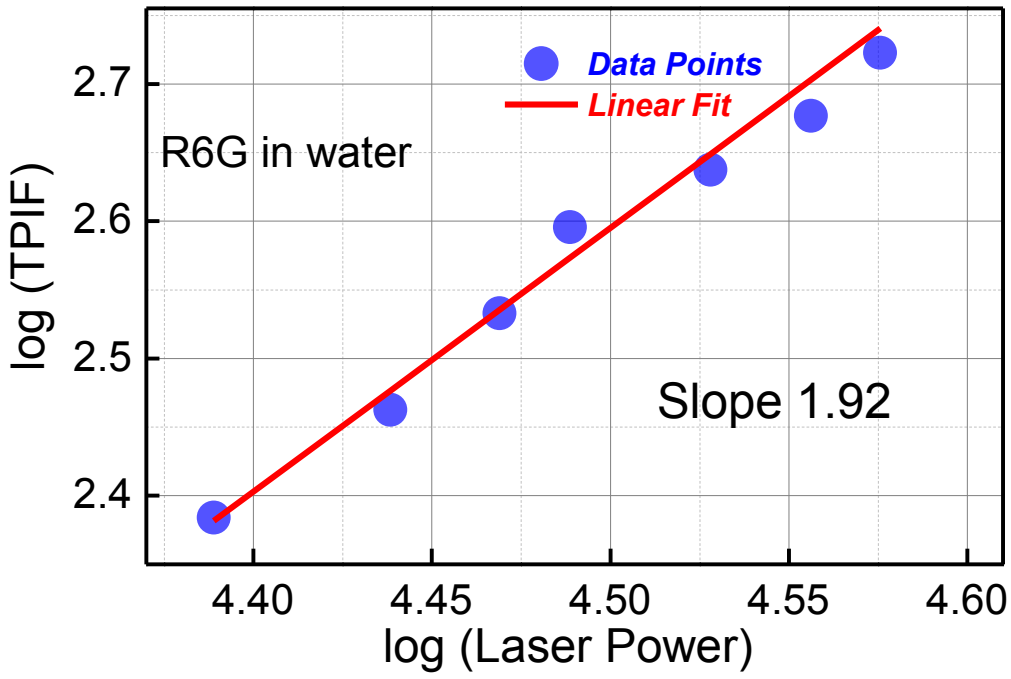

Scheme 2.7: The log-log plot of the two-photon-induced fluorescence (TPIF) intensities of R6G in pure water as a function of laser power.

2.2.6. Advantages and Applications

- ***Why 2PA spectroscopy is needed in biomolecular systems?***

For the study of biological systems using optical techniques, it is often essential to excite either the biological system directly or a biological indicator, including an organic dye molecule. There are several reasons why 2PA is preferable to 1PA when it comes to motivating a molecule. They are exactly as follows:

- ❖ This technique is suitable for measurements of absorption cross-section (σ_2) of a dye/molecule bound with biomolecule or macromolecule under different environments.

- ❖ The two-photon process happens only at the focal point (very tiny focus volume (<1 μm^3)), whereas the single-photon process occurs in the entire region (scheme 2.8).

- ❖ High penetration depth, which is better for imaging tissue.

- ❖ Two-photon processes (falls in "Biologically transparent window" (scheme 2.8)) are preferred compared to the single-photon process due to its low energy that doesn't damage the biomolecules or live cell.

- Reduced scattering.
- TPA probes are typically associated with lower sensitivity, making it an important field of research to design TPA fluorophores with a high probability of absorption.

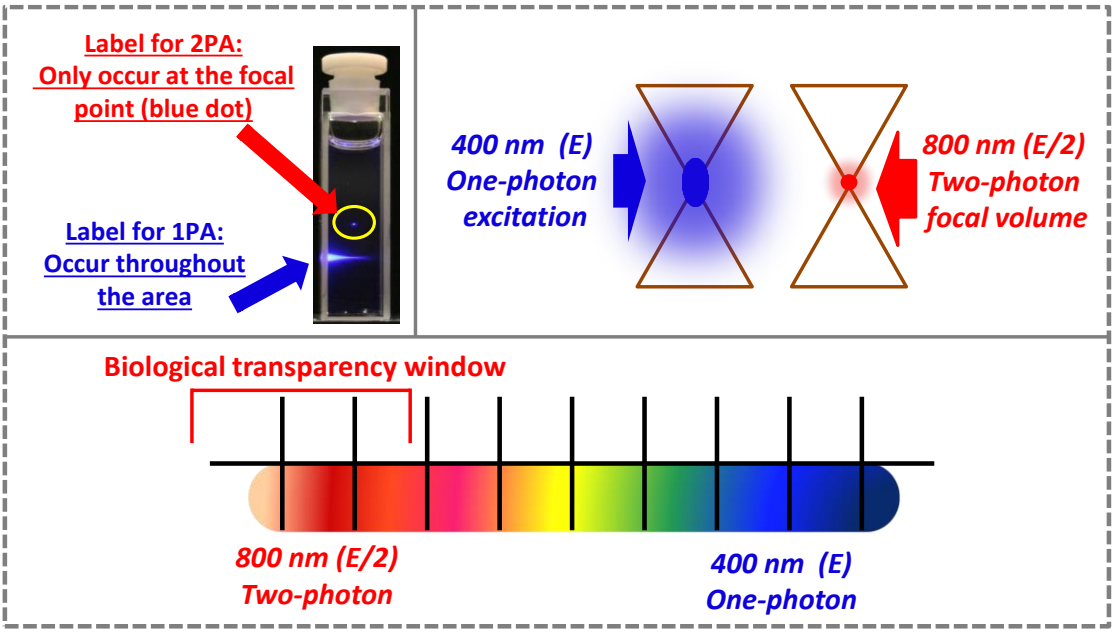

Scheme 2.8: For 1PA; the light beam on the right is speedily absorbed by a concentrated solution of fluorescent material. 2PA; the beam will solve without being attenuated before the beam focuses; the strength of light is high enough to cause two-photon induced fluorescence only near the focus.[42]

Two-photon absorption as a nonlinear process is an attractive candidate for several applications. TPA was used as a spectroscopy/spectroscopic instrument until the early 1980s. The 1PA and 2PA spectra of various organic molecules were compared by scientists and many basic structure-property relationships were obtained. Peter Rentzepis[43] first proposed "*3D optical memory or data storage*" in the 1980s, and it later became a first application.[43, 44] The ability to approach molecules deep inside a sample without impacting other areas through two-photon excitation makes it possible to store and retrieve information in a substance's volume rather than just on a surface as done on the DVD (Digital Versatile Disc). Therefore, media containing terabyte-level data capabilities on a single disk can be provided. "*Fluorescence microscopy and Imaging*" are suggested by Watt Webb.[45] This technique has also been successfully applied in different fields of science, including *nanofabrication*[46], *up-converted lasing*[47], *localized release of bio-active species*[48], *optical power limiting*[49], *protein (un)folding*[50, 51] and *photodynamic therapy*[52, 53].

2.3. Chemicals Used

2.3.1. Surfactants

There are two components of amphiphilic molecules, such as hydrophilic and hydrophobic, in the surfactant.

Hydrophilic groups: The "head group" is generally mentioned as the *hydrophilic* group of a surfactant and is either highly polar or charged. For the anionic charged group, the counterion is commonly Na^+, and the counterion is typically Cl^- for cationic surfactants. The traditional soaps carboxylates $(-CO_2^-)$ and primary synthetic detergents, the sulphonates $(-SO_3^-)$ and the sulfates $(-OSO_3^-)$ are included in the anionic surfactants. Generally, quaternary ammonium$(-N(CH_3)_3^+)$, imidazolinium $(-C_3H_5N_2^+)$ or alkyl pyridinium $(-C_5H_5NH^+)$ compounds are the cationic surfactants. The positively charged head group provides good adhesive properties to the surfactant on anionically charged fabrics, like cotton and hair, and is therefore used as fabric and hair conditioners. The Ethhoxylates $(-CH_2CH_2)_nOH$ groups are regulated by non-ionic surfactants. They are used widely as detergents and for low-temperature detergency. Many so-called semi-polar compounds, like amine oxides$(-R_3N^+ - O^-)$, sulphoxides, phosphine amides, are also included in this class of surfactants, but only amine oxides are commercially relevant.

Hydrophobic groups: This portion of the surfactant is generally referred to as the "tail" and is most often a basic group of hydrocarbons. The tail would be a mixture of certain alkyl groups found in the fatty acids produced from the hydrolysis of natural fats and oils if soaps were the only detergents.

In this dissertation we used the following surfactants : anionic: Sodium 1,4-bis(2-ethyl hexyl)-1,4-dioxobutane-2-sulfonate (AOT), sodium tetradecylsulfate (TSDS), sodium dodecylsulfate (SDS), sodium decylsulfate (SDeS), sodium octyl sulfate (SOS), non-ionic: polyoxy-ethylene(5)nonylphenylether (Ig-520), Triton X-100 (Tx-100), cationic: didodecyldimethylammonium bromide (DDAB), cetyltrimethylammonium bromide (CTAB) (Scheme 2.9).

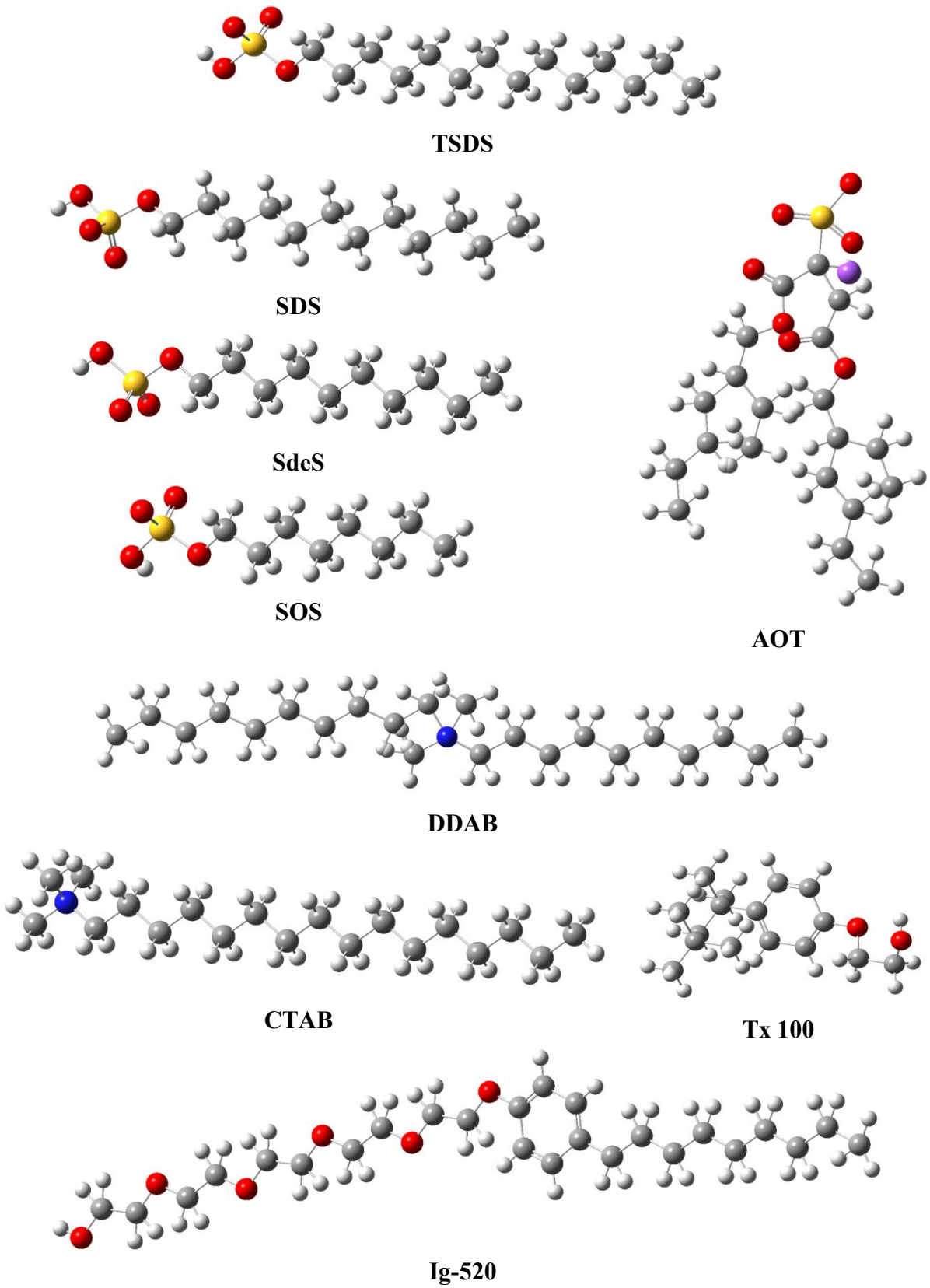

Scheme 2.9: Molecular structure of different surfactants.

2.3.2. Solvents

Cyclohexane (C_y) is a cyclic hydrocarbon consisting of a ring of six carbon atoms, a cyclic type of hexane, which is used in the manufacture of nylon as a raw material. As a non-polar solvent, it does have a function. It is a cycloalkane and an organic volatile compound. In this dissertation, hydrocarbon oil cyclohexane was used as a non-polar solvent for the preparation of RMs and mixed RMs.

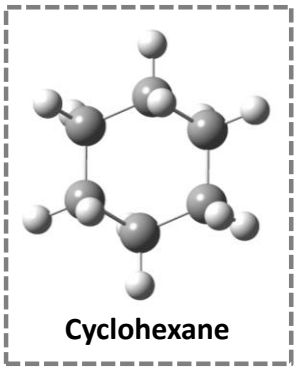

The organic chemical compound and its chemical formula, C_2H_6O (or CH_3-CH_2-OH), is simply ethanol (also called ethyl alcohol or EtOH). Ethanol (scheme 2.10), with a mild characteristic odor, is a toxic, flammable, colorless liquid. Again, the colorless, water-miscible organic compound with the formula CF_3CH_2OH is 2,2,2-Trifluoroethanol (TFE). TFE (scheme 2.10) is more acidic compared to EtOH due to the presence of highly electronegative fluorine atoms.

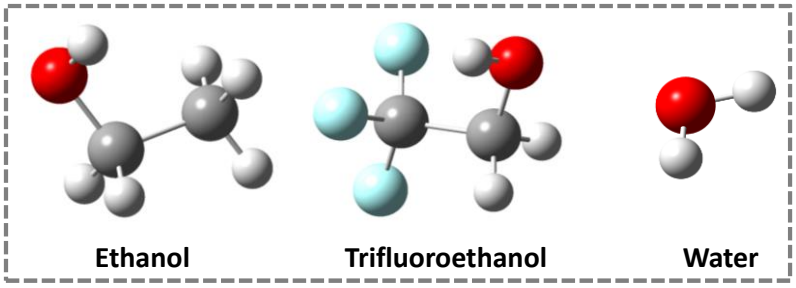

Scheme 2.10: Molecular structure of different solvents.

TFE is a flexible co-solvent in cell biology, pharmacology, protein denaturation, and peptide stabilization[54] and is also used as an inhibitor in biochemistry to study enzymes.[55] EtOH is extensively metabolized by the liver, particularly via the enzyme and as well as used in pharmacology and toxicology.[56] The solvent cluster formed between the blend of alcohol and water is the key to the development of the systems. The higher hydrophobic value of the TFE molecule is due to the lower electron donation capability compared to EtOH.[57]

2.3.3. Molecular Probes

A. D-Luciferin (D-LH_2):

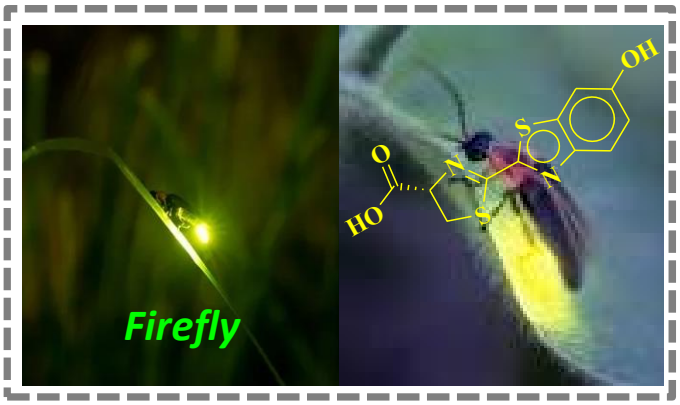

Remarkable developments in fields unrelated to bioluminescence can now be traced to simple bioluminescence studies, often carried out for the enjoyment of uncovering how species handle the feat of transforming chemical energy into light. Bioluminescence is a delightful process where living organisms turn light into chemical energy. Light comes from the oxidation of an organic substrate so-called luciferin, which is catalyzed by a luciferase enzyme. There is an immense variety of light-emitting species in the environment, including bacteria, fungi, crustaceans, mollusks, fish, and insects.[58] In 1949, along with synthesis and structure elucidation, luciferin was first isolated and purified.[59] Several researchers say that LH_2 first acted as an antioxidant, and when luciferase emerged, the bioluminescent reaction was later demanded.[60]

(4S)-2-(6-hydroxy-1,3-benzothiazole-2-yl)-4,5-dihydrothiazole-4-carboxylic acid (D-luciferin; from the Latin Lucifer, also known as ‘‘Light-bringer”) found in the “Lampyridae” family of fireflies and used in bioluminescent systems. It is the substrate of luciferase that is oxidized into oxy-luciferin, blameable for the emission of yellow-green light.[61, 62] It also has two isomers, “L” and “D”, and any of them can be used to form LH_2, resulting in L-LH_2 and D-LH_2. In this thesis, we used D-luciferin (D-LH_2) as a photoacid, which is an enzyme-catalyzed inversion derived from L-LH_2, and its chemical formula is $C_{11}H_8N_2O_3S_2$.[63] Firefly luciferin has two principal moieties, such as the moiety of hydroxyl benzothiazole and the thiazoline-carboxylic acid moiety. For the protonated species, D-luciferin was found to be fluorescent, which is a visible emission (from an excited single state down to its GS), absorbing

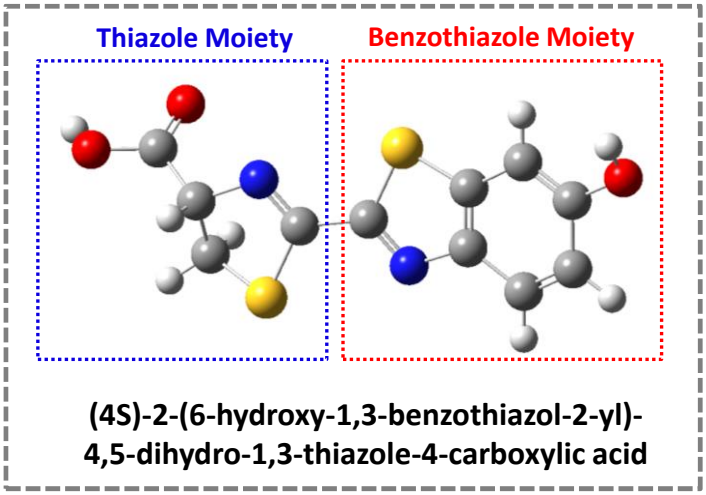

ultraviolet light at a peak of ~330 nm and releasing light after deprotonation at a peak of ~530 nm. Alkaline solutions developed a redshift of absorption (~390 nm) that may have been due to deprotonation benzothiazole hydroxyl group and redshift of emission spectra (~430 nm) due to neutral form.[64, 65] ESPT of D-luciferin is an intermolecular process via the transfer of a proton from benzothiazole hydroxyl hydrogen to the solvent, not an intramolecular process.[64, 65] ESPT of D-luciferin has earlier been studied in altered solvents of changeable polarity, pH, temperature and hydrogen-bonding ability.[66-69] The pK_a value of D-LH_2 is ~8 in the ground state (GS) which is higher than the excited-state (~0).[65] Photoacid D-luciferin is undergoing deprotonation in the excited-state and observed the ESPT rate in water is K_{PT} ~3×10^{10} s^{-1}.[64]

B. Coumarin 500 (C500): The well-known C500 solvation probe is only slightly soluble in water and has strong solubility in non-polar solvents such as cyclohexane (Cy). The absorption maxima (400 nm) are substantially red-shifted in bulk water relative to cyclohexane (~364 nm). The C500 emission maxima in bulk water (500 nm) also reveal a redshift of ~83 nm (~417 nm) relative to Cy (excitation at 350 nm). C500 is an appealing solvation probe for micro-heterogeneous conditions due to its significantly broad solvatochromic effect in the absorption and emission spectra. The probe's choice is dependent on the fact that the probe molecule remains at the interface while it is exciting.[70] The photophysics of the fluorescence probe has previously been thoroughly investigated.[71]

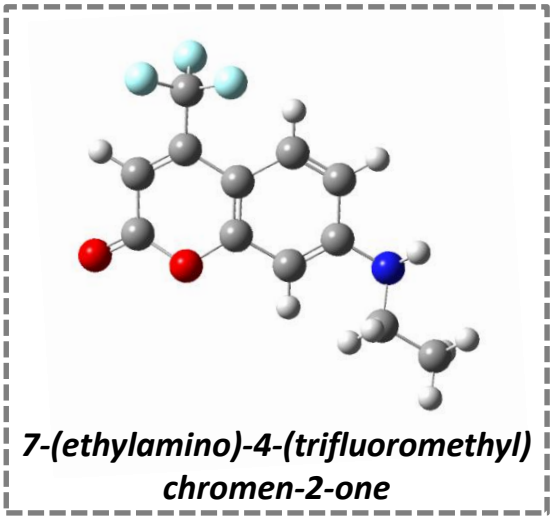

7-(ethylamino)-4-(trifluoromethyl) chromen-2-one

C. Rhodamine 6G (R6G) and Rhodamine B (RhB):

Two lipophilic dyes have been used in this dissertation (scheme 2.11), such as:[9-(2-ethoxycarbonylphenyl)-6-(ethylamino)-2,7-dimethylxanthene-3-ylidene]-ethylazanium; chloride (R6G) and [9-(2-carboxyphenyl)-6-(diethylamino)xanthene-3-ylidene]-diethylazanium; chloride (RhB). The photophysics and photochemistry of two fluorone dyes (R6G and RhB), a valuable fluorescence probe, have been subjected to challenging studies because of its many motivating properties. Rhodamines seem to be well xanthene's dyes that have long been commonly used in single-molecule detection[72], fluorescence labelling[73], etc.

for many widespread applications because of their intense fluorescence over the visible spectral region and often used as a laser dye.[74] These dyes serve a wide variety of users in TPA[75, 39], sensor[76] and non-linear optical material studies.[77] Molecular structure at the neutral P^H of the two isomers of fluorone dyes in aqueous solution; the form of Lactone and the form of Zwitterion.[78] Since of their relatively cheap and high quantum yields of fluorescence.[79]

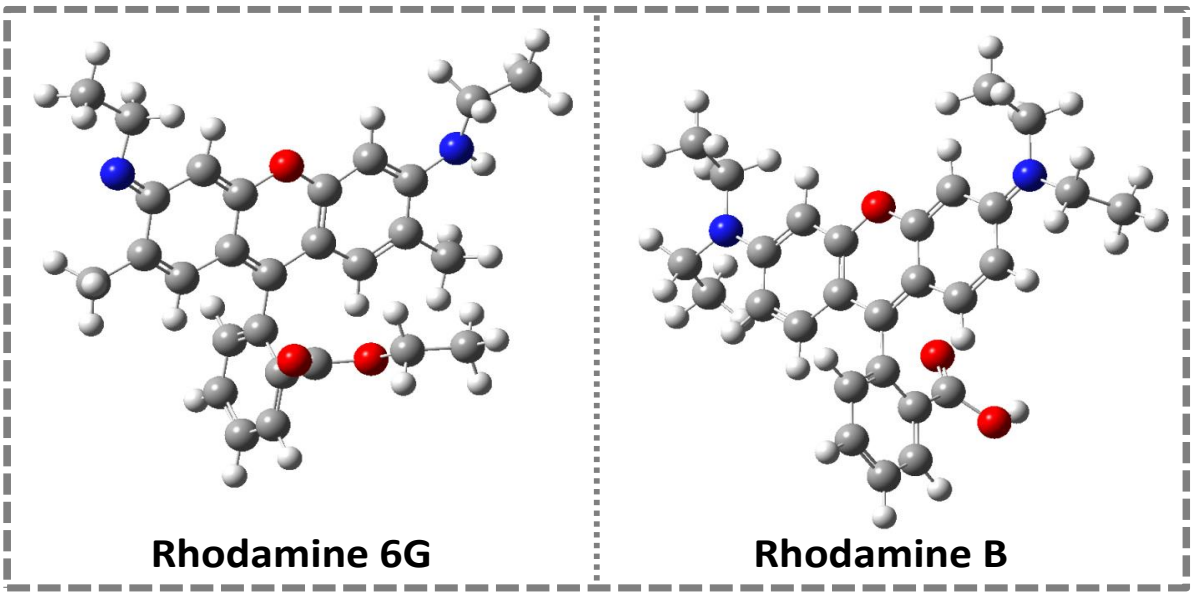

Scheme 2.11: Molecular structure of R6G and RhB.

D. Bovine serum albumin (BSA) Protein:

BSA protein (scheme 2.12) is an extracellular globular protein found in the blood plasma of cows (~70 percent identical to human serum albumin (HSA)). It contains about 583 amino acids with 17 bridges of disulfide with 1 group of sulfhydryl. The molecular weight of BSA is 66.4 kDa and the coefficient of molar extinction (ε) at 279 nm is 44318.9 $cm^{-1}M^{-1}$.[80, 81]

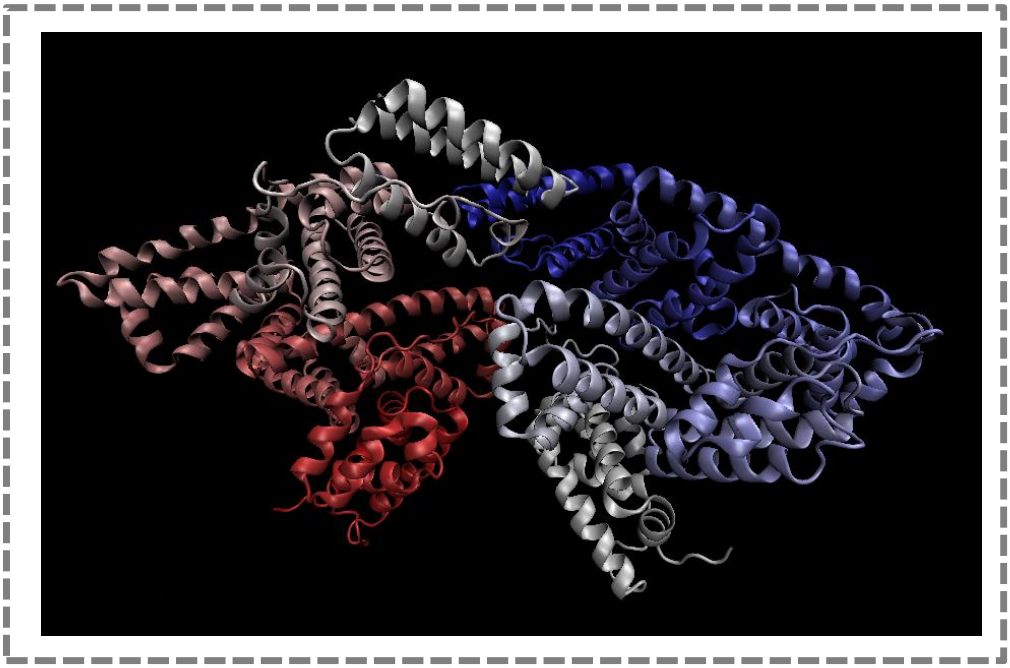

Scheme 2.12: 3D structure of the proteins (BSA) as obtained from the protein data bank. *[Modified by VMD software]*.

2.4. Systems

Organized assemblies (biomimetic): Amphiphilic molecules (such as surfactant aggregates), forming macromolecular assemblies (such as micelles and inverse micelles), which very often resemble the structural properties of biomolecules. We will address these organizations in the following sections.

2.4.1. Micelle

Micelles are made up of hydrophilic heads of surfactant molecules pointing towards the dissolving solvent (in this case, water) and hydrophobic tails pointing towards the assembly's interior (the micellar core) (scheme 2.13). Micelles appear to be the primary feature above the so-called 'critical micelle concentration (CMC)', but free surfactants are also existing as monomers in the system. The following surfactants are used in this dissertation for the formation of aqueous micelles, such as: anionic: TSDS, SDS, SDeS and SOS; non-ionic: Tx-100; cationic: CTAB (Scheme 2.9).

2.4.2. Reverse Micelle (RM)

RMs (scheme 2.13) are isotopic mixtures of water, surfactant, and organic solvent in which very small aqueous droplets are dispersed in a non-polar solvent covered with a coating of surfactant molecules. Various types of surfactants have been used in this thesis with different head groups such as anionic AOT, cationic DDAB, and nonionic Ig-520 (molecular structures of these surfactants are given in scheme 2.9). Cyclohexane (Cy) was used as an RM preparation oil.[82] The double-tailed anionic surfactant (AOT) is also applicable in the field of drug delivery and is one of the most expansively researched surfactants for the investigation of such heterogeneous systems (such as RM).[83, 84] DDAB-based systems are also used as an effective and safe vehicle for continuous drug release, called cationic surfactant.[85] The class of surfactant based on Ig-520 (non-ionic), has been commonly used in industrial and biochemical processes.[86] AOT is the most common surfactant that forms stable RM and has been thoroughly investigated for the properties of its aggregate.[87, 88] Compared to AOT, Ig-520 is also capable of developing well defined, slightly larger RMs.[89]

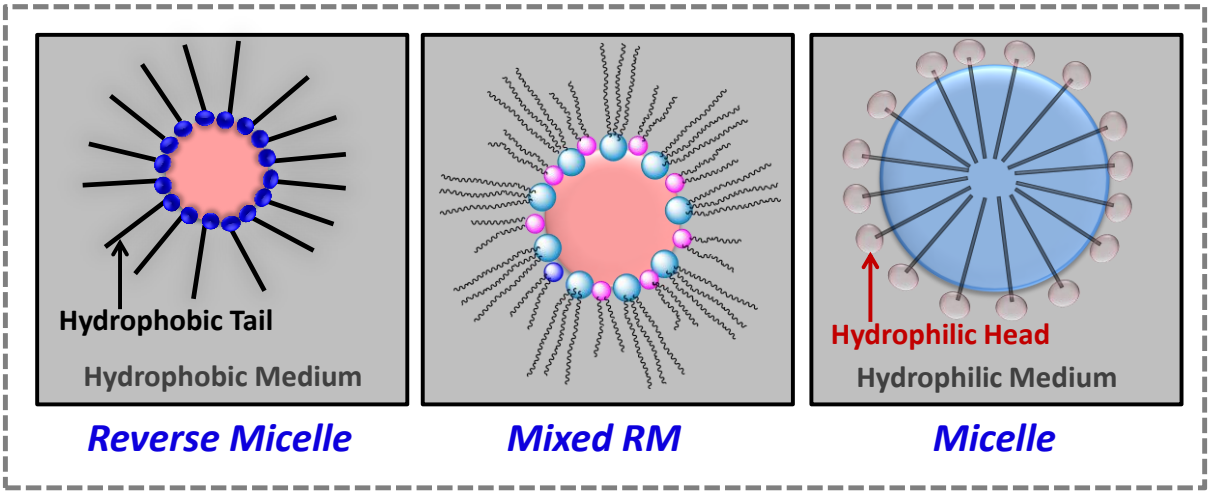

Scheme 2.13: A visualization of various biomimetic assemblies; the left panel is reverse micelle, the middle panel is mixed RM, and the right panel is micelle.

2.4.3. Biomolecule:

Biomolecules are molecules in living organisms that exist naturally and include macromolecules such as proteins, carbohydrates, lipids and nucleic acids. I will select protein (like bovine serum albumin (BSA)) from all of these biomolecules as the most essential for life. Proteins, which consist of amino acids, are responsible for a cell's enzymatic activities

and other structural needs. Amino acids are made of proteins (H_2N-HCR-CO_2H). Only L-amino acids were chosen by nature to constitute all proteins. Four levels of protein structure exist, such as **(i) Primary structure**: A sequence of amino acids that are bound to the polypeptide chain one after another by peptide bonds. **(ii) Secondary structure:** Polypeptide chains fold by hydrogen bonding into alpha-helix, beta-sheet, turns and coils. **(iii) Tertiary structure**: Water-soluble proteins are further folded into a compact structure by hydrogen bonding, van der Waals interaction, electrostatic interaction and di-sulphide bridges (covalent bonds formed between cysteine residues in different parts of the protein). **(iv) Quaternary structure:** Folded polypeptide chains are often assembled into multi-subunit structures.

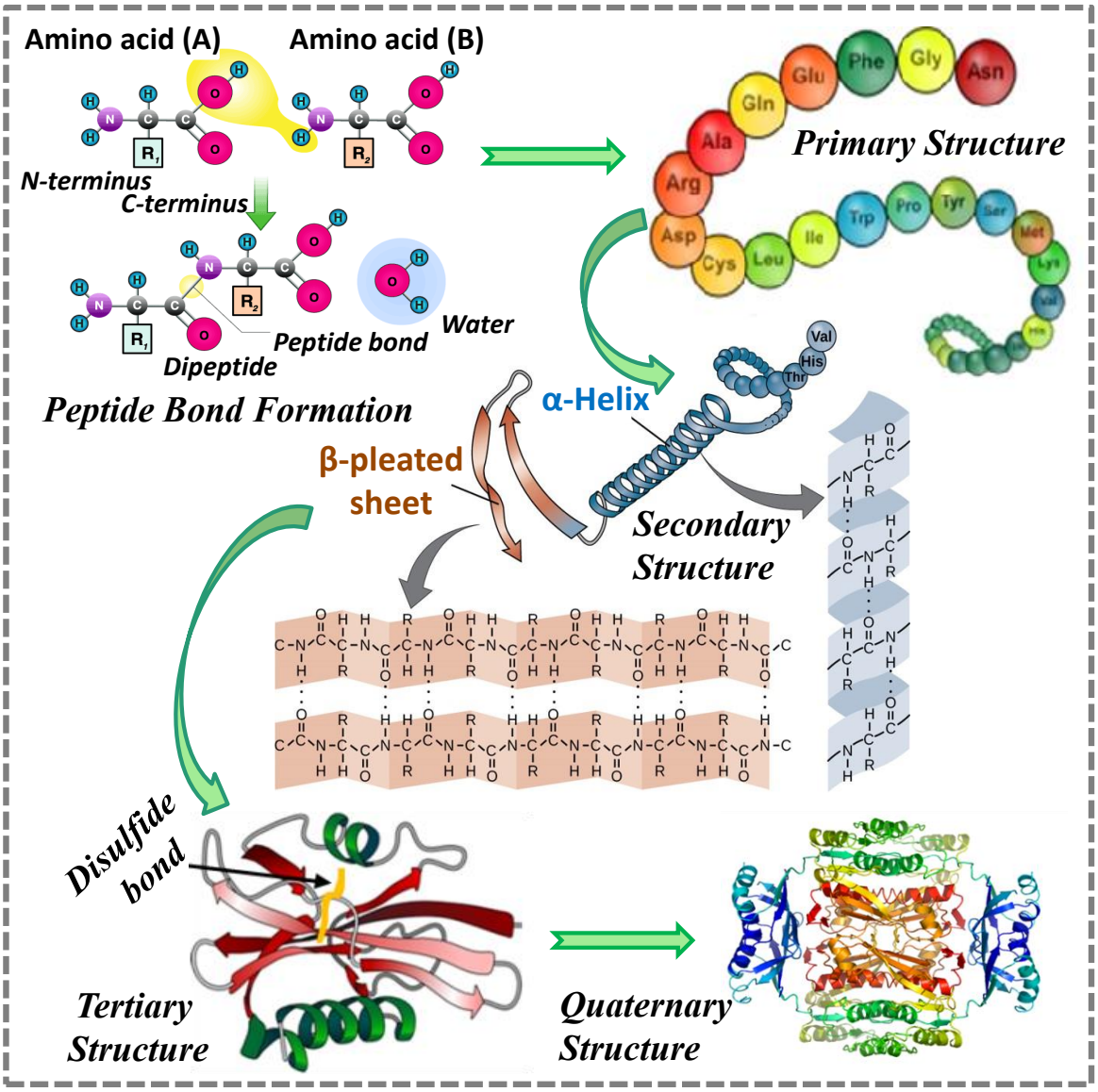

Scheme 2.14: Protein structures are classified into four levels: primary, secondary, tertiary, and quaternary. (Modified from the source file: *https://en.wikipedia.org/wiki/File:Main_protein_structure_levels_en.svg*).

It is possible to obtain protein secondary and tertiary structures from the study of CD spectra. It is a very accurate instrument to underline the modifications in protein conformation. The secondary and tertiary structures can sense the 190-260 nm (far UV CD) and 250-310 nm (near UV CD) regions, respectively. The distinctive CD spectrum for each pure secondary conformation is shown in scheme 2.15. A negative peak with different maximums of comparable magnitude at 208 nm and 222 nm is characterized by the CD spectrum of alpha-helices. The peptide $n \rightarrow \pi^*$ transition is responsible for the negative 222 nm band, while the 208 nm band outcomes from the exciton splitting of the lowest peptide $\pi \rightarrow \pi^*$ transition.[90, 91] The absorption of aromatic residues (phenylalanine, tyrosine, and tryptophan) and di-sulphide bonds are responsible for the spectrum characteristics occurring in the near UV zone.

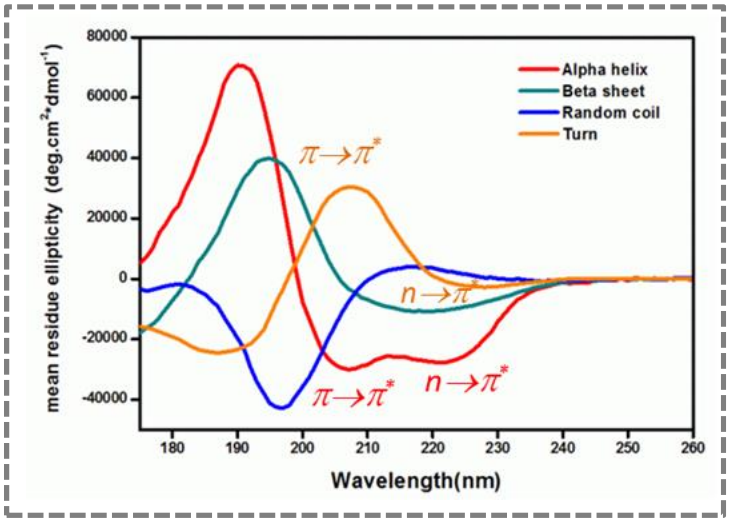

Scheme 2.15.: Typical CD spectra for each secondary structure content.[92]

2.5. Other Measurements

2.5.1. Solubilization Capacity Control of Water in RM

Water was progressively injected into a 2-ml surfactant solution using a micro-syringe of varying capacity in an organic solvent (oil) held at a constant room temperature while being stirred constantly in a vortex shaker. The beginning of persistent turbidity at every composition of the surfactant mixture in the oil indicates maximum water solubilization.

2.5.2. Preparation of Sample

We will explore the specifics of various sample preparations in this section to study water in restricted environments.

Preparation of Micellar Solution: Dissolving surfactants in water was used to prepare stock solutions of aqueous micellar solutions. The desired concentration of micelle was ensured by applying a quantitative quantity of stock solution to the water with the mixture being simultaneously stirred for an hour. To form micelles in water, cationic CTAB, anionic 'TSDS, SDS, SDeS, SOS', and nonionic Tx100 are used.

Preparation of Reverse Micellar Solution: The prepared to reverse micellar solutions with a specific degree of hydration (w_0 = [H_2O]/[Surfactant]) the calculated volume of water was added to the known volume of 0.1 M of surfactant solution in cyclohexane. A very small quantity of the aqueous solution of the probe was applied during the preparation of the particular RM in the case of dissolving a probe within the RM water. After baseline correction, all FTIR, steady-state fluorescence, and absorption spectra were collected by w_0=0 of that RM.

*** In this chapter, the chemical structures were drawn by the "Gaussview 05 software" and the symbols used are as follows:*

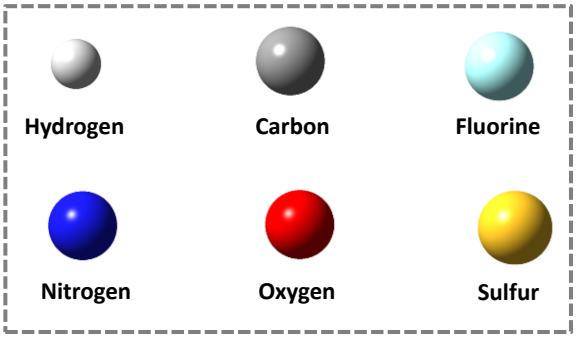

2.6. References

1. Parson, W. W., Electronic absorption. In *Modern Optical Spectroscopy*, Springer: 2015; pp 123-223.
2. Jabłoński, A., Über den mechanismus der Photolumineszenz von Farbstoffphosphoren. *Zeitschrift für Physik* **1935,** *94* (1-2), 38-46.
3. Lakowicz, J. R., *Principles of Fluorescence Spectroscopy*. 2nd ed.; Kluwer Academic/Plenum: New York, 2006.

4. Stokes, G. G., XXX. On the change of refrangibility of light. *Philosophical transactions of the Royal Society of London* **1852,** (142), 463-562.
5. Albani, J. R., *Principles and applications of fluorescence spectroscopy*. John Wiley & Sons: 2008.
6. Straughan, B.; Walker, S., Fluorescence and Phosphorescence Spectroscopy. In *Spectroscopy*, Springer: 1976; pp 161-198.
7. Birks, J. B., Photophysics of aromatic molecules. **1970**.
8. Lakowicz, J. R., *Principles of fluorescence spectroscopy*. Kluwer Academic/Plenum: New York, 1999.
9. Braslavsky, S. E., Glossary of terms used in photochemistry, 3rd edition (IUPAC Recommendations 2006). *Pure and Applied Chemistry* **2007,** *79* (3), 293-465.
10. Eftink, M., Topics in fluorescence spectroscopy. In *Principles*, Plenum Press New York: 1991; Vol. 2, pp 53-126.
11. Pal, S. K.; Peon, J.; Bagchi, B.; Zewail, A. H., Biological Water: Femtosecond Dynamics of Macromolecular Hydration. *The Journal of Physical Chemistry B* **2002,** *106* (48), 12376-12395.
12. Fleming, G. R.; Cho, M., Chromophore-Solvent Dynamics. *Annual review of physical chemistry* **1996,** *47* (1), 109-134.
13. Horng, M. L.; Gardecki, J. A.; Papazyan, A.; Maroncelli, M., Subpicosecond measurements of polar solvation dynamics: coumarin 153 revisited. *The Journal of Physical Chemistry* **1995,** *99* (48), 17311-17337.
14. Periasamy, N.; Koti, A. S. R., Time resolved fluorescence spectroscopy: TRES and TRANES. *Proceedings of Indian Academy of Sciences* **2003,** *69A*, 41-48.
15. Koti, A. S. R.; Krishna, M. M. G.; Periasamy, N., Time-resolved area-normalized emission spectroscopy (TRANES): A novel method for confirming emission from two excited states. *The Journal of Physical Chemistry A* **2001,** *105*, 1767-1771.
16. Lakowicz, J. R., Time-dependent anisotropy decays. In *Principles of Fluorescence Spectroscopy*, Springer: 1999; pp 321-345.
17. O'Connor, D., *Time-correlated single photon counting*. Academic Press: 2012.
18. Lipari, G.; Szabo, A., Effect of librational motion on fluorescence depolarization and nuclear magnetic resonance relaxation in macromolecules and membranes. *Biophysical Journal* **1980,** *30*, 489.
19. Wang, C. C.; Pecora, R., Time-correlation functions for restricted rotational diffusion. *The Journal of Chemical Physics* **1980,** *72*, 5333-5340.
20. Tan, H.-S.; Piletic, I. R.; Fayer, M. D., Orientational dynamics of water confined on a nanometer length scale in reverse micelles. *The Journal of Chemical Physics* **2005,** *122*, 174501.
21. Wilson, T.; Hastings, J. W., Bioluminescence. *Annual review of cell and developmental biology* **1998,** *14* (1), 197-230.
22. Nandi, N.; Sahu, K., Analysis of excited state proton transfer dynamics of HPTS in methanol-water mixtures from time-resolved area-normalised emission spectrum (TRANES). *Journal of Photochemistry and Photobiology A: Chemistry* **2019,** *374*, 138-144.
23. Pal, T.; Sahu, K., Anomalous Variation of Excited-State Proton Transfer Dynamics inside a Triblock Copolymer–Cationic Surfactant Mixed Micelle. *The Journal of Physical Chemistry B* **2019,** *123* (40), 8559-8568.
24. Lawler, C.; Fayer, M. D., Proton Transfer in Ionic and Neutral Reverse Micelles. *The Journal of Physical Chemistry B* **2015,** *119* (19), 6024-6034.
25. Vodopyanov, K.; Richard, L. S., Handbook of nonlinear optics. *Opt Photonics News* **1997,** *8*, 54-55.
26. Loudon, R., The quantum theory of light. Oxford University Press Inc. **1983**.

27. Göppert-Mayer, M., Über Elementarakte mit zwei Quantensprüngen. *Annalen der Physik* **1931,** *401* (3), 273-294.
28. Göppert- Mayer, M., Über elementarakte mit zwei quantensprüngen. *Annalen der Physik* **1931,** *401* (3), 273-294.
29. Kaiser, W.; Garrett, C., Two-photon excitation in Ca F 2: Eu 2+. *Physical review letters* **1961,** *7* (6), 229.
30. Mayer, M. G., Maria Goeppert-Mayer.
31. Parthenopoulos, D.; Rentzepis, P., Two- photon volume information storage in doped polymer systems. *Journal of Applied Physics* **1990,** *68* (11), 5814-5818.
32. Brust-Mascher, I.; Webb, W. W., Calcium waves induced by large voltage pulses in fish keratocytes. *Biophysical journal* **1998,** *75* (4), 1669-1678.
33. Denk, W.; Strickler, J. H.; Webb, W. W., Two-photon laser scanning fluorescence microscopy. *Science* **1990,** *248* (4951), 73-76.
34. Collins, J., Two-photon absorption and applications to biological systems. In *Biophotonics: Spectroscopy, Imaging, Sensing, and Manipulation*, Springer: 2011; pp 261-285.
35. Xu, C.; Webb, W. W., Measurement of two-photon excitation cross sections of molecular fluorophores with data from 690 to 1050 nm. *JOSA B* **1996,** *13* (3), 481-491.
36. Deiana, M.; Mettra, B.; Martinez-Fernandez, L.; Mazur, L. M.; Pawlik, K.; Andraud, C.; Samoc, M.; Improta, R.; Monnereau, C.; Matczyszyn, K., Specific Recognition of G-Quadruplexes Over Duplex-DNA by a Macromolecular NIR Two-Photon Fluorescent Probe. *The Journal of Physical Chemistry Letters* **2017**, 5915-5920.
37. Yang, W. J.; Kim, C. H.; Jeong, M.-Y.; Lee, S. K.; Piao, M. J.; Jeon, S.-J.; Cho, B. R., Synthesis and Two-Photon Absorption Properties of 9,10-Bis(arylethynyl)anthracene Derivatives. *Chemistry of Materials* **2004,** *16* (14), 2783-2789.
38. Tian, Y.; Chen, C. Y.; Cheng, Y. J.; Young, A. C.; Tucker, N. M.; Jen, A. K. Y., Hydrophobic Chromophores in Aqueous Micellar Solution Showing Large Two-Photon Absorption Cross Sections. *Advanced Functional Materials* **2007,** *17* (10), 1691-1697.
39. Nag, A.; Goswami, D., Solvent effect on two-photon absorption and fluorescence of rhodamine dyes. *Journal of Photochemistry and Photobiology A: Chemistry* **2009,** *206* (2–3), 188-197.
40. Tkaczyk, E. R.; Tkaczyk, A. H.; Mauring, K.; Ye, J. Y.; Baker, J. R.; Norris, T. B., Control of two-photon fluorescence of common dyes and conjugated dyes. *Journal of Fluorescence* **2009,** *19* (3), 517-532.
41. Birch, D. J., Multiphoton excited fluorescence spectroscopy of biomolecular systems. *Spectrochimica Acta Part A: Molecular and Biomolecular Spectroscopy* **2001,** *57* (11), 2313-2336.
42. Galas, L.; Gallavardin, T.; Bénard, M.; Lehner, A.; Schapman, D.; Lebon, A.; Komuro, H.; Lerouge, P.; Leleu, S.; Franck, X., "Probe, Sample, and Instrument (PSI)": the hat-trick for fluorescence live cell imaging. *Chemosensors* **2018,** *6* (3), 40.
43. Parthenopoulos, D. A.; Rentzepis, P. M., Three-dimensional optical storage memory. *Science* **1989,** *245* (4920), 843-845.
44. Burr, G., Volumetric storage Encyclopedia of Optical Engineering ed RB Johnson and RG Driggers. New York: Dekker: 2003.
45. Zipfel, W. R.; Williams, R. M.; Webb, W. W., Nonlinear magic: multiphoton microscopy in the biosciences. *Nature biotechnology* **2003,** *21* (11), 1369.
46. Kuebler, S. M.; Cumpston, B. H.; Ananthavel, S.; Barlow, S.; Ehrlich, J. E.; Erskine, L.; Heikal, A. A.; McCord-Maughon, D.; Qin, J.; Roeckel, H. In *Three-dimensional microfabrication using two-photon-activated chemistry*, Micro-and Nano-photonic Materials and Devices, International Society for Optics and Photonics: 2000; pp 97-106.

47. Lin, T.-C.; Chung, S.-J.; Kim, K.-S.; Wang, X.; He, G. S.; Swiatkiewicz, J.; Pudavar, H. E.; Prasad, P. N., Organics and polymers with high two-photon activities and their applications. *Polymers for Photonics Applications II* **2003**, 157-193.
48. Ellis-Davies, G. C., Caged compounds: photorelease technology for control of cellular chemistry and physiology. *Nature methods* **2007,** *4* (8), 619-628.
49. Spangler, C., Recent development in the design of organic materials for optical power limiting. *Journal of Materials Chemistry* **1999,** *9* (9), 2013-2020.
50. Wang, Y.; Goodson, T., Early aggregation in prion peptide nanostructures investigated by nonlinear and ultrafast time-resolved fluorescence spectroscopy. *The Journal of Physical Chemistry B* **2007,** *111* (2), 327-330.
51. Cotlet, M.; Goodwin, P. M.; Waldo, G. S.; Werner, J. H., A comparison of the fluorescence dynamics of single molecules of a green fluorescent protein: one- versus two-photon excitation. *ChemPhysChem* **2006,** *7* (1), 250-260.
52. Bhawalkar, J.; Kumar, N.; Zhao, C.-F.; Prasad, P., Two-photon photodynamic therapy. *Journal of clinical laser medicine & surgery* **1997,** *15* (5), 201-204.
53. Liu, J.; Zhao, Y.; Zhao, J.; Xia, A.; Jiang, L.; Wu, S.; Ma, L.; Dong, Y.; Gu, Y., Two-photon excitation studies of hypocrellins for photodynamic therapy. *Journal of Photochemistry and Photobiology B: Biology* **2002,** *68* (2-3), 156-164.
54. Buck, M., Trifluoroethanol and colleagues: cosolvents come of age. Recent studies with peptides and proteins. *Quarterly reviews of biophysics* **1998,** *31* (3), 297-355.
55. Taber, R. L., The competitive inhibition of yeast alcohol dehydrogenase by 2,2,2-trifluoroethanol. *Biochemical Education* **1998,** *26* (3), 239-242.
56. Harger, R. N., The Pharmacology and Toxicology of Alcohol. *JAMA* **1958,** *167* (18), 2199-2202.
57. Matsugami, M.; Yamamoto, R.; Kumai, T.; Tanaka, M.; Umecky, T.; Takamuku, T., Hydrogen bonding in ethanol–water and trifluoroethanol–water mixtures studied by NMR and molecular dynamics simulation. *Journal of Molecular Liquids* **2016,** *217*, 3-11.
58. Hastings, J. W., Bioluminescence. In *Cell physiology source book*, Elsevier: 1995; pp 665-681.
59. Strehler, B. L.; Mc, E. W., Purification of firefly luciferin. *Journal of cellular and comparative physiology* **1949,** *34* (3), 457-466.
60. Dubuisson, M.; Marchand, C.; Rees, J. F., Firefly luciferin as antioxidant and light emitter: the evolution of insect bioluminescence. *Luminescence: the journal of biological and chemical luminescence* **2004,** *19* (6), 339-344.
61. da Silva, L. P.; da Silva, J. C. G. E., Computational Studies of the Luciferase Light-Emitting Product: Oxyluciferin. *J. Chem. Theory Comput.* **2011,** *7*, 809-817.
62. Erez, Y.; Presiado, I.; Gepshtein, R.; da Silva, L. P.; da Silva, J. C. G. E.; Huppert, D., Comparative Study of the Photoprotolytic Reactions of d-Luciferin and Oxyluciferin. *J. Phys. Chem. A* **2012,** *116*, 7452-7461.
63. Marques, S. M.; Esteves da Silva, J. C., Firefly bioluminescence: a mechanistic approach of luciferase catalyzed reactions. *IUBMB life* **2009,** *61* (1), 6-17.
64. Erez, Y.; Huppert, D., Excited-State Intermolecular Proton Transfer of the Firefly's Chromophore d-Luciferin. *The Journal of Physical Chemistry A* **2010,** *114* (31), 8075-8082.
65. Presiado, I.; Erez, Y.; Huppert, D., Excited-State Intermolecular Proton Transfer of the Firefly's Chromophore d-Luciferin. 2. Water− Methanol Mixtures. *The Journal of Physical Chemistry A* **2010,** *114* (35), 9471-9479.
66. Erez, Y.; Huppert, D., Excited-state intermolecular proton transfer of the firefly's chromophore D-luciferin. *J. Phys. Chem. A* **2010,** *114*, 8075-8082.

67. Presiado, I.; Erez, Y.; Huppert, D., Excited-State Intermolecular Proton Transfer of the Firefly's Chromophore d-Luciferin. 2. Water− Methanol Mixtures. *J. Phys. Chem. A* **2010,** *114*, 9471-9479.
68. Erez, Y.; Presiado, I.; Gepshtein, R.; Huppert, D., Excited-state intermolecular proton transfer of firefly luciferin IV. Temperature and pH dependence. *J. Phys Chem. A* **2011,** *115*, 1617-1626.
69. Kuchlyan, J.; Banik, D.; Roy, A.; Kundu, N.; Sarkar, N., Excited-State Proton Transfer Dynamics of Firefly's Chromophore D-Luciferin in DMSO-Water Binary Mixture. *J. Phys. Chem. B* **2014,** *118*, 13946-13953.
70. Mitra, R. K.; Sinha, S. S.; Pal, S. K., Temperature-dependent solvation dynamics of water in sodium bis (2-ethylhexyl) sulfosuccinate/isooctane reverse micelles. *Langmuir* **2008,** *24* (1), 49-56.
71. Nad, S.; Pal, H., Photophysical Properties of coumarin-500 (C500): unusual behavior in nonpolar solvents. *J. Phys. Chem. A* **2003,** *107* (4), 501-507.
72. Keller, R. A.; Ambrose, W. P.; Goodwin, P. M.; Jett, J. H.; Martin, J. C.; Wu, M., Single-molecule fluorescence analysis in solution. *Applied Spectroscopy* **1996,** *50* (7), 12A-32A.
73. Fontaine, M.; Elmquist, W. F.; Miller, D. W., Use of rhodamine 123 to examine the functional activity of P-glycoprotein in primary cultured brain microvessel endothelial cell monolayers. *Life sciences* **1996,** *59* (18), 1521-1531.
74. Duarte, F. J.; Kelley, P.; Hillman, L. W.; Liao, P. F., *Dye laser principles: with applications*. A. P.: 1990.
75. Xu, C.; Webb, W. W., Measurement of two-photon excitation cross sections of molecular fluorophores with data from 690 to 1050 nm. *J. Opt. Soc. Am. B* **1996,** *13* (3), 481-491.
76. Chen, J.; Zheng, A.; Chen, A.; Gao, Y.; He, C.; Kai, X.; Wu, G.; Chen, Y., A functionalized gold nanoparticles and Rhodamine 6G based fluorescent sensor for high sensitive and selective detection of mercury (II) in environmental water samples. *Analytica chimica acta* **2007,** *599* (1), 134-142.
77. Rao, S. V.; Srinivas, N. N.; Rao, D. N., Nonlinear absorption and excited state dynamics in Rhodamine B studied using Z-scan and degenerate four wave mixing techniques. *Chemical physics letters* **2002,** *361* (5-6), 439-445.
78. Pepe, G.; Cole, J. M.; Waddell, P. G.; Griffiths, J. R., Molecular engineering of fluorescein dyes as complementary absorbers in dye co-sensitized solar cells. *Molecular Systems Design & Engineering* **2016,** *1* (4), 402-415.
79. Kubin, R. F.; Fletcher, A. N., Fluorescence quantum yields of some rhodamine dyes. *Journal of Luminescence* **1982,** *27* (4), 455-462.
80. Arnaud, P., The plasma proteins: Structure, function, and genetic control. Academic Press: Orlando, Fla., 1986; Vol. 4.
81. Hirayama, K.; Akashi, S.; Furuya, M.; Fukuhara, K.-i., Rapid confirmation and revision of the primary structure of bovine serum albumin by ESIMS and Frit-FAB LC/MS. *Biochemical and biophysical research communications* **1990,** *173* (2), 639-646.
82. Paul, B. K.; Mitra, R. K., Water solubilization capacity of mixed reverse micelles: Effect of surfactant component, the nature of the oil, and electrolyte concentration. *Journal of Colloid and Interface Science* **2005,** *288*, 261-279.
83. Gupta, R. R.; Jain, S. K.; Varshney, M., AOT water-in-oil microemulsions as a penetration enhancer in transdermal drug delivery of 5-fluorouracil. *Colloids and Surfaces B: Biointerfaces* **2005,** *41* (1), 25-32.

84. Chavanpatil, M. D.; Khdair, A.; Panyam, J., Surfactant-polymer nanoparticles: a novel platform for sustained and enhanced cellular delivery of water-soluble molecules. *Pharmaceutical research* **2007,** *24* (4), 803-810.
85. Zhao, L.; Liu, J.; Zhang, L.; Gao, Y.; Zhang, Z.; Luan, Y., Self-assembly properties, aggregation behavior and prospective application for sustained drug delivery of a drug-participating catanionic system. *International Journal of Pharmaceutics* **2013,** *452* (1–2), 108-115.
86. Sedgwick, M.; Crans, D.; Levinger, N., What is inside a nonionic reverse micelle? Probing the interior of Igepal reverse micelles using decavanadate. *Langmuir* **2009,** *25* (10), 5496-5503.
87. Riter, R. E.; Undiks, E. P.; Levinger, N. E., Impact of counterion on water motion in aerosol OT reverse micelles. *Journal of the American Chemical Society* **1998,** *120* (24), 6062-6067.
88. Nave, S.; Eastoe, J.; Heenan, R. K.; Steytler, D.; Grillo, I., What is so special about Aerosol-OT? 2. Microemulsion systems. *Langmuir* **2000,** *16* (23), 8741-8748.
89. Das, A.; Patra, A.; Mitra, R. K., Do the physical properties of water in mixed reverse micelles follow a synergistic effect: a spectroscopic investigation. *The Journal of Physical Chemistry B* **2013,** *117* (13), 3593-3602.
90. Woody, R. W.; Tinoco Jr., I., Optical Rotation of Oriented Helices. III. Calculation of the Rotatory Dispersion and Circular Dichroism of the Alpha- and 310- Helix. *J. Chem. Phys.* **1967,** *46*, 4927-4945.
91. Nordén, B., *Circular dichroism and linear dichroism*. Oxford University Press, USA: 1997; Vol. 1.
92. Rodger, A.; Ismail, M. A., In *Spectrophotometry and Spectrofluorimetry A Practical Approach*, Gore, M. G., Ed. Oxford University Press: Oxford, New York, 2000; pp 99-139.

Chapter 3

3. Instrumentation and Basic Principles

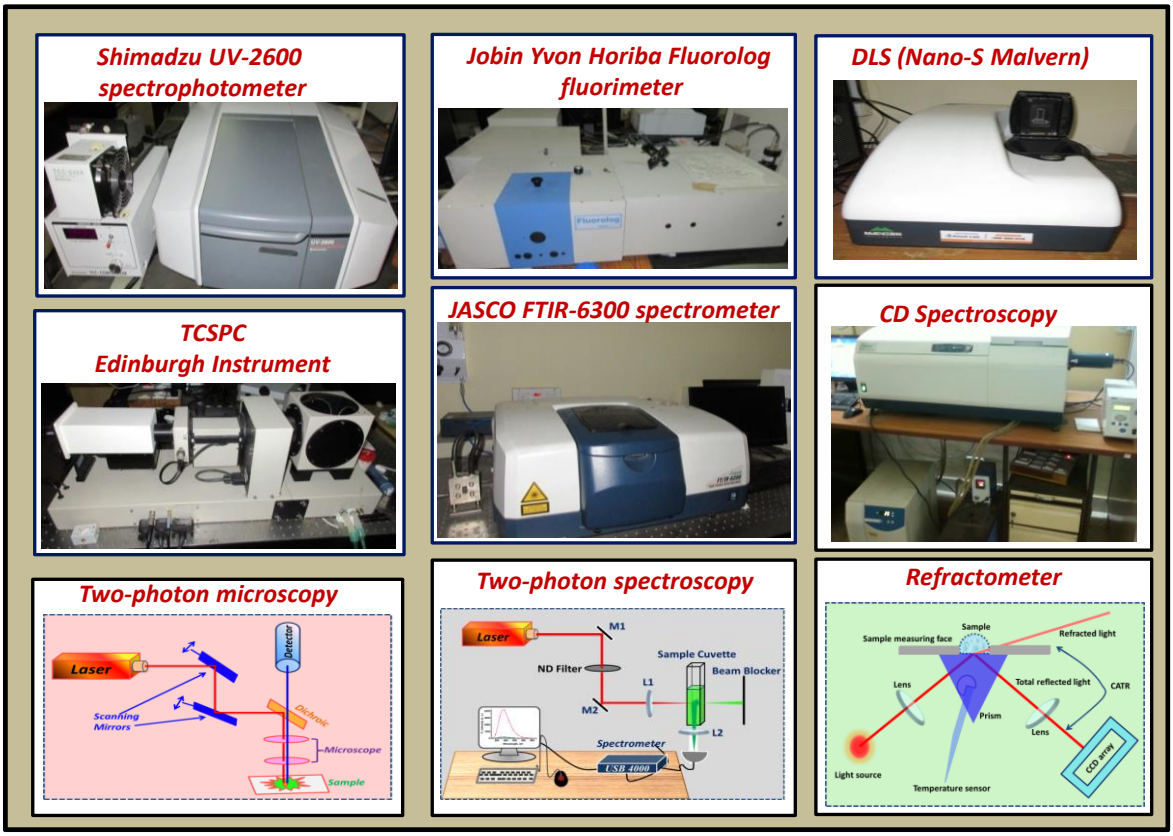

This chapter explains some of the experimental techniques and methods used in chapters 4, 5, 6, 7 and 8. Basic working principles and information behind those techniques will be briefly described. In order to explain the findings clearly, one should have a clear understanding of the instrumentation and underlining the physical processes.

3.1. Ultra Violet-Visible Spectrophotometer (UV-Vis)

The steady-state absorption spectrums shown in this dissertation were reported using the UV-2600 (SHIMADZU) spectrophotometer. Scheme 3.1 is a schematic description of the absorption spectrophotometer. Tungsten (W1) and deuterium (D2) lamps have been used as light sources for the visible and ultraviolet region in the absorption spectrophotometer, with a lamp exchange wavelength of 282-293 nm. The light that a mirror directs from the source lamp passes through a filter and enters the monochromator. High-performance blazed holographic grating, which extends the beam of light through its component wavelengths, is the only monochromator used in this instrument. A particular wavelength is then picked from the incoming light by the diffraction grating present in the monochromator. Until reaching the sample, the light with a particular wavelength (monochromatic light) is split into two beams.

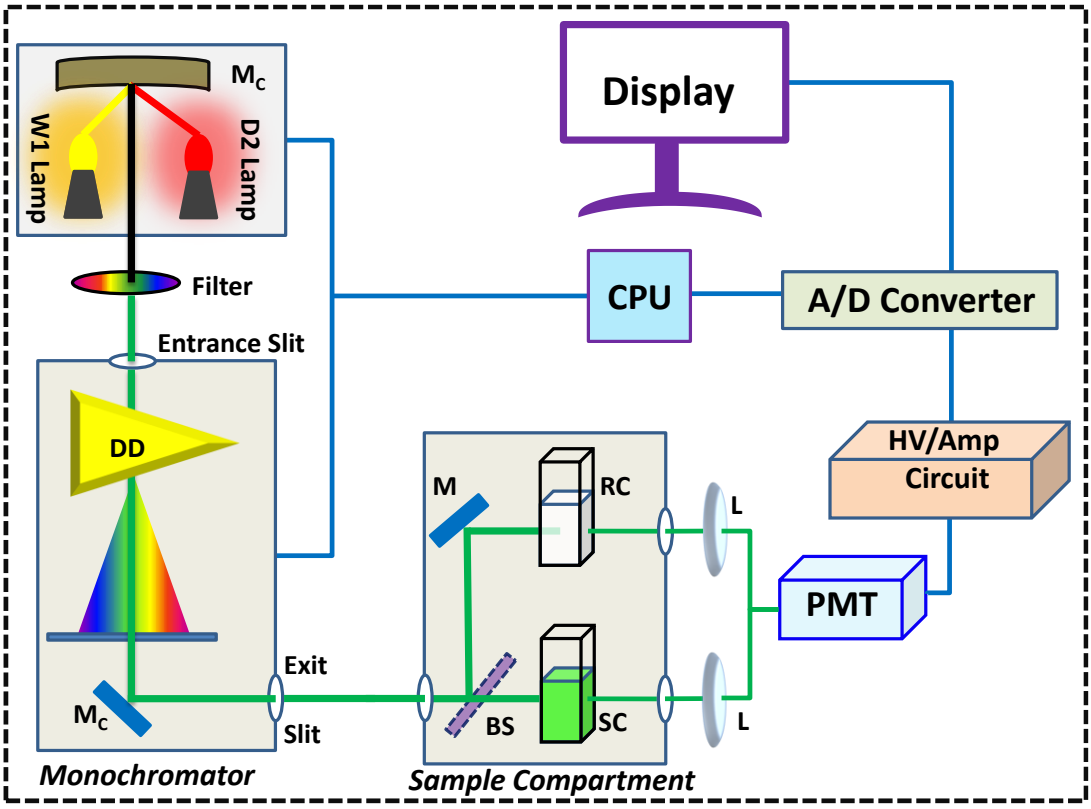

Scheme 3.1: Representation of an absorption spectrophotometer. Tungsten halogen (W1) and deuterium lamps (D2) are used in the visible and UV regions as light sources, respectively. M_c, M, L, RC, SC, BS, DD, PMT reflect concave mirror, plane mirror, lens, reference cell, sample cell, beam splitter, dispersion device, and photomultiplier tube, respectively. The A/D converter and the HV/Amp are analog to the digital converter and the high voltage/amplifier circuit respectively.

This is a typical double beam instrument; one of these two beams is used for reference while the other is moving through the sample. As a detector, a Photomultiplier Tube (PMT) is used. The final absorption data is produced after a few sequence steps, signal enhancement, analog to digital conversion.

As constant radiation passes through a substance, some of it may be absorbed. When this occurs, the residual radiation produces a spectrum with holes in it, known as an absorption spectrum, when it is passed through a prism. The molecules switch from a lower electronic energy state (S_0) to a higher energy state (S_1) by absorbing electromagnetic radiation. Both vibrational and rotational transitions are often correlated with such an electronic transformation in any molecule. But the states of electronic energy consist of a vast number of closely spaced rotational and vibrational levels that not every spectrophotometer can solve. Rather, an "envelope" is traced by the instrument. That's why a molecule's UV absorption spectrum typically provides a broad distribution band with a central peak wavelength where the maximum transition occurs. That is why a molecule's UV spectrum usually consists of a wideband centered close to the wavelength of the major transition.

This technique allows the measurement of the absorption spectrum in the 190-900 nm range with a spectral resolution of 0.1 nm; however, tests are conducted in a 1 cm path length cuvette at 1 nm wavelength intervals. There is an empirical equation known as the 'Beer-Lambert' law as given below as regards the degree of absorption of a molecule,

$$A = \log(I_0/I) = \varepsilon c l \qquad \text{(For a specified wavelength)} \qquad (3.1)$$

where A=absorption, "I_0" is the intensity of the light incident on the sample cell, "I" is the intensity of the light exit the sample cell, "ε" is the molar absorption coefficient, "c" is the molar concentration of the solute and "l" is the length of the sample cell. If 'c' is in mole l^{-1} and 'l' is in cm, then ε is called the molar extinction coefficient. This absorption is linearly proportional to the concentration of the molecules and the length of the path through the absorbing media that the light has to cross. With the support of Peltier, the temperature-dependent steady-state absorption spectrum was also obtained using a UV-Visible spectrophotometer.

3.2. Steady-State Fluorescence Spectroscopy

In this study, steady-state emission spectra were measured using Fluorolog (scheme 3.2), Horiba-JobinYvon, Edison, NJ (Model LFI-3751). As a source of continuous-wave light, the ozone-free Xe-Arc lamp was used. There are two monochromators[1], which are monochromators of excitation and emission. The monochromator's reflection gratings have 1200 grooves per mm and are blazed at 500 nm (emission) and 330 nm (excitation). Excitation wavelength coverage of 220-600 nm and emission wavelength coverage of 290-850 nm can be given by these gratings. All excitation and emission spectrum are collected in a quartz cuvette with such a length of 1 cm and a wavelength of 1 nm interval. Using a fluorimeter with the support of "Peltier", the temperature-dependent steady-state emission spectra were also collected.

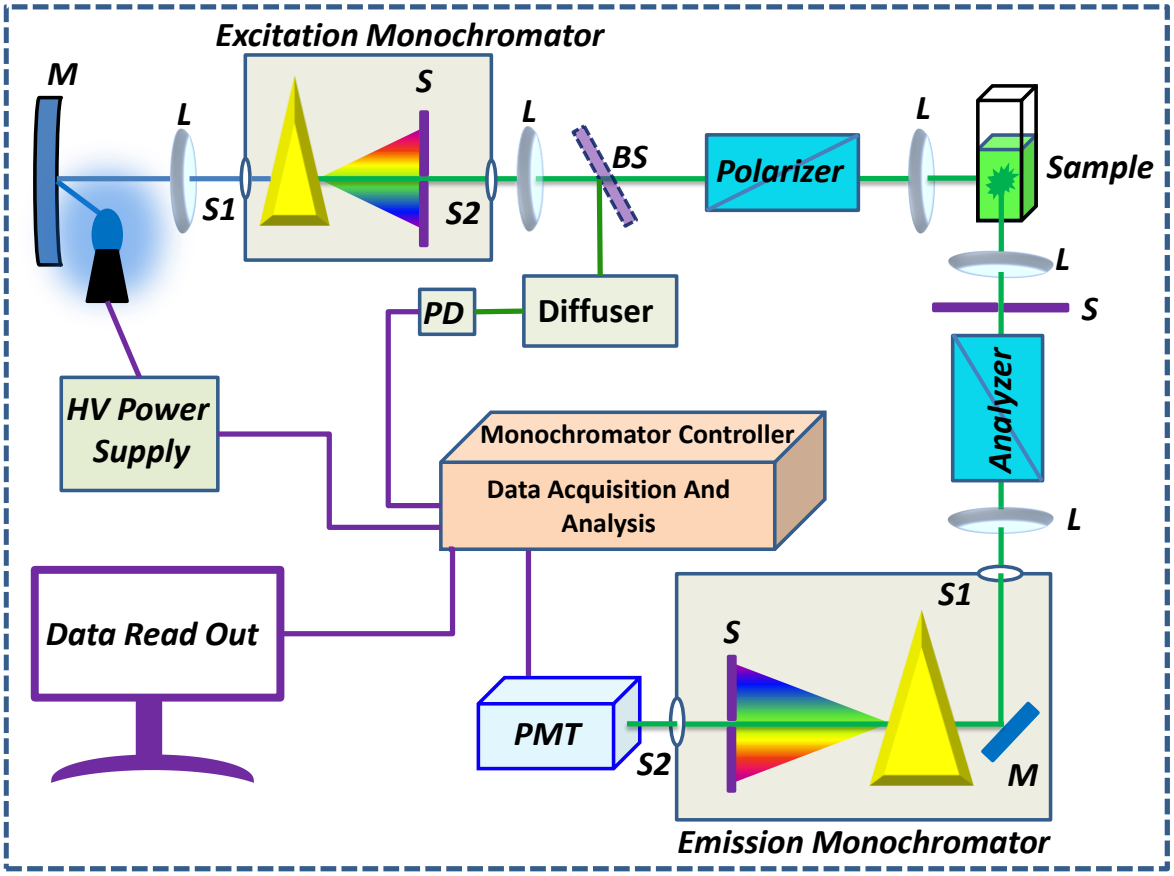

Scheme 3.2: Ray diagram of an emission spectrofluorimeter. M, S1, S2, S, L, BS, PMT, and PD represent mirror, entry slit, exit slit, shutter, lens, beam splitter, photomultiplier tube, and reference photodiode, respectively.

3.3. Time-Resolved Fluorescence Spectroscopy (TRFS)

TCSPC technique[1] was used to record all the picosecond-resolved fluorescence[2] transients. Scheme 3.3 displays the schematic block diagram of a TCSPC framework. During fluorescence decay acquisitions, the TCSPC setup from Edinburgh Instruments, U.K., was used. The instrument response functions (IRFs) of the laser sources ranged from 60 ps to 400 ps at different excitation wavelengths. After dispersion via a grating monochromator, a photomultiplier was detected by the fluorescence signal from the samples. The polarizer on the emission edge was calibrated for all the transients to have at 54.7° (magic angle) concerning the polarization axis of its excitation beam.

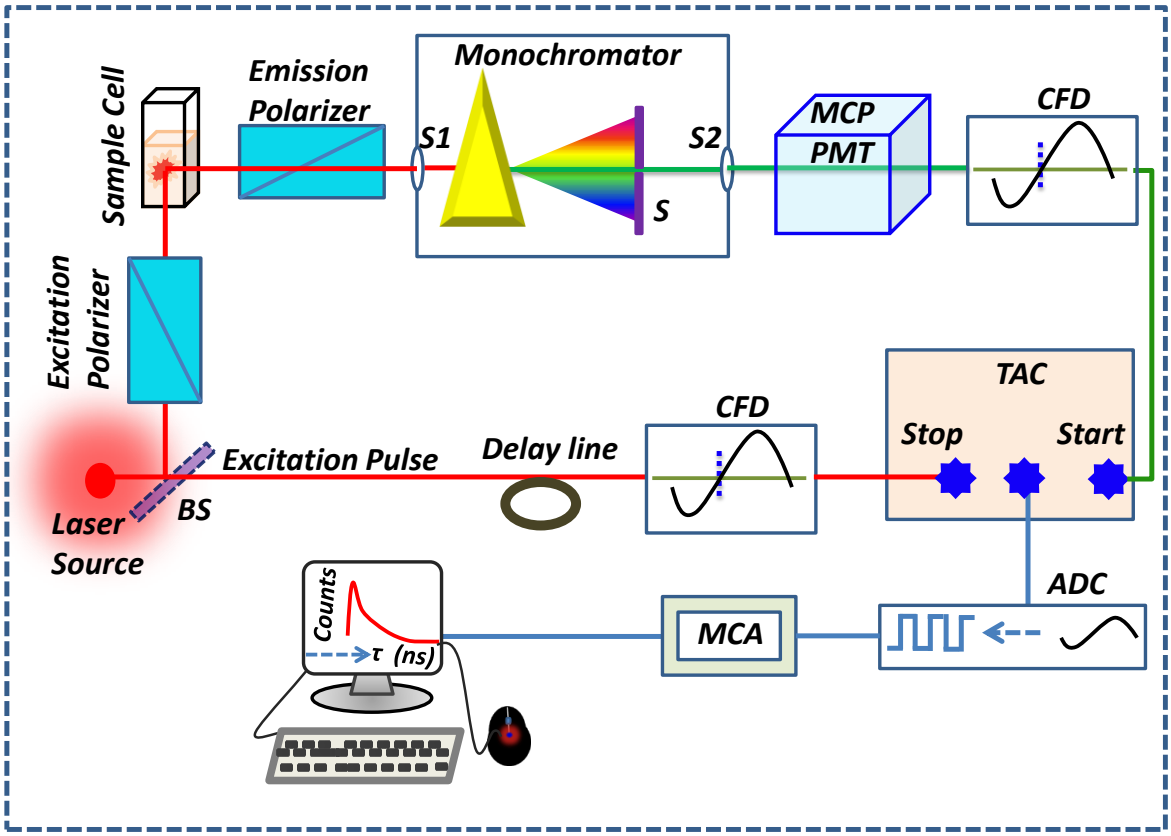

Scheme 3.3: A TCSPC spectrophotometer's ray diagram. The signal from the microchannel plate photomultiplier tube (MCP-PMT) is amplified and connected to the start channel from time to amplitude converter (TAC) through a constant fraction discriminator (CFD). The TAC's stop channel is linked through a delay line to the laser driver via a constant fraction discriminator. S, S1, S2, BS, ADC, MCA represent shutter, entry slit, exit slit, beam splitter, analog to digital converter, and multichannel analyzer respectively.

3.4. Dynamics Light Scattering (DLS)

One of the reliable techniques for determining the hydrodynamic diameter of a particle is dynamic light scattering (DLS) (scheme 3.4), also referred to as photon correlation spectroscopy (PCS) or quasi-elastic light scattering (QELS). In our laboratory, we measured the Nano S Malvern instrument using a 4mW He-Ne LASER (λ=632.8 nm) connected with a thermostated sample chamber.

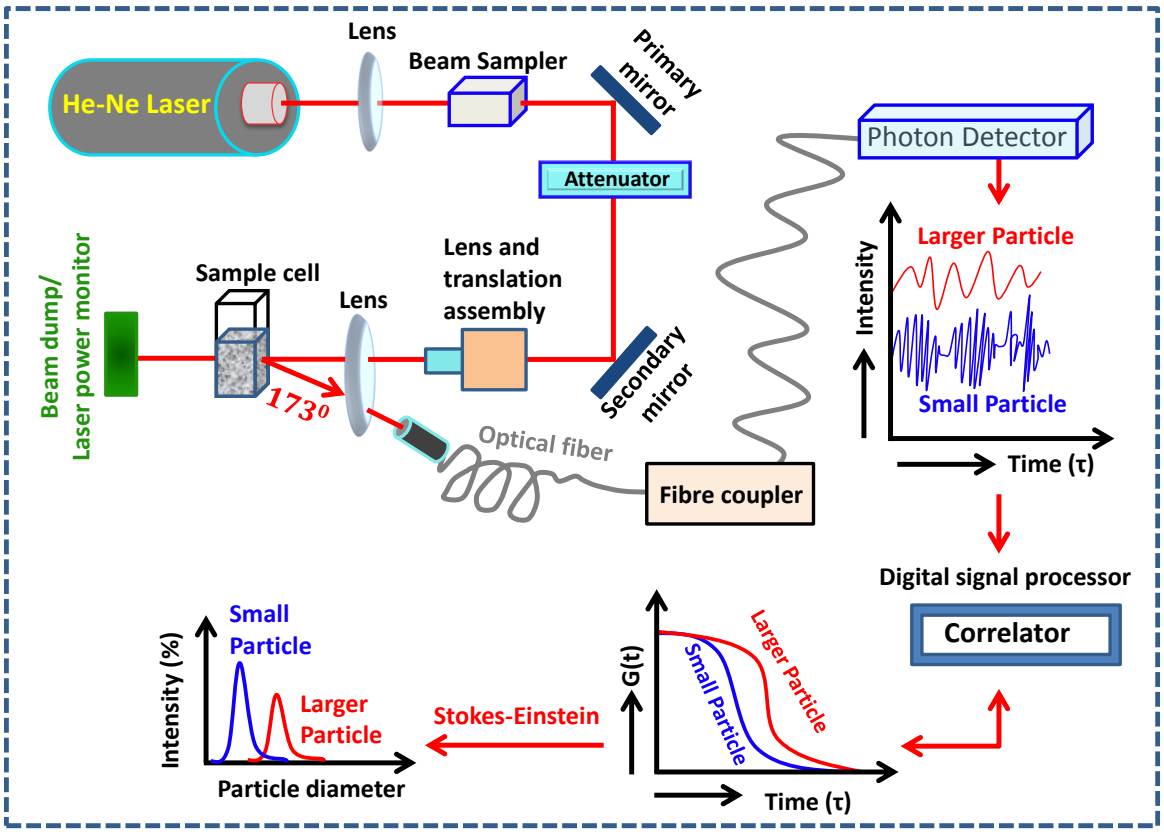

Scheme 3.4: Dynamic light scattering Ray diagram (DLS).

Compared to wavelength, as light reaches small or tiny particles, the light disperses in all particular directions (Rayleigh scattering). For monochromatic and coherent light, due to tiny molecules in solutions pursuing "*Brownian motion*", the scattering intensity fluctuates over time. Therefore, over time, the distance between the dispersers in the solution varies continuously. This dispersed light then undergoes either positive or destructive interference by the neighbouring particles, and knowledge about the scatterers' time scale of motion is found within this fluctuation of intensity. At a scattering angle of 173º, all the dispersed photons are captured and the specifics of DLS measurements have been recorded elsewhere.[3]

The correlation curve is the data calculated in the DLS experiment. All of the information about the diffusion of particles inside the sample that has been measured is described within this correlation curve. The diffusion coefficient (D) can be determined by the fitting of the correlation curve to an exponential equation (D is proportional to the lifetime of the exponential decay).

The hydrodynamic particle diameter (d_H) is calculated based on the intensity autocorrelation function of the time-dependent intensity variation. The viscosities, as well as diffusion coefficient of the solution, are linked to the d_H, as shown below, according to the "Stokes-Einstein (SE)" model,

$$d_H = \frac{k_B T}{6\pi\eta D} \qquad (3.2)$$

where the Boltzmann constant is k_B, T is the temperature, η is the viscosity, and D is the coefficient of translation diffusion. The viscosity of the solutions is derived from the literature.

3.5. Fourier Transform Infrared (FTIR) Spectroscopy

The spectrometer JASCO FTIR-6300 (transmission mode) was used to conduct FTIR measurements. The soul of the FTIR spectrometer is the 'Michelson Interferometer'.[4] As shown in scheme 3.5, it consists of a beam-splitter (BS), a fixed mirror, and a moving mirror. The collimated infrared (IR) beam from the source is partly transmitted to the moving mirror and partly reflected throughout the fixed mirror by the beam splitter. The mirrors then reflect the two IR beams onto the beam splitter. The detector then detects both the emitted and reflected beams from the fixed and moving mirrors at the same time. The two combined beams interact constructively or destructively depending on the wavelength of the light (or wavenumber frequency) and the optical path disparity introduced by the moving mirror. The resulting signal is known as an interferogram, and it has a distinct feature in that each data point (the moving mirror position function) in the signal contains information about each infrared frequency that arrives from the source. The measured interferogram signal is then processed through a Fourier transformation to obtain the final spectrum. Every spectrum is made up of 100 scans (1500−4000 cm^{-1}) with a 0.5 cm^{-1} resolution.

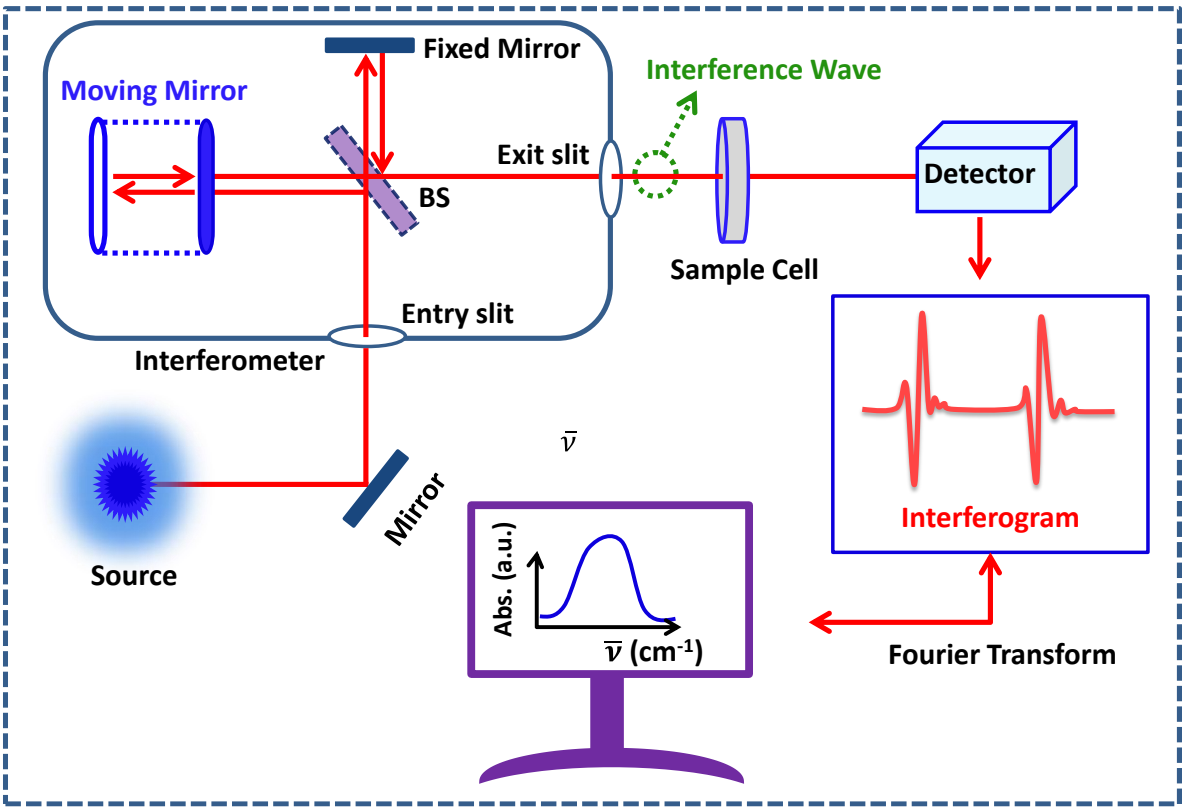

Scheme 3.5: Ray diagram of Fourier Transform Infrared (FTIR) spectrometer. It is primarily a "Michelson Interferometer" in which one of the two fully reflective mirrors is movable, allowing a variable delay to be used in one of the beams (in the travel time of the light). BS represents the beam splitter.

3.6. Circular Dichroism (CD) Spectrometer

The CD data provided throughout the next chapters are measured by JASCO J-815 (Scheme 3.6). Spectro-polarimeter with a Peltier temperature controller attached with that. A Xe-lamp is used as a light source. N_2 is purged to remove O_3 gas from the chamber.

CD is characterized as the difference in absorption of circularly polarized left-handed (L) and right-handed (R) light and occurs when one or more chiral chromophores are present in a molecule (light-absorbing groups).

$$CD = A_L(\lambda) - A_R(\lambda) \tag{3.3}$$

Molar ellipticity [θ] is defined as,

$$[\theta] = \frac{\theta\ (mdeg)}{C_M \times l \times 10}\ (\text{deg cm}^2\ \text{decimal}^{-1}) \tag{3.4}$$

where θ *(mdeg)* is the CD in the unit of mdeg, C_M is the molar concentration of the sample, l is the path length of the cell in the unit of cm.

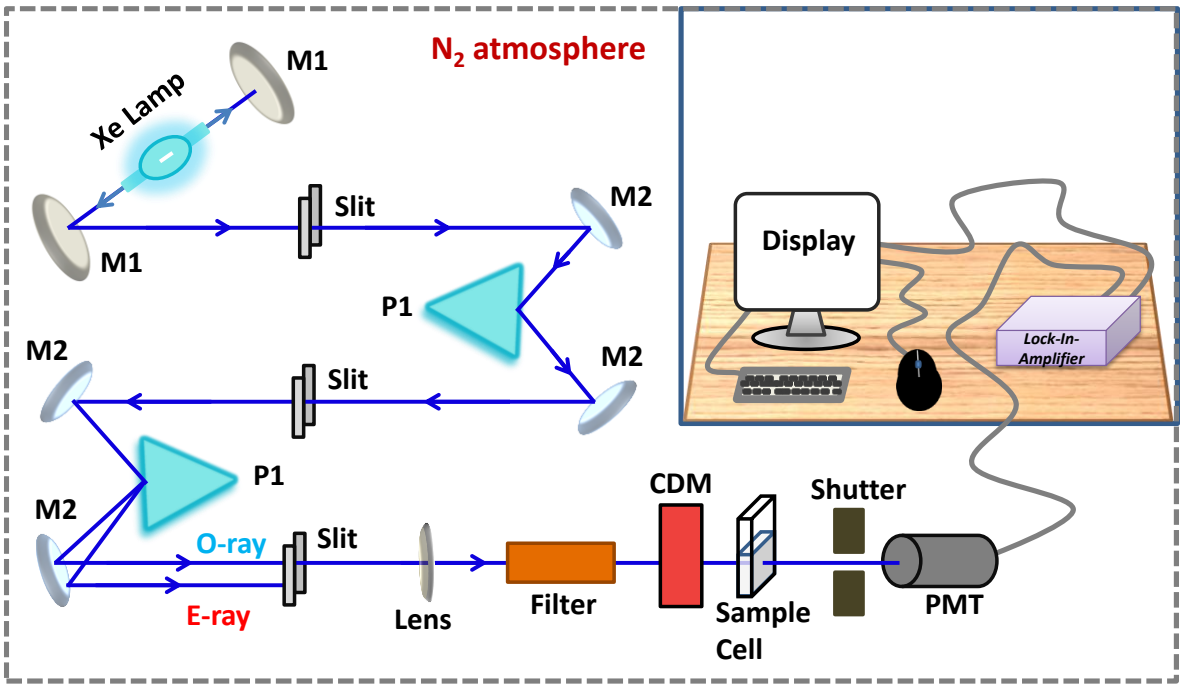

Scheme 3.6: Ray diagram of a Circular Dichroism (CD) spectropolarimeter. M1, M2, P1, PMT, CDM, O-ray, and E-ray represent concave mirror, plain mirror, reflecting prism, photomultiplier tube, CD-modulator, ordinary ray, and extraordinary ray, respectively.

3.7. Refractive Indices (RI) Refractometer

A refractometer (RUDOLPH, J357) was also used to measure the refractive indices (n) of various types of solvents or different compositions of solvents. Automatic refractometers determine the refractive index of a sample automatically. The automated calculation of the sample's refractive index is based on the determination of the total reflection's critical angle. Scheme 3.7, under a wide range of angles, an LED light source is imaged onto a prism surface that is in contact with a sample. The light is partially transmitted or entirely reflected according to the alteration in the refractive index between the prism material and the sample. As a function of the incident angle, the critical angle of total reflection is determined by calculating the reflected light intensity. With a high-resolution sensor array, this dependency of the reflected light intensity from the incident angle is calculated. The refractive index of the sample can be measured from the video signal obtained using the CCD (charge-coupled device) sensor. For each solution, five independent readings of the refractive index were made. The average value of the five determinations is the refractive index used to calculate the QY.

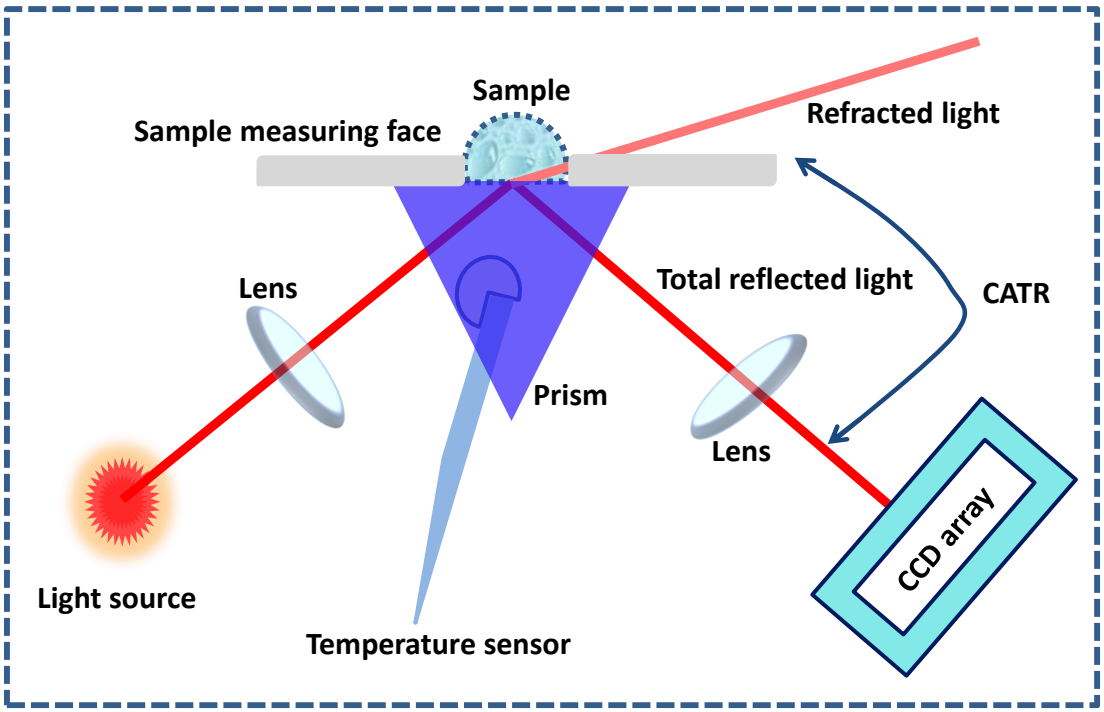

Scheme 3.7: An Automated Refractometer Ray Diagram. CCD and CATR represent charge-coupled devices and the critical angle of total reflection, respectively.

3.8. Two-Photon (TP) Spectroscopy

In all of the experiments involving two-photon mediated fluorescence, a home-built fluorescence spectrometer was used. A femtosecond regenerative amplifier laser system (Libra HE, New Port, USA, Inc.) with a central wavelength of 800 nm, a repetition rate of 1 kHz, and a pulse width of 40 fs was used (full width at half maxima, FWHM). Scheme 3.8 depicts a schematic experimental setup. To minimize scattering from the excitation laser beam, we focused the laser pulses onto the sample using a 10 cm lens, and we observed fluorescence using a 5 cm lens held perpendicular to the excitation laser beam. The emission data were recorded using a high-resolution miniature grating spectrometer, the USB 4000 (Ocean Optics, USA), connected to a personal computer. Temperature-dependent two-photon fluorescence experiments were performed using a temperature controller. Our experiments were carried out using laser pulses at 800 nm to excite the laser dyes since they have a large two-photon absorption cross-section. The laser power dependency experiments were performed using a neutral density filter (Model: 100FS04DV.4, Newport, USA, Inc.) to vary the laser intensity and register data at different laser powers. The two-photon phase was identified in this dissertation via a slope of ~2 after linear fitting of power dependence studies (see chapter 2, scheme 2.7).

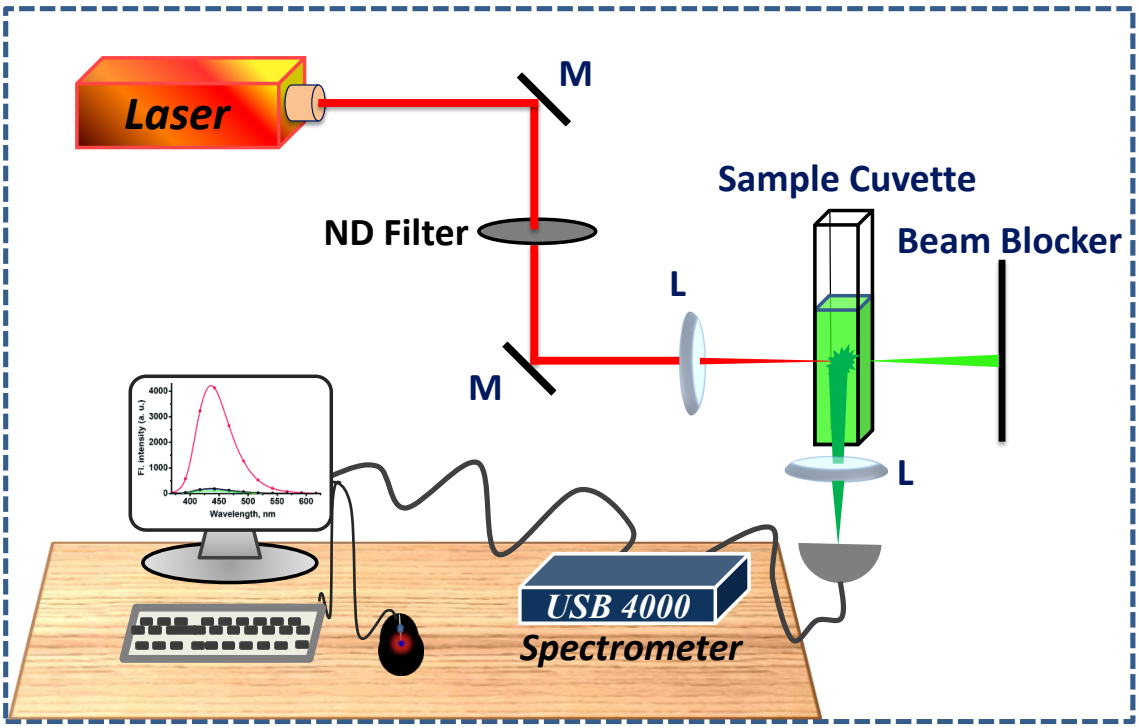

Scheme 3.8: Schematic experimental setup for two-photon spectroscopy. M, L, and ND filter represent mirror, lens, and neutral-density filter, respectively.

3.9. Two-Photon (TP) Microscopy (*In collaboration with IIT Kanpur, India*):

The imaging was done with a fluorescent microscope (FV300 linked with IX71, Olympus, Inc., Tokyo, Japan) that had been modified for two-photon imaging (Scheme 3.9). Two perpendicular-axis pair of galvanometer mirrors scanned the target of the laser beam on the sample through a pupil-transfer lens into the side port of the inverted microscope. The focal point was chosen by scanning the entire sample in the Z-direction (from top to bottom) and choosing the fluorescence region's middle point. A stepping motor was used to adjust the focal point depth in the specimen. Finally, a 100x and 1.25 NA oil-immersion objective lens from 'iNEA' was used to focus the beam on the specimen. A photomultiplier tube was used to collect two-photon fluorescence (PMT).

The excitation wavelength used to excite the laser dye and the dye-protein complex in this dissertation had a central wavelength of 800 nm (6 nm bandwidth, FWHM), a pulse duration of 120 fs, and a repetition rate of 76 MHz. Using a MATLAB program, we integrated the image area as a function of increasing BSA concentration (see chapter 7).

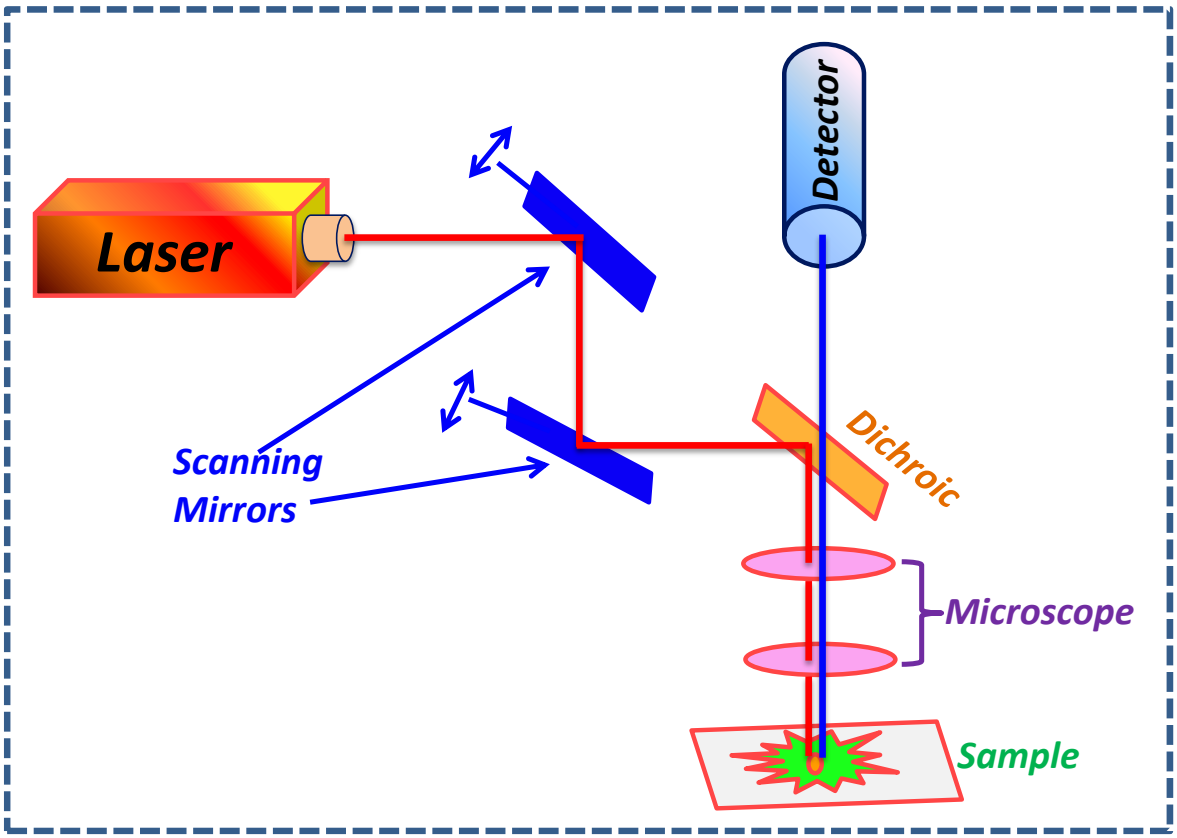

Scheme 3.9: Two-Photon Microscopy Ray Diagram.

3.10. References

1. Lakowicz, J. R., *Principles of fluorescence spectroscopy*. Springer science & business media: 2013.
2. O'Conner, D. V.; Philips, D., *Time correlated single photon counting*. Academic Press: London, 1984.
3. Mitra, R. K.; Sinha, S. S.; Pal, S. K., Hydration in protein folding: Thermal unfolding/refolding of human serum albumin *Langmuir* **2007,** *23*, 10224-10229.
4. Saptari, V., *Fourier transform spectroscopy instrumentation engineering*. SPIE Optical Engineering Press: 2004.

1st Part of Dissertation

ESPT dynamics of D-luciferin in various micro-heterogeneous environments: *the possible role of hydration dynamics on controlling the ESPT dynamics*

Chapter 4

4. Modulation of Excited-State Proton Transfer Rate of D-luciferin in Mixed Reverse Micellar Systems

The excited-state proton transfer (ESPT) rate of photo-acids in the confined medium depends on several physical parameters of the immediate environment. In this chapter, we introduce a new parameter to modulate the ESPT rate: the interface charge type of reverse micellar (RM) systems. We investigate the ESPT reaction of D-luciferin in mixed RM systems composed of non-ionic (Igepal CO-520) with cationic (DDAB) and anionic (AOT) in cyclohexane (Cy) at different mole fractions of Ig (X_{Ig}) and fixed hydration (w_0=10). The various physical parameters of water in the mixed RM water pool has been investigated using DLS and FTIR spectroscopy. The ESPT process is monitored using steady-state and time-resolved fluorescence measurements. We found that ESPT is feeble in AOT RM, while it is favourable in the other two RMs. The addition of Ig is observed to introduce ESPT in AOT/Ig mixed RMs; in DDAB/Ig mixed RMs it shows a synergistic effect.

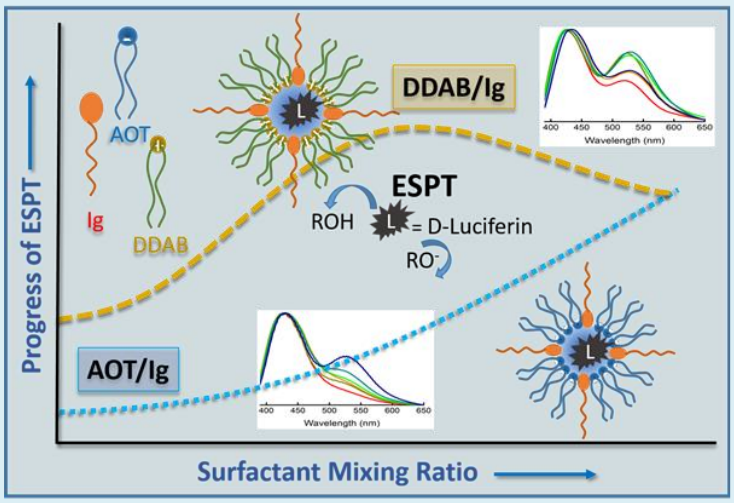

4.1. Introduction

Excited-state proton transfer (ESPT) reaction in confined media has emerged as a fascinating field of research in chemistry and biology.[1, 2] There have been several studies discussing the pathways of ESPT reaction of different excited-state photo-acids and roles of the environment on proton transfer dynamics.[3-10] ESPT is mostly governed by the local concentration of water molecules near the photo-acid and solvent reorganization.[11] Following photo-acid excitation a proton is transferred to the surrounding solvent. In case of a reversible process proton diffusion recombines the two species, and in irreversible cases recombination of the RO^{-*} with the proton re-forms the ground-state ROH.[12] Reverse micelles (RM) often mimic the biological environment and ESPT in RM can be modeled for the specific activity of chromophores in real systems. ESPT offers valuable insights on the dynamical nature of water inside RM systems.[3, 5, 7, 13-15] Location of the probe and corresponding ESPT dynamics inside RM has been found to be dependent markedly on the nature of the surfactant charge,[3, 16] pH and dielectric constant of water inside RM environment,[1] polarity of the environment and screening effects of counter-ions present at the interface.[8] An important aspect in this regard is the role of the interface in deciding the fate of the ESPT reaction, and accordingly, the ESPT dynamics modulate with the charge type of the RM head groups. For example, in anionic AOT RMs the rate of ESPT increases with an increase in the water content (w_0)[3,7] while in cationic RMs, interface-localized probe offers only subtle changes with w_0.[16,4,5] Lawler et al. reported that in AOT RM ESPT kinetics of 8-hydroxypyrene-1,3,6-trisulfonate (HPTS) resembles that in bulk water, suggesting a diffusion-controlled power-law time-dependent process whereas ESPT rate in non-ionic Ig-520 RM shows a slow, two-component model with one relatively bulk water-like population and secondly surface-bound population with slower lifetime.[3] A few studies have also correlated the solvation dynamics around ESPT probe and its intramolecular proton transfer dynamics.[11, 14, 15] In this chapter we introduce a new parameter in terms of the interfacial polarity of RMs by systematically varying the interfacial charge by mixing of surfactants of different charge types and to investigate its effect on the ESPT of D-luciferin.

D-luciferin, found in the Lampyridae family of fireflies, is the substrate that is oxidized into oxyluciferin, responsible for the emission of yellow-green light.[17, 18] ESPT of D-luciferin has previously been studied in different solvents of varying polarity, pH, temperature and hydrogen-bonding ability.[12, 19-21] Such studies in restricted water environments like in RMs are only in sparse.[7] The study by Kuchlyan et al. suggests that

ESPT of D-luciferin in AOT RM is only feeble at $w_0 \geq 12$ and gets favourable as water content increases.[7] ESPT of D-luciferin proceeds when sufficient water molecules stabilize the polar transition state (TS) and the products (proton and anion). The authors also found that ESPT changes as the polar protic core of RM are replaced with polar aprotic solvents like DMF and DMSO. In light of all these investigations, it is of interest whether the ESPT could be tuned by any other physical parameter, for example, the charge type at the interface, which could easily be achieved by mixing surfactants. In the present chapter, we have studied the ESPT process of D-luciferin in two different mixed RMs: anionic-nonionic (AOT/Igepal-520) and cationic-nonionic (DDAB/Igepal-520). Mixed surfactant-based RMs could potentially be employed in a wide range of practical applications because of their enriched performance over the individual components and the unique advantage of tuning the interface vis-à-vis water properties with simply changing the composition.[22-24] Double-tailed anionic sodium bis(2-ethylhexyl)sulfosuccinate (AOT), double-tailed cationic didodecyldimethylammonium bromide (DDAB) and non-ionic polyoxyethylene(5)nonylphenylether (Igepal CO-520) are the most widely used and well-studied surfactants to form RM in cyclohexane (Cy).[23,25, 26] In our earlier studies we have explored how the physical properties of water in mixed surfactant RM systems tune with the interface stoichiometry.[23, 24] DDAB RMs are known to exhibit unusual physical properties compared to the conventional AOT and Ig RMs. They offer unique phase behaviour; with increasing hydration its microstructure changes from cylindrical rod-like aggregated structures to discrete droplet type at $w_0 \geq 8$.[26] In order to exclude any effect arising out of the morphology of the concerned RM on the ESPT dynamics we perform all the studies fixing w_0 at 10 with the assumption that all the RMs exist as spherical droplets. In both AOT and DDAB RMs, Ig is gradually added at different mixing ratios of X_{Ig} =0, 0.2, 0.4, 0.6, 0.8 and 1.0. We measure the micellar droplet sizes by dynamic light scattering (DLS) technique. To understand the structure and dynamics of the entrapped water in these RM waterpool we have used Fourier transform infrared spectroscopy (FTIR) and time (sub-ns) resolved fluorescence spectroscopy (TRFS) using coumarin 500 (C500) as the fluorophore. We have investigated the ESPT reaction in these RM systems spectroscopically and tried to correlate if the process could indeed be modulated by the modification of the interface.

4.2. Materials and Methods

Sodium bis(2-ethylhexyl) sulfosuccinate (AOT), didodecyldimethylammonium bromide (DDAB), polyoxyethylene(5)nonylphenylether (Igepal-520), cyclohexane (Cy), Coumarin-500 (C-500) and D-luciferin [see chapter 2] were products of Sigma-Aldrich. All the chemicals were used without further purification. AOT, DDAB and Ig were individually dissolved in Cy keeping the surfactant concentration fixed at 0.1 (M) to prepare two stock solutions and then mixed in the desired proportions to vary the mole fraction of Igepal, X_{Ig} = [Igepal]/([AOT] or [DDAB] + [Igepal]), from 0 to 1. Reverse micelles (RM) are produced by adding a calculated amount of water into it so as to fix w_0 ([water]/[surfactant])=10. All the measurements were carried out at 298 K.

We have used the following instruments and tools (for details see chapters 2 & 3). We determine the water solubilization capacity of these mixed RM systems by titration followed by visual inspection as described in our earlier studies.[23] *DLS* is used to measure the hydrodynamic diameter (d_H) of RM droplets. In the 2200-2800 cm^{-1} frequency window, FTIR spectra with 4% D_2O in H_2O were recorded in the *FTIR spectrometer* (transmission mode). Cy shows negligible absorbance in this frequency range. We measured absorbance of the wet RM (i.e. surfactant (s)/Cy/water mixture) following a baseline correction with the stock solutions (i.e. dry RM, w_0=0) which takes care of the absorbance (if any) of the surfactant(s).

To probe the local environment of *fluorescence* measurements done by *steady-state absorption and fluorescence spectrometers. Time-resolved fluorescence* measurements were performed using a diode laser with the central wavelength 375 nm and 409 nm (80 ps instruments response function (IRF)). Fluorescence decay data were fitted using commercially available F900 software provided by Edinburgh Instruments.

4.3. Results and Discussion

Solubilization Capacity Measurements:

Figure 4.3.1a depicts the maximum water solubilization capacity (SC) of the mixed DDAB/Ig/Cy RM systems. The corresponding values of AOT/Ig mixed systems[23] have also been plotted for comparison. DDAB is soluble in Cy only beyond w_0=2 while Ig is soluble in Cy and Ig/Cy system can offer maximum solubilization capacity ($w_{0,max}$) of 20-25.[27] The highest solubilization capacity of the DDAB/Cy system has been observed to be ~13.[27] DDAB/Ig mixed RM exhibits a noticeable synergism at X_{Ig}=0.8, which in AOT/Ig was

observed at X_{Ig}=0.4 (Figure 4.3.1a). The observed synergism manifests an optimization between two opposing factors, namely, inter-droplet interaction and surfactant monolayer elasticity.[27, 28] The major driving force of water solubilization limit of water in RM is the spontaneous curvature and the elasticity (or rigidity) of the interfacial film formed by the surfactant separating the water droplets from the oil continuum. It can be maximized by minimizing the interfacial bending stress of the rigid interface and increasing the attractive inter-droplet interaction.[29] As the interface is doped with a nonionic surfactant (herein Ig-520) it decreases the spontaneous curvature of the interfacial film making the interface more fluid and increases the interaction between the droplets. Solubilization increases up to the point where the spontaneous radius of curvature approaches the critical radius R_c. Solubilization maximum is usually smaller in DDAB RM due to the low hydrophilicity as well as the bulkier quaternary ammonium head group size.[26] Doping with Igepal increases $w_{0,max}$ in DDAB RMs as hydrophilicity increases. It is evident that in AOT/Ig system the decrease in interfacial bending elasticity of rigid AOT interface and increase in the inter-droplet interaction with doping of Igepal content is more effective to display higher synergism compared to that in DDAB/Ig systems.

DLS Measurements:

DDAB RMs in Cy is unique in the sense that at low hydration ($2 \leq w_0 \leq 8$), aggregated rod-like cylindrical structures predominate (length ~14–20 nm, and radius ~ 1.5.[26, 30] At higher hydration (w_0 ~ 10) spherical aggregates of smaller size are formed (Figure 4.3.1b).

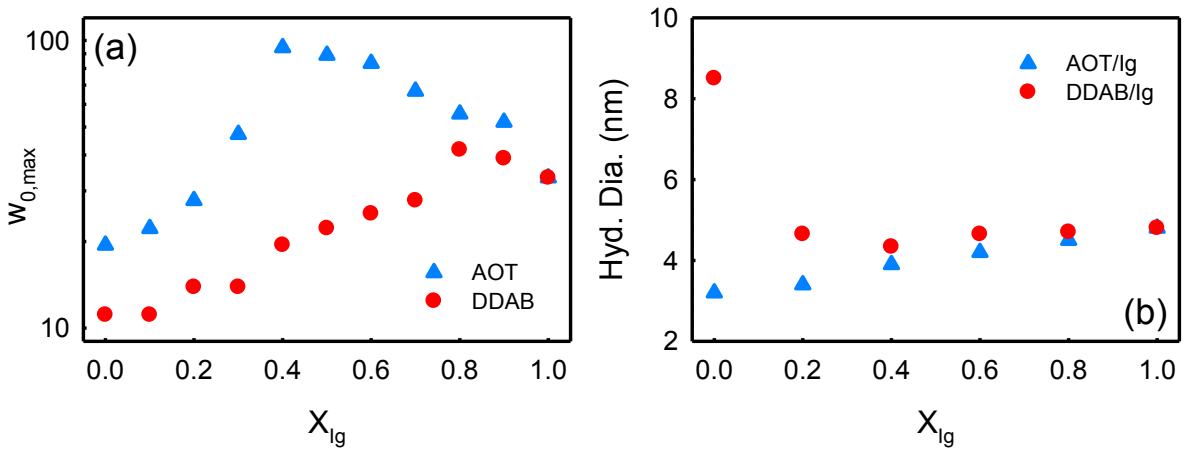

Figure 4.3.1: (a) Maximum solubilization capacity ($w_{0,\,max}$) of DDAB/Ig and AOT/Ig mixed RM systems as a function of X_{Ig}. (b) The hydrodynamic diameter of mixed RMs as a function of X_{Ig}.

Droplet size of DDAB/Ig RMs decreases drastically as Ig is mixed and does not change appreciably with further addition of Ig. Interestingly beyond X_{Ig}=0.2, the droplet sizes are comparable to those of AOT/Ig mixed RMs and changes only marginally with X_{Ig}. It is evident from figure 4.3.1b that in DDAB/Ig mixed systems, with increasing in the Ig content, the droplet sizes first decrease to show a minimum at X_{Ig}=0.4 and 0.6, and then increases. The results indicate that at X_{Ig}=0.4 to 0.6 smaller droplets formation prevails rather than forming less number of big droplets.

FTIR Measurements:

O-D stretching in the MIR region (2200–2800 cm^{-1}) is a potential tool to extract structural information of water encapsulated in the RM nanopool.[31-34] The overall spectrum of pure water in this frequency window produces a smooth curve peaking at ~2508 cm^{-1}. In DDAB/Ig mixed RMs, however, the curves get broadened and could be deconvoluted into three Gaussian sub-bands peaking at 2450 cm^{-1}: H-bonded water (HW), 2545±5 cm^{-1}: intermediated water (IW) and 2640±10 cm^{-1}: multimer water (MW).[35] We calculate the relative area contribution of each curve towards the total spectra and plot it as a function of X_{Ig} at different w_0 values of the mixed RMs (figure 4.3.2 and 4.3.3, a-f). Progressive inclusion of Ig in AOT interface increases HW content which is compensated by a concomitant decrease in IW and MW abundance confirming a linear mixing behaviour at the interface. We observe a somewhat unusual trend in DDAB/Ig mixed RMs in which the abundance of HW and IW increases slightly as compensated by a decrease in the MW content. This study leads to conclude that the interaction of water molecules with the polar uncharged head group of Ig is weaker in comparison to that of the charged head group while for DDAB, bromine ion might play a role to interact with water molecules. The lower droplet size and rigid interface of AOT decrease HW contribution while H-bond formation with water molecules through anionic charged AOT head group increases the IW contribution in AOT RM compared to that in the Igepal RMs. However, the situation is contrasting in DDAB RM as droplet size is big with high HW contribution and a large head group of DDAB inhibits interaction with water molecules which decreases IW contribution compared to that in the Igepal RMs, wherein feeble interaction between water and polyethylene oxide (PEO) head group of Igepal predominates.

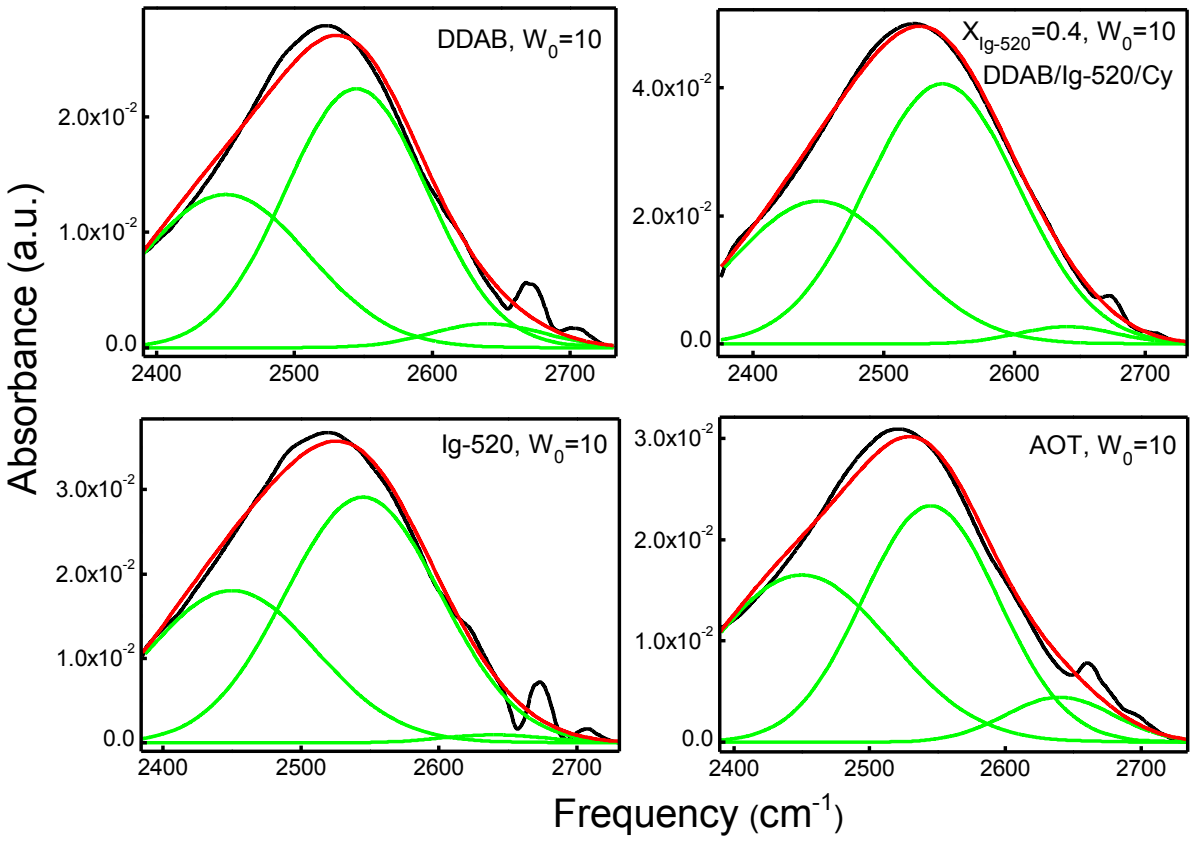

Figure 4.3.2: FTIR spectra of AOT or DDAB/Igepal-520/Cy mixed RM systems at w_0=10. The total curve (black colour) has been deconvoluted into three different Gaussian curves (green lines) peaking at 2450, 2545 and 2640 cm^{-1}. The red lines represent overall fits.

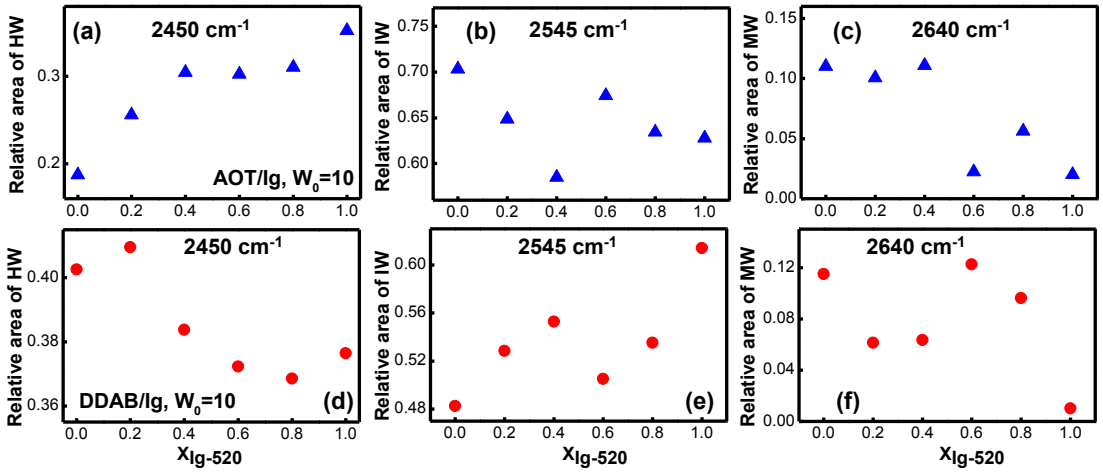

Figure 4.3.3: Relative area under curves peaking at 2450 cm^{-1} (a), 2545 cm^{-1} (b) and 2640 cm^{-1} (c) for AOT/Ig mixed RM systems and peaking at 2450 cm^{-1} (d), 2545 cm^{-1} (e) and 2640 cm^{-1} (f) for DDAB/Ig mixed RM systems at w_0=10 as a function of X_{Ig}.

Fluorescence Measurements:

We use C-500 as the fluoroprobe as its excitation at 409 nm selectively excites the C-500 molecules at the interface only.[25] The decay transients of C-500 are shown in figure 4.3.4. C-500 in water produces an emission maximum (λ_{max}) at ~505 nm, and in DDAB/Ig RM it suffers a progressive blue shift with decreasing w_0[25], however, the change is only modest with X_{Ig} (Figure 4.3.5a). We construct the solvation correlation curves and some representative C(t) plots for different $X_{Ig\text{-}520}$ values at w_0=10 are shown in figure 4.3.5b. All the C(t) curves are fitted bi-exponentially and the time constants are presented in table 4.3.1. The time constants are in the order of hundreds of ps and a few ns.[36] The average solvation time is calculated as $\langle \tau_{sov} \rangle = \sum a_i \tau_i$. $<\tau_{sov}>$ is faster in DDAB RM compared to that in Ig RM at w_0=10. $<\tau_{sov}>$ shows a noticeable minimum at X_{Ig} = 0.6 (Figure 4.3.5c) while it changes monotonically in AOT/Ig mixed RMs.[23] A similar trend also follows in the anisotropy measurements (Figure 4.3.5d).

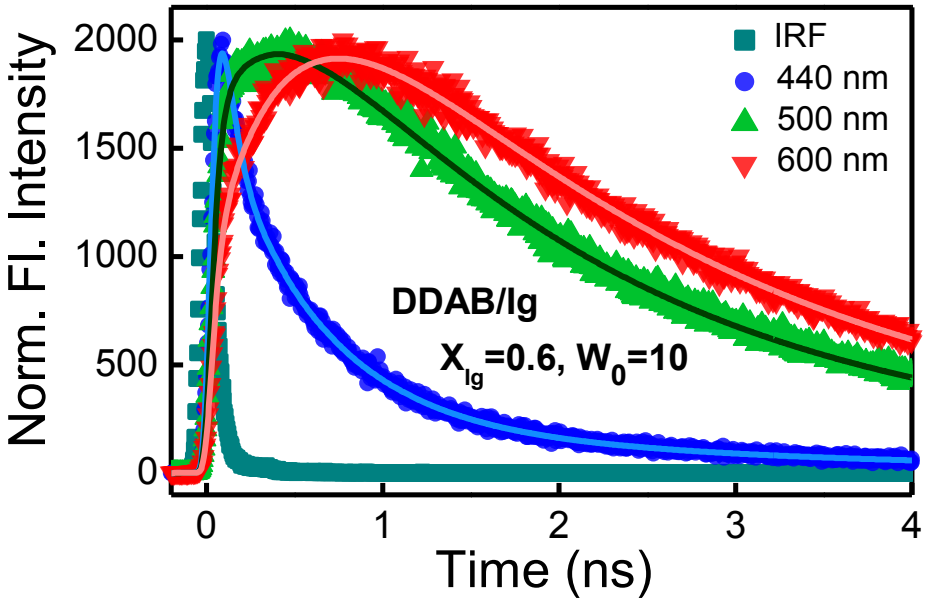

Figure 4.3.4: Fluorescence transients of the C-500 in DDAB/Ig mixed RM system at X_{Ig}=0.6, w_0 = 10 (λ_{ex} = 409 nm). The solid line stands for fitting.

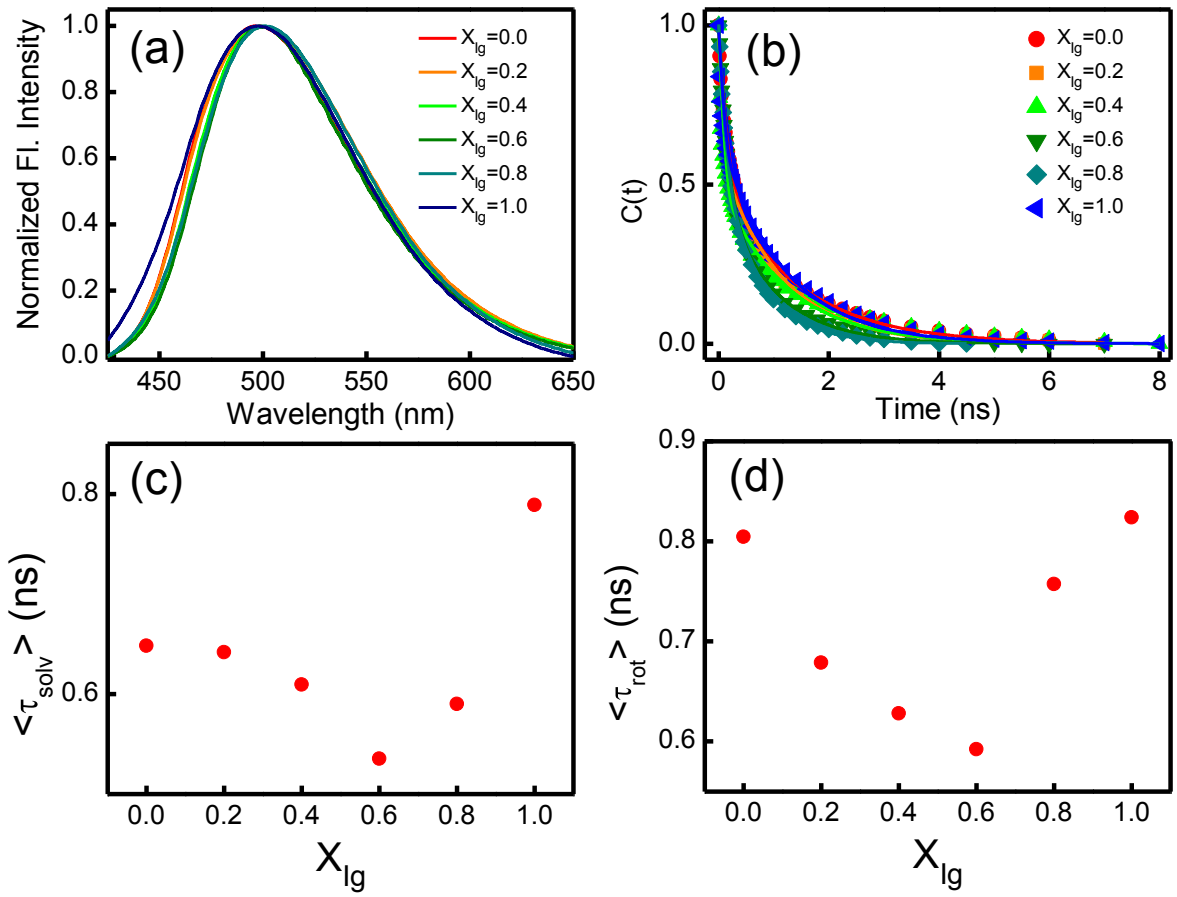

Figure 4.3.5: (a) Emission spectra of C-500 in DDAB/Igepal-520/Cy RM systems at different $X_{Ig\text{-}520}$ with w_0=10 (b) Representative solvent correlation function, C(t) curves of C-500 for mixed RM systems at w_0=10 for different X_{Ig} values. The solid lines are bi-exponential fittings. (c) Average solvation time constant $<\tau_{sol}>$ and (d) Average rotational time constant, $<\tau_{rot}>$ as a function of X_{Ig}.at w_0=10.

Excited-state Proton Transfer (ESPT) Study

Steady-state Measurements:

The protonated and the deprotonated forms of D-luciferin show absorption maximum at ~330 and ~390 nm, respectively.[19] D-luciferin in water exists in deprotonated form while in AOT RM it exists in the protonated form mostly.[19] In AOT RM D-luciferin prefers to stay mostly in the protonated form as the pH inside AOT RM is lower compared to that in pure water.[37] Taking into consideration its oil insolubility one can expect D-luciferin to occupy the water-facing interfacial domain of the RMs. In neat water, the emission spectrum of D-luciferin is dominated by the emission from the deprotonated (λ_{max}^{em}= 535 nm) excited-state. In Ig and DDAB RMs it shows two distinct emission peaks, one at ~430 nm (protonated or the neutral form, ROH^*) and the other at ~530 nm (deprotonated or the anionic form, RO^{-*}) while in AOT RM the peak of the deprotonated species in only feeble (Figure 4.3.6a). Figure

4.3.6b depicts the emission spectra of D-luciferin in DDAB/Ig mixed RMs at w_0=10 at different X_{Ig}, the corresponding figure for AOT/Ig mixed RM is shown in figure 4.3.7. Fluorescence intensity of the protonated form increases along with a slight red-shift as X_{Ig} increases. For a comprehensive understanding, we plot the ratio of apparent intensity of the deprotonated and the protonated form ($I_{RO^-}{}^*$ /$I_{ROH}{}^*$) as a function of X_{Ig} (Figure 4.3.6c,d). We observe different trends in two different mixtures. In AOT/Ig mixture the relative abundance of RO^- increases monotonically with increasing X_{Ig}, however, in DDAB/Ig we found a maximum at X_{Ig}~0.6.

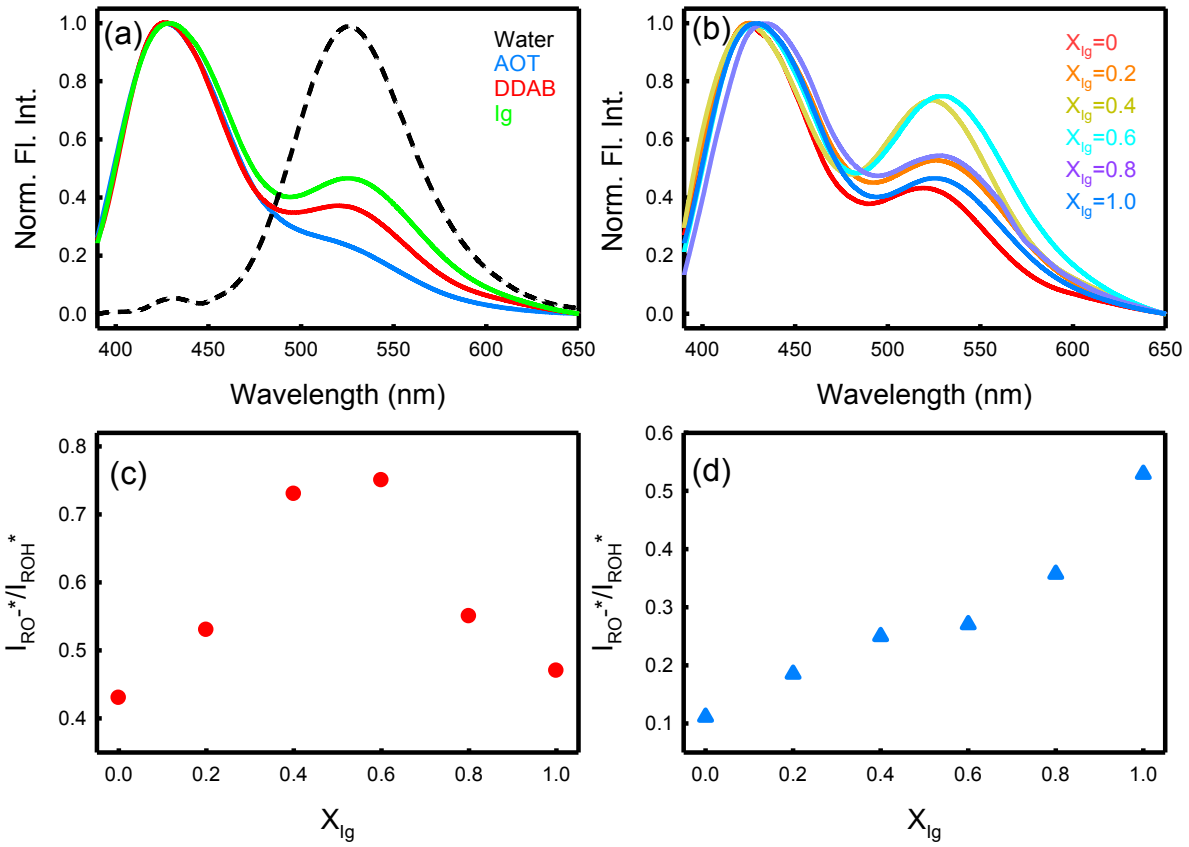

Figure 4.3.6: (a) Emission spectra (λ_{ex} = 375 nm) of D-luciferin in water (dotted line) and in DDAB (red), AOT (blue) and Igepal (green) RM at w_0=10. (b) Emission spectra of D-luciferin in DDAB/Ig mixed RM with varying X_{Ig}. The apparent ratio of the intensity of the deprotonated and protonated forms of D-luciferin in (c) DDAB/Ig and (d) AOT/Ig mixed RMs.

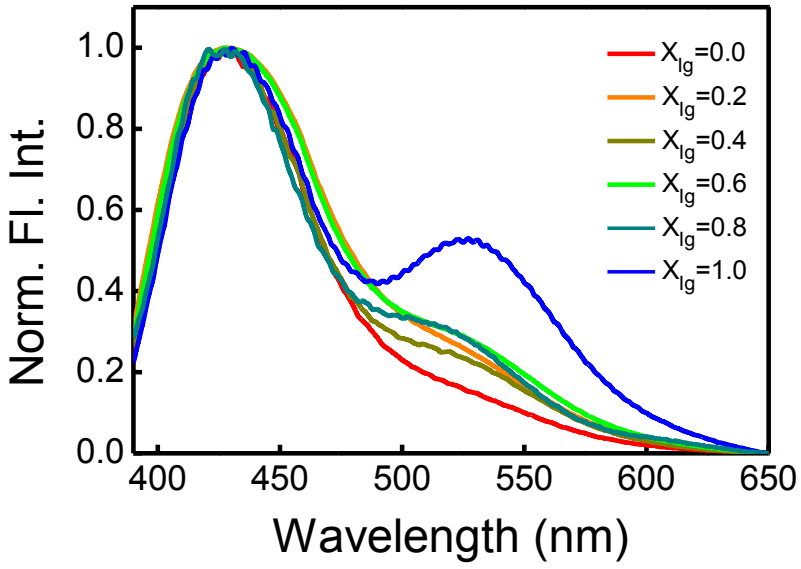

Figure 4.3.7: Steady-state emission spectra of D-luciferin (λ_{ex} = 375 nm) in AOT/Ig mixed RMs.

Time-resolved Measurements:

We measure the fluorescence transients at two selective wavelengths (420 and 590 nm) corresponding to the protonated and the deprotonated forms, respectively (Figure 4.3.8 and table 4.3.2). We chose a slightly blue-shifted wavelength for the protonated form and a slightly red-shifted one for the deprotonated form in order to minimize the undesired mixing of the contribution of the two forms.[4, 5] The decay transients at 420 nm could be fitted with multiple decay components fixed at 80, 600 and ~1500 ps while those in the red end could be fitted only after considering rise component(s) (Table 4.3.2). The decay of D-luciferin at 450 nm in pure water is rather fast and is dominated by the ~80 ps component (99%) while at 540 nm it is slow with components 535 ps (40%) and 5.1 ns (60%).[38] The observed rise component for the deprotonated species unambiguously confirms the presence of an excited-state process in which emission is emanating from a previously formed excited-state rather than the species getting directly excited. We plot the contribution of the fast component (~80 ps), which is the fall time for the protonated as well as the rise time of the deprotonated species (Figure 4.3.9a). It is higher in DDAB RMs and decreases first modestly and then sharply beyond X_{Ig}=0.4 (Figure 4.3.9a). The ~600 ps component is the lifetime of the excited-state of D-luciferin which undergoes proton transfer and forms ground state product and is comparable to the recombination time of HPTS in different RMs.[3] In AOT RM the 600 ps component has comparable contributions as that of the faster one and does not change appreciably with X_{Ig}.

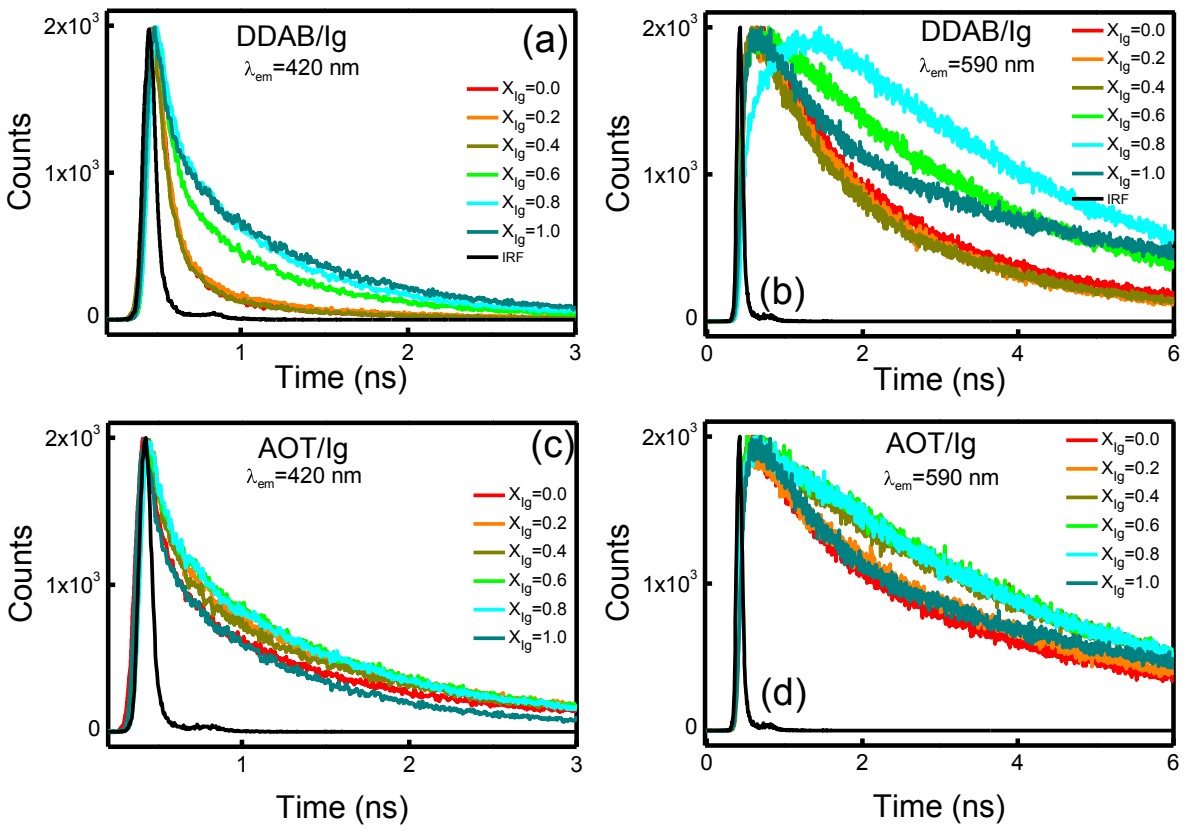

Figure 4.3.8: Fluorescence transients of the protonated (λ_{em} = 420 nm) (a and c) and deprotonated (λ_{em} = 590 nm) (b and d) forms of D-luciferin in DDAB/Ig and AOT/Ig mixed RMs at w_0 = 10 (λ_{ex} = 375 nm).

The multiple decay pattern of D-luciferin in the RMs can be rationalized assuming an approximate bimodal distribution in a way that only a fraction of the probe undergoes ESPT (Scheme 4.3.1). It can be shown that the concentration of ROH^* at any time t can be given as:

$$[ROH^*] = [ROH^*]_{0,Y} e^{-\left(\frac{1}{\tau_{dp}}+\frac{1}{\tau_f}\right)t} + [ROH^*]_{0,N} e^{-\left(\frac{1}{\tau_f}\right)t} \qquad (4.3.1)$$

where τ_f and τ_{dp} stands for the time constants for fluorescence emission of protonated form and deprotonation respectively. The subscript Y and N stand for ROH molecules that *'do'* and *'do not'* undergo ESPT reaction. We fit the ROH^* decay transients using equation 4.3.1 for both AOT/Ig and DDAB/Ig mixed RM systems. The τ_f and τ_{dp} values for the AOT, DDAB and Ig RM systems are found to be: (1.05, 0.12 ns), (0.75, 0.11 ns) and (0.83, 0.10 ns), respectively. The τ_f values for the single RM systems are in good agreement with the average of the two slow components taken together (Table 4.3.2). We plot the relative population of D-luciferin undergoing ESPT reaction (Figure 4.3.9b) in both the mixed RM systems.

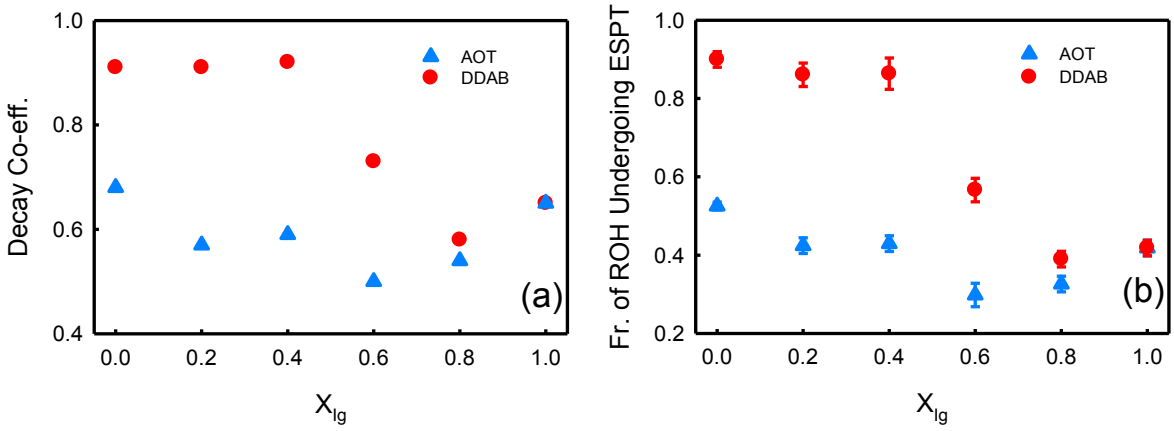

Figure 4.3.9: (a) Fluorescence decay coefficient of the ~80 ps component of the protonated form of D-luciferin measured in mixed RM systems at w_0=10. (b) Fraction of D-luciferin molecules undergoing ESPT reaction in mixed RM systems at w_0=10.

The fraction is low (~0.4) and comparable in AOT and Ig RMs, while it is high (~0.9) in the DDAB RMs. The trend in DDAB/Ig mixed RM is much similar to that of the relative contribution of the fast component and shows a dip at X_{Ig}=0.4.

ESPT is generally a fast process, yet we observe some slow components (of the order of ns) while fitting the emission decay transient of the ROH^* species which is due to the recombination of the dissociated proton with the RO^{-*} base. Such recombination is expected to be governed by a diffusive motion and thus by a $t^{-3/2}$ power-law.[3, 39, 40] At a long time the intensity of the protonated species thus can be assumed to follow a relation

$$I \propto e^{-t/\tau_f} t^{-n/2} \qquad (4.3.2)$$

with the ideal value of n being 3. We try to fit the ROH^* decay transients beyond 600 ps using equation 4.3.2 fixing the value of τ_f as the slowest component of the decay transient (see table 4.3.2). Some representative fittings are provided in figure 4.3.10a. The fittings are reasonably good except for a few systems[41] and the estimated values of n are plotted as a function of X_{Ig} in figure 4.3.10b. The analysis based on equation 4.3.2 should be considered after a note of caution that the long-time fitting is best represented for bulk systems, however, has been successfully employed in AOT RMs by Fayer et al.[3] and for the purpose of comparison could possibly be extended in other RM systems also. For AOT RM the value of n is rather low (0.96) and is in good accordance with that obtained for the ESPT of HPTS in AOT/heptane RMs.[3] In Ig RM it is also comparable (n=1.1), however, in AOT/Ig mixed system the value lies low (n~0.4) (Figure 4.3.10b). For DDAB RMs, however, the value is relatively high (~1.63). With increasing X_{Ig}, it shows a subtle increase up to X_{Ig}=0.4

(n=1.81), beyond which it decreases sharply. It can be noted here that the power-law dependency emanates from the fact that following deprotonation, protons diffuse away prohibiting possible recombination. In RM systems the diffusion is prohibited by the confinement of water molecules, however, it eases with the increasing size of the water pool.[3] Thus a straightforward power-law dependency is a mere simplification of the complex process, specially considering the fact that there are multiple locations of the protonated species inside the RMs and a fraction of them do not at all undergo any ESPT process (see figure 4.3.9b), however, the trend in the estimated value of n is intriguing. Clearly, the bigger size of the DDAB RM is not the sole reason for the high n value as it does not decrease appreciably at X_{Ig}=0.2 RM, which has a comparable size as that of AOT/Ig mixed system. The RO^{-*} gets specifically stabilized at the DDAB interface and the proton could be diffused with more ease as DDAB RM possesses more HW than AOT and Ig RMs as concluded from the FTIR measurements (see figure 4.3.3,a-f).

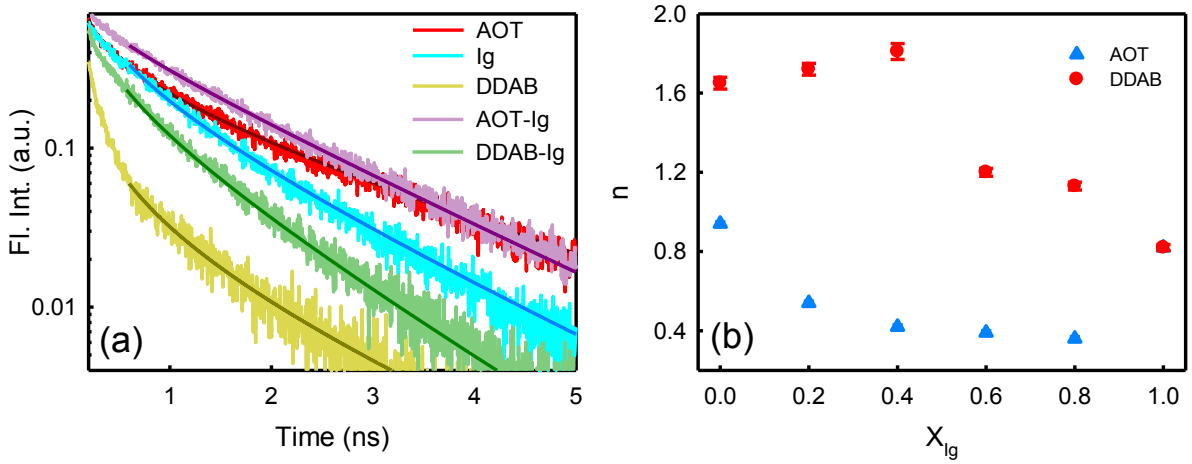

Figure 4.3.10: (a) Representative time-dependent fluorescence intensity of protonated D-luciferin in different single and mixed RM systems. The solid lines represent the best fit to the function, $e^{-\frac{t}{\tau_f}}t^{-n/2}$. (b) The values of n obtained for different mixed RM systems as a function of X_{Ig}.

To interpret the decay components more analytically, we measure the fluorescence transients at several wavelengths across the full emission spectrum and construct the time-resolved area-normalized emission spectra (TRANES)[42] (representative figures for DDAB/Ig and AOT/Ig mixed RMs with X_{Ig}=0.6 are provided in figure 4.3.13b,d). We observe a distinct iso-emissive point at ~500 nm which unambiguously indicates the simultaneous presence of two distinct species. The TRANES profile also clearly manifests that initially the emission is dominated by the protonated species which then diminishes with time with a concomitant increase in the emission intensity of the deprotonated species. For a better apprehension of

the time evolution of the two species, we deconvoluted each time-resolved emission spectrum into two Gaussian curves corresponding to the two concerned species, a representative deconvolution carried out in DDAB/Ig mixed RM at X_{Ig}=0.8 is shown in figure 4.3.11. The yellow shaded curves refer to the protonated form while the cyan ones represent the deprotonated form.

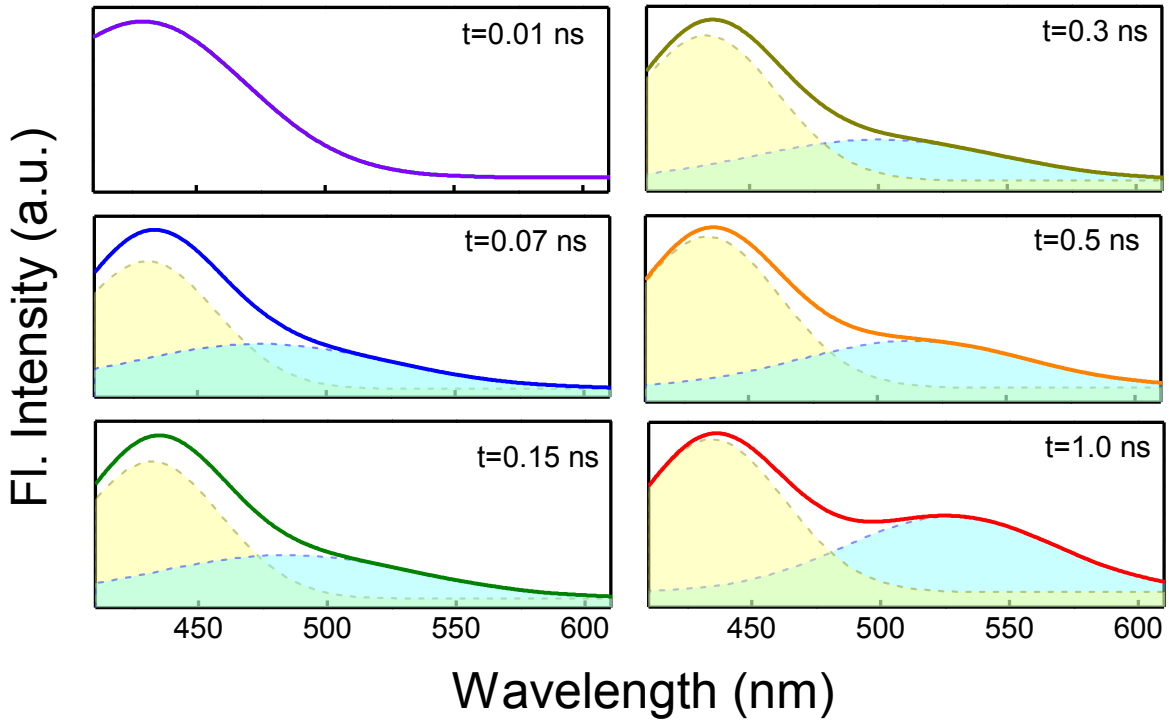

Figure 4.3.11: Representative time-dependent emission spectra of D-luciferin in DDAB/Ig mixed RM system at X_{Ig}=0.8 and w_0=10. The total spectra are deconvoluted into two Gaussian curves.

From the time-dependent deconvoluted curves, we calculate the relative intensity (R.I.) of the RO^{-*} species compared to the maximum peak height; thus R.I. approximately corresponds to the progress of the ESPT process. We plot R.I. as a function of time for different mixed systems (Figure 4.3.12a, b). The curves are linear, however, with a noticeable change in the slope over the longer time as it approaches the equilibrium values. The slope of the linear fits (insets of figure 4.3.12) is a manifestation of the time evolved formation of the deprotonated form RO^{-*}. In AOT/Ig mixed RM the slope is low and increases monotonically indicating the ease of ESPT with progressive addition of Ig. In DDAB/Ig mixed RM the ESPT process is fast as evident from the slope, however, it is not monotonic showing a distinct maximum at X_{Ig}~0.4. It could be noticed that in X_{Ig}=0.6, the equilibrium value of R.I., which is comparable to that of X_{Ig}=0.4 (Figure 4.3.6c), is reached at a longer time.

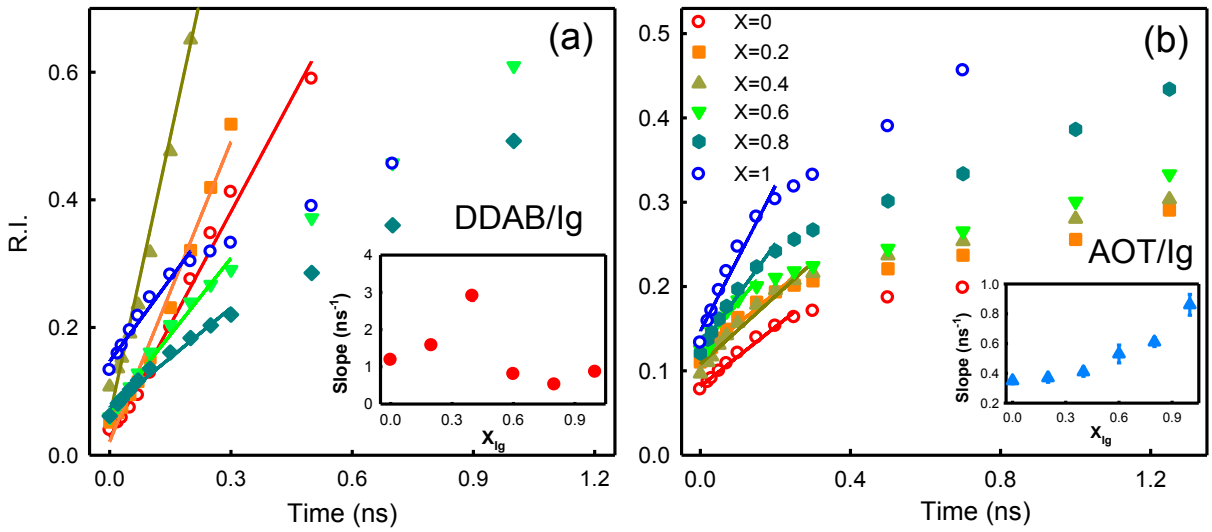

Figure 4.3.12: Relative Intensity (R.I.) of the deprotonated species (as normalized to the maximum peak height) in (a) DDAB/Ig and (b) AOT/Ig-mixed RMs at w_0=10.

It is evident from the representative TRES of D-luciferin (Figure 4.3.13a,c) that the emission peak of the protonated species undergoes noticeable red-shift with time which indicates its solvation.[43] We plot the emission peak frequency as a function of time for both the mixed RMs (Figure 4.3.14a,b). We fit the curves with a single exponential decay function and the corresponding time constants are plotted as a function of X_{Ig} (Figure 4.3.14c). The Stokes shift observed in both the mixed systems are in the order of 500-1000 cm^{-1}, and is higher in the DDAB RMs. Solvation is in general slower in DDAB RM and is faster in AOT RM, that of Ig RM being intermediate. The solvation in DDAB/Ig mixed RMs decreases sharply beyond X_{Ig}=0.4, while in AOT/Ig mixed RMs it shows a subtle maximum at X_{Ig}=0.6.

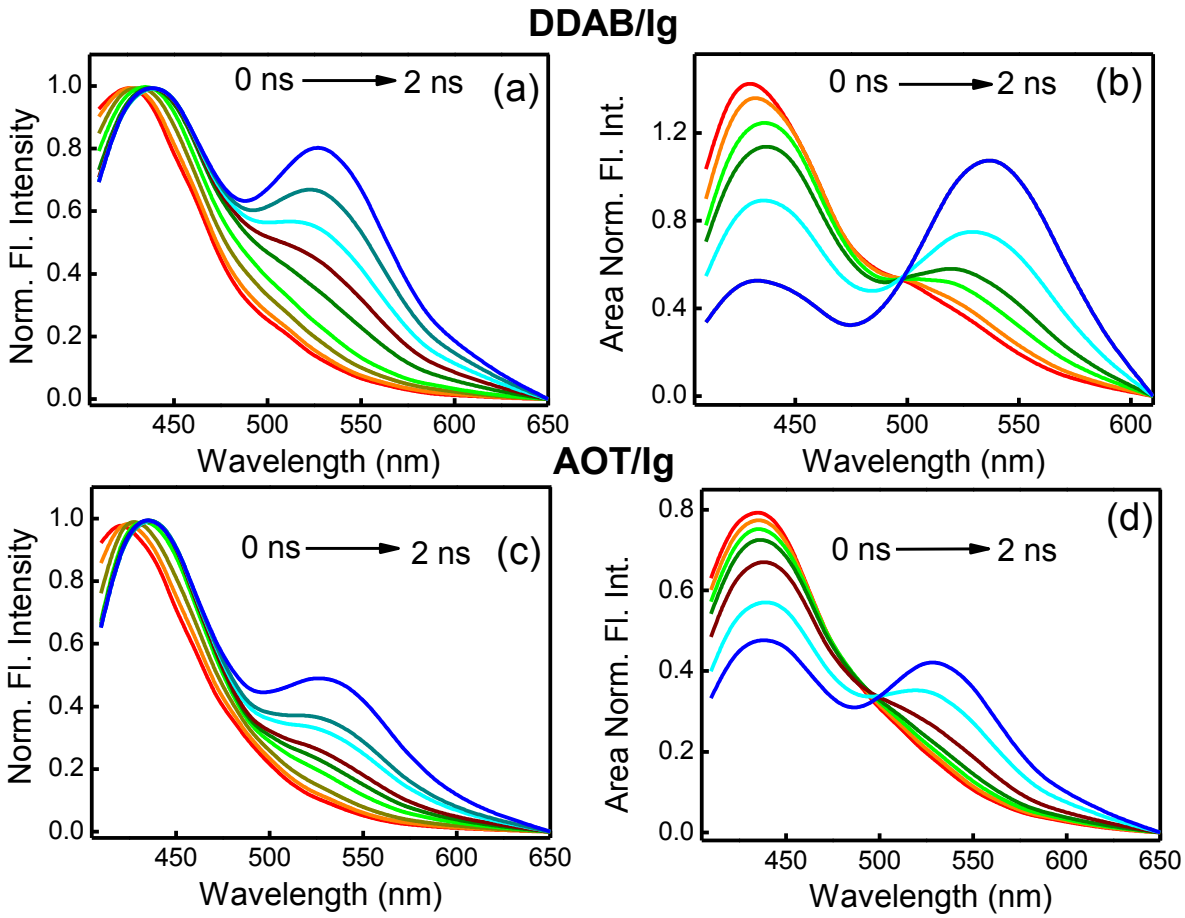

Figure 4.3.13: (a) Time-resolved emission spectra (TRES) and (b) the time-resolved area normalized emission spectra (TRANES) of D-luciferin in DDAB/Ig mixed RMs at w_0=10 and X_{Ig} = 0.6. (c) and (d) are the corresponding TRES and TRANES of D-luciferin in AOT/Ig mixed RMs.

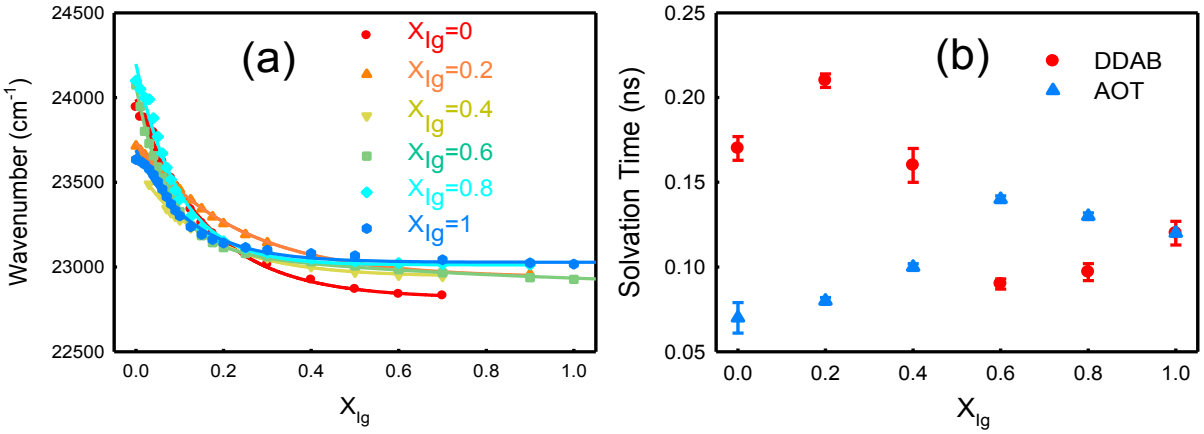

Figure 4.3.14: (a) Time-dependent change in the peak frequency of the protonated form of D-luciferin in DDAB/Ig mixed RMs at w_0=10. (b) Solvation dynamics of the protonated species as a function of surfactant mixing ratio at w_0=10.

We also measure time-resolved fluorescence anisotropy to understand the restriction imposed by the RM environment on the fluorophore, of both the protonated and deprotonated forms of D-luciferin in mixed RMs (a representative depiction is provided in figure 4.3.15). We observe that anisotropy of both the forms of D-luciferin is slower in DDAB RMs compared to the AOT RMs, the value is intermediate in the Ig RMs (Figure 4.3.16, Table 4.3.3). Fluorescence anisotropy of a fluorophore is intimately related to its location inside RM.[3]

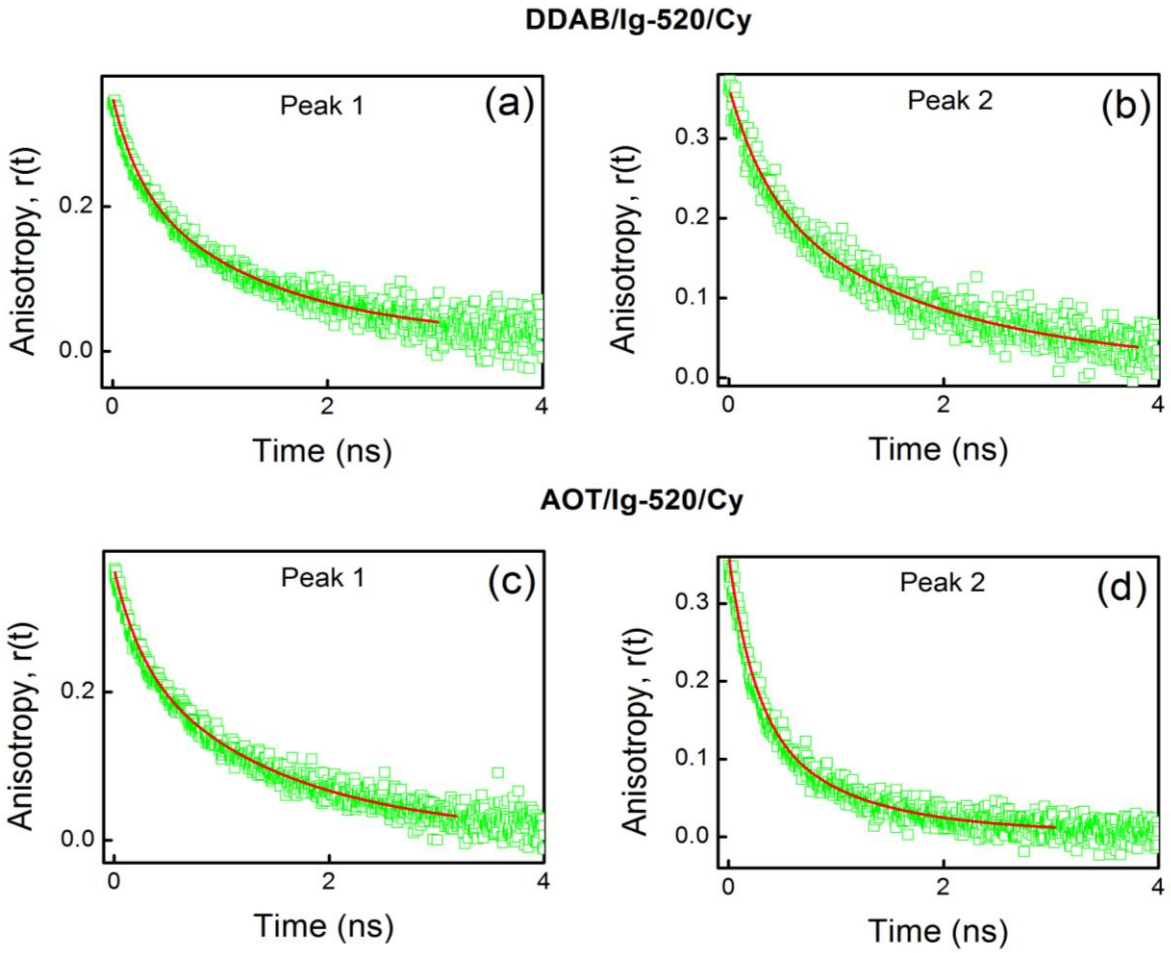

Figure 4.3.15: Representative rotational anisotropy decay of D-luciferin of two forms for peak 1 (protonated) and peak 2 (deprotonated) inside (a, b) DDAB/Ig and (c, d) AOT/Ig mixed RMs w_0=10 and X_{Ig}= 0.6. The solid lines are bi-exponential decay.

As the probe D-luciferin prefers to stay in the core in anionic RM, its rotational anisotropy is relatively faster compared to cationic DDAB in which the probe is more interface bound and thus slow rotating. In the case of Ig, the polyethylene oxide (PEO) head group of Ig inhibit the rotation of the probe molecule. The deprotonated species shows noticeably slower rotational anisotropy compared to the protonated species in DDAB RMs, intuitively because of being more inclined to stay at the interface owing to charge neutralization. The charge

repulsion, on the other hand, makes the deprotonated species stay at the water pool of AOT RMs and shows a faster rotational dynamics (Figure 4.3.16b). The addition of Ig in DDAB RM does not ease the rotation noticeably up to X_{Ig}=0.4, beyond which it accelerates (Figure 4.3.16a). In AOT/Ig RM system the rotation gets slower with X_{Ig} more or less linearly.

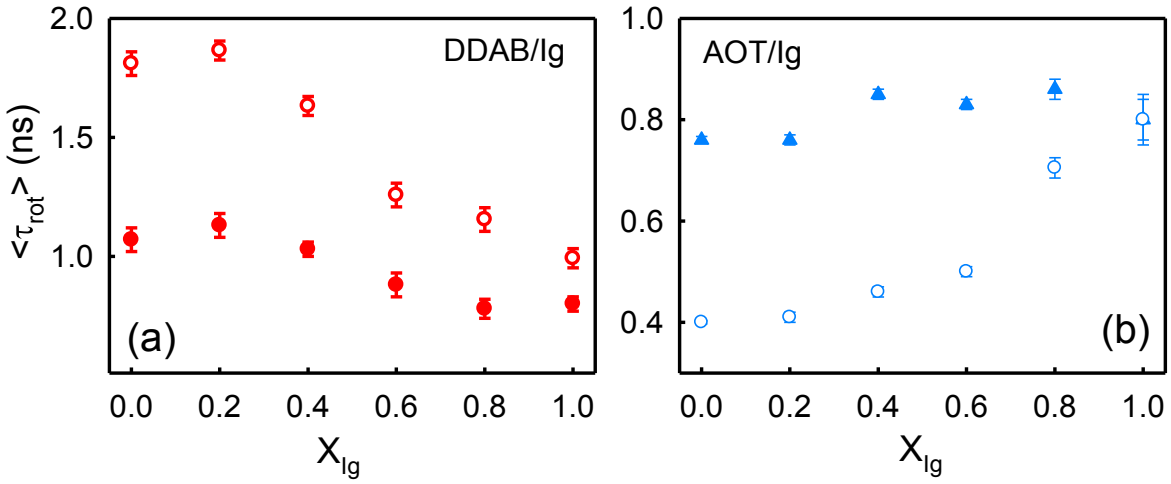

Figure 4.3.16: Average rotational time constant $<\tau_{rot}>$ of D-luciferin as a function of X_{Ig} for the protonated (filled symbols) and deprotonated (open symbols) species inside (a) DDAB/Ig and (b) AOT/Ig-mixed RMs at w_0=10.

4.4. Summary

The proton transfer rate of D-luciferin depends on various parameters like the size of the RMs, water content (w_0), pH of the interface in RM, etc. In this chapter, we introduce a new parameter in the form of mixing of surfactant(s) of different charge types. DLS measurements conclude that pure DDAB RMs are bigger in size compared to AOT RMs. The addition of Ig decreases the size of the former, while it increases the size of the latter. However, at and beyond X_{Ig}=0.2, the sizes of both the mixed RMs are more or less comparable (Figure 4.3.1b). FTIR measurements indicate an abundance of intermediate water (IW) inside RMs, which is highest in AOT RM followed by Ig and DDAB RMs. In AOT/Ig mixed RMs IW passes through a relatively low value at X_{Ig}~0.4, while in DDAB/Ig mixture the change is more or less monotonic (Figure 4.3.3b,e). ESPT is mostly prohibited in the AOT RMs even at w_0=10 (Figure 4.3.6), this result is in accordance with a previous finding by Kuchlyan et al.[7] On the other hand ESPT is relatively favourable in both Ig and DDAB RMs. The gradual addition of Ig in AOT RMs induces the formation of the deprotonated species. It can be noted that Ig RM is only slightly bigger in size than the AOT RMs (Figure 4.3.1b), however, the ESPT process is 90% less in the latter one, which confirms the

predominant role of charge stability of the deprotonated species at the RM interface. The amount of HW is relatively less in AOT (Figure 4.3.3a-c) which could also inhibit the formation and stability of deprotonated species. ESPT is more efficient in Ig rather than in DDAB RMs, which has a positively charged interface and can presumably stabilize the negatively charged deprotonated species. Rotational anisotropy results also suggest that the deprotonated species is highly restricted in the DDAB interface indicating its preferred location therein. Interestingly the most efficient ESPT has been observed at X_{Ig}=0.6 wherein the emission peaks of the protonated and the deprotonated species have comparable intensities (Figure 4.3.6b). Notably, solvation dynamics and anisotropy of C-500 shows its minimum in this mixing ratio of DDAB/Ig mixed RM indicating the system to approaching more bulk-like behaviour. It seems that ESPT and solvation usually follow each other. It has recently been shown that when solvation gets faster, so does the ESIPT in 4'-N,N-Dimethylamino-3-hydroxyflavone (DMA3HF) in AOT RM.[14] Datta et al. have correlated the slowing down of the ESPT process of 2-(2'-pyridyl)benzimidazole (2PBI) with the slow solvation of the more polar excited-state of the tautomeric form of the probe in the restricted environment of RMs.[15] This leads to infer that the Ig-induced promotion of ESPT of D-luciferin could be due mostly to its solvatochromic behaviour. AOT interface is expected to be more acidic compared to the core as the H_3O^+ species balances the surfactant charge by diffusing to the interfacial domain as also confirmed from the long-time fitting (see figure 4.3.10). In neutral Ig RMs, the H_3O^+ species could get partially stabilized at the interface by both enthalpic and entropic contributions for the interfacial solvation of the proton.[44] Thus the pH of the interface in AOT RM is lower compared to that of Ig RM.[44] A similar argument infers that the core of DDAB water pool is more acidic. It has also been concluded that buffer-like action of RM is more prominent in AOT RM than positively charged CTAB RMs.[45, 46] This makes the neutral species preferably get stabilized at the AOT interface. The addition of Ig reduces the effective charge at the AOT interface which favours the formation of the deprotonated species. Similarly, the apparent increase in ROH^* with X_{Ig} above 0.6 in DDAB/Ig system is due to a decrease of pH in the interface by dilution of charge of DDAB with addition of Ig.

From the fluorescence decay transients, we obtain the fraction of D-luciferin undergoing ESPT and we observe contrasting behaviours in the two mixed RMs (Figure 4.3.9b). Surprisingly in pure AOT and Ig the decay patterns of the protonated form are quite comparable and so also the fraction of the protonated forms (Figure 4.3.9), which predicts

comparable ESPT in these two systems. However, the strong charge repulsion and possible recombination probability eventually inhibits the ESPT process in AOT RMs. In DDAB, the fraction of protonated D-luciferin undergoing ESPT is high and it decreases rapidly at and beyond X_{Ig}=0.6. The time-resolved evolution of the deprotonated species, as manifested by the value of the change in the slope of R.I., is an approximate yet useful parameter to a priori understand the progress of the ESPT process. In AOT the slope is rather low corroborating the less ease to form the charged RO^{-*} species, while in DDAB it presumably is high which is a manifestation of the fact that a larger number of the probe molecules are undergoing ESPT than the former (Figure 4.3.9b). The addition of Ig increases the slope in AOT/Ig mixed RMs almost linearly. In DDAB/Ig mixed RM it initially increases with increasing X_{Ig} and passes through a maximum. ESPT is favoured if the deprotonation step speeds up by the stabilisation of H_3O^+ and/or RO^{-*}. Initially, larger droplet size, comparative higher HW content, diffusion of H_3O^+ to the core and RO^{-*} stabilisation by electrostatic interaction in DDAB RM collectively assist the progress of ESPT to a greater extent compared to Ig. Additionally, the interaction of the PEO head-group in Ig interface could initially hinders the complete exposure of D-luciferin towards water molecules. However, as H_3O^+ and RO^{-*} are formed they get stabilised by the PEO head-group and the forward deprotonation step gets accelerated. The high proton diffusion rate and a high fraction of ESPT undergoing ROH^* is expected to show the maximum rate at an intermediate mixing ratio. Our results show that the ESPT rate inside RM water-pool can be modulated (both increase and decrease) by only mixing surfactants of different charge types keeping all other parameters unchanged. This finding could find its applicability in its broader implications, specially in situations where the proton is generated in restricted environments and at an interface exposed to water.

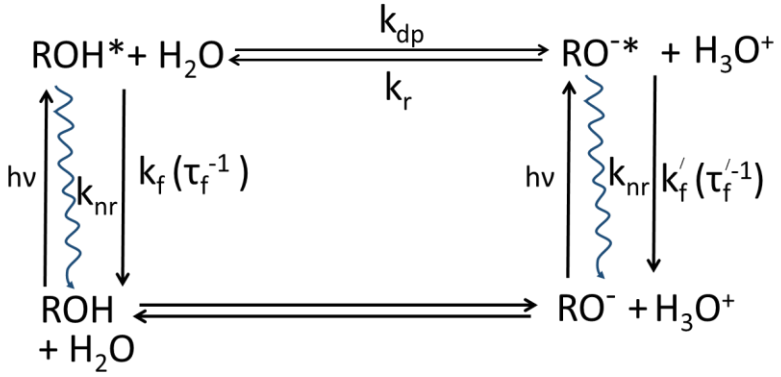

Scheme 4.3.1: Scheme of excited-state proton transfer of a model photo-acid ROH.

Table 4.3.1: Bi-exponential fitting parameters of the solvation dynamics, C(t) and rotational anisotropy r(t) decay curves of C-500 in DDAB/Ig/ mixed RMs at w_0=10 and different mixing ratios.

X_{Ig}	Solvation dynamics					Rotational anisotropy				
	a_1	τ_1 (ns)	a_2	τ_2 (ns)	$\langle\tau_s\rangle$ (ns)	a_{r1}	τ_{r1} (ns)	a_{r2}	τ_{r2} (ns)	$\langle\tau_r\rangle$ (ns)
0	0.47	0.05	0.53	1.17	0.65	0.38	0.13	0.62	1.22	0.80
0.2	0.75	0.27	0.25	1.76	0.64	0.43	0.12	0.57	1.10	0.68
0.4	0.59	0.17	0.41	1.23	0.61	0.59	0.22	0.41	1.21	0.63
0.6	0.51	0.15	0.49	0.94	0.53	0.53	0.12	0.47	1.12	0.59
0.8	0.53	0.13	0.47	1.10	0.59	0.44	0.16	0.56	1.22	0.76
1	0.58	0.24	0.42	1.51	0.79	0.37	0.14	0.63	1.22	0.82

Table 4.3.2: Fluorescence decay fitting parameters of protonated and deprotonated forms of D-luciferin in mixed RMs.

X_{Ig}	Protonated form (420 nm)				Deprotonated form (590 nm)			
	τ_1 (a_1) (ns)	τ_2 (a_2) (ns)	τ_3 (a_3) (ns)	χ^2	τ_1 (a_1) (ns)	τ_2 (a_2) (ns)	τ_3 (a_3) (ns)	χ^2
DDAB/Ig								
0	0.08 (0.91)	0.6 (0.07)	1.93 (0.02)	1.2	0.08 (-1.26)	0.6 (1.04)	2.62 (1.22)	1.06
0.2	0.08 (0.91)	0.6 (0.07)	1.28 (0.02)	1.20	0.08 (-0.83)	0.6 (0.61)	2.14 (1.22)	1.14
0.4	0.08 (0.92)	0.6 (0.07)	1.68 (0.01)	1.17	0.08 (-1.09)	0.6 (0.91)	2.39 (1.18)	1.06
0.6	0.08 (0.73)	0.6 (0.22)	1.24 (0.05)	1.14	0.08 (-0.84)	0.6 (-0.13)	3.13 (1.97)	1.10
0.8	0.08 (0.58)	0.6 (0.32)	1.28 (0.10)	1.09	0.08 (-0.76)	0.6 (-0.15)	3.15 (1.91)	1.06
1	0.08 (0.65)	0.6 (0.15)	1.60 (0.2)	1.09	0.08 (-1.1)	0.6 (0.96)	5.05 (1.14)	1.05
AOT/Ig								
0	0.08 (0.68)	0.6 (0.16)	2.51 (0.16)	1.22	0.08 (-0.31)	0.6 (0.5)	3.96 (0.81)	1.10
0.2	0.08 (0.57)	0.6 (0.19)	1.73 (0.24)	1.03	0.08 (-0.04)	0.6 (-0.13)	3.77 (1.17)	1.24
0.4	0.08 (0.59)	0.6 (0.18)	1.64 (0.23)	1.05	0.08 (-0.05)	0.6 (-0.04)	3.84 (1.09)	1.17
0.6	0.08 (0.5)	0.6 (0.21)	1.53 (0.29)	1.04	0.08 (-0.28)	0.6 (0.28)	3.75 (1.0)	1.14
0.8	0.08 (0.54)	0.6 (0.18)	1.47 (0.28)	1.07	0.08 (-0.12)	0.6 (-0.11)	3.81 (1.23)	1.04

Table 4.3.3a: Anisotropy decay parameters of the protonated and the deprotonated forms of D-luciferin in DDAB/Ig mixed RMs.

X_{Ig}	a_1	τ_1 (ns)	a_2	τ_2 (ns)	$\langle\tau_r\rangle$ (ns)
Protonated form (λ_{em}= 420 nm)					
0	0.44	0.34	0.56	1.65	1.07
0.2	0.43	0.36	0.57	1.71	1.13
0.4	0.45	0.31	0.55	1.62	1.03
0.6	0.3	0.23	0.7	1.16	0.88
0.8	0.31	0.18	0.69	1.05	0.78
1	0.32	0.19	0.68	1.09	0.80
Deprotonated form (λ_{em}= 530 nm)					
0	0.12	0.21	0.83	2.15	1.81
0.2	0.15	0.25	0.85	2.15	1.86
0.4	0.1	0.21	0.9	1.79	1.63
0.6	0.28	0.3	0.72	1.63	1.26
0.8	0.34	0.31	0.66	1.59	1.15
1	0.26	0.23	0.74	1.26	0.99

Table 4.3.3b: Anisotropy decay parameters of the protonated and the deprotonated forms of D-luciferin in AOT/Ig mixed RMs.

X_{Ig}	a_1	τ_1 (ns)	a_2	τ_2 (ns)	$<\tau_r>$ (ns)
Protonated form (λ_{em}= 420 nm)					
0	0.45	0.21	0.55	1.21	0.76
0.2	0.44	0.22	0.56	1.20	0.76
0.4	0.38	0.23	0.62	1.23	0.85
0.6	0.37	0.2	0.63	1.20	0.83
0.8	0.35	0.21	0.65	1.22	0.86
Deprotonated form (λ_{em}= 525 nm)					
0	0.69	0.18	0.31	0.91	0.40
0.2	0.72	0.25	0.28	0.83	0.41
0.4	0.52	0.19	0.48	0.77	0.46
0.6	0.56	0.21	0.44	0.87	0.50
0.8	0.55	0.26	0.45	1.25	0.17

4.5. References

1. Cohen, B.; Huppert, D.; Solntsev, K. M.; Tsfadia, Y.; Nachliel, E.; Gutman, M., Excited State Proton Transfer in Reverse Micelles. *J. Am. Chem. Soc.* **2002,** *124*, 7539-7547.
2. Mallick, A.; Purkayastha, P.; Chattopadhyay, N., Photoprocesses of excited molecules in confined liquid environments: An overview. *J. Photochem. Photobiol. C: Photochem. Rev.* **2007,** *8*, 109-127.
3. Lawler, C.; Fayer, M. D., Proton Transfer in Ionic and Neutral Reverse Micelles. *J. Phys. Chem. B* **2015,** *119*, 6024-6034.
4. Phukon, A.; Ray, S.; Sahu, K., Effect of Cosurfactants on the Interfacial Hydration of CTAB Quaternary Reverse Micelle Probed Using Excited State Proton Transfer. *Langmuir* **2016,** *32*, 10659-10667.
5. Phukon, A.; Ray, S.; Sahu, K., How does interfacial hydration alter during rod to sphere transition in DDAB/water/cyclohexane reverse micelles? Insights from excited state proton transfer and fluorescence anisotropy. *Langmuir* **2016,** *32*, 6656-6665.

6. Khorwal, V.; Sen, P., Ultrafast excited state intermolecular proton transfer dynamics of 2-(4'-Pyridyl)benzimidazole inside the nanocavity of reverse micelles. *J. Photochem. Photobiol. A: Chem.* **2017,** *347*, 86-92.
7. Kuchlyan, J.; Banik, D.; Kundu, N.; Ghosh, S.; Banerjee, C.; Sarkar, N., Effect of Confinement on Excited-State Proton Transfer of Firefly's Chromophore d-Luciferin in AOT Reverse Micelles. *J. Phys Chem. B* **2014,** *118*, 3401-3408.
8. Koninti, R. K.; Gavvala, K.; Sengupta, A.; Hazra, P., Excited State Proton Transfer Dynamics of Topotecan Inside Biomimicking Nanocavity. *J. Phys. Chem. B* **2015,** *119*, 2363-2371.
9. Spry, D. B.; Goun, A.; Glusac, K.; Moilanen, D. E.; Fayer, M. D., Proton transport and the water environment in nafion fuel cell membranes and AOT reverse micelles. *J. Am. Chem. Soc.* **2007,** *129*, 8122-8130.
10. Choudhury, S. D.; Nath, S.; Pal, H., Excited-State Proton Transfer Behavior of 7-Hydroxy-4-methylcoumarin in AOT Reverse Micelles. *J. Phys. Chem. B* **2008,** *112*, 7748-7753.
11. Rakshit, S.; Saha, R.; Verma, P. K.; Pal, S. K., Role of Solvation Dynamics in Excited State Proton Transfer of 1- Naphthol in Nanoscopic Water Clusters Formed in a Hydrophobic Solvent. *Photochem. Photobiol.* **2012,** *88*, 851-859.
12. Erez, Y.; Presiado, I.; Gepshtein, R.; Huppert, D., Excited-state intermolecular proton transfer of firefly luciferin IV. Temperature and pH dependence. *J. Phys Chem. A* **2011,** *115*, 1617-1626.
13. Choudhury, S. D.; Pal, H., Modulation of Excited-State Proton-Transfer Reactions of 7-Hydroxy-4-methylcoumarin in Ionic and Nonionic Reverse Micelles. *J. Phys. Chem. B* **2009,** *113*, 6736-6744.
14. Ghosh, D.; Batuta, S.; Begum, N. A.; Mandal, D., Proton transfer dynamics in a polar nanodroplet: ESIPT of 4'-n,n-dimethylamino-3-hydroxyflavone in AOT/alkane/water reverse micelles. *J. Lumin.* **2017,** *184*, 64-73.
15. Mukherjee, T. K.; Panda, D.; Datta, A., Excited-State Proton Transfer of 2-(2'-Pyridyl)benzimidazole in Microemulsions: Selective Enhancement and Slow Dynamics in Aerosol OT Reverse Micelles with an Aqueous Core. *J. Phys. Chem. B* **2005,** *109* 18895-18901.
16. Sedgwick, M.; Cole, R. L.; Rithner, C. D.; Crans, D. C.; Levinger, N. E., Correlating proton transfer dynamics to probe location in confined environments. *J. Am. Chem. Soc.* **2012,** *134*, 11904-11907.
17. da Silva, L. P.; da Silva, J. C. G. E., Computational Studies of the Luciferase Light-Emitting Product: Oxyluciferin. *J. Chem. Theory Comput.* **2011,** *7*, 809-817.
18. Erez, Y.; Presiado, I.; Gepshtein, R.; da Silva, L. P.; da Silva, J. C. G. E.; Huppert, D., Comparative Study of the Photoprotolytic Reactions of d-Luciferin and Oxyluciferin. *J. Phys. Chem. A* **2012,** *116*, 7452-7461.
19. Erez, Y.; Huppert, D., Excited-state intermolecular proton transfer of the firefly's chromophore D-luciferin. *J. Phys. Chem. A* **2010,** *114*, 8075-8082.
20. Presiado, I.; Erez, Y.; Huppert, D., Excited-State Intermolecular Proton Transfer of the Firefly's Chromophore d-Luciferin. 2. Water− Methanol Mixtures. *J. Phys. Chem. A* **2010,** *114*, 9471-9479.
21. Kuchlyan, J.; Banik, D.; Roy, A.; Kundu, N.; Sarkar, N., Excited-State Proton Transfer Dynamics of Firefly's Chromophore D-Luciferin in DMSO-Water Binary Mixture. *J. Phys. Chem. B* **2014,** *118*, 13946-13953.
22. Shiao, S. Y.; Chhabra, V.; Patist, A.; Free, M. L.; Huibers, P. D. T.; Gregory, A.; Patel, S.; Shah, D. O., Chain length compatibility effects in mixed surfactant systems for technological applications. *Adv. Colloid Interface Sci.* **1998,** *74*, 1-29.

23. Das, A.; Patra, A.; Mitra, R. K., Do the physical properties of water in mixed reverse micelles follow a synergistic effect: a spectroscopic investigation. *J. Phys. Chem. B* **2013,** *117*, 3593-3602.
24. Das, A.; Mitra, R. K., Does the optimum hydrophilic lipophilic balance condition affect the physical properties of mixed reverse micelles? A spectroscopic investigation. *J. Phys. Chem. B* **2014,** *118*, 5488-5498.
25. Patra, A.; Luong, T. Q.; Mitra, R. K.; Havenith, M., Solvent dynamics in a reverse micellar water-pool: a spectroscopic investigation of DDAB–cyclohexane–water systems. *Phys. Chem. Chem. Phys.* **2013,** *15*, 930-939.
26. Eastoe, J.; Heenan, R. K., Water-induced structural changes within the L2 phase of didodecyldimethylammonium bromide–cyclohexane–water systems. *J. Chem. Soc., Faraday Trans.* **1994,** *90*, 487-492.
27. Paul, B. K.; Mitra, R. K., Water solubilization capacity of mixed reverse micelles: Effect of surfactant component, the nature of the oil, and electrolyte concentration. *J. Colloid Interface Sci.* **2005,** *288*, 261-279.
28. Hou, M. J.; Shah, D. O., Effects of the molecular structure of the interface and continuous phase on solubilization of water in water/oil microemulsions. *Langmuir* **1987,** *3*, 1086-1096.
29. Leung, R.; Shah, D. O., Solubilization and phase equilibria of water-in-oil microemulsions : I. Effects of spontaneous curvature and elasticity of interfacial films. *J. Colloid Interface Sci.* **1987,** *120*, 320-329.
30. Eastoe, J., Small-angle neutron scattering from dilute didodecyldimethylammonium bromide water-in-oil microemulsions. Evidence for polymer-like aggregates. *Langmuir* **1992,** *8*, 1503-1506.
31. Durantini, A. M.; Falcone, R. D.; Silber, J. J.; Correa, N. M., Effect of the Constrained Environment on the Interactions between the Surfactant and Different Polar Solvents Encapsulated within AOT Reverse Micelles. *ChemPhysChem* **2009,** *10*, 2034–2040.
32. Calvaruso, G.; Minore, A.; Liveri, V. T., FT-IR Investigation of the Urea State in AOT Reversed Micelles. *J. Colloid Interface Sci.* **2001,** *243*, 227-232.
33. Odella, E.; Darı´o Falcone, R.; Silber, J. J.; Correa, N. M., How TOPO affects the interface of the novel mixed water/AOT:TOPO/n-heptane reverse micelles: dynamic light scattering and Fourier transform infrared spectroscopy studies. *Phys. Chem. Chem. Phys.* **2014,** *16*, 15457-15468.
34. Novaki, L. P.; Correa, N. M.; Silber, J. J.; El Seoud, O. A., FTIR and 1H NMR Studies of the Solubilization of Pure and Aqueous 1,2-Ethanediol in the Reverse Aggregates of Aerosol-OT. *Langmuir* **2000,** *16*, 5573-5578.
35. Bardhan, S.; Kundu, K.; Das, S.; Poddar, M.; Saha, S. K.; Paul, B. K., Formation, thermodynamic properties, microstructures and antimicrobial activity of mixed cationic/non-ionic surfactant microemulsions with isopropyl myristate as oil. *J. Colloid Interface Sci.* **2014** *430*, 129-139.
36. Jimenez, R.; Fleming, G. R.; Kumar, P. V.; Maroncelli, M., Femtosecond Solvation Dynamics of Water. *Nature* **1994,** *369*, 471-473.
37. Hasegawa, M., Buffer-like action in water pool of aerosol OT reverse micelles. *Langmuir* **2001,** *17*, 1426-1431.
38. Presiado, I.; Erez, Y.; Simkovitch, R.; Shomer, S.; Gepshtein, R.; Pinto da Silva, L.; Esteves da Silva, J. C. G.; Dan Huppert, D., Excited-State Proton Transfer of Firefly Dehydroluciferin. *J. Phys. Chem. A* **2012,** *116*, 10770-10779.
39. Huppert, D.; Goldberg, S. Y.; Masad, A.; Agmon, N., Experimental Determination of the Long-Time Behavior in Reversible Binary Chemical Reactions. *Phys. Rev. Lett.* **1992,** *68*, 3932−3935.

40. Hong, K. M.; Noolandi, J., Solution of the Smoluchowski Equation with a Coulomb Potential. I. General Results. . *J. Chem. Phys.* **1978,** *68*, 5163−5171.
41. Solntsev, K. M.; Huppert, D.; Agmon, N., Challenge in Accurate Measurement of Fast Reversible Bimolecular Reaction. *J. Phys. Chem. A* **2001,** *105*, 5868−5876.
42. Koti, A.; Krishna, M.; Periasamy, N., Time-resolved area-normalized emission spectroscopy (TRANES): a novel method for confirming emission from two excited states. *J. Phys. Chem. A* **2001,** *105*, 1767-1771.
43. Maroncelli, M.; Fleming, G. R., Picosecond solvation dynamics of coumarin 153: the importance of molecular aspects of solvation. *J. Chem. Phys.* **1987,** *86*, 6221-6238.
44. Crans, D. C.; Levinger, N. E., The Conundrum of pH in Water Nanodroplets: Sensing pH in Reverse Micelle Water Pools. *Acc. Chem. Res.* **2012,** *45*, 1637-1645.
45. Mukherjee, P.; Gupta, S.; Rafiq, S.; Yadav, R.; Jain, V. K.; Raval, J.; Sen, P., Ramping of pH Across the Water-Pool of a Reverse Micelle. *Langmuir* **2016,** *32*, 1693-1699.
46. Marques, B. S.; Nucci, N. V.; Dodevski, I.; Wang, K. W. C.; Athanasoula, E. A.; Jorge, C.; Wand, A. J., Measurement and Control of pH in the Aqueous Interior of Reverse Micelles. *J. Phys. Chem. B* **2014,** *118*, 2020-2031.

Chapter 5

5. Excited-state Proton Transfer in Reverse Micelles: Effect of Temperature and a Possible Interplay with Solvation

A fundamental question in ESPT dynamics is related to its inherent coupling with the solvation process. A much-debated issue is which process precedes? This chapter addresses this fundamental question by conducting a detailed study of the ESPT process of a photo-acid D-luciferin at various temperatures in RMs composed of: anionic AOT, cationic DDAB, and neutral Igepal-520 using steady-state and time-resolved fluorescence measurements at fixed hydration, w_0=10. We found that with increasing temperature both solvation as well as the ESPT rate accelerates, however, the extent of the increase is RM specific, and they even not necessarily complement each other. Our study clearly identifies the pivotal role of solvation in such RM systems to guide the ESPT process.

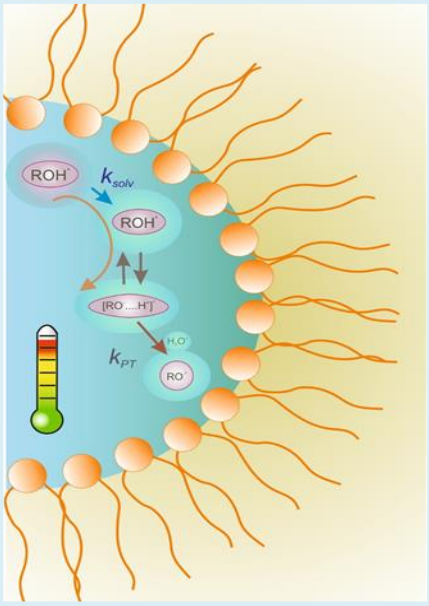

5.1. Introduction

Excited-state proton transfer (ESPT), in which, upon electronic excitation, a fluorophore photo-acid gives up a proton to the neighboring solvent to promote forms of its anionic form[1], is a fundamental process of many chemicals and biological interest[2] and it plays key roles in several processes including photosynthesis[3], green fluorescence protein[4, 5], in interchanging of the inter-base H-bond network in DNA[6] and other chemical applications.[7-10] Considering the inherent heterogeneity in real biological environments it deems informative to investigate ESPT reactions in constrained and confined environments rather than in conventional aqueous surroundings.[11] Reverse micelles (RM) offer with such an unique bio-mimicking platform to study ESPT reaction. Owing to the varied physical nature of the water encapsulated in the RM water-pool and with the additional control of tuning the physical properties of water by changing the head group charge, dissipating solvent and water to surfactant ratio (w_0), considerable interest has been paid in the recent past to investigate ESPT reaction of various photoacids in RM systems.[12-20] ESPT is found to be relatively delayed in RMs compared to that in bulk solvents which manifests the bound nature of the water present in the RMs.

While most of these studies have been carried out at ambient conditions, the effect of temperature on the ESPT process has been assessed only in limited attempts.[21-24] It has been observed that temperature does play a pivotal role in determining the ESPT dynamics; however, a general comprehension has not yet been achieved. While most of the temperature-dependent studies reported earlier have been carried out in neat or mixed solvents, those are sparse in RM systems. In this chapter, we have made a detailed investigation on the effect of temperature on ESPT dynamics of a well-known photoacid D-luciferin in three different RM systems of various charge types (anionic: AOT; cationic: DDAB and neutral: Igepal) using steady-state and ps-resolved fluorescence measurements.

ESPT process of a photoacid can efficiently be probed by monitoring the fluorescence profiles of the protonated form (ROH^*) and the deprotonated form (RO^{-*}) of the fluorophore. Additionally, time-resolved fluorescence measurements enable to estimate of the ESPT dynamics. D-luciferin (Scheme 4.3.1) is a light-emitting compound, found in organisms that generate bioluminescence.[25] This molecule consists of two rings 6-hydroxy-benzothiazole system that undergoes an efficient excited-state deprotonation process of the hydroxyl group.

ESPT of D-luciferin in water is a fast process with a rate constant of 3×10^{10} s^{-1}, however, is associated with a noticeable quenching of the deprotonated form due to an irreversible geminate recombination process.[26] This fluorescence quenching of deprotonated form is mainly attributed to the excited-state protonation of the nitrogen heteroatom of the benzothiazole moiety.[27] It has been found that this ESPT process is dependent on the solvent composition[28], pH[29] and temperature.[21,30,22, 31, 32] From the previous result it has been observed that D-luciferin is a weak acid in its ground state with pK_a value of ~7, while in excited-state it turns into a much stronger acid with pK_a^* value approximately 0.5.[32] A few early reports suggest that ESPT of D-luciferin is mild in AOT RMs at low hydration, however, it gets favoured as the content of water increases in the RM.[14] In a recent study[19] we have explored the effect of surfactant charge type on the ESPT dynamics of D-luciferin in three different RMs composed of AOT (ionic), DDAB (cationic) and Igepal-520 (non-ionic) and their mixtures. We found that the ESPT rate could be modulated by varying the mixing ratio of the surfactant(s). As a pertaining continuation of that study in the present chapter, we investigate the effect of temperature on ESPT dynamics in those RM systems. We fix the surfactant concentration at 0.1 M and w_0 at 10 in order to ensure all the RMs are spherical in nature.[33] Since ESPT in a micro-heterogeneous environment is believed to be an optimization between the local concentration of water and solvent relaxation,[24] hydration dynamics is expected to play a pivotal role in determining the dynamics. We measure both ESPT dynamics and solvation dynamics using ps-resolved fluorescence measurements and we observe marked distinction between the two rates depending on the surfactant charge type and also on temperature.

5.2. Materials and Methods

Sodium bis(2-ethylhexyl) sulfosuccinate (AOT), didodecyldimethylammonium bromide (DDAB), polyoxyethylene (5) nonylphenylether (Igepal-520), cyclohexane (Cy), D-luciferin and coumarin 500 (C-500) (chapter 2) were products of Sigma-Aldrich. All the chemicals were used without further purification. AOT, DDAB, and Igepal were dissolved in Cy at a concentration of 0.1 (M). Then a suitable amount of water was added into it to produce the RMs of $w_0 = 10$.

We have used the following instruments and methods (for details see chapters 2, 3). For the measurement of the droplet size of the RM water pool by *DLS technique*. A UV-Vis, spectrophotometer was used for all the absorption spectrum measurements. To understand the

local environment of the fluorophore probe done by *steady-state fluorescence* techniques. *Time-resolved fluorescence* measurements were performed using a diode laser with the central wavelength 375 nm and 80 ps instruments response function (IRF). Fluorescence decay data were fitted using commercially available F900 software provided by Edinburgh Instruments.

5.3. Results and Discussion

DLS Measurements:

We measure the size of the RM droplets using DLS technique and the results are depicted in figure 5.3.1. The droplet size follows the order DDAB>Ig>AOT and it decreases with temperature.

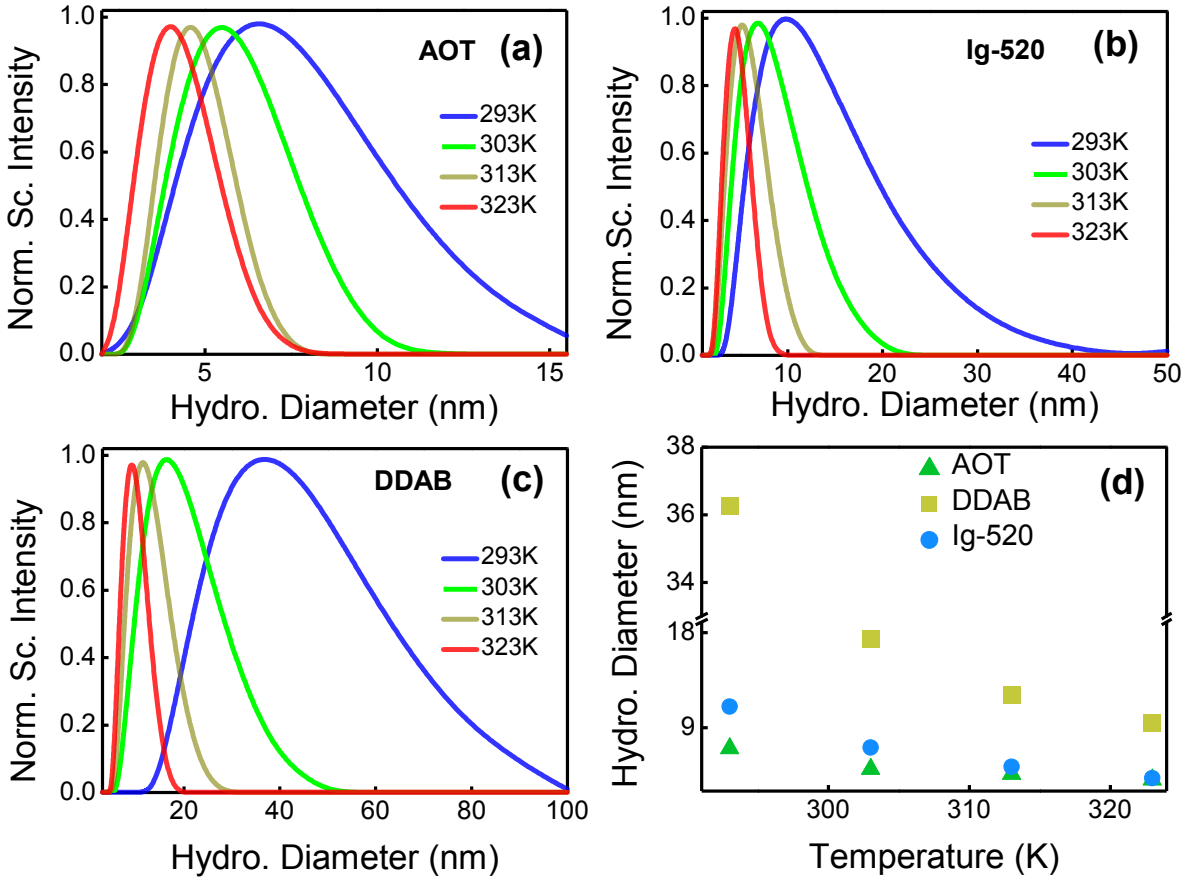

Figure 5.3.1: Dynamic light scattering profiles of (a) AOT (b) Ig-520 and (c) DDAB RMs at different temperatures at a fixed w_0=10. (d) The average hydrodynamic diameter of different RMs at different temperatures.

Steady-State Fluorescence Measurements:

Steady-state fluorescence spectra of D-luciferin in different RMs (at 293 K) are shown in figure 5.3.2a. For comparison, the emission spectrum in pure water is shown in the same figure. The ESPT behaviour is rather contrasting in these RMs. In bulk water we observe only one peak at ~530 nm which is due to the deprotonated species RO^{-*}. However, in the RMs we observe two peaks, one at ~430 nm (protonated form, ROH^{*}) and another one at ~530 nm (deprotonated form, RO^{-*}). The protonated species is predominantly present in AOT RM while in DDAB and Ig-520 RMs, the RO^{-*} peak is also prominent.[19] With temperature both the peak intensities decrease (Figure 5.3.3), a representative figure for DDAB RM is shown in figure 5.3.2b. A mild temperature-induced blue-shift (3-4 nm) in the ROH^{*} emission peak is observed for Ig RM. The decrease in the emission intensity could be ascribed to the possible increase in the associated non-radiative processes with temperature. We plot the ratio of the intensities of the deprotonated and the protonated species ($I_{RO^{-*}}/I_{ROH^{*}}$) in figure 5.3.2c. The ratio is high and comparable for DDAB and Ig at all temperatures, while it is quite low in AOT RMs. This ratio is more or less featureless showing only a subtle decrease with temperature.

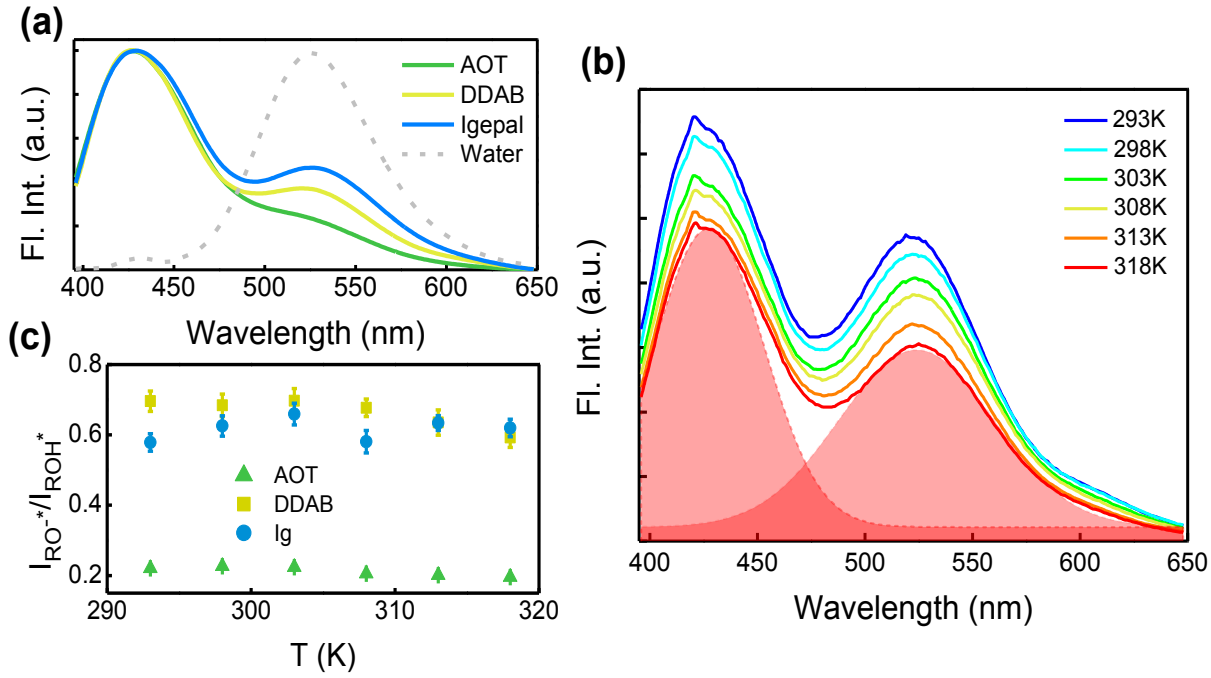

Figure 5.3.2: (a) Emission spectra of D-luciferin (λ_{ex}=375 nm) in AOT, DDAB and Ig RM systems (w_0=10) at 293 K. Emission spectrum of D-luciferin in pure water is shown in the broken line. The peaks at ~430 nm are due to the protonated form (ROH^{*}) and the peaks at ~530 nm are due to the deprotonated form (RO^{-*}) of D-luciferin. (b) Emission spectra of D-luciferin in DDAB RM at six different temperatures. The emission curves (due to ROH^{*} and RO^{-*}) are deconvoluted into two Gaussian curves. A representative such deconvolution at 318 K is shown as the filled curves. (c) The ratio of the intensities of RO^{-*} and ROH^{*} (at the peak) in three different RM systems as a function of temperature.

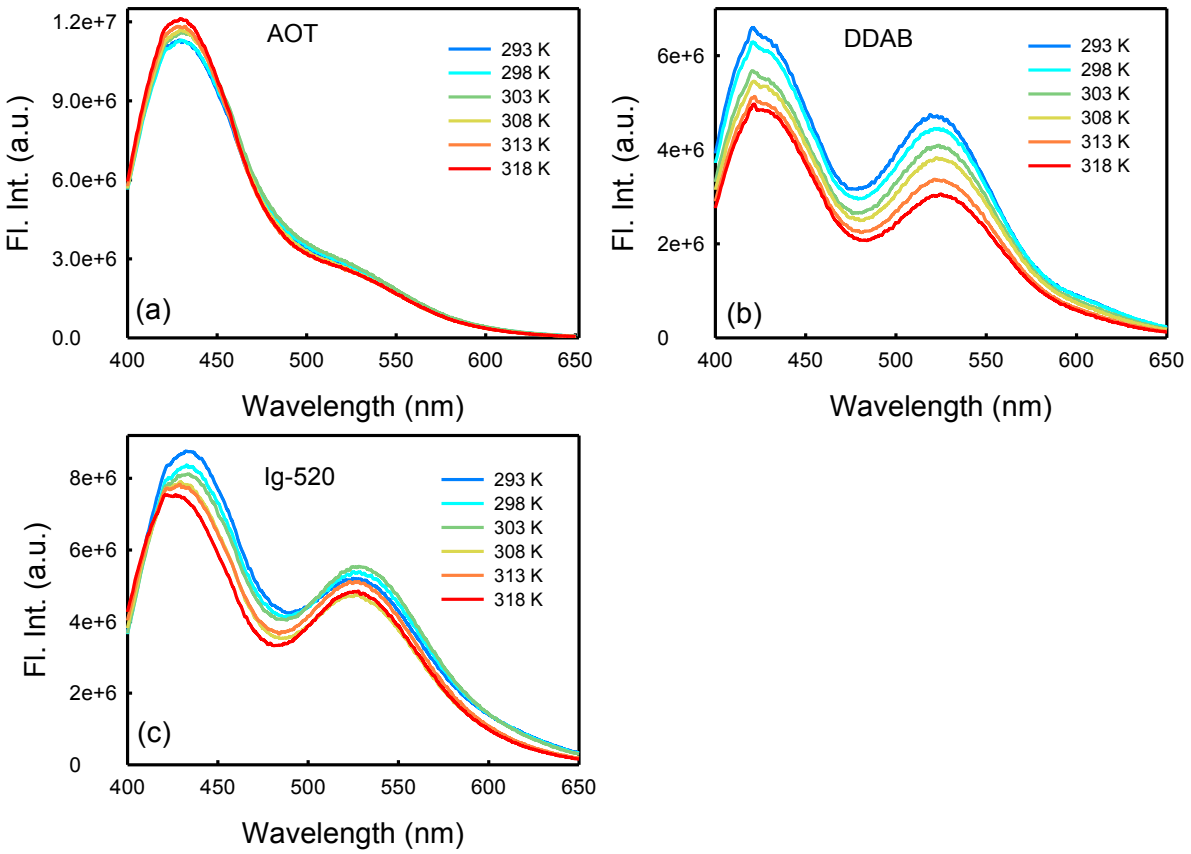

Figure 5.3.3: Emission spectra of D-luciferin in three different RMs at different temperatures (excited at 375 nm).

Time-Resolved Fluorescence Measurements:

We monitor fluorescence transients at 420 and 590 nm corresponding to the ROH^* and the RO^{-*} forms, respectively. Note that 420 nm is at slightly blue-sided while 590 nm is at the red side of the respective emission maximum of the two emitting forms. It can be observed from the deconvolution plot that the intensities of ROH^* and RO^{-*} are negligibly small at 590 and 420 nm, respectively. These wavelengths are intentionally chosen so as to minimize any undesired mixing of the contributions of the two emitting species.[34] We fit the fluorescence transients using a triple exponential decay model and the fitting parameters are depicted in table 5.3.1. Representative decay transients in DDAB RM at different temperatures are shown in figure 5.3.4a. The ROH^* species decays with time constants of 80 ps (τ_1), 600 ps (τ_2) and a relatively longer component (τ_3) of ~2.6 ns (AOT), ~2 ns (DDAB) and ~1.6 ns (Ig) at 293 K. On the other hand, the 590 nm transients (of RO^{-*}) could only be fitted considering a rise (negative) contribution of the 80 ps component (τ_1), which exactly matches with that of the faster decay time constant of the protonated form at all temperatures. We plot the relative contribution of τ_1 (a_1) in all the RMs at different temperatures in figure

5.3.4b. The increase in the a_1 in RO^{-*} with temperature unambiguously indicates an ease in the ESPT dynamics with temperature. The ESPT reaction could be modelled as a sequential process (Scheme 5.3.1) in which ROH^* dissociates to form RO^{-*} and H_3O^+. The ESPT dynamics of D-luciferin inside RMs are slower than that compared in bulk water.[14] Therefore, we could expect to reconstruct most of the ESPT process using the transients from ps-resolved TCSPC measurements. It should be taken into consideration that some ultrafast components might remain undetected due to the limited TCSPC resolution. However, the slow dynamics obtained in the ps-resolution grossly emanates from the bound water at the RM interface, and we, therefore, can conclude on the dynamics of the ESPT process in the vicinity of the RM interface only.

In RMs the photoacid can locate itself in two regions: (i) in a relatively hydrated or core region where it can easily undergo ESPT and (ii) in the interfacial region wherein ESPT is constrained.[19,34] The multiple decay profile of D-luciferin in the RMs can be interpreted assuming such a spatial distribution of the probe and keeping in mind that only a fraction of the probe molecules could undergo ESPT. The concentration of ROH^* at any given time 't' can be expressed as:

$$[ROH^*] = [ROH^*]_{0,Y} e^{-\left(\frac{1}{\tau_{dp}}+\frac{1}{\tau_p}\right)t} + [ROH^*]_{0,N} e^{-\left(\frac{1}{\tau_p}\right)t} \qquad (5.3.1)$$

where, τ_p and τ_{dp} denote the lifetime of the protonated and the deprotonated species, respectively. The subscripts *'Y'* and *'N'* stand for ROH^* molecules that *'do'* and *'do not'* undergo ESPT reaction, respectively. We fit the normalized time-resolved decay transients of the ROH^* at 420 nm using equation 5.3.1. The fitted parameters are listed in table 5.3.2. We calculate and plot the relative population of D-luciferin that are undergoing ESPT reaction in all three RM systems (Figure 5.3.4c). We observe that this fraction is the highest in DDAB RM and lowest in Ig RM. The fraction does not change noticeably in DDAB RMs, while in both AOT and Ig RMs, it decreases near-linearly with temperature.

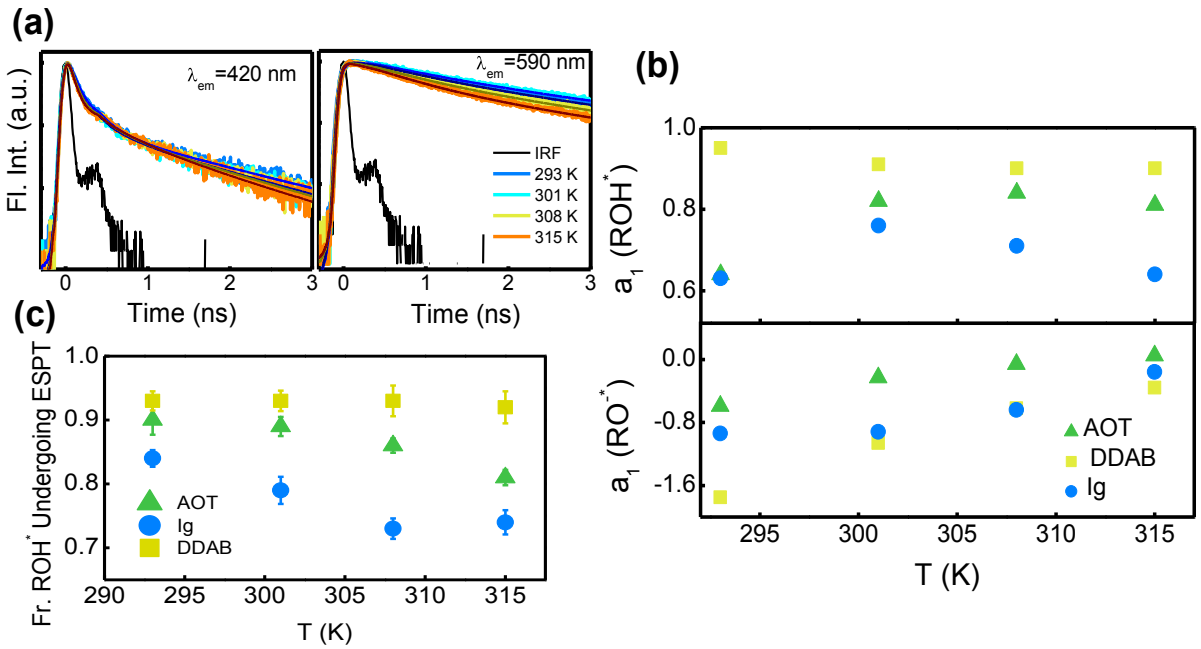

Figure 5.3.4: (a) Fluorescence transients of D-luciferin (λ_{ex}=375 nm) in DDAB RM at different temperatures measured at 420 nm (left panel) and 590 nm (right panel). The solid black lines are tri-exponential fittings. (b) Fitting co-efficient, a_1, of the ROH^* and RO^{-*} fluorescence transients (see table 5.3.1) as a function of temperature in three different RMs. (c) Fraction of ROH^* undergoing ESPT reaction as a function of temperature (for more details, see equations 5.3.1 and 2.49 in chapter 2).

We measure the decay transients in equal intervals in the wavelength window of 410 to 650 nm, and fitted all the transients using a triple exponential decay model. The fitted parameters (τ_i's and a_i's) are used to construct time-resolved emission spectra (TRES) and correspondingly time-resolved area-normalized emission spectra (TRANES) of D-luciferin.[35] The TRANES profiles, which essentially manifest the time evolution of the emission spectra, are provided in figure 5.3.5. TRANES is an efficient analysis tool to illustrate the spectral changes occurring in the excited state. It has been concluded that decay of the protonated (or the rise of the deprotonated) TRANES intensity directly correlates ESPT dynamics.[20, 36] Analogous to the steady-state feature we observe two distinct peaks in all the TRANES profiles. We fit the TRANES data (filled circles in the figures) using a bi-lognormal fitting function (see Ch. 2, equation 2.42) (solid lines).[37] In all the curves the red coloured symbols correspond to those in the steady-state ($t\approx\infty$). At time $t\approx0$ (purple points) we observe predominantly ROH^* emission, which suggests that, in accordance of our intuition, we could capture the early events of the ESPT process. The RO^{-*} intensity gradually increases at the expense of that of ROH^* as the reaction progresses. Interestingly we observe iso-emissive points at ~480 nm in DDAB RM and at ~473 nm in AOT RM. Presence of a single iso-emissive point in TRANES profile unambiguously establishes the absence of any other

intermediate form of the photoacid during the ESPT process. However, in Ig RM, no such iso-emissive point is evidenced (Figure 5.3.5).

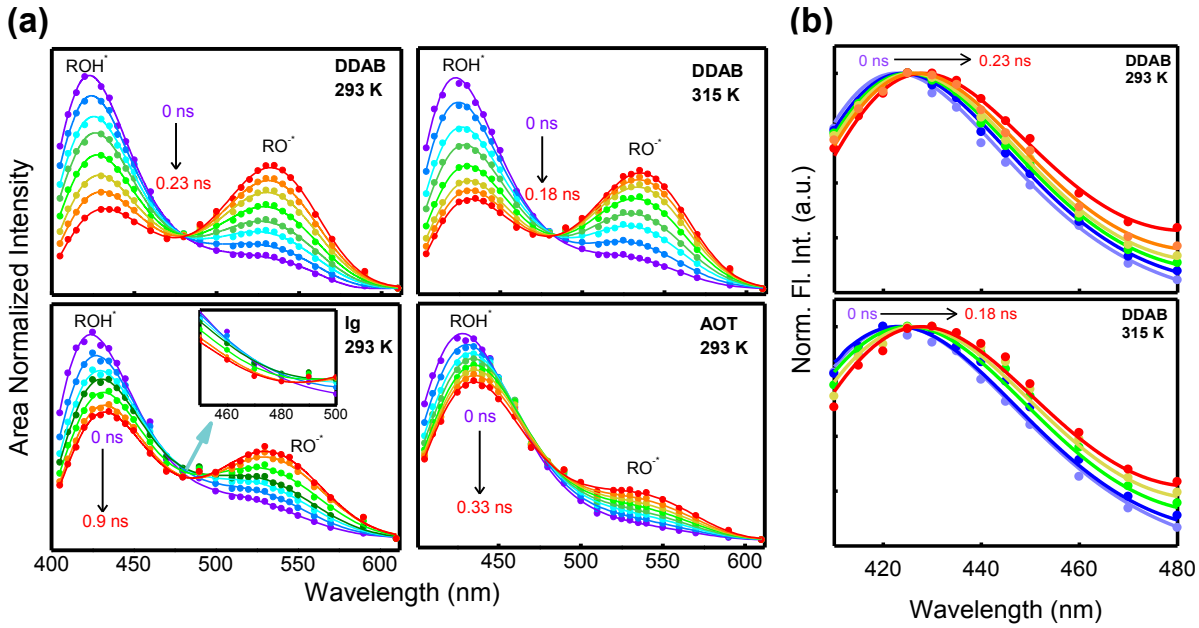

Figure 5.3.5: (a) Area normalized time-resolved emission spectra (TRANES) of D-luciferin in different RM systems. The filled points are experimental points and the solid lines are bi-log normal fits (see chapter 2, equation 2.42). In all the plots it is evident that the population of RO^{-*} grows with time while that of ROH^{*} diminishes. In DDAB and AOT RMs iso-emissive points are observed. Such a point is not evident in Ig RM. (b) Peak (ROH^{*}) normalized time-resolved emission spectra (TRES) of D-luciferin in DDAB RM at 293 and 315 K. The filled points are experimental points and the solid lines are bi-log normal fits. Note that the peak wavelength suffers red-shift with time.

Since we capture the early events of the ESPT process, we attempt to calculate the dynamics of the ESPT process using the time evolution of the two emitting species from the TRANES profiles, and identify the $I_{RO^{-*}}(t)$ growth kinetics with the proton transfer rate (k_{PT}). Consequently, we express an ESPT correlation function $C(t)_{PT}$[20] as:

$$C(t)_{PT} = \frac{I(t)-I(0)}{I(\infty)-I(0)} \qquad (5.3.2)$$

where $I(t)$ is the intensity at any given time 't', $I(0)$ is that at t=0 and $I(\infty)$ is that at a very long time (equivalent to the steady-state intensity). Representative $C(t)_{PT}$ plots for different RM systems at 293 K are shown in figure 5.3.6a (left panel). The $C(t)_{PT}$ plots are fitted single exponentially (solid lines) and the corresponding time constants (τ_{PT}) are provided in table 5.3.3. We also construct the $C(t)_{PT}$ at different temperatures; representative plots for DDAB RM at four different temperatures are shown in figure 5.3.6a (right panel). We found that with increasing temperature τ_{PT} decreases indicating an unambiguous enhancement in the ESPT dynamics (k_{PT}).

The slow solvation inside RMs enables us to estimate the time constant using ps-resolved fluorescence measurements. From the wavelength-dependent decay transients (figure 5.3.4a) we construct time-resolved (ROH^*) peak intensity normalized emission spectrum profiles of D-luciferin in different RMs (a representative profile for DDAB RM is shown in figure 5.3.5b). It is evident that the peak at ~0 ns appears at a shorter wavelength and with time it suffers a progressive red-shift. This unambiguously indicates solvation of the emitting species and measuring the emission peak frequency we construct solvent correlation function ($C(t)_{solv}$) as

$$C(t)_{solv} = \frac{\tilde{\nu}(t)-\tilde{\nu}(\infty)}{\tilde{\nu}(0)-\tilde{\nu}(\infty)} \qquad (5.3.3)$$

where, $\tilde{\nu}(0)$, $\tilde{\nu}(t)$ and $\tilde{\nu}(\infty)$ are the emission maximum wavenumber (in cm^{-1}) at time zero, t, and infinity, respectively. The $\tilde{\nu}(\infty)$ values were taken to be the emission wavenumber beyond which an insignificant or no spectral shift was observed. Some representative $C(t)_{solv}$ curves are shown in figure 5.3.6b.

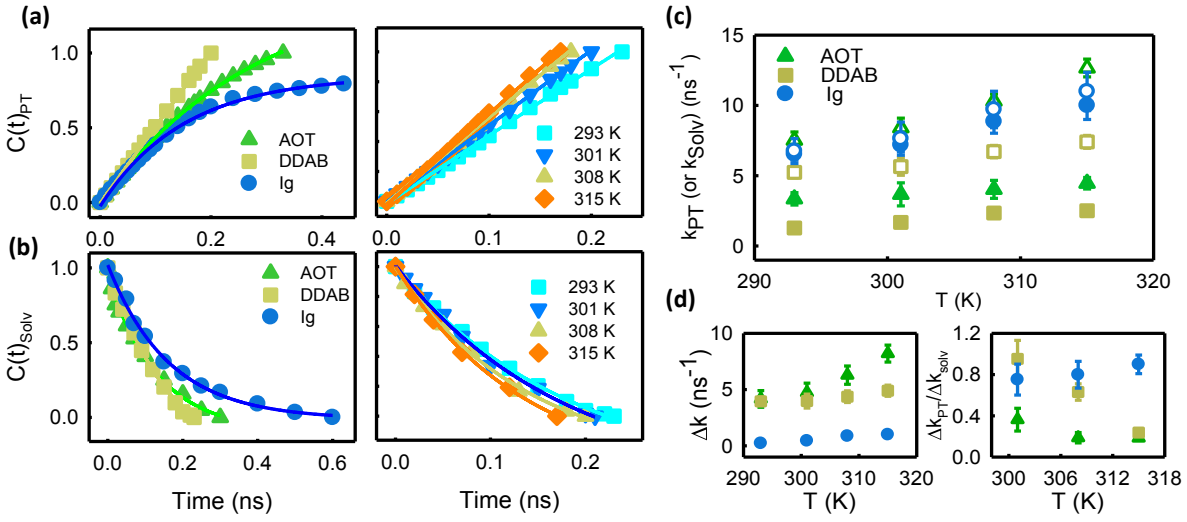

Figure 5.3.6: (a) *Left panel:* Proton transfer correlation function ($C(t)_{PT}$) of D-luciferin in three different RM systems as. The solid lines are exponential fits. *Right panel:* $C(t)_{PT}$ of D-luciferin in DDAB RM at different temperatures. The solid lines are exponential fits. (b) *Left panel:* ROH^* solvation correlation function ($C(t)_{Solv}$) of D-luciferin in three different RM systems as. The solid lines are exponential fits. *Right panel:* $C(t)_{Solv}$ of D-luciferin in DDAB RM at different temperatures. The solid lines are exponential fits. (c) Proton transfer rate, k_{PT} (filled symbols) and solvation rate, k_{Solv} (open symbols) of D-luciferin in three different RM systems. Note that the solvation dynamic is faster than the PT kinetics. (d) *Left panel:* Difference of solvation and proton transfer kinetics ($\Delta k = k_{Solv} - k_{PT}$) of D-luciferin as a function of temperature in three different RMs. *Right panel:* $\Delta k_{PT}/\Delta k_{solv}$ as a function of temperature in three different RMs.

These profiles are fitted single-exponentially and the corresponding time constants (τ_{solv}) are presented in table 5.3.7. The observed Stoke's shifts are found to be in the order of 250-600 cm^{-1}. It should be reemphasized here that the solvation of the photoacids in pure water is

ultrafast[38] and could not be identified with the ps-resolved setup. We could recover solvation of ROH^* only due to the restricted water dynamics in the RMs.[39] We observe that τ_{solv} follows the order AOT<Ig<DDAB and it decreases with increasing temperature. Interestingly, solvation dynamics of C-500 is the fastest in DDAB (table 5.3.6) while for ROH^* it is the slowest.

We also measure the rotational anisotropy of the photoacids at different temperatures to identify the spatial restriction on both ROH^* and RO^{-*} in different RMs. All the rotational decay traces are fitted bi-exponentially (Figure 5.3.7) according to equation 2.30 in chapter 2. The fitting parameters are presented in table 5.3.4. It is observed that the average rotational time constant $<\tau_r>$ is higher in DDAB RM compared to that in Ig and AOT RMs and it decreases with increasing temperature indicating an ease in the spatial restriction of both the forms of the photoacid in the RM waterpool at elevated temperatures.

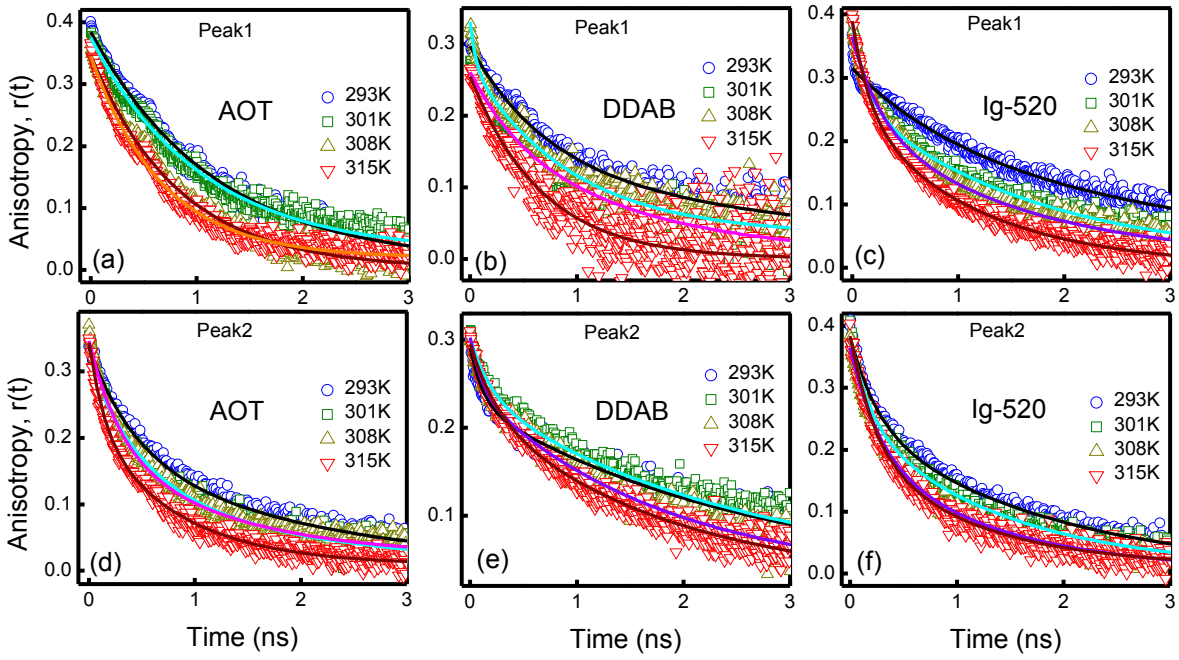

Figure 5.3.7: Fluorescence anisotropy decays of D-luciferin are plotted as a function of time (ns) for (a-c) Peak1 for ROH^* and (d-f) Peak2 for RO^{*-} in AOT, DDAB and Ig-520 at w_0 = 10 RMs at different temperatures measured at emission maxima. The solid lines indicate bi-exponential fits.

To quantify this further we analyse the anisotropy data using 'wobbling-in-cone' model (as described in the 2.16 section in chapter 2) and calculate the related parameters (table 5.3.5)[40,41], of which the ones with a special interest are the wobbling angle *(θ)* and the wobbling diffusion coefficient *(D_w)*. It is observed that both θ and D_w increases with temperature unambiguously indicating that both ROH^* and RO^{-*} experience ease in rotation

and consequently in rotational diffusion as the temperature is increased, irrespective of the RM type.

Discussions:

ESPT reaction in constrained environments of RMs is contrasting when compared to that in the bulk solvents, the reason mostly being the reduced polarity[42], higher micro-viscosity[39] of the water molecules encapsulated, which in turn also makes solvation dynamics slower in RMs.[11, 39] A pioneering work by Rini et al.[38] using fs-resolved IR spectroscopy revealed that ESPT process initiates through a fast solvation stage (diffusion-controlled) followed by an encounter and finally a reaction stage in which proton transfer occurs through the connected H-bond within a few hundreds of fs. Several other studies have also concluded ESPT and solvation dynamics to be intrinsically coupled.[24, 43] We therefore expect a similar sequence to follow in the RM systems, however, with a slower timescale. Recent THz dielectric relaxation study from our group[44] has identified that static dielectric constant (ε_s) of water is low in these three RM systems (16.0, 17.7 and 22.8 in DDAB, AOT and Ig RMs as compared to ~80 in bulk water) and the strength of the cooperative relaxation (ε_s-ε_1) is ~67%, 70% and 80% in these RMs. It is therefore also plausible that the inherent solvation dynamics of water would also be perturbed and that too would vary depending on the RM systems. The sluggish solvation that we recover from the ps-resolved transients are due to such sluggish dynamics of the water in the vicinity of the interface which mainly depends on the specific interaction of the probe molecules with the interface of RM and the analysis made therefrom grossly manifests local information. Thus the dynamic picture might vary from the steady-state scenario, wherein ESPT from the total waterpool contributes.

Interestingly, we observe that the fraction of ROH^* undergoing ESPT decreases with the increase in temperature in Ig and AOT RMs, while in DDAB RM, the fraction is relatively high[19] and does not change much with temperature (Figure 5.3.4c). This fact is apparently contrasting with the observed enhancement in the ESPT dynamics (Figure 5.3.6c). It has been argued that rapid solvation of the Frank Condon states of the photoacid moves the system away from the neighbourhood of the transition state which increases the barrier to proton transfer reaction eventually slowing down the reaction.[43] In accordance to this argument an increase in temperature is expected to increase solvation dynamics and accordingly ESPT rate is expected to get slower. To verify the incurred temperature-induced change in solvation, we measure the solvation dynamics of the fluoroprobe C-500 (which

does not exhibit ESPT dynamics) in these RM systems at two terminal temperatures (293 and 315 K) (Table 5.3.6). We notice that the average solvation time constants are slow and comparable (0.65-0.74 ns) in the three RMs at 293 K[41], and it decreases when the temperature is increased to 323 K indicating an accelerated dynamics of RM bound water.[39] From the anisotropy study of D-luciferin, we had already identified more precisely that spatial restriction on both the species of the photoacid are indeed released and they tend to move faster inside the RMs at higher temperature (Table 5.3.5). It has been discussed previously that ESPT efficiency is very low in AOT RM compared to DDAB and Ig because of it's small droplet size, a relatively less amount of H-bonded water (which is responsible for ESPT), preferable stabilization of the neutral species (ROH^*) at the AOT interface compared to its anionic species (RO^{-*}).[19] It is also interesting to note here that the size of the RMs vary much, specially DDAB has a considerably larger waterpool compared to the others (Figure 5.3.1). Also, the size decreases with increasing temperatures. However, we observe that the rotational diffusion of the probe relaxes with temperature indicating that the extent of the incurred acceleration in water dynamics is irrespective of the size and geometry of the RM interface.[33] With this background we now identify the rationale behind the observed enhanced ESPT dynamics at elevated temperatures. As discussed earlier, ESPT dynamics essentially depend on two factors: the local concentration of water molecules near the photo-acid and solvent reorganization.[24, 31] Therefore, at this point it deems essential to understand the solvation around ROH^* variation with the temperature inside RMs. From the solvation and anisotropy study it is observed that with increasing temperature the probe is located at bulk-like waterpool of RM as well as rapid solvent reorganization favour ESPT.

Earlier studies have concluded that iso-emissive point in a TRANES of a two-state ESPT process could annihilate when solvation and ESPT take place at comparable time scales.[20] While the solvation process involves time-dependent stabilization in the excited energy state of the probe molecule it does not usually change with time during the ESPT process. Thus an iso-emissive point is witnessed only when the solvation time scale of the probe molecule does not interfere with the ESPT time scale.[20] Presence of an iso-emissive point intuits that ESPT process is independent of solvation in AOT and DDAB, in which solvation completes prior to the initiation of the ESPT process. A similar phenomenon has previously been demonstrated in the case of ESPT in 1-napthol in water-dioxane mixtures.[24] In Ig RM, however, they co-occur. It can therefore be concluded that only fully solvated AOT

and DDAB participate in ESPT while in Ig ESPT process can initiate prior to full solvation. This perhaps reasons the observed high k_{PT} in Ig.

We now compare the temperature dependency of these two processes (Figure 5.3.6c). We observe that the solvation rate (k_{solv}) is always higher than the ESPT rate (k_{PT}) and both of them increases with increasing temperature. It is evident from the anisotropy measurements that the rotational ease of both the emitting species increases with temperature, so at any given point of time, both these species tend to diffuse faster inside the RMs at elevated temperatures. So the effects of temperature on the physical mobility of both forms are equally favouring. For a better apprehension on the correlation between solvation and the ESPT we measure Δk (the difference between k_{Solv} and k_{PT}). We observe that this parameter is comparable in AOT and DDAB, and the difference increases linearly with temperature (Figure 5.3.6d, left panel). This implies that with temperature both k_{PT} and k_{Solv} increases which also corroborates the anisotropy findings. Interestingly we observe that the extent of increase of both time constants is RM specific. For a further quantification we plot the ratio between $\Delta k_{PT}(T)$ ($=k_{PT}^{(T)}-k_{PT}^{(293K)}$) and $\Delta k_{solv}(T)$ ($=k_{solv}^{(T)}-k_{solv}^{(293K)}$) (figure 5.3.6d, right panel) as a function of temperature. This parameter identifies the change in the ESPT dynamics in response to the increased solvation at elevated temperatures. We observe contrasting effects, in DDAB RMs the increase in solvation does not reciprocate the ESPT dynamics and it actually decreases noticeably with temperature. In AOT the effect is mild and decreasing, whereas in Ig it is actually assisting as the ratio increases with temperature. The differences appear striking as the temperature is expected to favour the process independent of RM type. Keeping in mind that from the ps-resolved study we only can restore the information of the interface, it is important to consider the interaction of the emitting species with the interface. Having a polar end D-luciferin could extend selective propensity towards the charged interface, specially the electrostatic preference of RO^{-*} at the DDAB interface, while that is not significant in the case of an uncharged interface of Ig. This model perfectly corroborates the finding of the larger fraction of ROH^{*} undergoing ESPT is high in DDAB while for Ig it is rather small, however, does not answer the low ESPT proficiency at DDAB. It is therefore the solvation that decides the fate of the reaction. The increased solvation at elevated temperatures perhaps in its turn competes with geminate recombination. It can only be inferred that the observed change is an optimization result of all these apparently counter-interacting phenomena. These experimental findings needs to be justified with detailed theoretical and simulation studies.

5.4. Conclusions

ESPT of D-luciferin in three different RM systems were studied; from the steady-state measurements it was found that ESPT is most prominent in DDAB followed by Ig while in AOT the formation of the deprotonated species is highly restricted, the electrostatic (in)stability of the deprotonated species rationale the steady-state findings. Time-resolved anisotropy measurements revealed that both species enjoy the ease of rotational relaxation at elevated temperatures. From the time-resolved measurements, we obtain both ESPT (k_{PT}) and solvation (k_{solv}) dynamics and we found that ESPT is the slowest in DDAB while it is rather fast in Ig. Interestingly we observed that in the charged RMs solvation precedes ESPT, however, in Ig they co-occur. Both k_{PT} and k_{solv} increased near-linearly with temperature, however, it was found that the increase in k_{solv} does assist ESPT in Ig while it actually was disfavoured in DDAB. Our study has established the pivotal role of solvation to be considered to explain the ESPT process, specially in constrained environments like in RMs. We understand our present results would encourage further experimental insights wherein hydration dynamics during an ESPT process could explicitely and independently be monitored (using IR pump-probe or THz pump-probe experiments) and revisit the authenticity our claims.

Scheme 5.3.1: ESPT proceeds through the formation of a transient species $[^{-}OR\ldots H^{+}]^{*}$. It then follows a pair isolation process (k_{PT}) to form RO^{-*}. This process is opposed by the possibility of diffusion-assisted geminate recombination between RO^{-*} and H^{+} to reform ROH^{*}.

Table 5.3.1: Tri-exponential fitting parameters of the fluorescence transients of the protonated (ROH^*) and the deprotonated (RO^{-*}) forms of D-luciferin in AOT, DDAB and Ig-520 RM systems at w_0 = 10 measured at 420 and 590 nm (λ_{ex}=375 nm), respectively at different temperatures. All the values are obtained from the exponential fitting with an uncertainty of ≤ 5%.

T (K)	ROH^* (420 nm)			RO^{-*} (590 nm)		
	τ_1 (ns) (a_1)	τ_2 (ns) (a_2)	τ_3 (ns) (a_3)	τ_1 (ns) (a_1)	τ_2 (ns) (a_2)	τ_3 (ns) (a_3)
AOT						
293	0.08 (0.64)	0.6 (0.22)	2.63 (0.14)	0.08 (-0.59)	0.6 (0.85)	3.98 (0.74)
301	0.08 (0.82)	0.6 (0.13)	2.6 (0.05)	0.08 (-0.23)	0.6 (0.65)	4.03 (0.58)
308	0.08 (0.84)	0.6 (0.10)	2.47 (0.06)	0.08 (-0.06)	0.6 (0.54)	4.03 (0.52)
315	0.08 (0.81)	0.6 (0.13)	2.42 (0.06)	0.08 (0.05)	0.6 (0.45)	4.03 (0.50)
DDAB						
293	0.08 (0.95)	0.6 (0.02)	1.98 (0.03)	0.08 (-1.75)	0.6 (1.25)	2.60 (1.50)
301	0.08 (0.91)	0.6 (0.07)	1.52 (0.02)	0.08 (-1.06)	0.6 (1.03)	2.48 (1.03)
308	0.08 (0.91)	0.6 (0.07)	1.40 (0.02)	0.08 (-0.62)	0.6 (0.89)	2.34 (0.72)
315	0.08 (0.90)	0.6 (0.06)	1.20 (0.03)	0.08 (-0.36)	0.6 (0.86)	2.26 (0.5)
Ig-520						
293	0.08 (0.63)	0.6 (0.16)	1.58 (0.21)	0.08 (-0.94)	0.6 (0.97)	5.18 (0.97)
301	0.08 (0.76)	0.6 (0.11)	1.48 (0.13)	0.08 (-0.92)	0.6 (0.97)	4.96 (0.95)
308	0.08 (0.71)	0.6 (0.13)	1.42 (0.16)	0.08 (-0.64)	0.6 (0.90)	5.11 (0.74)
315	0.08 (0.64)	0.6 (0.17)	1.39 (0.19)	0.08 (-0.16)	0.6 (0.55)	5.19 (0.61)

Table 5.3.2: Fraction and lifetime of protonated ROH^* and deprotonated RO^{-*} forms of D-luciferin in different RM systems at various temperatures at w_0=10. The transients were fitted using equation 5.3.1 with an error ≤ 5%..

T (K)	a_1	τ_{dp} (ns)	a_2	τ_p (ns)
AOT				
293	0.90	0.20	0.10	1.10
301	0.89	0.17	0.11	1.38
308	0.86	0.14	0.14	1.49
315	0.81	0.13	0.19	1.66
DDAB				
293	0.93	0.16	0.07	0.78
301	0.93	0.14	0.07	0.86
308	0.93	0.12	0.07	0.87
315	0.92	0.11	0.08	0.89
Ig-520				
293	0.84	0.09	0.16	0.92
301	0.79	0.09	0.21	1.20
308	0.73	0.08	0.27	1.13
315	0.74	0.07	0.26	0.98

Table 5.3.3: ESPT kinetics time constant (τ_{PT} in ns) of D-Luciferin in different RMs at different temperature.

T (K)	AOT	DDAB	Ig
293	0.30±0.04	0.78±0.02	0.15±0.01
301	0.27±0.06	0.60±0.02	0.14±0.01
308	0.25±0.04	0.43±0.05	0.11±0.01
315	0.22±0.02	0.40±0.03	0.10±0.01

Table 5.3.4: Fit of anisotropy decay of ROH* form of D-luciferin in different RM systems at various temperatures at w_0=10. All the time constants are obtained from the exponential fitting with an uncertainty of ≤ 5%.

T (K)	τ_{fast} (ns) (a_1)	τ_{slow} (ns) (a_2)	$<\tau_r>$ (ns)		τ_{fast} (ns) (a_1)	τ_{slow} (ns) (a_2)	$<\tau_r>$ (ns)
ROH*					**RO^{-*}**		
DDAB							
293	0.41(0.07)	1.75(0.93)	1.66		0.29(0.09)	2.16(0.91)	1.99
301	0.37(0.27)	1.47(0.73)	1.17		0.24(0.20)	2.08(0.80)	1.71
308	0.31(0.35)	1.40(0.65)	1.02		0.16(0.28)	1.87(0.72)	1.39
315	0.28(0.46)	1.00(0.54)	0.67		0.14(0.30)	1.54(0.70)	1.12
AOT							
293	0.25(0.08)	1.25(0.92)	1.17		0.27(0.11)	1.13(0.89)	1.03
301	0.22(0.09)	1.18(0.91)	1.10		0.23(0.22)	1.09(0.78)	0.89
308	0.19(0.12)	1.12(0.88)	1.00		0.20(0.31)	1.05(0.69)	0.79
315	0.17(0.36)	1.08(0.64)	0.75		0.17(0.43)	0.99(0.57)	0.64
Ig-520							
293	0.23(0.10)	1.43(0.90)	1.30		0.29(0.15)	1.36(0.85)	1.20
301	0.13(0.18)	1.36(0.82)	1.14		0.20(0.25)	1.23(0.75)	0.97
308	0.10(0.23)	1.22(0.77)	0.96		0.18(0.40)	1.18(0.60)	0.77
315	0.09(0.32)	0.97(0.68)	0.69		0.17(0.45)	1.07(0.55)	0.66

Table 5.3.5: Anisotropy parameters extract from "Wobbling-in-the-Cone" Model for ROH^* and RO^{-*} forms of D-luciferin in DDAB, AOT and Ig-520 RMs. All the values are reported with an uncertainty of ≤ 5%.

T (K)	r_0	P	τ_w (ns)	θ (deg)	$D_w \times 10^8$ (S^{-1})		r_0	P	τ_w (ns)	θ (deg)	$D_w \times 10^8$ (S^{-1})
ROH^*							**RO^{-*}**				
DDAB											
293	0.23	0.96	0.53	12.58	0.27		0.24	0.95	0.34	14.26	0.54
301	0.20	0.86	0.49	25.75	1.21		0.24	0.90	0.27	21.76	1.55
308	0.21	0.80	0.40	30.34	1.86		0.23	0.85	0.18	26.40	3.54
315	0.18	0.73	0.38	35.78	2.62		0.22	0.84	0.16	27.25	4.15
AOT											
293	0.22	0.96	0.31	13.72	0.55		0.23	0.94	0.35	16.24	0.67
301	0.25	0.95	0.27	14.05	0.66		0.24	0.88	0.28	23.20	1.68
308	0.20	0.94	0.22	16.92	1.14		0.22	0.83	0.25	27.97	2.79
315	0.19	0.80	0.20	30.62	3.76		0.21	0.76	0.21	34.07	4.35
Ig-520											
293	0.25	0.95	0.28	15.43	0.77		0.19	0.92	0.36	18.74	0.86
301	0.26	0.91	0.14	20.49	2.68		0.24	0.87	0.24	24.48	2.25
308	0.25	0.88	0.11	23.73	4.39		0.22	0.77	0.21	32.93	4.06
315	0.25	0.82	0.10	28.69	7.00		0.21	0.74	0.20	35.30	4.83

Table 5.3.6: Solvation time constants (in ns) of the C-500 solvation in three different RM systems at different temperatures.

T (K)	a_1	a_2	τ_1 (ns)	τ_2 (ns)	$<\tau_s>$ (ns)
AOT					
293	0.43	0.57	0.27±0.03	1.03±0.03	0.71
323	0.76	0.24	0.22±0.02	0.87±0.05	0.38
DDAB					
293	0.63	0.37	0.24±0.01	1.35±0.05	0.65
323	0.69	0.31	0.14±0.01	0.93±0.05	0.38
Ig					
293	0.47	0.53	0.22±0.01	1.19±0.04	0.74
323	0.45	0.55	0.21±0.01	1.13±0.05	0.72

Table 5.3.7: Solvation time constants (in ns) of the ROH^* solvation in three different RM systems at different temperatures.

T (K)	AOT	DDAB	Ig
293	0.13±0.01	0.19±0.014	0.15±0.02
301	0.12±0.01	0.18±0.02	0.13±0.02
308	0.10±0.005	0.15±0.01	0.10±0.013
315	0.08±0.004	0.14±0.009	0.09±0.011

5.5. References

1. Agmon, N., Elementary steps in excited-state proton transfer. *J. Phys Chem. A* **2005,** *109* (1), 13-35.
2. Zhou, P.; Han, K., Unraveling the Detailed Mechanism of Excited-State Proton Transfer. *Acc. Chem. Res.* **2018,** *51*, 1681−1690.
3. Weinberg, D. R.; Gagliardi, C. J.; Hull, J. F.; Murphy, C. F.; Kent, C. A.; Westlake, B. C.; Paul, A.; Ess, D. H.; McCafferty, D. G.; Meyer, T. J., Proton-Coupled Electron Transfer. *Chem. Rev.* **2012,** *112*, 4016−4093.
4. Tonge, P. J.; Meech, S. R., Excited State Dynamics in Green Fluorescent Protein. *J. Photochem. Photobiol. A* **2009,** *205*, 1−11.

5. Fang, C.; Frontiera, R. R.; Tran, R.; Mathies, R. A., Mapping GFP structure evolution during proton transfer with femtosecond Raman spectroscopy. *Nature* **2009,** *462*, 200-204.
6. Jacquemin, D.; Zuñiga, J.; Requena, A.; Ceron-Carrasco, J. P., Assessing the Importance of Proton Transfer Reactions in DNA. *Acc. Chem. Res.* **2014,** *47*, 2467−2474.
7. Mallick, A.; Purkayastha, P.; Chattopadhyay, N., Photoprocesses of excited molecules in confined liquid environments: An overview. *J. Photochem. Photobiol. C: Photochem. Rev.* **2007,** *8*, 109-127.
8. Bhattacharya, B.; Samanta, A., Excited-State Proton-Transfer Dynamics of 7-Hydroxyquinoline in Room Temperature Ionic Liquids. *J. Phys. Chem. B* **2008,** *112*, 10101-10106.
9. Choi, K.; Hamilton, A. D., A dual channel fluorescence chemosensor for anions involving intermolecular excited state proton transfer. *Angew. Chem. Int. Ed.* **2001,** *40*, 3912-3915.
10. Leiderman, P.; Genosar, L.; Huppert, D., Excited-State Proton Transfer: Indication of Three Steps in the Dissociation and Recombination Process. *J. Phys. Chem. A* **2005,** *109*, 5965-5977.
11. Bhattacharyya, K., Solvation Dynamics and Proton Transfer in Supramolecular Assemblies. *Acc. Chem. Res.* **2003,** *36*, 95-101.
12. Mukherjee, T. K.; Panda, D.; Datta, A., Excited-State Proton Transfer of 2-(2‘-Pyridyl)benzimidazole in Microemulsions: Selective Enhancement and Slow Dynamics in Aerosol OT Reverse Micelles with an Aqueous Core. *J. Phys. Chem. B* **2005,** *109* 18895-18901.
13. Phukon, A.; Ray, S.; Sahu, K., How does interfacial hydration alter during rod to sphere transition in DDAB/water/cyclohexane reverse micelles? Insights from excited state proton transfer and fluorescence anisotropy. *Langmuir* **2016,** *32*, 6656-6665.
14. Kuchlyan, J.; Banik, D.; Kundu, N.; Ghosh, S.; Banerjee, C.; Sarkar, N., Effect of Confinement on Excited-State Proton Transfer of Firefly’s Chromophore d-Luciferin in AOT Reverse Micelles. *J. Phys Chem. B* **2014,** *118*, 3401-3408.
15. Khorwal, V.; Sen, P., Ultrafast excited state intermolecular proton transfer dynamics of 2-(4'-Pyridyl)benzimidazole inside the nanocavity of reverse micelles. *J. Photochem. Photobiol. A* **2017,** *347*, 86-92.
16. Cohen, B.; Huppert, D.; Solntsev, K. M.; Tsfadia, Y.; Nachliel, E.; Gutman, M., Excited State Proton Transfer in Reverse Micelles. *J. Am. Chem. Soc.* **2002,** *124*, 7539-7547.
17. Choudhury, S. D.; Nath, S.; Pal, H., Excited-State Proton Transfer Behavior of 7-Hydroxy-4-methylcoumarin in AOT Reverse Micelles. *J. Phys. Chem. B* **2008,** *112*, 7748-7753.
18. Spry, D. B.; Goun, A.; Glusac, K.; Moilanen, D. E.; Fayer, M. D., Proton transport and the water environment in nafion fuel cell membranes and AOT reverse micelles. *J. Am. Chem. Soc.* **2007,** *129*, 8122-8130.
19. Das, A.; Islam, S. I.; Das, D. K.; Mitra, R. K., Modulation of the Excited-State Proton Transfer Rate of d-luciferin in Mixed Reverse Micellar Systems. *ACS Omega* **2018,** *3* (5), 5715-5724.
20. Singh, S.; Koley, S.; Mishra, K.; Ghosh, S., An Approach to a Model Free Analysis of Excited-State Proton Transfer Kinetics in a Reverse Micelle. *J. Phys. Chem. C* **2018,** *122* (1), 732-740.
21. Leiderman, P.; Gepshtein, R.; Uritski, A.; Genosar, L.; Huppert, D., Temperature Dependence of Excited-State Proton Transfer in Water Electrolyte Solutions and Water−Methanol Solutions. *J. Phys. Chem. A* **2006,** *110* (29), 9039-9050.

22. Simkovitch, R.; Shomer, S.; Gepshtein, R.; Shabat, D.; Huppert, D., Temperature Dependence of the Excited-State Proton-Transfer Reaction of Quinone-cyanine-7. *J. Phys Chem. A* **2013,** *117* (19), 3925-3934.
23. Fujii, K.; Aramaki, M.; Kimura, Y., Excited-State Proton Transfer of 5,8-Dicyano-2-naphthol in High-Temperature and High-Pressure Methanol: Effect of Solvent Polarity and Hydrogen Bonding Ability. *J. Phys Chem. B* **2018,** *122*, 12363-12374.
24. Rakshit, S.; Saha, R.; Verma, P. K.; Pal, S. K., Role of Solvation Dynamics in Excited State Proton Transfer of 1- Naphthol in Nanoscopic Water Clusters Formed in a Hydrophobic Solvent. *Photochem. Photobiol.* **2012,** *88*, 851-859.
25. Hastings, J. W., Chemistries and colors of bioluminescent reactions: a review. *Gene* **1996,** *173*, 5-11.
26. Erez, Y.; Huppert, D., Excited-state intermolecular proton transfer of the firefly's chromophore D-luciferin. *J. Phys. Chem. A* **2010,** *114*, 8075-8082.
27. da Silva, L. P.; Simkovitch, R.; Huppert, D.; da Silva, J. C. G. E., Theoretical study of the efficient fluorescence quenching process of the firefly luciferin. *J. Photochem. Photobiol. A* **2013,** *266*, 47-54.
28. Presiado, I.; Erez, Y.; Huppert, D., Excited-State Intermolecular Proton Transfer of the Firefly's Chromophore d-Luciferin. 2. Water− Methanol Mixtures. *J. Phys. Chem. A* **2010,** *114*, 9471-9479.
29. Presiado, I.; Erez, Y.; Huppert, D., Excited-State Intermolecular Proton Transfer of Firefly Luciferin III. Proton Transfer to a Mild Base. *J. Phys. Chem. A* **2010,** *114*, 13337-13346.
30. Cohen, B.; Leiderman, P.; Huppert, D., Unusual temperature dependence of proton transfer. 2. Excited-state proton transfer from photoacids to water. *J. Phys. Chem. A* **2002,** *106* (46), 11115-11122.
31. Freitas, A. A.; Quina, F. H.; Maçanita, A. A. L., Femtosecond and Temperature-Dependent Picosecond Dynamics of Ultrafast Excited-State Proton Transfer in Water–Dioxane Mixtures. *J. Phys Chem. A* **2014,** *118* (45), 10448-10455.
32. Erez, Y.; Presiado, I.; Gepshtein, R.; Huppert, D., Excited-state intermolecular proton transfer of firefly luciferin IV. Temperature and pH dependence. *J. Phys Chem. A* **2011,** *115*, 1617-1626.
33. Patra, A.; Luong, T. Q.; Mitra, R. K.; Havenith, M., Solvent dynamics in a reverse micellar water-pool: a spectroscopic investigation of DDAB-cyclohexane-water systems. *Phys. Chem. Chem. Phys.* **2013,** *15* (3), 930-939.
34. Phukon, A.; Ray, S.; Sahu, K., Effect of cosurfactants on the interfacial hydration of CTAB quaternary reverse micelle probed using excited state proton transfer. *Langmuir* **2016,** *32* (41), 10659-10667.
35. Koti, A.; Krishna, M.; Periasamy, N., Time-resolved area-normalized emission spectroscopy (TRANES): a novel method for confirming emission from two excited states. *J. Phys. Chem. A* **2001,** *105*, 1767-1771.
36. Phukon, A.; Sahu, K., How do the interfacial properties of zwitterionic sulfobetaine micelles differ from those of cationic alkyl quaternary ammonium micelles? An excited state proton transfer study. *Phys. Chem. Chem. Phys.* **2017,** *19* (46), 31461-31468.
37. Sahu, K.; Nandi, N.; Dolai, S.; Bera, A., A Ratio-Analysis Method for the Dynamics of Excited State Proton Transfer: Pyranine in Water and Micelles. *The Journal of Physical Chemistry B* **2018,** *122* (25), 6610-6615.
38. Rini, M.; Magnes, B.-Z.; Pines, E.; Nibbering, E. T. J., Real-Time Observation of Bimodal Proton Transfer in Acid-Base Pairs in Water

Science **2003,** *301* (5631), 349-352.

39. Mitra, R. K.; Sinha, S. S.; Pal, S. K., Temperature-Dependent Solvation Dynamics of Water in Sodium Bis(2-ethylhexyl)sulfosuccinate/Isooctane Reverse Micelles. *Langmuir* **2008,** *24*, 49-56.
40. Quitevis, E. L.; Marcus, A. H.; Fayer, M. D., Dynamics of ionic lipophilic probes in micelles: picosecond fluorescence depolarization measurements. *J. Phys. Chem.* **1993,** *97* (21), 5762-5769.
41. Mitra, R. K.; Sinha, S. S.; Pal, S. K., Temperature-dependent solvation dynamics of water in sodium bis (2-ethylhexyl) sulfosuccinate/isooctane reverse micelles. *Langmuir* **2008,** *24* (1), 49-56.
42. Senapati, S.; Chandra, A., Dielectric Constant of Water Confined in a Nanocavity. *J. Phys Chem. B* **2001,** *105*, 5106-5109.
43. Rumble, C. A.; Breffke, J.; Maroncelli, M., Solvation Dynamics and Proton Transfer in Diethylaminohydroxyflavone. *J. Phys. Chem. B* **2017,** *121*, 630-637.
44. Patra, A.; Luong, T. Q.; Mitra, R. K.; Havenith, M., Influence of Charge on the Structure and Dynamics of Water Encapsulated in Reverse Micelles. *Phys. Chem. Chem. Phys.* **2014,** *16*, 12875-12883.

Chapter 6

6. Role of Micro-Heterogeneity in the H-bonded Network on the ESPT Mechanisms of D-Luciferin

In this chapter, we use steady-state and ps time-resolved fluorescence spectroscopic techniques to investigate the Proton transfer (PT) from excited D-luciferin to water as a function of mole fraction of water in two different aqueous-alcohol (ethanol and trifluoroethanol) mixtures. The PT process from the excited states of the photoacid D-luciferin is mediated by water clusters and restricted with the increment of alcohol concentration in the solutions. However, the two alcohols behave quite differently due to their different nature of H-bonding affinity towards the polar water molecules. In this chapter, we aim to understand the differences in the H-bonding affinity of EtOH and TFE with water and its subsequent effect on the ESPT mechanism in these two mixtures. We observe contrasting behavior in emission intensity, fluorescence quantum yield, fluorescence lifetime, radiative/non-radiative decay constant, and ESPT kinetics of both the forms (protonated and deprotonated) of D-luciferin in these two alcohol-water binary mixtures. We have found that the ESPT kinetics of D-luciferin in EtOH-water is faster than that in the TFE-water mixture. It increases near-linearly with X_w (mole fraction of water in the mixture) in EtOH while in TFE the change is not linear. From the time-resolved emission measurements at different wavelengths, we construct the time-resolved area normalized emission spectra (TRANES) and find an iso-emissive point for the TFE-water system (up to X_w=0.6) while it is not evident in the EtOH-water mixture. We infer that the solvation dynamics and ESPT kinetics are comparable in EtOH while it is not so in TFE-water mixture.

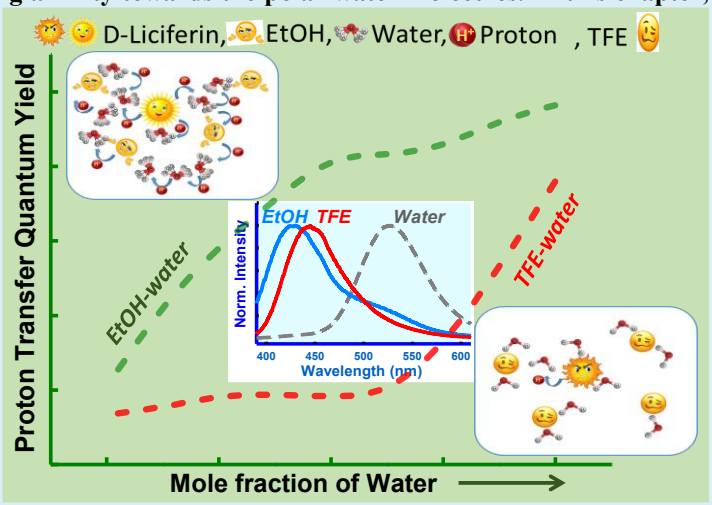

6.1. Introduction

Small amphiphilic co-solvents can perturb the hydrogen bond (H-bond) structure and dynamics of water. The extent of perturbation depends on their physical properties like hydrophobicity, polarity and H-bond forming capability, which may create micro-heterogeneity in solutions. Such inherent micro heterogeneities are sometimes defined by the clusters of similar species and/or H-bond formation between different species. The dynamic of water in such systems are very much different from the bulk dynamics of pure water, and therefore is important to investigate. A lot of well-established experimental, as well as simulation techniques, are available to probe the micro-heterogeneity of aqueous solutions.[1-3] Here, we intend to study the PT mechanism to investigate the inhomogeneity in the H-bonded network which is mainly controlled by the H-bond connectivity in the solutions. The microscopic structure and dynamics of liquid water have its obvious imprint on proton solvation and transportation. Aromatic organic photoacids are generally weak acids in their ground electronic states and are known to have electronically excited states with much lower pK_a values (i.e. the excited states are more acidic than those of the ground states). Therefore, upon photo-excitation, HA undergoes the photo-protolytic process, $HA \rightleftharpoons H^+ + A^-$, in which it can release proton (H^+) into the solutions. Since the transfer of that proton depends on the degree of connectivity of the percolating network of H-bonds in the solutions, we choose this PT process as probes to investigate the micro-heterogeneity in solutions by studying the photo-induced ESPT mechanisms.

PT in binary mixtures has received much attention in the field of chemistry and biology as PT reactions usually take place in the interfaces.[4-8] PT in an aqueous medium is a fundamental route for many chemical and biological processes ranging from enzyme catalysis to acid reactions.[6, 7, 9-11] Biological PT reactions take place at the interfaces that gives additional facility to probe the solute-solvent interactions.[12, 13] The PT reactions are broadly categorized into four different classes: (i) intermolecular PT, in which photo-acids from its electronically excited-states transfer H^+ to nearby solvent molecules through intermolecular H-bonded bridges.[11, 13, 14] (ii) intramolecular PT processes, where PT takes place in the same molecule via its constituent donor (hydroxyl group) and accepter (heterocyclic nitrogen atom or a carbonyl group) moieties.[15] (iii) Some molecules, known as photo-based (such as 7-hydroxy-coumarin, 1-naphthol, etc.), can accept an excess proton (H^+) from the solvent or the solution, and (iv) the fourth type of photo-protic reaction arises in bi-functional compounds (e.g. 1-ammonium-2-naphthol) in presence of H^+ donor (photo-acidic) and accepter (photo-

basic) when these groups are in close proximity with each other.[5, 16] Here, we are interested in studying the intermolecular PT, where the H^+ of photoacid is transferred to the nearest solvent molecule in the electrically excited-state via intermolecular H-bonds. Proton transportation between molecules in contact is generally a fast process (in the order of several femtoseconds (fs)) and hard to track in equilibrium or steady-state measurements. However, time-resolved studies have proven to be a perfect candidate to follow the relaxation mechanisms of the instantaneous electronic excited-states, intermolecular transportations of the proton through H-bonds and also the solvent reorientation around the proton.[17, 18] ESPT dynamics is mainly controlled by several factors such as the type of acid and base, local concentration of water and the conformation of H-bonded network around the photo-acids.[11] ESPT rate is remarkably affected and depends on the micro-heterogeneity of the H-bond network in the solutions.[11] It is to note here that the enol and keto forms are stable in nonpolar and polar solvents, respectively.[19] For cyanine dyes the ESPT rate (k_{PT}= 1.5×10^{12} s^{-1} in pure water) is larger than that in methanol or ethanol[20] whereas, in neat TFE, the rate is even slower.[18] In spite of a lot of studies on ESPT mechanisms in various neat solvents and solvent mixtures[7, 11, 18, 20], several questions need yet to be answered. *Why and how the PT dynamics depend on the polarity of the solution? How the solvation rearrangement takes place around the protons? How can one probe the micro-heterogeneity of the solutions as introduced by the hydrophobic molecules[21] through the PT process?*

Recently our group has used various binary mixtures with different hydrophobicity and ionic strength and has explored the micro-heterogeneous hydration properties in these aqueous solutions using various experimental techniques as well as by simulation studies.[21-23] Here, we extend our investigations in binary aqueous mixtures intending to understand the differences of H-bond affinity of the solvent molecules by probing the ESPT mechanisms. We choose D-luciferin as a photoacid, which has found its applications in pharmaceutical and biomedical sciences.[24] D-luciferin is one of the dye molecules, which are widely used for investigation of the acid-base reactions. In the excited state of D-luciferin[6, 12, 25-27]one proton is transferred from the hydroxyl group on the benzothiazole moiety to the solvent.[6] It is reported that the PT rate for D-luciferin ($k_{PT} \approx 3\times10^{10}$ s^{-1}) is almost three times faster in pure water molecules than that in neat alcohol.[11] Alcohol clusters and water clusters give the hydrophobic and hydrophilic solvation fields to the photoacid molecules involving two different hydrophobic (neutral, ROH^*) and hydrophilic (negative, RO^{-*}) moieties of the probe. Our group has observed a non-monotonic dependency of the hydration dynamics of

alcohol molecules with their concentration in the mixtures, which certainly leads to a non-monotonic change in the protein hydrations.[28] Formation of aliphatic alcohols cluster in aqueous solutions may sometimes lead to dilute the net hydrophobicity.[29] Here we choose two alcohol molecules, namely, ethanol (EtOH) and 2,2,2-trifluoroethanol (TFE) to compare their micro-heterogeneous environments in aqueous solutions through the ESPT process of D-luciferin. TFE (CF_3-CH_2-OH) has a similar molecular structure as that of EtOH (CH_3-CH_2-OH); the only difference is that the hydrogen (H) atoms are replaced by fluorine (F) atoms (see details in chapter 2). TFE, a water-miscible, colorless organic fluid, has a strong acidic character than EtOH due to its high electronegativity. It creates stable complex formation with cyclic organic moiety (e.g. THF or pyridine) via H-bonding. It is a flexible co-solvent in cell biology, pharmacology that can stabilize peptides and proteins.[30] It is also used in biochemistry as an inhibitor to study enzymes.[31] On the other hand, EtOH metabolizes in the liver, particularly via the enzymes[32] is a strong protein denaturant.[28, 33] Being a more hydrophobic molecule, TFE has less electron-donating capabilities as compared to EtOH.[10] Due to the presence of electronegative fluorine atoms, fluorinated alcohol can donate H-bond but cannot act as an H-bond acceptor because of its lower electron density of the hydroxyl oxygen atom.[10] Guttmann et. al.[34] has shown that the electron-donating ability is negligible for TFE compared to EtOH (~20) and water (~18) whereas the electron-accepting ability of TFE (~53.3) is larger than EtOH (~37.1) and water (~54.8).[34] Due to the lack of H-bonding ability TFE cannot accept H^+ from the hydroxyl group of photo-acid in its ES, whereas EtOH can. It is interesting to compare the H-bonding interactions between these two aqueous solutions. We found that two distinct dynamics for ESPT and solvation processes where the ESPT process of D-luciferin in The TFE-water mixtures occurs after completing the solvation process. For The TFE-water mixtures, the electronegative fluorine atoms provide more hydrophobicity in the solutions which leads to lower ESPT rate (k_{PT}) than EtOH-water mixtures.

6.2. Materials and Methods

D-Luciferin [(4S)-2-(6-hydroxybenzothiazole-2-yl)-4, 5 dihydrothiazole-4 carboxylic acid (99%)], TFE and ethanol (chapter 2) were purchased from Sigma-Aldrich and used without further purification. Milli-Q water was used to prepare the EtOH-water and TFE−water binary mixtures.

We have used the following instruments and tools (for details see chapters 2 & 3). A UV-Vis. spectrophotometer has been used for all absorption spectrum measurements and the fluorophore probe local environment of *fluorescence* measurements done by *steady-state fluorescence spectrometer* with slits set at 2 nm. *Time-resolved fluorescence* measurements were performed using a diode laser with the central wavelength 375 nm (80 ps instruments response function (IRF)). Fluorescence decay data were fitted using commercially available F900 software provided by Edinburgh Instruments.

6.3. Results and Discussion

Steady-state absorption and emission study:

Figures 6.3.1 show the absorption spectra of D-luciferin in The TFE-water and EtOH–water binary mixtures. For pure water, we found Gaussian-like absorption spectra with an absorption maximum at ~330 nm which corresponds to the absorption for the neutral form (ROH) of D luciferin.[11] In neutral solutions in the ground state, D-luciferin is generally present in its ROH form and not in its RO^- form.[26] In a basic medium, the absorption maxima appeared at ~390 nm from its deprotonated (RO^-) form.[7, 11] Extinction coefficient (ε) for D-luciferin increases monotonically with water content (X_w) in TFE–water mixed solvents (Figures 6.3.1). However, in the case of EtOH–water mixtures, we found an increment of the ε-value with X_w (up to 0.8), and after that, it starts decreasing. In figure 6.3.1c, we plot the variation of the absorption coefficient at the peak maximum as a function of X_w, in those two solvent mixtures. We find two distinct breakpoints in the ε vs X_w curves. In the case of The TFE-water mixtures, the extinction coefficient remains almost constant up to X_w=0.3, following which we find a sharp increase in the ε value beyond X_w 0.4. For EtOH–water mixtures, the trend is much similar, but we find a decrease in the ε value beyond X_w=0.8. Due to the higher hydrophobicity (non-polar interactions) of TFE compared to EtOH,[18] the ROH form becomes more stable in The TFE-water than in EtOH-water mixtures. Hence, ε value of EtOH-water system is higher than The TFE-water mixtures. These observations suggest that the electronic structure of D-luciferin is extremely sensitive to solvent interactions.

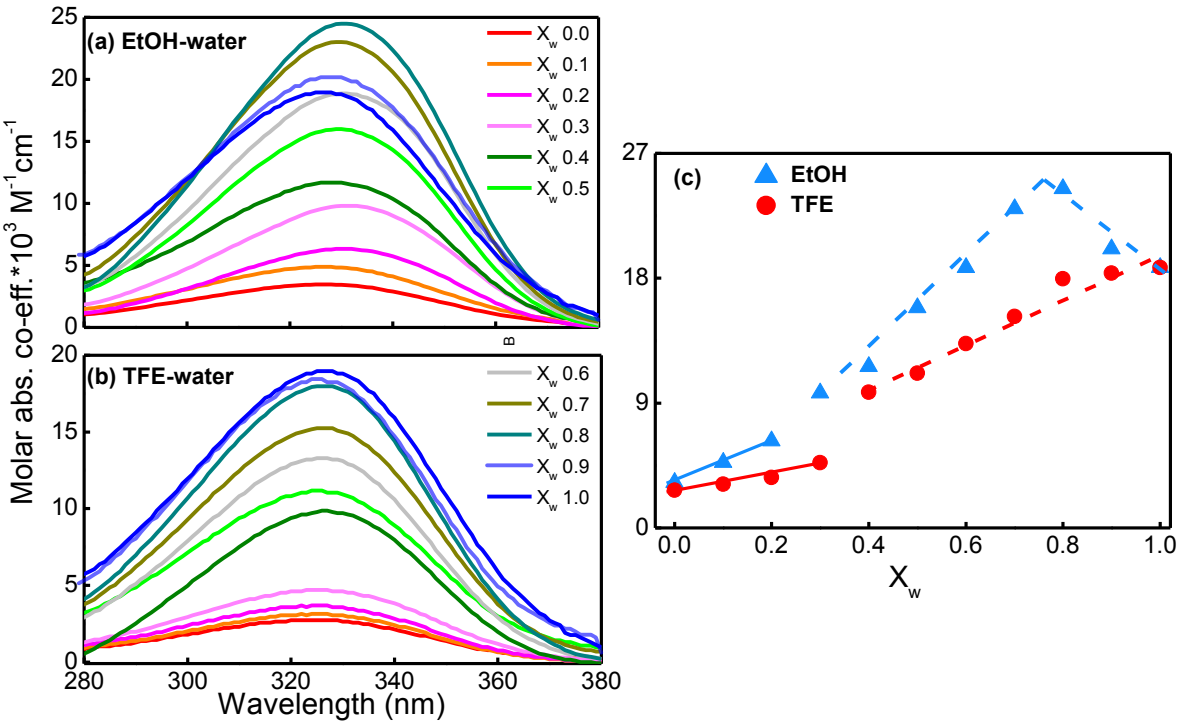

Figure 6.3.1: Absorption spectra of D-luciferin in the TFE-water (a) and EtOH–water (b) mixed solvents as the mole fraction of water, X_w, varies. (c) Variation of the extinction coefficient of absorption as a function of X_w. The dotted (with solid) lines are a guide to the eyes.

The steady-state emission spectrum of D-luciferin in The TFE-water binary mixtures is shown in figure 6.3.2a (for EtOH-water the same can be found in figure 6.3.3a). We plot the individual steady-state emission spectra for pure water, pure EtOH, and pure TFE (Figure 6.3.2b). Pure water (~530 nm for RO^{-*}) and pure TFE (~445 nm for ROH^{*}) show single peaks, whereas pure EtOH shows two peaks (~428 nm for ROH^{*} and ~530 nm for RO^{-*}). This signifies that only the deprotonated and the protonated species are always get stabilized in pure water and pure TFE, respectively, whereas both the forms can co-exist in pure EtOH.[10] We found two distinct peaks for protonated (ROH^{*}) or neutral form (~445 nm for The TFE-water and ~430 nm for EtOH-water) and for deprotonated (RO^{-*}) or anionic form (~530 nm for both the mixtures). The emission intensity of the deprotonated species increases as we increase X_w with the expenses of its protonated species. For pure EtOH (Figure 6.3.2b) the emission spectra show two distinct peaks ~428 nm (for ROH^{*}) and ~530 nm (for RO^{-*}). On the other hand, in pure TFE, the emission spectrum contain only one emission peak (~445 nm) for the ROH^{*} species.[18] This implies that no ESPT occurs in pure TFE. In figure 6.3.2c (and figure 6.3.3b) we plot the emission maximum intensities of ROH^{*} and RO^{-*} forms of D-luciferin for The TFE-water (and EtOH-water) mixtures as a function of X_w. With increasing X_w the intensity of the RO^{-*} increases at the expense of ROH^{*} emission. Beyond a certain

water concentration (X_w ~0.6 for EtOH and X_w ~0.4 for TFE), the ROH^* intensity decreases to almost zero. Similarly, RO^{-*} intensity starts increasing from X_w ~0.4 (for EtOH) and X_w ~0.8 (for TFE). For The TFE-water mixtures, in the region of X_w ~ (0.4-0.8), we found highly suppressed emission intensities, where the individual peak intensities show similar values (see figure 6.3.2c). This indicates the formation of a strong H-bonded network between TFE and water molecules in this specific concentration region. It is to note here that the polar medium can stabilize the RO^{-*} species of D-luciferin and hence it prefers to stay in a polar environment while the ROH^* form is more stable in hydrophobic medium.[6, 25, 35]

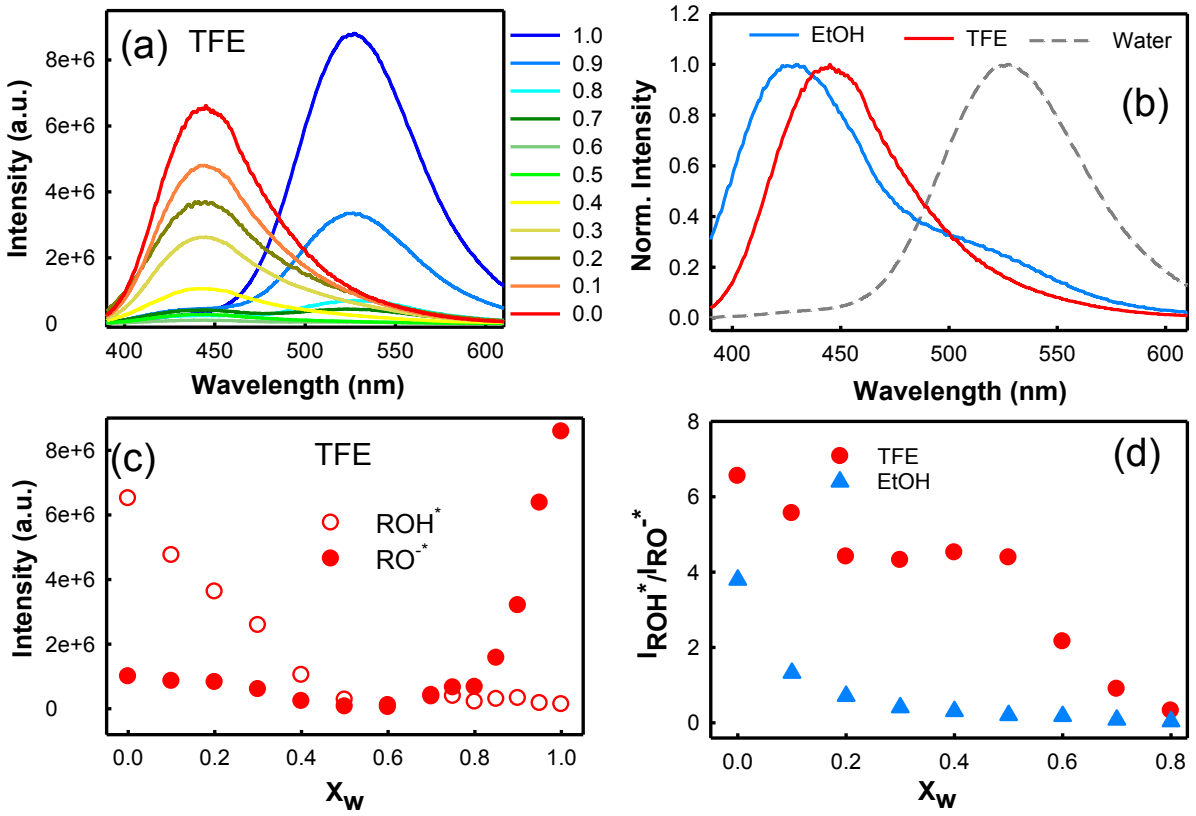

Figure 6.3.2: Representative plot of D-luciferin inside two binary mixtures, (a) The steady-state spectrum (SSS) inside the TFE-water binary composition, (b) for normalizing SSS of three different pure solvents, (c) Variation of SS maximum individual intensity for both forms ROH^* and RO^{-*}, (d) The ratio of ROH^* and RO^{-*} SS intensity as a function of mole fraction of water inside both the binary compositions.

We observed that the ROH^* peak suffers ~17 nm red-shift in TFE as compared to EtOH (see figure 6.3.2b) due to preferential hydrophobic interaction. Hence ROH^* species are more stabilized in pure TFE than in pure EtOH. Also, the positions of the fluorescence maximum in ethanol and TFE show a good correlation with Catalan's solvent polarity parameters (SPP) or Kamlet–Taft's di-polarity (π^*) parameters (Table 6.3.1), the values have been extracted from previous literature.[36, 37] We plot the ratio of protonated and deprotonated intensity

($I_{ROH^*/RO^{-*}}$) in figure 6.3.2d. For both the mixtures, the ratio decreases with X_w. The ratio is always larger for The TFE-water than EtOH-water mixtures due to the lack of H-bonding acceptability for the TFE system in the ES.

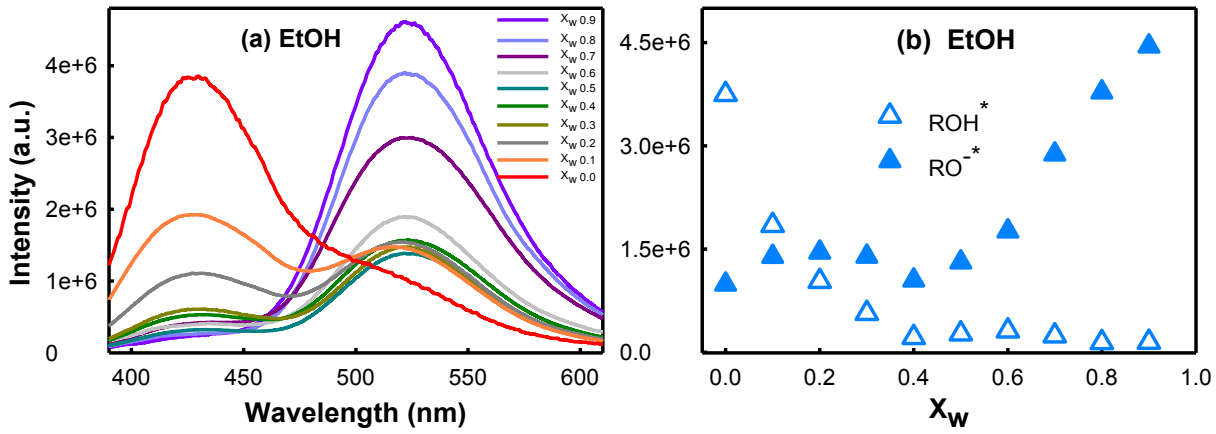

Figure 6.3.3: Steady-state emission spectra of D-luciferin (λ_{ex} = 350 nm) for (a) EtOH-water and (b) variation of steady-state maximum individual intensity for both forms ROH^* and RO^{-*} at different X_w.

Quantum yield (QY) measurement:

In figures 6.3.4, we plot the variation of total fluorescence quantum yield (Φ_T) as well as quantum yields of ROH^* (Φ_{ROH^*}) and RO^{-*} ($\Phi_{RO^{-*}}$) as a function of X_w. The values for the pure solvents are comparable with previous reports.[6] TFE–water mixtures show extremely weak emission of RO^{-*} in the low water concentration range (X_w~0 to 0.6). This is a direct consequence of the low basicity or poor H-bond accepting ability of TFE. However, as the water content is further increased beyond X_w =0.6, the intensity of emission from RO^{-*} sharply increases. On the other hand, in the case of EtOH–water mixed solvents, the emission quantum yields due to RO^{-*} remains more or less constant ($\Phi_{RO^{-*}}$~0.21±0.05) up to X_w =0.6 and after that, it increases sharply. Interestingly the ROH^* quantum yield quenches to zero around X_w ~0.4. The $\phi_{RO^{-*}}$ value for EtOH-water mixtures is always greater than the TFE-water mixtures, which signifies a stabilization of RO^{-*} species in the EtOH-water mixtures through H-bonding. TFE is hydrophobic than EtOH due to the presence of high electronegative fluorine (F) atoms. It is also to remember here is that the -OH group of TFE has a lower electron-donating ability than EtOH.[10] Thus, the affinity towards water is always greater for EtOH than TFE. The total fluorescence yield of D-luciferin is quenched strongly as the water concentration is increased up to about X_w = 0.6 because no increase in emission intensity due to the RO^{-*} species is observed in spite of an observed quenching of ROH^* emission. This suggests that, if the ESPT process is responsible for quenching of ROH^*

species, very efficient quenching of RO^{-*} via reverse PT process leading to a population of a non-fluorescent excited-state or the ground state of ROH.

In figure 6.3.4 (c and d), we have shown the Stern–Volmer (S-V) plots for fluorescence (quantum yield of ROH^{*}) quenching vs concentration of water in the two mixed solvents. The S-V plots show a distinct behavior for low and high-water concentration regions where the variation of the quantum yield produces two distinct slopes with water content. The slop of the S-V plot is associated with the diffusion-controlled rates in the mixed solvent. This breakpoint appears at X_w = 0.4 and 0.3 in the cases of TFE–water and EtOH–water mixed solvents, respectively. In the concentration range above the breaking point, the fluorescence quenching rate is significantly increased in both these solvents. The appearance of the breakpoint in the S-V plots suggests a sudden change in the microscopic structures of the alcoholic solvents beyond a particular water concentration in these mixed solvents.

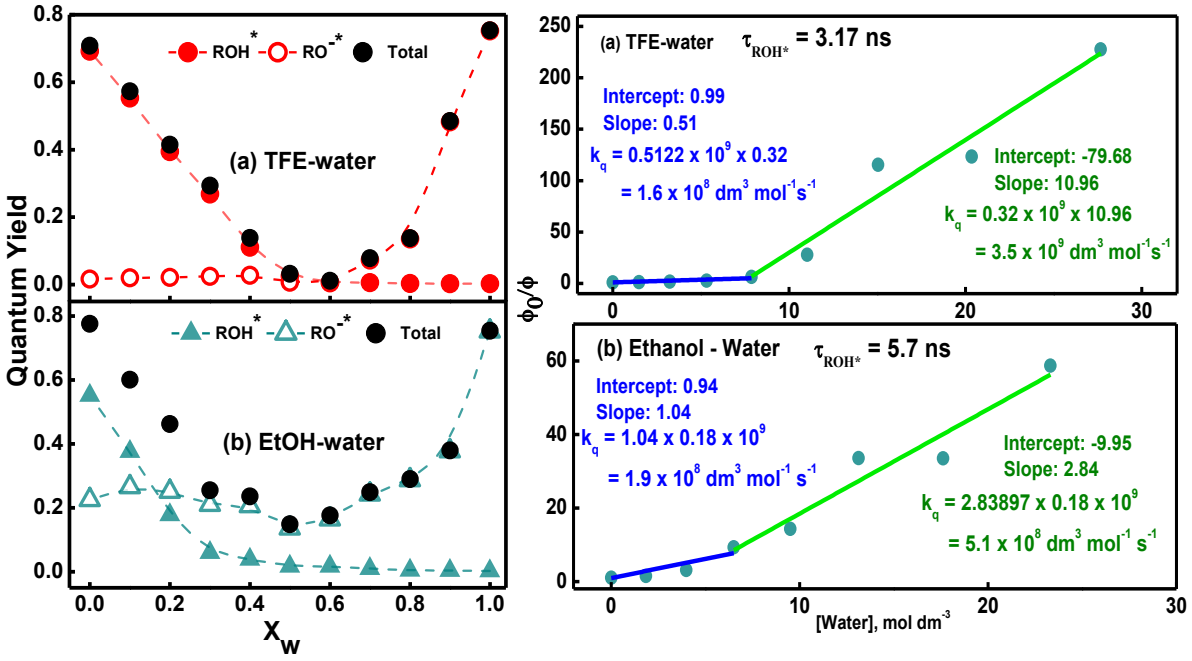

Figure 6.3.4: The fluorescence quantum yield of D-Luciferin (including the quantum yield of ROH^{*} and RO^{-*} forms) as a function of mole fraction of water inside both binary compositions (a) TFE-water & (b) EtOH-water respectively (the dotted lines are guided to the eyes.). Stern–Volmer plot for quenching of ROH^{*} fluorescence by water molecules in TFE–Water (c) and EtOH–water (d) mixed solvents.

Time-resolved emission study:

To determine the emission kinetics associated with the ESPT process, we monitor the fluorescence transients separately for ROH^{*} (at 420 nm for EtOH-water and 440 nm for The TFE-water mixtures) and RO^{-*} species (at 530 nm for both the mixtures) of D-luciferin. In

figure 6.3.5 (a & b), we provide representative emission transient decays of ROH^* and RO^{-*} for The TFE-water mixtures (for EtOH-water mixtures the decays are given in figure 6.3.6). With increasing water content (X_w) in EtOH-water mixtures, the transient decay profiles for ROH^* form drops down whereas the decay profiles for RO^{-*} form develops (see figure 6.3.6). For The TFE-water mixtures the changes are somehow random with X_w (see figure 6.3.5a, b). The transient decay profiles for both ROH^* and RO^{-*} species are fitted with a bi-exponential decay function.[6] For both the mixtures we found two distinct fluorescence lifetimes for both ROH^* and RO^{-*}forms of D-luciferin. For the protonated species (ROH^*) we found a faster timescale ~80-250 ps (for EtOH) and ~150-500 ps (for TFE) whereas for the deprotonated species the faster time component is ~400-700 ps (for EtOH) and ~600 ps-1.3 ns (for TFE). The slower components are very much similar for both the species in both the solutions. The fitted parameters (see table 6.3.2) match with the previous reports.[38] The contribution of faster decay component of the protonated species signifies PT in ES.[25] A larger contribution of the faster time scale (τ_1) for the protonated species (>90%) for all X_w indicates a favorable ESPT process in EtOH-water mixtures (Figure 6.3.5c). The faster time contributions for The TFE-water are around ~60-80%. The faint slower time component also arises (<5% for EtOH-water mixtures and 20-40% for The TFE-water mixtures) due to the different H-bonding ability of the mixtures. Similarly, for RO^{-*} species also we observe two timescales for both the mixtures evolving from the differently H-bonded environment of D-luciferin molecules. We also found that the contribution of the faster component decreases while the contribution for the slower timescale increases with X_w. However, for The TFE-water mixtures, we found a very low contribution for the faster component and a large influence for the retarded component. This is due to the different types of the H-bond donor-acceptor ability and the existence of different types of water-cosolutes clusters formed in the mixtures. These inter and intramolecular H-bonded clusters introduce the micro-heterogeneity in the solutions. An earlier study has shown that both protonated and the deprotonated emission transients are bi-exponential and it can be interpreted by assuming bimodal distribution function.[39] They have also proposed that one fraction can undergo ESPT, where probe located in the hydrated region and the other fraction cannot undergo ESPT due to the lack of water interfaces. Recently, Sahu and coworkers have shown a single step deprotonation scheme concerning without any intermediate step can explain the experimental ESPT dynamics qualitatively.[39] The concentration of ROH^* form at any time t is given by,

$$[ROH^*] = [ROH^*]_{0,Y} e^{-\left(\frac{1}{\tau_{ROH^*}} + \frac{1}{\tau_{RO^{-*}}}\right)t} + [ROH^*]_{0,N} e^{-\left(\frac{1}{\tau_{ROH^*}}\right)t} \qquad (6.3.1)$$

where τ_{ROH}^{*} and τ_{RO}^{-*} stands for the time constants for fluorescence emission of protonated and deprotonation form respectively. The subscript Y and N stand for ROH molecules that *'do'* and *'do not'* undergo ESPT reaction. We fit the ROH^{*} decay transients using equation 6.3.1 for both systems. We plot the relative population of D-luciferin undergoing ESPT reaction (Figure 6.3.5d) and found a larger value for EtOH-water mixtures as compared to The TFE-water mixtures. The contributions as calculated from the decay transient and from the bimodal fitting by equation 6.3.1 follow a similar trend.[25] For EtOH-water mixtures the PT contribution is higher than The TFE-water mixtures. For The TFE-water PT favors in the water-rich region. Such conclusion also reflects from the estimation of the *n* value also (see below).

ESPT is a very fast process in neat water (~25-30ps) at room temperature.[7, 14] Yet the population of the protonated species even at several nanoseconds is due to the recombination process. The rate of this recombination process depends on proton transport in the solution as well as on the kinetics of the back reaction. Earlier studies infer about a phenomenon known as "*geminate recombination*" (GR), which corresponds to reversible recombination of the solvated proton (H^{+}) and the RO^{-*} anion. This can reforms the excited ROH^{*} with a certain rate constant (K_{GR}).[18, 40] According to Huppert and co-workers, an ESPT dynamics connects an intermediate ion-pair formation followed by the formation of the deprotonated species via contact ion-pair dissociation.[41] GR process depends on several parameters like forwarding (K_{BT}) and backward rates (K_{GR}), pair isolated (K_{PI}), radiative rate constants (K_r) and on the populations of ROH^{*}, RO^{-*}species.[18] The RO^{-*} species involved in the irreversible processes is strongly affected by the presence of excess protons in the solutions. The recombination of the dissociated proton with the RO^{-*} base following a diffusive motion ($\sim t^{-n/2}$ power-law),[4, 42, 43] where *n* is the dimensionality of the relevance of the problem. The ideal value of *n* is 3 (three-dimensional) for a pure water system. Thus, at a long time the fluorescence intensity, I(t), of the protonated form of D-Luciferin in different binary mixtures can be written as,

$$I(t) \propto t^{\frac{-n}{2}} e^{\frac{-t}{\tau_{ROH^*}}} \qquad (6.3.2)$$

We fit the ROH^{*} decay transients from 100 ps to 5 ns using equation 6.3.2 for a fixed τ_{ROH}^{*} (fluorescence lifetime of ROH^{*}) value (Figure 6.3.5, e & f). Two representative fittings (at X_w = 0.5) for both the EtOH and TFE are provided in figure 6.3.5e. In figure 6.3.5f the estimated values of *n* are plotted with X_w. It can be noted here that the power-law dependency originates from the deprotonation, protons diffusion and its possible recombination.[4] Decay

tails follow power-laws with various *n* values (Figure 6.3.5f).[44] The value of "*n*" depends on several factors such as proton diffusion, its recombination and the activation energy, etc.

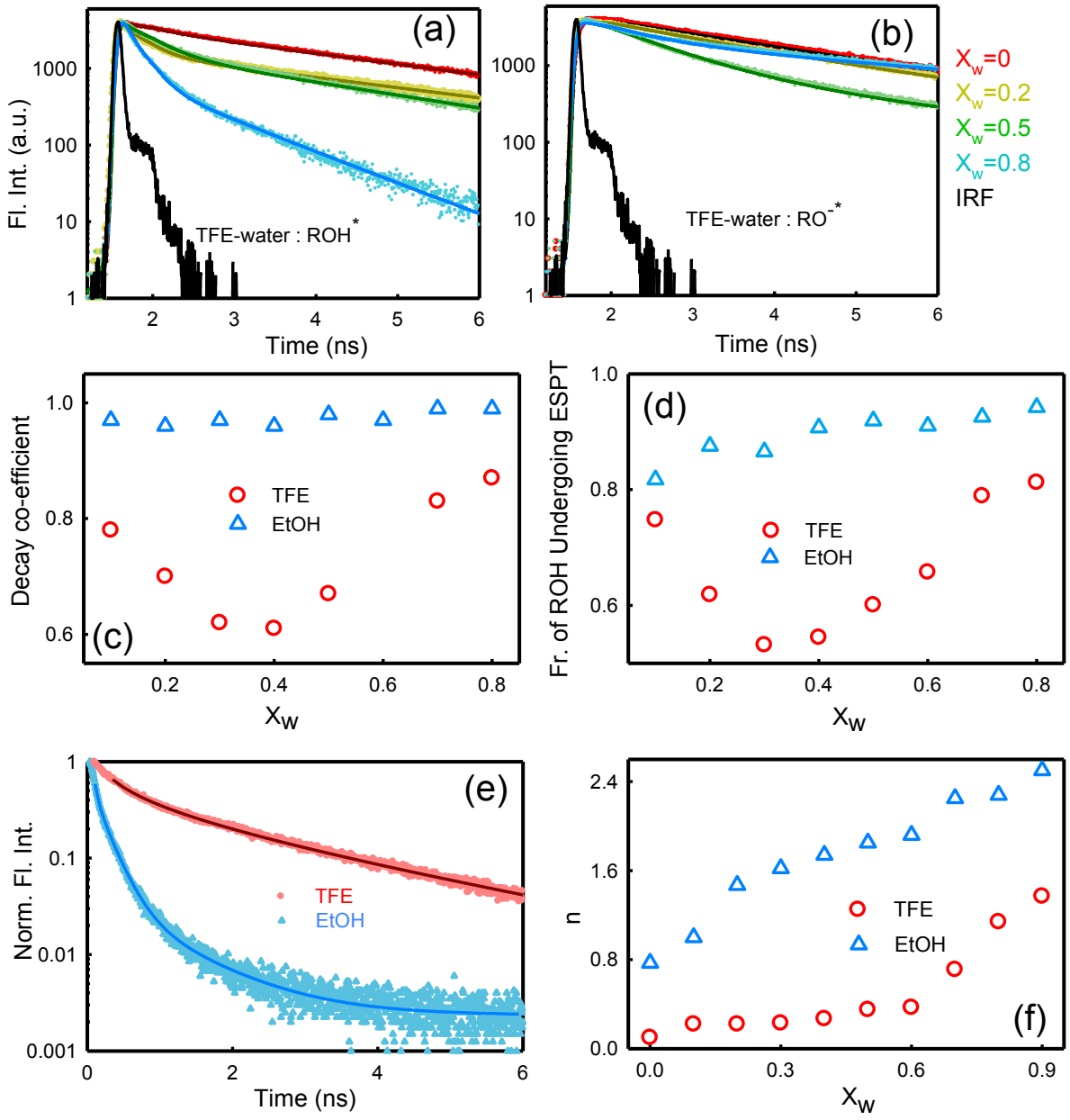

Figure 6.3.5: Representative plot of D-luciferin in the TFE-water binary compositions (a & b) the fluorescence transients of the protonated (λ_{em} = 420 nm) and deprotonated (λ_{em} = 530 nm) forms (λ_{ex} = 375 nm) in a logarithm scale, (c) The fluorescence decay coefficient of the faster component of the protonated form, (d) Fraction of D-luciferin molecules undergoing the ESPT reaction, (e) The time-dependent fluorescence intensity of protonated form in different binary compositions at X_W~0.5. The solid lines represent the best fit to the $t^{\frac{-n}{2}}\, e^{\frac{-t}{\tau_{ROH^*}}}$ function. (f) Values of n obtained for the different binary mixture as a function of mole fraction of water.

The *n*-value is found to be larger for EtOH-water mixtures than The TFE-water (Figure 6.3.5f) indicating faster ESPT processes through the over-populated H-bonded network in EtOH-water mixtures. Due to the presence of a strong electronegative fluorine atom, TFE can form a strong intermolecular H-bond with another TFE molecule and/or with water molecules. For The TFE-water mixtures in the low X_w region (X_w ~0-0.6), n bears a very low value which favors the recombination processes. RO^{-*} species are not stable in this region. However, in a large X_w region, the solution evolves with water-water H-bonded connectivity, which accelerates the ESPT rate (*n* value increases).

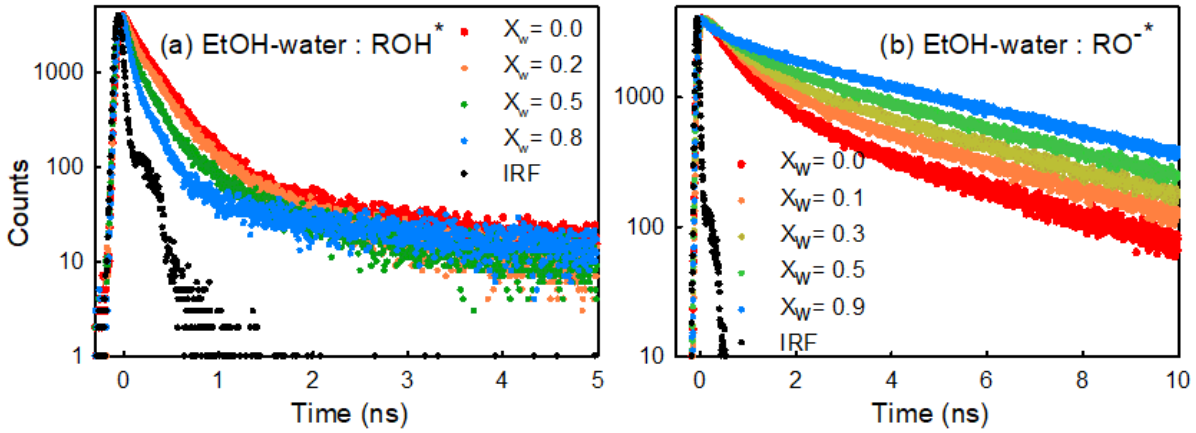

Figure 6.3.6: Fluorescence transients of the (a) protonated (λ_{em} = 420 nm) and (b) deprotonated (λ_{em} = 530 nm) forms of D-luciferin in EtOH-H_2O binary mixtures at a different mole fraction of water (λ_{ex} = 375 nm) in a logarithm scale.

Radiative/non-radiative decay constant:

We calculate average fluorescence life time(τ_{avr}).[6, 18] For ROH^* form in pure TFE, τ_{avr} shows a retarded dynamics (~1.4 ns) than that of pure EtOH (~250 ps). With increasing X_w, τ_{avr} of the ROH^* form decreases for both the mixtures. From this τ_{avr} value of ROH^* form and RO^{-*} form, we compute the radiative (K_r) and non-radiative (K_{nr}) rate constants for both the species[6] (see table 6.3.3) using the following equations,

$$K_r = \emptyset_{ROH^*/RO^{-*}} \Big/ < \tau >_{ROH^*/RO^{-*}} \qquad (6.3.3)$$

$$K_{nr} = (1 - \emptyset_{ROH^*/RO^{-*}}) \Big/ < \tau >_{ROH^*/RO^{-*}} \qquad (6.3.4)$$

where, $\emptyset_{ROH^*/RO^{-*}}$ is the fluorescence quantum yield and $< \tau >_{ROH^*/RO^{-*}}$ is the average fluorescence lifetime of the neutral/deprotonated species of D-luciferin respectively. The fluorescence lifetimes can directly provide the decay rate constants ($K_{ROH^*} = \tau^{-1}_{ROH^*}$, $K_{RO^{-*}} =$

$\tau_{RO^{-*}}^{-1}$) for the ES photoacids. The value of K_r and K_{nr} (for ROH^* species) are plotted in figure 6.3.7. K_r value decreases with X_w for both the mixtures. The K_r value for EtOH-water mixtures is larger than The TFE-water mixtures, whereas K_{nr} value gradually increases with X_w for EtOH-water mixtures. For The TFE-water mixtures, it remains almost constant up to X_w 0.6 and then increases linearly. This infers that the ESPT process enhance with X_w.[8] The larger value of K_{nr} in EtOH-water than that of The TFE-water mixtures indicates a contrasting H-bonding ability of these two mixtures.[6, 8] We also calculate K_r and K_{nr} value for RO^{-*} form of D-luciferin (see table 6.3.3). K_r value of EtOH-water mixtures increases whereas it decreases for The TFE-water mixtures with X_w. K_{nr} value of EtOH-water remains almost constant while for The TFE-water it increases beyond X_w ~0.6.

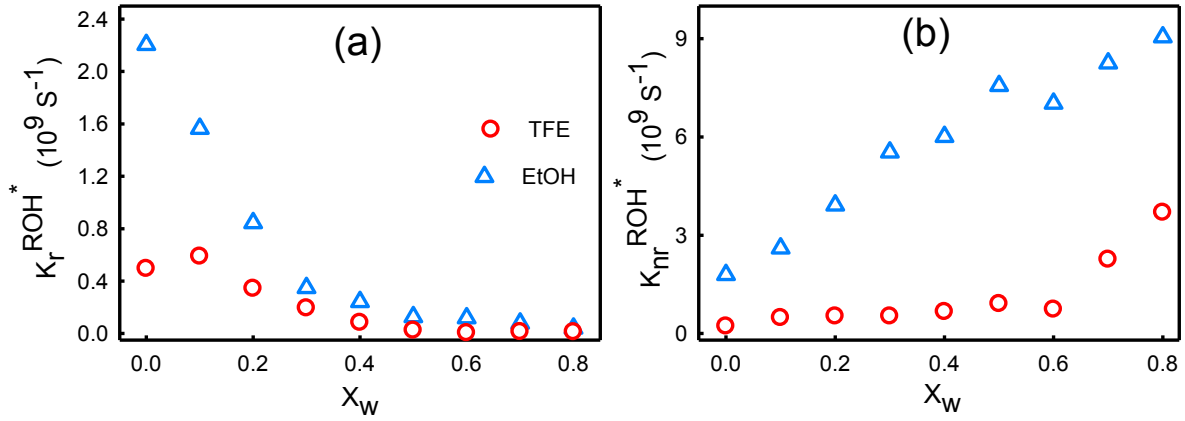

Figure 6.3.7: The variance plot of (a) radiative (K_r) and (b) non-radiative (K_{nr}) decay constant of ROH^* form of D-luciferin as a function of mole fraction of water inside both binary compositions.

PT quantum yield:

We further calculate the PT quantum yield ($\emptyset_{PT}$) (see figure 6.3.10e) according to the following equation,[7, 11]

$$\emptyset_{PT} = \frac{\frac{I_{RO^{-*}}}{ROH^*} * K_{ROH^*}}{K_r + K_{nr} + (\frac{I_{RO^{-*}}}{ROH^*} * K_{ROH^*})} \qquad (6.3.5)$$

The parameters are described previously. For pure water, we found a higher $\emptyset_{PT}$ value (>0.9), similar findings are reported by Huppert et. al.[7] The PT quantum yield of D-luciferin for EtOH-water mixtures is higher than The TFE-water mixtures. For The TFE-water mixtures, the value remains constant in the low X_w region upto X_w ~0.5 and then increases sharply. This indicates that due to the presence of electronegative fluorine atoms TFE can strongly bind with other water molecules in low $X_w$and hence the water molecules are not available to

capture the protons in the solutions. In high X_w, the H^+ can transfer through the percolating water-water H-bonded network.[10]

ESPT mechanisms and its kinetics (obtained from TRANES analysis):

Fluorescence transient decays at fixed wavelength provide qualitative information about the time scale of the ESPT process. From the emission decays of D-luciferin at various wavelengths, we reconstruct the time-resolved emission spectra (TRES) and time-resolved area-normalized emission spectra (TRANES).[45]

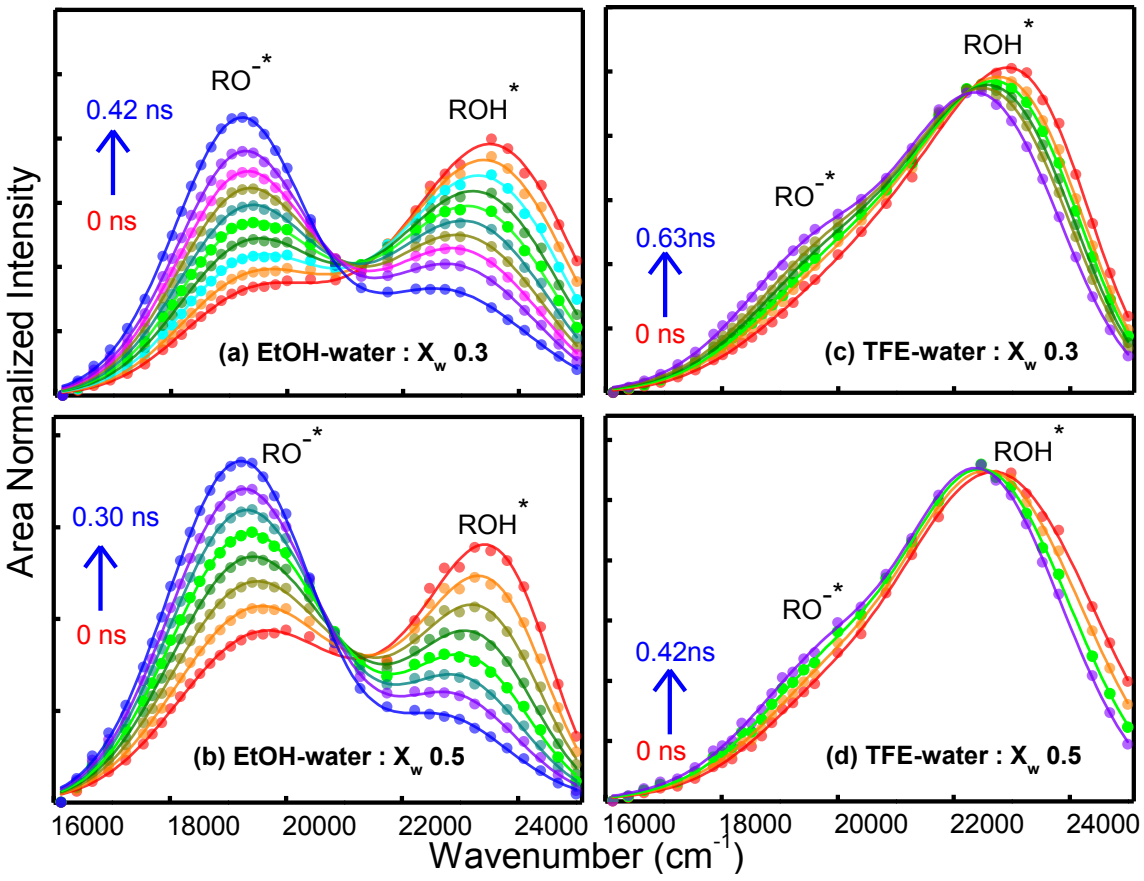

Figure 6.3.8: Bi-lognormal fitting plot of Time-resolved area normalized emission (TRANE) spectra of D-luciferin at different water mole fractions of X_W 0.3 and X_W 0.5.inside (a, b) EtOH-water and (c, d) TFE-water binary compositions.

TRANES shows (see figures 6.3.8 & 6.3.9) two distinct regions for ROH*(peaks ~23255 cm^{-1}) and for RO^{-}* form (peaks ~18868 cm^{-1}) with an iso-emissive point at ~22300 cm^{-1}. These two forms of D-luciferin are kinetically coupled with each other. We fit those TRANES data with a bi-lognormal function[46] (see equation Ch. 2). Due to ESPT, the population of RO^{-*} grows at the expense of ROH* intensity with time, until the intensity ratio reaches its steady-state value.

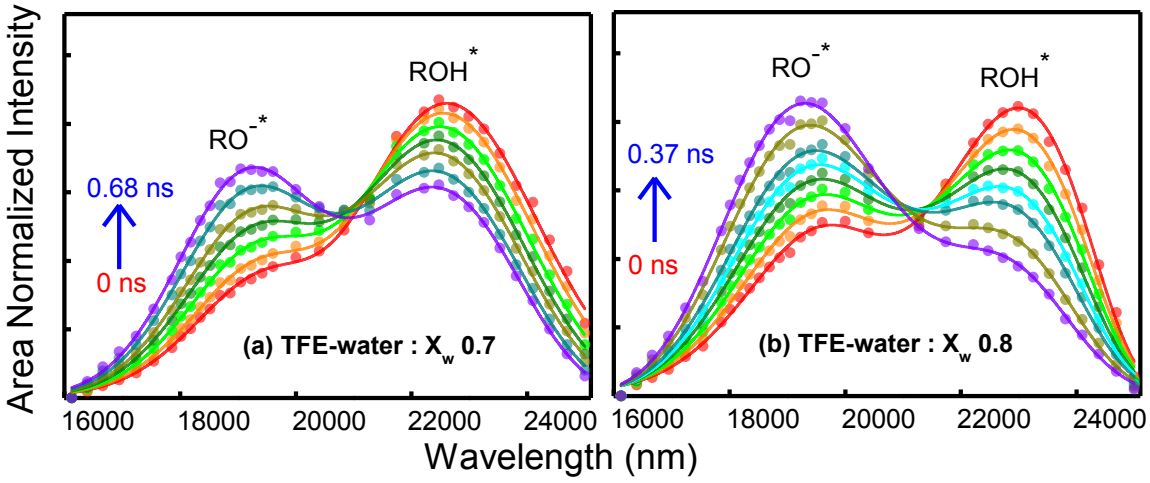

Figure 6.3.9: Bi-lognormal fitting plot of Time-resolved area normalized emission (TRANE) spectra of D-luciferin inside the TFE-water binary composition at two different water mole fractions of (a) X_W 0.7 and (b) X_W 0.8 respectively.

From the intensities ($I_p(t)$ for ROH* and $I_d(t)$ for RO^{-*} species) of the TRANES, we construct the time-dependent correlation function from the following equation.

$$C(t)_{PT}^{RO^{-*}} = \left[\frac{\{I(t)-I(0)\}}{\{I(\infty)-I(0)\}}\right] \qquad (6.3.6)$$

$$C(t)_{PT}^{ROH^{*}} = \left[\frac{\{I(t)-I(\infty)\}}{\{I(0)-I(\infty)\}}\right] \qquad (6.3.7)$$

where, I(0), I(t) and I(∞) are the intensities at time t=0, at an intermediate time "t" and after a long time (when ESPT has completed and intensity become almost the same as of steady-state). The correlation functions [$C(t)_{PT}$] for ROH* and RO^{-*} forms can be fitted with an exponential decay equation for both the binary mixtures.[9] One representative fit plot (for X_w = 0.3) is shown in figure 6.3.10a for the two different mixtures. We found (Figure 6.3.10a (inset)) two different kinetic parameters; a bond tear (BT) of ROH* and a pair isolation (PI) forming of RO^{-*}(Table 6.3.4). For EtOH-water mixtures, the bond tear rate for ROH*(K_{BT}) is 7.69 ns^{-1} and the rate of pair isolated for RO^{-*} (K_{PI}) is 6.67 ns^{-1}, whereas for The TFE-water

mixtures K_{BT} is found to be 6.10 ns^{-1} and K_{PI} is 5.35 ns^{-1} at X_W~0.8, respectively. The unexpected difference between BT rate and PI rate is due to the presence of some geminate recombination process between H^{+*} and RO^{-*} to produces an excited-state ROH^* form, which is related to the "*n*" value that has already been described.

The growth intensity of RO^{-*} reflects the ESPT dynamics.[9] PI generally occurs after bond tear of ROH^* form and formation of RO^{-*} after PI or PT to the solvent. We therefore, have taken the growth intensity with time progress for the determination of the ESPT kinetics parameter from TRANE spectra. Furthermore, we fit the growth time progress with an exponential equation to accrue information on the kinetics parameter (see Table 6.3.4). A representative plot of the time evolution of the PT process for EtOH-water is shown in figure 6.3.10b. The growth intensity increases rapidly with time as we increase the water concentration in the mixtures. The kinetics parameter for the PT process with X_w is shown in figure 6.3.10 (d & f). For EtOH-water mixtures, ESPT gradually accelerates with X_w, whereas, for The TFE-water mixtures we found three regions. In the low X_w region (X_w= 0-0.4) ESPT decreases with X_w and then it changes moderately up to X_w~0.7. Further addition of water accelerates ESPT. For both the systems, beyond X_W~ 0.4, H_{EA}--O_{EA} (hydrogen-oxygen of EtOH) interactions become saturated whereas H_{EA}---O_{HO} (HO refers to hydrogen oxide) interaction gradually increases due to interactions of alcohol –OH groups with water molecules. At low X_w region (X_W~0-0.4), due to the lack of electron-donating ability of hydroxyl oxygen atom of TFE, H_{FA}---O_{FA} (FA refers fluorinated alcohol) interaction overwhelms H_{EA}---O_{EA} interaction. On the other hand, due to more electron acceptability of the hydroxyl oxygen-hydrogen atom of TFE, H_{FA}---O_{FA} interaction is more rather than H_{EA}---O_{EA} interaction. It is to note here that the coordination number of EtOH is larger than TFE. EtOH molecules have a stronger H-bonding ability than TFE molecules at high X_w.

Effect of Solvation Dynamics on ESPT:

A comprehensive understanding of the solvation dynamics is obtained from time-resolved fluorescence studies of D-luciferin with selective excitation at 375 nm. In the blue end of the spectrum, the decay transients of D-luciferin could be fitted with multiple decay components whereas in the red end it could be fitted only by considering an extra rise component. We construct the solvation correlation function following equation (Ch. 2, equation 2.21).[47] Some representative plots for both the mixtures at X_w 0.3 and X_w~0.8 are shown in figure 6.3.10c. All the curves follow a single-exponential decay, and the time

constants are presented in table 6.3.4. We observe that the time constants are in the order of hundreds of ps. Selective photo-excitation of interfacial probe molecules coupled with the limitation of our instrumental resolution (IRF~80 ps) refrained us from detecting the signals responsible for the ultrafast dynamics of bulk water molecules. For both the mixtures, solvation dynamics at high X_w are found to be much faster as compared to that in low X_w. This is because pure water pool remains undetected due to its ultrafast nature, however, before X_w~0.8 it reveals slower solvation dynamics.[9] We found that with increasing X_w, solvation dynamics get faster for both the mixtures (Figure 6.3.10, d & f). It could also be noted that a significant part of solvation arises due to the fast-moving bulk-like water molecules, which is missing because the present experimental technique is limited by its IRF values. Thus, the probed solvation properties are broadly due to the bound water molecules (with different strengths of H-bonding interactions) present in the mixtures. Continuous H-bond network and a direct access of hydroxyl (OH) group of D-luciferin to the surrounded water molecules are the basic for enabling an effective ESPT process.

The relaxation time constant is broadly related to diffusional motion. Relaxation dynamics also gradually accelerates with increasing X_w due to preferential water-water H-bonding with the deficiency of interaction between alcohols and water molecules. It has been revealed[26] that the occurrence of photo-protolytic processes i.e. the anionic and neutral species of D-luciferin may form complexes by specific H-bonding interaction inside different solvent clusters. It is expected that with X_w the H-bond interaction i.e. the stability of D-luciferin at interface decreases and the probe molecule moves from the cluster to the polar core of solvent for the stabilization of excited species in water pool. The single exponent fitting indicates that the probe molecule prefers to exist in the bulk water pool due to less electrostatic interaction between alcohol and the probe. The time scale of ESPT kinetics is closely comparable with the time scale of solvation dynamics of D-luciferin in the two binary mixtures which signifies that the ESPT process starts before the ending of solvation. Even in the case of the slowest solvation which means the solvation dynamics is completed at a much faster time scale as compared to the fastest component of ESPT kinetics (Tables 6.3.4). The PT process is significantly affected by the nature of the H-bond of water molecules with another water and/or with the probe molecules. Ghosh et al. have reported that an iso-emissive point in TRANE spectra of D-luciferin when the time scale of solvation and ESPT kinetics becomes comparable.[9]

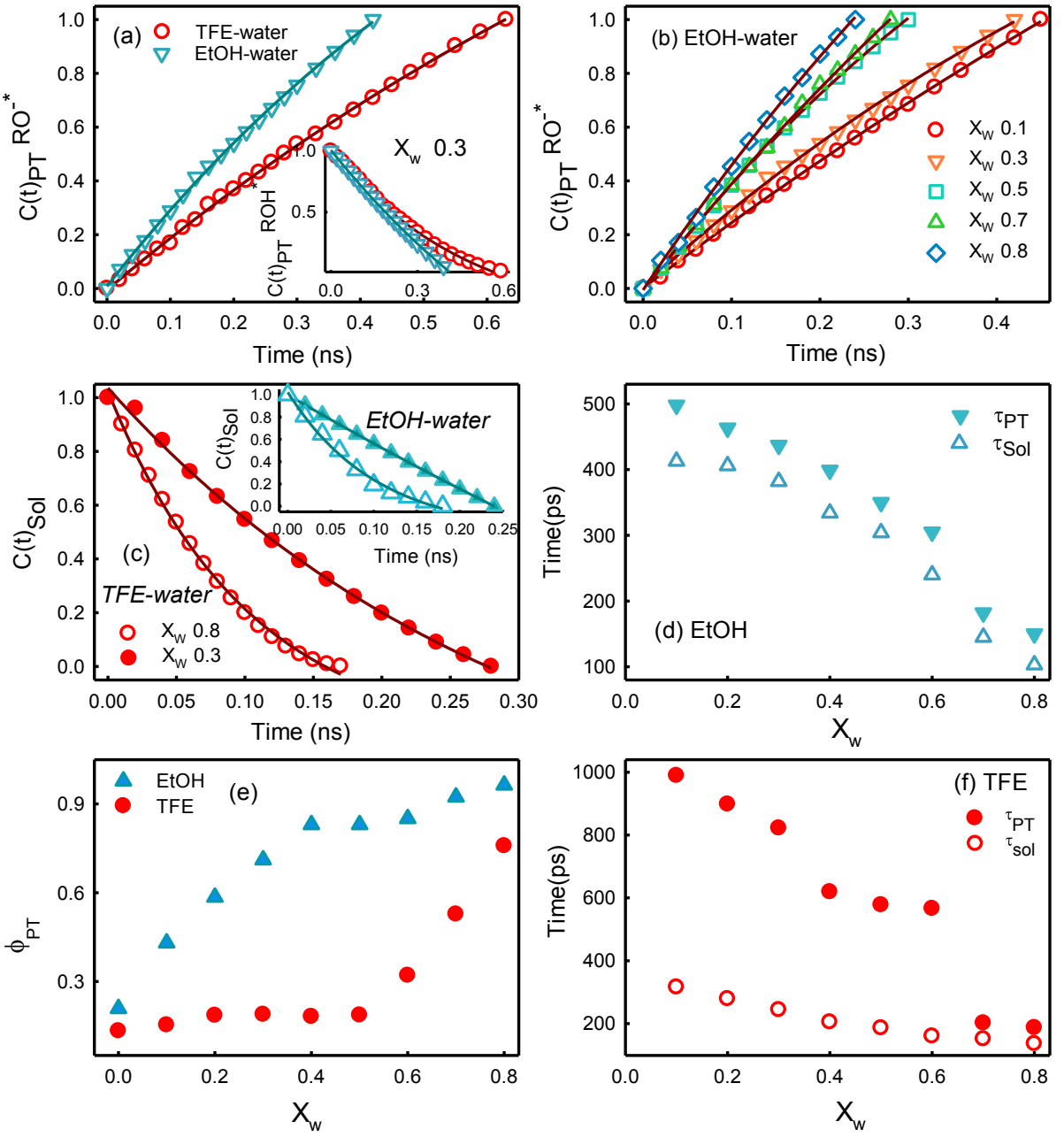

Figure 6.3.10: (a) Time development of ESPT correlation function $C(t)_{PT}$ for RO^{-*} population inside two different binary compositions at X_W 0.3 (insert graph are ROH^* population at the same system and as well as same X_W), (b) The $C(t)_{PT}$ for RO^{-*} population of EtOH-water at different X_W (solid dark red lines are representing the mono-exponential decay and growth fittings to the experimental $C(t)_{PT}$ vs time curves), (c) The solvent correlation function C(t) of D-luciferin with time progress (the dark red lines represent the best fittings to the experimental data points), (d & f) Representative plot of proton transfer time constant and solvation time constant with the function of X_W in two different binary compositions and (e) Representative plot of proton transfer quantum yield inside two binary mixtures at different X_w.

ESPT occurs in water by several phases (geminate ion-pair formation, recombination, dissociation of ion-pair, etc.) (see scheme 6.3.1).[48] Solvation dynamics in The TFE-water binary composition is found even a bit faster than EtOH-water mixtures. The solvation dynamics and ESPT kinetics both are comparable within hundreds of ps for all X_w for EtOH-

water mixtures, while in TFE-water such kind of behavior is found beyond X_w~0.7. Up to X_w~0.6, the solvation shows faster dynamics than ESPT kinetics for The TFE-water mixtures (solvation trigger the ESPT process). After X_w =0.8 (for both the mixtures), solvation and ESPT kinetics are faster than the instrument response (IRF value ~80 ps). However, the absence of an iso-emissive point indicates the presence of an intermediate form of photoacid during the ESPT process. It is to note here that the energy state changes in solvation processes whereas it remains constant during the ESPT process. Again, an iso-emissive point is expected to be observed when individual energy states are not changing with time during ESPT. The presence of an iso-emissive point is not only indicative of two emission species, it also evidence that ESPT process occurs after the completion of solvation.[9] Previous reports suggest that the time difference between solvation dynamics and ESPT kinetics is ~150 ps, which is the limiting condition for finding an iso-emissive point in TRANES. We observe that the solvation process was completed much before the initiation of the ESPT process for The TFE-water system (at least up to X_w~0.6). For the EtOH-water system (for all X_w) and The TFE-water mixtures (after X_w~0.7) solvation is occurring simultaneously with the ESPT. In TRANES, the emergence of an iso-emissive point during ESPT indicates that solvation dynamics is not occurring during the ESPT process (Figure 6.3.8 and 6.3.9).

6.4. Summary

ESPT mechanisms of D-luciferin inside two different binary mixtures with different water mole fractions (X_w) have been studied here. The main motivation is to probe the nature of the micro-heterogeneous environment as provided by the alcohol molecules in the H-bonded water network using the ESPT process as a tool. We choose two simple alcohol molecules (EtOH and TFE) with comparable sizes but with different H-bond affinity and hydrophobicity. EtOH is a protic solvent that can act as both H-bond donor and acceptor whereas on the other side TFE molecules are comparably less polar and do not have H-bond accepting ability due to the presence of electronegative halide fluorine (F) atom. ESPT, mainly mediated through water networks, is mostly prohibited in alcohol reach mixtures.[7, 18, 25] We found that the ESPT rate is slightly faster in EtOH/water mixtures than TFE/water.[18] TFE provides more hydrophobic interfaces towards water as compared to EtOH which leads to a smaller diffusion coefficient and larger geminate recombination rate in The TFE-water mixtures.

Inadequacy of a single physical solvent parameter, such as dielectric constant or H-bonding ability, to describe the effect of solvent on the absorption and emission characteristics of a solute molecule has been realized time to time. This led Kamlet and Taft to introduce the so-called empirical solvent polarity parameters, such as H-bond donating (α), accepting (β) ability, and dipolarity parameter (π^*) to describe its ability to register dispersion, dipole/dipole, H-bond, and other possible intermolecular interactions with the solute and hence the response of a solvent to the chemical structure and properties of the probe molecule in solution.[49] In a similar manner, three important parameters of the solvents, which may affect the yields and rates of PT processes, have been defined by Catalan as the solvent acidity (SA) or proton donating ability, solvent basicity (SB), or proton accepting ability and the polarity parameter of the medium (SPP).[50] See table 6.3.1 for the Kamlet – Taft and Catalan's parameters for three solvents used here. Because of widely different values of these three parameters of those solvents used here, the extent of perturbation of the electronic structure of ROH through solvent interaction is expected to be quite significant in neat solvents and this effect has been reflected in the values of the extinction coefficient of absorption of D-luciferin in these solvents. Based on the results of investigations on the physicochemical properties of The TFE-water mixed solvents, it has been proposed that TFE and water molecules are heterogeneously mixed with each other at the molecular level. In this mixed solvent system, none of these properties shows an ideal behavior. While the solvent basicity of this mixed solvent shows positive deviations from ideal behavior through the entire solvent composition, X_w = 0 to 1, both solvent acidity and dipolarity show negative deviations.[51] Their results reveal that SA or SB parameter shows only a very minor change in the range of X_w=0-0.5 and remain very similar to that of neat TFE solvent. However, as the X_w value changes in the range of 0.5 to 0.8, both these parameters increase very sharply. With further increase in the X_w value, SB decreases sharply but SA continues to increase to achieve the value of neat water.

We find a nice correlation between the variations of the absorption coefficient of D-luciferin in The TFE-water mixed solvents with X_w (Figure 6.3.1) and that of solvent basicity with X_w, except that in the region where X_w varies in the range 0.8 – 1.0, where we find only a slow increase of absorption coefficient instead of a sharp decrease. However, in the case, EtOH–water mixed solvent system, this correlation is surprisingly in good agreement and this suggests that the SA and SB properties follow a similar trend with the variation of X_w in both the TFE–water and ethanol-water mixed solvent systems. The discussion below on the

variation of emission properties as well as then PT properties on the composition of the solvent mixtures follow a similar trend in both the solvent systems.

It was proposed that the interaction between the hydroxyl group of EtOH (H_{EA}--O_{EA}) coordination number moderately increases and then linearly increases beyond X_w~0.4 and again changes the interaction between the hydroxyl group of EtOH and oxygen group of water or hydrogen oxide (H_{EA}—O_{HO}) coordination number with decreasing water contains.[10] On the other hand, the solute-solvent interactions of EtOH (H_{EA}---O_{HO}) gradually decreases with increasing X_w due to the more acidic character of hydroxyl hydrogen of water rather than EtOH. For The TFE-water mixtures, these two interactions (H_{EA}--O_{EA} and H_{EA}---O_{HO}) are comparable due to its different H-bond donating and accepting ability. We observe that the steady-state intensity (Figure 6.3.2) of both forms are suppressed and more or less the same in the region of X_w ~(0.4 - 0.7). This indicates that the water-TFE interactions and the number of both the forms (ROH^* and RO^{-*}) are the same. However, for EtOH solvent such behavior is vague. The electron donicity and acceptability for water and EtOH are comparable while for TFE it is different. After X_W~0.5, TFE hydroxyl H-atom can act as the electron stoichiometry (1:1 H-bond between TFE and water molecules).[10] We also found that the intensity ratio linearly decreases beyond X_W~0.5 for the TFE-water mixtures but RO^{-*} formation is very less before X_w~0.5 and then after (X_w~0.5) with addition of water it increases due to the hydration of the protons. It is also to note that the H-bond accepting ability of polar water molecules is larger than hydrophobic TFE molecules. The ratio of ROH^*/RO^{-*} in EtOH-water mixtures are always less than The TFE-water mixtures and ratio become almost constant from X_w~0.2 to ~0.5 due to the polarity and different types of H-bonding interaction. The solute-solvent interactions is higher in TFE than in EtOH (O_{HO}---H_{FA} > O_{HO}---H_{EA}) due to more acidic hydroxyl hydrogen is more H-bond acceptability of TFE system and also the O_{EA}---H_{HO} interaction is greater than O_{FA}---H_{HO} interactions due to electron deficiency of hydroxyl oxygen for the presence of high electronegative fluorine atom of TFE system. For a better understanding of the photophysical properties of D-luciferin in these mixed solvents, it is important to know how the microscopic structure of the solvent medium changes with variation of water content in the medium. From the large-angle X-ray and neutron diffraction as well as NMR studies of the solvent mixtures, it has been proposed that both TFE and water clusters, which are responsible for the micro-heterogeneity of the solvent medium, coexist in the TFE-water mixtures.[51] This micro-heterogeneity is most enhanced in the TFE-water mixtures at X_w ~ 0.85. In the range of X_w> 0.85 the tetrahedral-

like structure of water predominates in the TFE-water mixtures and TFE monomers may be hydrated in the water clusters. In the range of X_w = 0 - 0.3, the inherent TFE structure is dominant. When the water content increases (i.e. X_w> 0.3), the tetrahedral-like structure of water gradually start evolving in the mixtures. The structural transition point for the ethanol-water mixture is X_w= 0.8.[15-17] above which (i.e. X_w >0.8) tetrahedral water structure predominates. In the ethanol-water mixed solvents with $X_w \leq 0.6$, the formation of clathrate-like structures of ethanol molecules has been predicted.

The lower transition point in The TFE-water is due to the larger CF_3 group of TFE molecule than the CH_3 group of ethanol one, i.e., the tetrahedral-like structure of water is quickly disrupted by the addition of TFE to water. Below the structural transition point (X_w< 0.85), TFE molecules form their clusters in the TFE-water mixtures. Here, a driving force of the clustering may be the hydrophobic interaction among the CF_3 groups rather than H-bonding between TFE molecules because of the weak H-bond acceptor (low electron-donicity) of the hydroxyl group due to the strong electron-drawing of F atoms. For the same reason, TFE molecules cannot be strongly H-bonded with water molecules. On the other hand, the ethanol molecule can be easily H-bonded with other ethanol molecules and water due to the suitable abilities for the H-bond acceptor and donor ability of the hydroxyl group. Thus, the micro-heterogeneity of the TFE-water mixtures is more significant than that for ethanol-water mixtures. The weaker intermolecular interactions between TFE molecules than ethanol ones influence the dynamics of TFE molecules in the TFE-water mixtures. The motions of TFE molecules in TFE clusters gradually become free with increasing water content, while those of ethanol molecules in ethanol clusters are retarded with increasing water content probably because ethanol clusters are strengthened by the hydration of water molecules.

With the above knowledge about the structure and properties of the neat solvents and solvent mixtures, we now try to explain the solvent dependence of the fluorescence emission and PT properties of D-luciferin. In the alcoholic solvents, we could find a good correlation between the proton accepting ability or SB parameter of the solvents with the quantum yield values of ROH^* and RO^{-*} species. For example, weaker solvent basicity or proton acceptability of TFE as compared to that of ethanol (Table 6.3.1) is the reason for a larger quantum yield of ROH^* in TFE. On the other hand, the larger solvent acidity or proton donating ability of TFE solvent is the responsible factor for a larger quantum yield of RO^{-*}.

This explanation becomes quite obvious from the fact that the ESPT reaction occurs at the phenolic OH site by acceptance of a proton by the solvent but the probability of geminate recombination of the RO^{-*} species leading to populate back the ground state of D-luciferin molecule depending on the ability of the solvent to donate a proton to the imidazole nitrogen atom. Absence of emission due to RO^{-*} following photo-excitation of D-luciferin in neat TFE suggests the possibility of either of the absence of ESPT reaction in the excited-state in this solvent or very fast geminate recombination of the deprotonated form with a proton leading to negligible emission quantum yield of RO^{-*} species. In spite of the lowest solvent basicity and the largest solvent acidity of water, the quantum yield of ROH^* is nearly negligible and that of RO^{-*} species is the largest among the solvent media. It is possible that apart from solvent acidity and basicity parameters, the solvent structure also plays an important role in the PT dynamics.

The ROH^* QY of both TFE/water and EtOH/water decreases monotonically up to X_W~0.4 and then becomes more or less the same for both the systems. Before X_w~0.4 the QY value of TFE solvent is higher due to the stability of ROH^* species in the solvent. The QY of RO^{-*} form in the TFE-water, X_W~0.4-0.7 region is almost constant since the water-water and TFE-TFE cluster formations are almost the same.[18] We found the steady-state intensity for both forms are the same and they quench significantly. In the case of mixed solvents, both the acidity and basicity parameters of both the mixed solvent systems remain very similar in the range X_w = 0-0.6 and we observe that the emission yield of RO^{-*} species does not change significantly. In the case of the TFE-water mixed solvents, we observe negligible emission from RO^{-*} species because of the very weak solvent basicity of the solvent mixture. While in the ethanol-water mixed solvents, $\phi^*_{RO^-}$= 0.22 ± 0.05 in the solvents with X_w= 0-0.6, in spite of strong quenching of ROH^* species with increasing concentration of water, which acts as an efficient quencher of fluorescence of ROH^* species in the mixed solvents. However, as X_w value in the solvent mixture increases beyond 0.6, $\phi^*_{RO^-}$ increases sharply to attend the value of $\phi^*_{RO^-}$=0.75 as in the case of the neat water. After X_w~0.4, the water molecules might not be available in the network up to X_w~0.7, since they are restricted by the F atom of the fluorinated alcohol through H-bonds. That is why the population of RO^{-*} form is the same due to the lack of hydrated water. After X_w ~0.4 for both mixtures, solute-solute interactions (H_{EA}--O_{EA}) are almost saturated and solute-solvent interactions (H_{EA}---O_{HO}) increase gradually due to the preferential H-bond of water with alcohol –OH groups. At a very low X_w region (X_w ~ 0.0-0.4), H_{FA}---O_{FA} interactions are too steeper than H_{EA}---O_{EA} interactions due

to the lack of electron-donating ability of hydroxyl oxygen atom of TFE. On the other hand, interactions of H_{FA}---O_{FA} are more than H_{EA}---O_{EA} interactions due to more electron acceptability of hydroxyl hydrogen atom and more electron deficiency of hydroxyl oxygen atom of TFE.

The S-V plots for quenching of ROH^* fluorescence by added water molecules in the mixed solvents as presented in figure 6.3.4 provide valuable information regarding the transformation from the inherent domination of TFE cluster structure or clathrate structure of ethanol in mixed solvents beyond X_w= 0.3. From the fluorescence decay transients, we calculate the fraction of D-luciferin molecules that are undergoing ESPT. We found that the contribution for EtOH-water mixtures is larger than The TFE-water mixtures; it linearly grows with X_w (Figure 6.3.5c, d). Surprisingly with increasing X_w the value increase which signifies that the protons diffused more in the solvent with less probability of associate between proton and deprotonated form of D-luciferin (Figure 6.3.5e, f). In EtOH-water ESPT rate is higher as compared to the TFE-water as the higher number of ROH^* is undergoing ESPT and the most easiness to form the charged RO^{-*} species. On the other hand, in The TFE-water mixtures, a lower number of ROH^* undergoing ESPT indicates less diffusion of the proton. It seems that ESPT and solvation usually follow each other.[52,53] Co-ordination number of EtOH is greater than TFE and decreasing trend with decreasing X_w. In high X_w H-bonding of TFE molecules with water, molecules are saturated while EtOH is enhanced. EtOH contains ultra-short time components while for TFE it is too slow. The lifetime for EtOH is found to be very fast than TFE, again proton geminate recombination rate is even larger for TFE rather than EtOH system.[18]

We know ESPT occurs when the deprotonation step speeds up by the stabilisation of H_3O^+ and/or RO^{-*}. Initially, the diffusion of H_3O^+ to the solvent and RO^{-*} stabilisation by solvent molecule through solvation relaxation in the binary mixture in a group assists the progress of ESPT. Additionally, with the increase in water mole fraction the fast solvation relaxation of D-luciferin precedes the ESPT rate. An explanation as discussed earlier that ESPT is mainly controlled by two factors namely the local concentration of water molecules near the photoacid and solvent reorganization.[54,55] From the relaxation dynamics and lifetime data it can be concluded that with an increase in water mole fraction the probe D-luciferin goes to the bulk-like cluster from the alcohol cluster. A recent study has been shown TRANES analysis for the accurate determination of ESPT time scale in the different reverse

micelle.[9] It has been noted that ESPT of D-luciferin in solvent mixture water-pool does not involve any fluorescent intermediate. If an intermediate were present a single isoemissive point would not have existed in TRANES. Retaining of single isoemissive point in TRANES during the ESPT process with an increase in water content indicates that solvation dynamics do not interfere with the energy states of D-luciferin during the ESPT process (Figure 6.3.8 & 6.3.9). Ghosh and co-workers have shown that how the isoemissive point in TRANES of a two-state ESPT process is lost when solvation dynamics and ESPT are taking place at similar time scales.[9] Therefore, the appearance of a single isoemissive point in TRANES is only possible when energies of the individual emitting states are not changed during the ESPT process which means that ultrafast solvation precedes the slow ESPT process. According to our findings, the solvation and ESPT are happening simultaneously instead of that with adding water inside the EtOH-water system.

Scheme 6.3.1: The ESPT mechanism (K_{BT}, K_{GR}, K_{PI} are the rate constants of bond tear, geminate recombination, and pair isolated processes respectively).

Table 6.3.1: Solvent parameters[36, 37] and emission characteristics of D-luciferin inside of EtOH, TFE and H_2O solution.

Solvent	Catalan's Parameters			Kamlet-Taft Parameters			λ_{max} (Fl)	Quantum Yields (Φ)		
	SA	SB	SPP	α	β	π*		Φ_T	Φ_{ROH*}	Φ_{RO-*}
EtOH	0.400	0.658	0.853	0.86	0.75	0.54	427	0.78	0.56	0.22
TFE	0.893	0.107	0.912	1.51	0.00	0.73	445	0.71	0.68	0.03
Water	1.062	0.025	0.962	1.17	0.47	1.09	462	0.75	0.00	0.75

Table 6.3.2: Fluorescence decay fitting parameters of D-luciferin inside of EtOH-water and TFE-water binary compositions measured at 420 nm (for EtOH-water) and 440 nm (for TFE-water) for ROH^* form and 530 nm for RO^{-*}form at a different mole fraction of water.

X_w	Protonated form (420 nm)			Deprotonated form (530 nm)		
	τ_1 (ns) (a_1)	τ_2 (ns) (a_2)	$<\tau>_{ROH^*}$ (ns)	τ_1 (ns) (a_1)	τ_2 (ns) (a_2)	$<\tau>_{RO^{-*}}$ (ns)
Ethanol-water						
0.00	0.22(0.99)	2.29(0.01)	0.25	0.69(0.82)	4.10(0.18)	1.31
0.10	0.20(0.97)	1.45(0.03)	0.24	0.73(0.75)	4.32(0.25)	1.64
0.20	0.18(0.96)	1.10(0.04)	0.21	0.79(0.70)	4.41(0.30)	1.87
0.30	0.15(0.97)	1.08(0.03)	0.17	0.75(0.66)	4.54(0.34)	2.04
0.40	0.13(0.96)	0.99(0.04)	0.16	0.70(0.62)	4.64(0.38)	2.21
0.50	0.11(0.98)	1.11(0.02)	0.13	0.72(0.54)	4.72(0.46)	2.54
0.60	0.10(0.97)	1.46(0.03)	0.14	0.61(0.58)	5.19(0.42)	2.53
0.70	0.10(0.99)	1.93(0.01)	0.12	0.57(0.52)	5.00(0.48)	2.71
0.80	0.09(0.99)	2.24(0.01)	0.11	0.52(0.46)	5.12(0.54)	2.99
0.90	0.08(0.99)	3.58(0.01)	0.12	0.47(0.40)	4.91(0.60)	3.14
TFE-water						
0.00	0.15(0.58)	3.11(0.42)	1.40	1.33(0.19)	2.93(0.81)	2.63
0.10	0.28(0.78)	3.22(0.22)	0.94	1.28(0.27)	3.03(0.73)	2.56
0.20	0.24(0.70)	3.26(0.30)	1.15	1.24(0.36)	3.04(0.64)	2.38
0.30	0.27(0.62)	3.18(0.38)	1.39	1.16(0.50)	2.79(0.50)	1.97
0.40	0.31(0.61)	2.98(0.39)	1.34	1.36(0.74)	3.99(0.26)	2.05
0.50	0.35(0.67)	2.59(0.33)	1.08	0.90(0.84)	4.08(0.16)	1.41
0.60	0.53(0.47)	2.05(0.53)	1.35	0.81(0.71)	4.67(0.29)	1.92
0.70	0.23(0.83)	1.47(0.17)	0.44	0.64(0.69)	4.56(0.31)	1.85
0.80	0.16(0.87)	1.04(0.13)	0.27	0.70(0.51)	5.01(0.49)	2.81
0.90	0.17(0.83)	1.08(0.17)	0.32	0.69(0.54)	4.72(0.46)	2.55

Table 6.3.3: Fluorescence radiative and non-radiative decay constant of ROH^* (K_r^{ROH*} and K_{nr}^{ROH*}) and RO^{-*} (K_r^{RO-*} and K_{nr}^{RO-*}) forms of D-luciferin inside of EtOH-H_2O and TFE-H_2O binary compositions with various water contain.

Parameter of radiative and non-radiative decay constant				
X_W	K_r^{ROH*} (10^9 S^{-1})	K_{nr}^{ROH*} (10^9 S^{-1})	K_r^{RO-*} (10^9 S^{-1})	K_{nr}^{RO-*} (10^9 S^{-1})
EtOH-water				
	ROH^* form		**RO^{-*} form**	
0.00	2.205	1.795	0.171	0.592
0.10	1.564	2.603	0.161	0.448
0.20	0.844	3.917	0.134	0.401
0.30	0.349	5.533	0.103	0.388
0.40	0.242	6.008	0.093	0.359
0.50	0.126	7.566	0.053	0.340
0.60	0.118	7.025	0.065	0.331
0.70	0.078	8.255	0.089	0.280
0.80	0.039	9.051	0.096	0.239
0.90	0.029	8.304	0.120	0.198
The TFE-water				
	ROH^* form		**RO^{-*} form**	
0.00	0.494	0.220	0.006	0.374
0.10	0.588	0.476	0.008	0.383
0.20	0.342	0.527	0.009	0.411
0.30	0.193	0.526	0.012	0.495
0.40	0.083	0.664	0.013	0.474
0.50	0.023	0.903	0.005	0.704
0.60	0.004	0.736	0.003	0.518
0.70	0.013	2.260	0.039	0.501
0.80	0.011	3.692	0.048	0.308
0.90	0.008	3.117	0.189	0.203

Table 6.3.4: The solvation time scale (τ_{Sol}) for ROH^* form and proton transfer time scale (τ_{PT}) of D-luciferin inside both binary solutions at different water mole fractions.

Solvation and ESPT dynamics					
X_W	τ_{PT} (ps)	τ_{Sol} (ps)		τ_{PT} (ps)	τ_{Sol} (ps)
EtOH-H_2O				TFE-H_2O	
0.80	150	103		187	136
0.70	182	145		202	151
0.60	305	240		566	160
0.50	350	304		578	186
0.40	399	334		619	205
0.30	437	382		822	244
0.20	463	406		898	279
0.10	498	413		989	316

6.5. References

1. Nagasaka, M.; Yuzawa, H.; Kosugi, N., Microheterogeneity in Aqueous Acetonitrile Solution Probed by Soft X-ray Absorption Spectroscopy. *The Journal of Physical Chemistry B* **2020,** *124* (7), 1259-1265.
2. Takamuku, T.; Kumai, T.; Yoshida, K.; Otomo, T.; Yamaguchi, T., Structure and dynamics of halogenoethanol− water mixtures studied by large-angle X-ray scattering, small-angle neutron scattering, and NMR relaxation. *The Journal of Physical Chemistry A* **2005,** *109* (34), 7667-7676.
3. Takamuku, T.; Tanaka, M.; Sako, T.; Shimomura, T.; Fujii, K.; Kanzaki, R.; Takeuchi, M., Solvation of the amphiphilic diol molecule in aliphatic alcohol− water and fluorinated alcohol− water solutions. *The Journal of Physical Chemistry B* **2010,** *114* (12), 4252-4260.
4. Lawler, C.; Fayer, M. D., Proton Transfer in Ionic and Neutral Reverse Micelles. *The Journal of Physical Chemistry B* **2015,** *119* (19), 6024-6034.
5. Nelson, K. J.; Brown, P. J.; Rudel, H. E.; Takematsu, K., Divergent excited state proton transfer reactions of bifunctional photoacids 1-ammonium-2-naphthol and 3-

ammonium-2-naphthol in water and methanol. *Physical Chemistry Chemical Physics* **2019,** *21* (44), 24383-24392.
6. Kuchlyan, J.; Banik, D.; Roy, A.; Kundu, N.; Sarkar, N., Excited-State Proton Transfer Dynamics of Firefly's Chromophore D-Luciferin in DMSO–Water Binary Mixture. *The Journal of Physical Chemistry B* **2014,** *118* (48), 13946-13953.
7. Presiado, I.; Erez, Y.; Huppert, D., Excited-State Intermolecular Proton Transfer of the Firefly's Chromophore d-Luciferin. 2. Water− Methanol Mixtures. *The Journal of Physical Chemistry A* **2010,** *114* (35), 9471-9479.
8. Tolbert, L. M.; Solntsev, K. M., Excited-State Proton Transfer: From Constrained Systems to "Super" Photoacids to Superfast Proton Transfer. *Accounts of Chemical Research* **2002,** *35* (1), 19-27.
9. Singh, S.; Koley, S.; Mishra, K.; Ghosh, S., An Approach to a Model Free Analysis of Excited-State Proton Transfer Kinetics in a Reverse Micelle. *The Journal of Physical Chemistry C* **2018,** *122* (1), 732-740.
10. Matsugami, M.; Yamamoto, R.; Kumai, T.; Tanaka, M.; Umecky, T.; Takamuku, T., Hydrogen bonding in ethanol–water and trifluoroethanol–water mixtures studied by NMR and molecular dynamics simulation. *Journal of Molecular Liquids* **2016,** *217*, 3-11.
11. Erez, Y.; Huppert, D., Excited-State Intermolecular Proton Transfer of the Firefly's Chromophore d-Luciferin. *The Journal of Physical Chemistry A* **2010,** *114* (31), 8075-8082.
12. Cohen, B.; Martin Álvarez, C.; Alarcos Carmona, N.; Organero, J. A.; Douhal, A., Proton-Transfer Reaction Dynamics within the Human Serum Albumin Protein. *The Journal of Physical Chemistry B* **2011,** *115* (23), 7637-7647.
13. Wilson, T.; Hastings, J. W., Bioluminescence. *Annual review of cell and developmental biology* **1998,** *14* (1), 197-230.
14. Presiado, I.; Erez, Y.; Huppert, D., Excited-state intermolecular proton transfer of firefly luciferin III. Proton transfer to a mild base. *The Journal of Physical Chemistry A* **2010,** *114* (51), 13337-13346.
15. Takeuchi, S.; Tahara, T., Coherent Nuclear Wavepacket Motions in Ultrafast Excited-State Intramolecular Proton Transfer: Sub-30-fs Resolved Pump− Probe Absorption Spectroscopy of 10-Hydroxybenzo [h] quinoline in Solution. *The Journal of Physical Chemistry A* **2005,** *109* (45), 10199-10207.
16. Simkovitch, R.; Huppert, D., Photoprotolytic processes of umbelliferone and proposed function in resistance to fungal infection. *The Journal of Physical Chemistry B* **2015,** *119* (46), 14683-14696.
17. Ghosh, R.; Mondal, J. A.; Palit, D. K., Ultrafast dynamics of the excited states of curcumin in solution. *The Journal of Physical Chemistry B* **2010,** *114* (37), 12129-12143.
18. Simkovitch, R.; Shomer, S.; Gepshtein, R.; Shabat, D.; Huppert, D., Excited-state proton transfer from quinone-cyanine 9 to protic polar-solvent mixtures. *The Journal of Physical Chemistry A* **2014,** *118* (10), 1832-1840.
19. Rauf, M. A.; Hisaindee, S.; Saleh, N., Spectroscopic studies of keto–enol tautomeric equilibrium of azo dyes. *RSC Advances* **2015,** *5* (23), 18097-18110.
20. Green, O.; Simkovitch, R.; Pinto da Silva, L. s.; Esteves da Silva, J. C.; Shabat, D.; Huppert, D., Excited-State Proton Transfer and Formation of the Excited Tautomer of 3-Hydroxypyridine-Dipicolinium Cyanine Dye. *The Journal of Physical Chemistry A* **2016,** *120* (31), 6184-6199.
21. Das Mahanta, D.; Patra, A.; Samanta, N.; Luong, T. Q.; Mukherjee, B.; Mitra, R. K., Non-monotonic dynamics of water in its binary mixture with 1,2-dimethoxy ethane: A combined THz spectroscopic and MD simulation study. *J. Chem. Phys.* **2016,** *145* (16), 164501.

22. Das Mahanta, D.; Islam, S. I.; Choudhury, S.; Das, D. K.; Mitra, R. K.; Barman, A., Contrasting hydration dynamics in DME and DMSO aqueous solutions: A combined optical pump-probe and GHz-THz dielectric relaxation investigation. *Journal of Molecular Liquids* **2019,** *290*, 111194.
23. Das Mahanta, D.; Rana, D.; Patra, A.; Mukherjee, B.; Mitra, R. K., Heterogeneous structure and solvation dynamics of DME/water binary mixtures: A combined spectroscopic and simulation investigation. *Chemical Physics Letters* **2018,** *700*, 50-56.
24. Roda, A.; Guardigli, M., Analytical chemiluminescence and bioluminescence: latest achievements and new horizons. *Analytical and bioanalytical chemistry* **2012,** *402* (1), 69-76.
25. Das, A.; Islam, S. I.; Das, D. K.; Mitra, R. K., Modulation of the Excited-State Proton Transfer Rate of d-luciferin in Mixed Reverse Micellar Systems. *ACS Omega* **2018,** *3* (5), 5715-5724.
26. Kuchlyan, J.; Banik, D.; Kundu, N.; Ghosh, S.; Banerjee, C.; Sarkar, N., Effect of Confinement on Excited-State Proton Transfer of Firefly's Chromophore d-Luciferin in AOT Reverse Micelles. *The Journal of Physical Chemistry B* **2014,** *118* (12), 3401-3408.
27. Imadul Islam, S.; Das, A.; Mitra, R. K., Excited state proton transfer in reverse micelles: Effect of temperature and a possible interplay with solvation. *Journal of Photochemistry and Photobiology A: Chemistry* **2021,** *404*, 112928.
28. Das, D. K.; Das Mahanta, D.; Mitra, R. K., Nonmonotonic Hydration Behavior of Bovine Serum Albumin in Alcohol/Water Binary Mixtures: A Terahertz Spectroscopic Investigation. *ChemPhysChem* **2017,** *18* (7), 749-754.
29. Großmann, G. H.; Ebert, K. H., Formation of Clusters in 1- Propanol/Water-Mixtures. *Berichte der Bunsengesellschaft für physikalische Chemie* **1981,** *85* (11), 1026-1029.
30. Buck, M., Trifluoroethanol and colleagues: cosolvents come of age. Recent studies with peptides and proteins. *Quarterly reviews of biophysics* **1998,** *31* (3), 297-355.
31. Taber, R. L., The competitive inhibition of yeast alcohol dehydrogenase by 2,2,2-trifluoroethanol. *Biochemical Education* **1998,** *26* (3), 239-242.
32. Harger, R. N., The Pharmacology and Toxicology of Alcohol. *JAMA* **1958,** *167* (18), 2199-2202.
33. Hong, D.-P.; Hoshino, M.; Kuboi, R.; Goto, Y., Clustering of Fluorine-Substituted Alcohols as a Factor Responsible for Their Marked Effects on Proteins and Peptides. *Journal of the American Chemical Society* **1999,** *121* (37), 8427-8433.
34. Gutmann, V., *Donor-Acceptor Approach to Molecular Interactions*. Plenum Press: 1978.
35. Mitra, R. K.; Sinha, S. S.; Pal, S. K., Temperature-Dependent Solvation Dynamics of Water in Sodium Bis(2-ethylhexyl)sulfosuccinate/Isooctane Reverse Micelles. *Langmuir* **2008,** *24* (1), 49-56.
36. Reichardt, C.; Welton, T., *Solvents and solvent effects in organic chemistry*. John Wiley & Sons: 2011.
37. Kamlet, M. J.; Abboud, J. L. M.; Abraham, M. H.; Taft, R., Linear solvation energy relationships. 23. A comprehensive collection of the solvatochromic parameters,. pi.*,. alpha., and. beta., and some methods for simplifying the generalized solvatochromic equation. *The Journal of Organic Chemistry* **1983,** *48* (17), 2877-2887.
38. Presiado, I.; Erez, Y.; Simkovitch, R.; Shomer, S.; Gepshtein, R.; Pinto da Silva, L. s.; Esteves da Silva, J. C.; Huppert, D., Excited-state proton transfer of firefly dehydroluciferin. *The Journal of Physical Chemistry A* **2012,** *116* (44), 10770-10779.
39. Phukon, A.; Ray, S.; Sahu, K., How does interfacial hydration alter during rod to sphere transition in DDAB/water/cyclohexane reverse micelles? Insights from excited state proton transfer and fluorescence anisotropy. *Langmuir* **2016,** *32* (26), 6656-6665.

40. Erez, Y.; Presiado, I.; Gepshtein, R.; Huppert, D., Excited-state intermolecular proton transfer of firefly luciferin IV. Temperature and pH dependence. *The Journal of Physical Chemistry A* **2011,** *115* (9), 1617-1626.
41. Leiderman, P.; Genosar, L.; Huppert, D., Excited-state proton transfer: Indication of three steps in the dissociation and recombination process. *The Journal of Physical Chemistry A* **2005,** *109* (27), 5965-5977.
42. Huppert, D.; Goldberg, S. Y.; Masad, A.; Agmon, N., Experimental determination of the long-time behavior in reversible binary chemical reactions. *Physical review letters* **1992,** *68* (26), 3932.
43. Hong, K.; Noolandi, J., Solution of the Smoluchowski equation with a Coulomb potential. I. General results. *The Journal of Chemical Physics* **1978,** *68* (11), 5163-5171.
44. Leiderman, P.; Ben-Ziv, M.; Genosar, L.; Huppert, D.; Solntsev, K. M.; Tolbert, L. M., Study of the long-time fluorescence tail of the green fluorescent protein. *The Journal of Physical Chemistry B* **2004,** *108* (23), 8043-8053.
45. Koti, A.; Krishna, M.; Periasamy, N., Time-resolved area-normalized emission spectroscopy (TRANES): a novel method for confirming emission from two excited states. *The Journal of Physical Chemistry A* **2001,** *105* (10), 1767-1771.
46. Sahu, K.; Nandi, N.; Dolai, S.; Bera, A., A Ratio-Analysis Method for the Dynamics of Excited State Proton Transfer: Pyranine in Water and Micelles. *The Journal of Physical Chemistry B* **2018,** *122* (25), 6610-6615.
47. Maroncelli, M.; Fleming, G. R., Picosecond solvation dynamics of coumarin 153: the importance of molecular aspects of solvation. *The Journal of chemical physics* **1987,** *86* (11), 6221-6239.
48. Tran-Thi, T.-H.; Gustavsson, T.; Prayer, C.; Pommeret, S.; Hynes, J. T., Primary ultrafast events preceding the photoinduced proton transfer from pyranine to water. *Chemical Physics Letters* **2000,** *329* (5-6), 421-430.
49. Reichardt, C., Solvatochromic Dyes as Solvent Polarity Indicators *Chem. Rev.* **1994,** *1594*, 2319-2358.
50. Reichardt, C. a. W., T., Solvents and Solvent Effects in Organic Chemistry. *4*.

51. Sevilla Sierra, P.; Civera Tejuca, C.; García-Blanco, F.; Díaz Oliva, C.; Catalán Sierra, J.; Gorostidi, G. E., Properties of 2,2,2-Trifluoroethanol/Water Mixtures: Acidity, Basicity, and Dipolarity. *Helvetica Chimica Acta* **2005,** *88* (2), 312-324.
52. Ghosh, D.; Batuta, S.; Begum, N. A.; Mandal, D., Proton transfer dynamics in a polar nanodroplet: ESIPT of 4'-n,n-dimethylamino-3-hydroxyflavone in AOT/alkane/water reverse micelles. *J. Lumin.* **2017,** *184*, 64-73.
53. Mukherjee, T. K.; Panda, D.; Datta, A., Excited-State Proton Transfer of 2-(2‘-Pyridyl)benzimidazole in Microemulsions: Selective Enhancement and Slow Dynamics in Aerosol OT Reverse Micelles with an Aqueous Core. *J. Phys. Chem. B* **2005,** *109* 18895-18901.
54. Rakshit, S.; Saha, R.; Verma, P. K.; Pal, S. K., Role of Solvation Dynamics in Excited State Proton Transfer of 1- Naphthol in Nanoscopic Water Clusters Formed in a Hydrophobic Solvent. *Photochemistry and photobiology* **2012,** *88* (4), 851-859.
55. Freitas, A. A.; Quina, F. H.; Maçanita, A. n. A., Femtosecond and Temperature-Dependent Picosecond Dynamics of Ultrafast Excited-State Proton Transfer in Water–Dioxane Mixtures. *The Journal of Physical Chemistry A* **2014,** *118* (45), 10448-10455.

2nd Part of Dissertation

Probing Two-Photon Induced Emission of a Dye to Extract Information on the Local Environment of Aggregated Systems using Two-Photon Absorption Spectroscopy

Chapter 7

7. Two-photon Spectroscopy Can Serve as a Marker of Protein Denaturation Pathway

Rhodamine groups of molecules are widely used dyes for imaging of biological molecules. Application of these dyes however includes a limitation that these molecules absorb in the visible range of the spectrum, which does not fall in the 'biologically transparent window' (BTW). Two-photon absorption (TPA) processes could come up with an alternate solution to this as these dyes could be excited in the near-infrared (NIR) window to extract similar information. To validate this, we have investigated TPA cross-section (TPACS, σ_2) of two rhodamine dyes, namely Rhodamine 6G (R6G), Rhodamine B (RhB), site selectively bound with a model protein, bovine serum albumin (BSA), by exciting at 800 nm. Two-photon spectroscopy and imaging confirm the binding of the dye to the protein. The decreases in TPACS with increasing temperature at a fixed BSA concentration excellently follow the temperature-induced structural transition of BSA as the protein transforms from a molten globule to unfolded conformation beyond 60°C, which has previously been established through circular dichroism (CD)measurements. The thus established resemblance in TPACS and CD measurement trends thus strongly affirms the suitability of the TPA process in protein imaging and as an alternative marker to tracking its conformational transformations using NIR radiation.

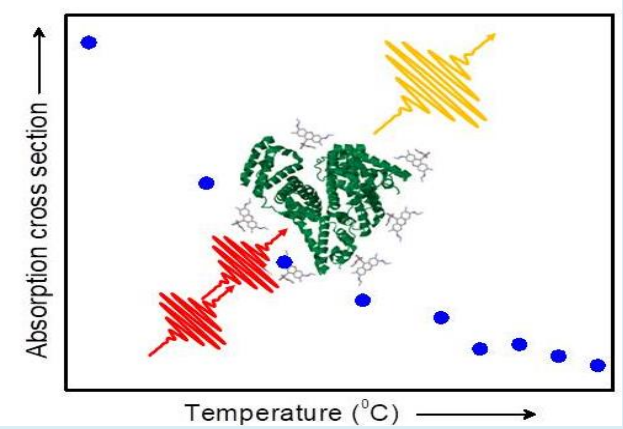

A model to represent (not to the scale) the temperature induced protein (un)folding pathways as a sharp change in the σ_2 value with the growing temperatures.

7.1. Introduction

Interaction of proteins with small molecules as well as their structural stability under external perturbation are important issues to be understood prior to their pharmaceutical applications.[1] There have been several experimental techniques that have conventionally been used to extract information, however, with certain limitations. Fluorescence spectroscopy and microscopy have been one of the most leading tools in this field of research using both intrinsic and externally labeled fluorophores.[2] Most of these fluoroprobes have their excitation and emission wavelength outside the biologically transparent window (BTW, 680-1300 nm) in which interference from the biologically important molecules are minimum, and thus is useful for explicit biological imaging.[3,4,5] There is therefore an urge to develop optimization in the protein-probe interaction window that can resolve this ambiguity. Two-photon absorption (TPA) study comes up with an excellent solution to this problem as visible probes bound to proteins can be excited with near-infrared (NIR) radiation and extract information of the systems involved. To validate this hypothesis, we, in this contribution, have studied the site specific binding of two such molecular probes e.g. Rhodamine 6G (R6G), Rhodamine B (RhB) with a well-known model transport protein bovine serum albumin (BSA) using two-photon induced fluorescence and examined whether it can follow the temperature induced unfolding of the protein. The information extracted from the TPA measurements has been compared with those obtained from conventional circular dichroism and time-resolved fluorescence measurements with comparable proteins[6] in order to authenticate this process to be of biological importance.

TPA is the simultaneous absorption of two photons by a molecule when their frequencies correspond exactly to the energy between two eigenstates.[7, 8] In the recent past this technique has been used in photodynamic therapy (PDT), [9, 10] bio-imaging, [11, 12] bio-sensing, [13, 14] bio-physics[15, 16] and various other applications. It was found that TPA cross-section (TPACS, σ_2) for a molecular system strongly depends on the excitation laser wavelength[8, 17] and solvent environments.[17] Very recently, it was shown that the two-photon fluorescence technique is able to differentiate the mode of binding, either intercalation or minor groove binding, of various probes with DNA.[18,19] This study shows that the σ_2 value of groove binding molecules are enhanced while those of intercalative binding molecules exhibit suppressed values. Recently Deiana et al. have established specific recognition of G-quadruplex over duplex DNA using a two-photon induced fluorescence study.[20] While application of TPA is reported for DNA molecules, such studies using proteins are in sparse.

[21, 22] Deiana et al. [21] in their recent work has investigated the TPA process of a macro-molecular probe Ant-PIm which specifically binds to human serum albumin (HSA) and BSA. They found that the σ_2 values strongly depend on the excitation wavelength with a maximum occurring at 820 nm. This study confirms that TPA can probe the specific binding of probes to proteins, which prompted us to investigate whether this fact could be exploited to understand site-specific binding as well as conformational changes in proteins undergoing thermal denaturation.

Rhodamine dyes are the most commonly used markers in the TPA studies [8, 17] due to their high fluorescence quantum yields[23] and low cost which find important applications in two-photon imaging of living cells.[24] Recent studies have shown that these dyes have a very strong affinity towards site selective binding with the active sites of proteins.[25, 26,27] In the light of these preliminary studies we investigate whether TPA of such dyes can extract fruitful information of various biophysical processes in proteins. To accomplish such intent, we have monitored the TPA cross-section of R6G and RhB in presence of a widely studied serum protein BSA at different concentrations and temperatures. The choice of BSA as a model protein is rooted in the sense that the structure and the thermal denaturation pathway of this protein have unambiguously been established in the literature using various conventional techniques and would be helpful to correlate the data obtained from the TPACS measurements. The decrease of σ_2 value with increasing BSA concentration indicates a strong site-selective binding of the dye with BSA. We also found that the changes in the σ_2 value with temperature also follow the protein denaturation pathway, as has also been established with CD and other spectroscopic techniques.

7.2. Materials and Methods

All the chemicals, Rhodamine 6G (R6G), Rhodamine B (RhB) and lyophilized powder of bovine serum albumin (BSA) protein (for more details in chapter 2) were procured from Sigma Aldrich and used without further purification. For making the protein stock solution, we used a phosphate buffer solution at pH~7.4. The same buffer solution was also used to make the stock solutions of R6G and RhB. The concentration-dependent studies were performed by diluting the stock BSA solution by adding a calculated amount of aqueous buffer.

We have used the following instruments and methods (for details see chapters 2 & 3). A *UV-Vis. spectrophotometer* was used for all the absorption spectrum measurements. For temperature-dependent absorption studies, we increase the temperature by 5^0C and wait for 5 minutes for the system to equilibrate and then recorded the absorption data. To probe the local environment *fluorescence* measurements were done by *steady-state* with slits set at 2 nm. For the temperature-dependent fluorescence study, we used a temperature controller attached to the fluorimeter after ensuring temperature equilibrium. The protein structure was measured by the *CD spectroscopy*, using a wavelength step of 0.5 nm and a bandwidth of 1.0 nm. For absorption and CD measurements we used a 1 mm path length quartz sample cell while the fluorescence measurements were done in a 10 mm path length quartz sample cell. *Time-resolved fluorescence* measurements were performed using a diode laser with the central wavelength 299 nm and 480 ps instruments response function (IRF). Fluorescence decay data were fitted using commercially available F900 software provided by Edinburgh Instruments. We used a home-built fluorescence spectrometer for all the *two-photon induced fluorescence* studies. We specifically used 800 nm laser pulses as an excitation source for our studies due to the pronounced two-photon absorption cross-section of these two dyes (R6G and RhB) in water.[16] TPA cross-section (σ_2) was measured using two-photon induced fluorescence technique, using standard values have been obtained from previously published kinds of literature (e.g. for R6G, $\sigma_2 \sim 10.3$ GM and for RhB, $\sigma_2 \sim 4$ GM, where, 1 GM = 10^{-50} cm^4 s $photon^{-1}$).[17] Quantum yields were individually measured at each protein concentration. Temperature-dependent quantum yields were also estimated at each individual temperature in the presence and absence of the protein. For two-photon imaging was measured by a *fluorescence microscope* and we have integrated the area of the image as a function of increasing BSA concentration using a MATLAB program.

7.3. Results and Discussion

Steady-state measurements:

The absorption spectra of R6G and RhB dyes in buffer and in presence of different concentrations of BSA are shown in figure 7.3.1 (a & b). The observed absorption peak maxima at ~527 nm for R6G and ~555 nm for RhB are due to the electronic transition from $S_0 \rightarrow S_1$ electronic states of the dyes.[17] The small hump observed at ~350 nm for both the systems are due to the $S_0 \rightarrow S_2$ electronic transitions in the dyes.[28] The ~285 nm peak appearing in the UV region is mostly due to the absorption of BSA. We found that with

increasing BSA concentration the intensity at ~285 nm increases, whereas that in the dye (visible) region decreases, which unambiguously concludes the dye to bind with the protein. We also notice that absorption in the visible region does change almost linearly as a function of the protein concentration (Figure 7.3.1. c & d) which indicates a selective binding procedure of the dye to the protein as had previously been reported for other dye-protein pairs.[25, 26, 29, 30, 31]

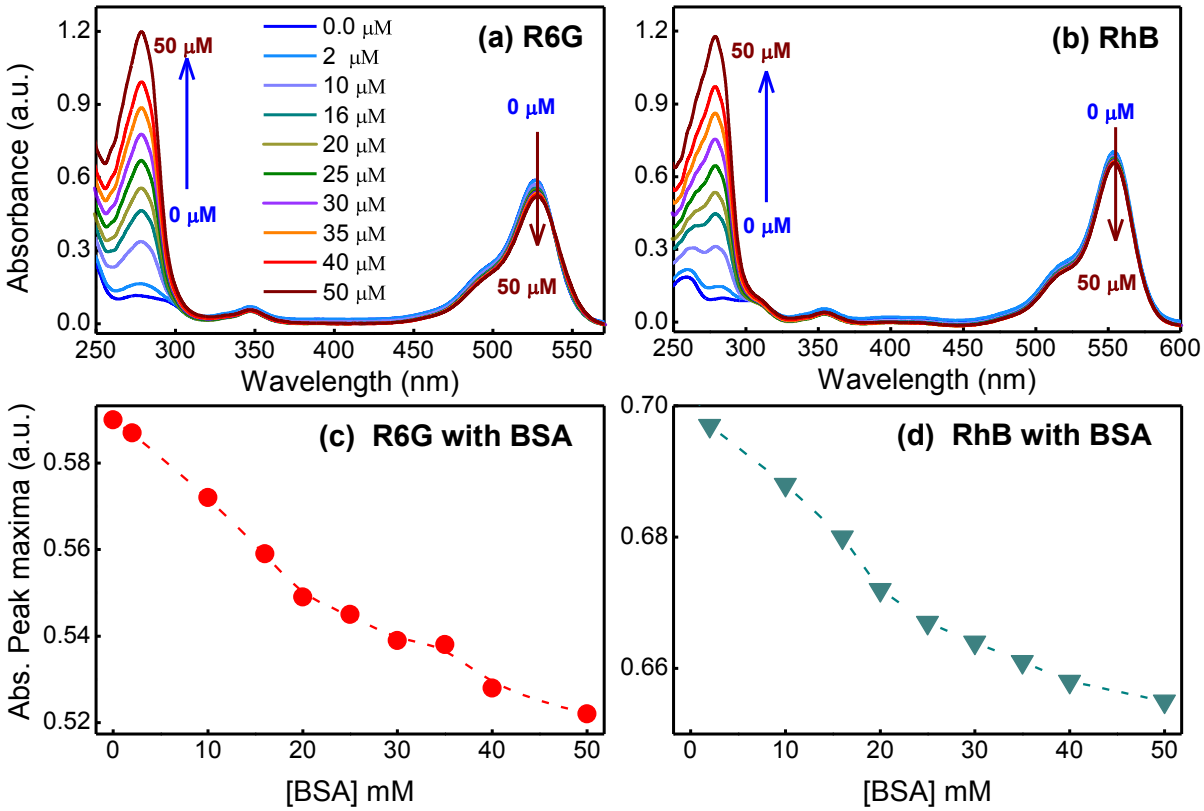

Figure 7.3.1: Absorption spectra of rhodamine dyes as a function of BSA concentrations for R6G (a) and RhB (b) respectively. The arrows indicate increasing BSA concentration (from 0 to 50 μM). The spectra indicate a decrease of absorbance in the dye region whereas increases in the BSA region with increasing BSA concentration. The plot of the absorption of the dye peak maxima as a function of BSA concentration for (c) R6G and (d) RhB respectively. The dotted lines are a guide to the eyes.

Molecular docking studies have established that RhB binds with BSA pocket and one of the diethyl-amino groups of RhB fits into the bottom of the binding pocket of BSA, surrounded by the residues Trp213, Arg194 and Arg198, while the other diethyl-amino group locates at the entrance of the pocket and interacts with the hydrophobic residues Val342, Ala341 and Pro446 of the protein. The carboxyl groups of the dyes form two key hydrogen bonds (2.0 and 3.3 Å) with Arg194 of the protein rendering their affinity towards binding.[27] A subtle peak shift (~1-3 nm) is observed for both the dyes in both UV and visible regions. The observed marginal change in the peak frequency in the visible region excludes the possibility

of dye aggregation. The absorption profile exhibits minimal changes as temperature is increased up to 90° C in the presence as well as in absence of the protein.

Emission spectra of R6G and RhB, excited at 480 nm, as a function of the protein concentrations are shown in figure 7.3.2 (c & d). Strong fluorescence profile peaking at ~556 nm for R6G and ~580 nm for RhB in water are observed. The addition of BSA progressively quenches the emission in both the dyes which can be explained considering site-specific binding of these dyes corroborating earlier findings.[25, 26, 29, 30]

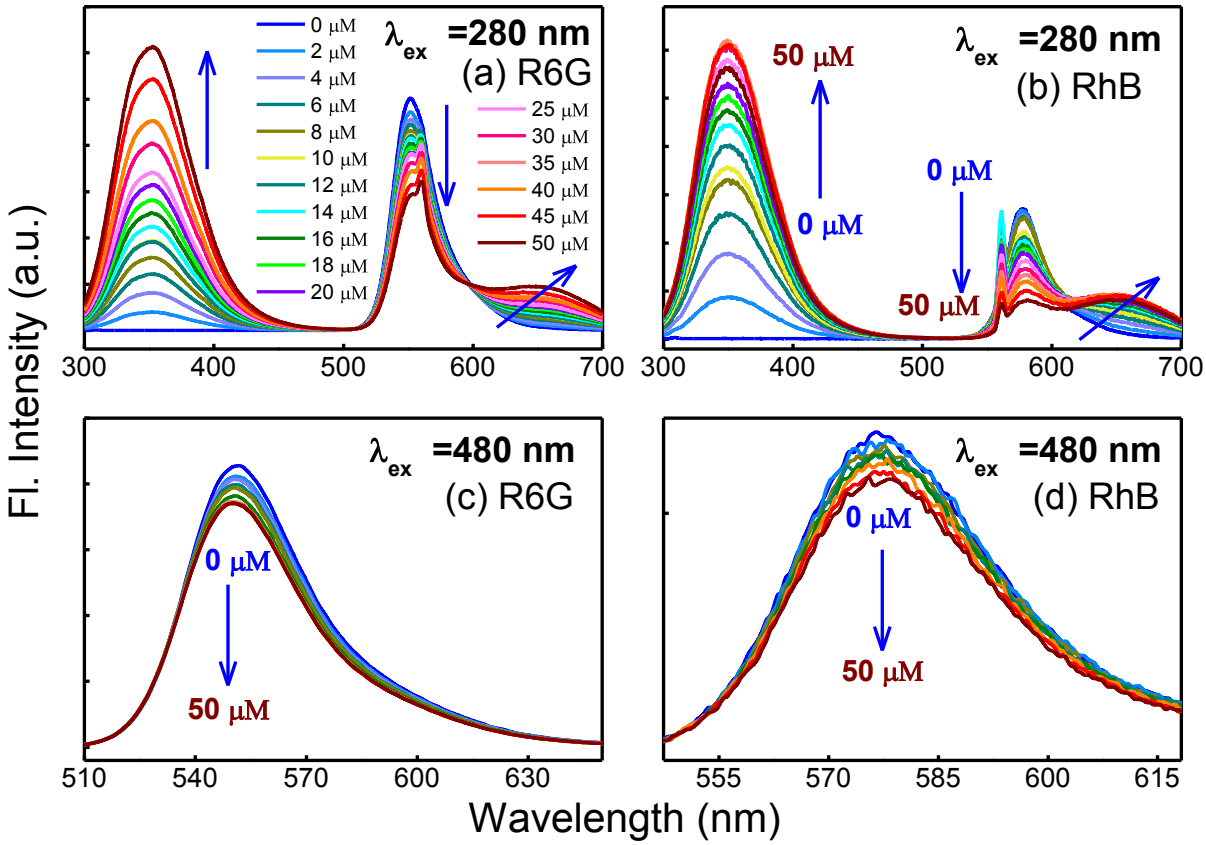

Figure 7.3.2: Emission spectra of rhodamine dyes as a function of BSA concentration for R6G (a) and RhB (b) excited at 280 nm. The three distinct emission bands indicate the emissions coming from BSA (peak max ~350 nm), from the dye (peak max ~556 nm for R6G and peak max ~580 nm for RhB) and from the dye-BSA complex (peak max ~660 nm) which arises due to the energy transfer from BSA towards the dye. The arrows indicate increasing protein concentration. Emission spectra of rhodamine dyes as a function of BSA concentrations for (c) R6G and (d) RhB respectively, excited at 480 nm.

The difference in the emission intensity of these two dyes is due mainly to the difference in their respective quantum yields (ϕ_{R6G} ~ 0.95 and ϕ_{RhB} ~ 0.31).[23, 32] When excited at 280 nm, we surprisingly observe the appearance of a new emissive peak in the visible region (~660 nm) (Figure 7.3.2. a & b), which otherwise was not evident in water and most likely emanates

from dye-BSA complex formation and consequent energy transfer from the protein to the dye(s).

The intensity of the new emission peak (at ~660 nm) increases with increasing protein concentration which indicates that the energy transfer rate enhances as more of such complexes are formed. We also notice that as the protein concentration increases the emission of the dye (at ~560 nm) quenches, which unambiguously supports the energy transfer phenomenon to be the most accountable reason for the increase in the new emission peak intensity. It can also be noted that the dye concentration has been kept rather low (~2 μM) in order to rule out any possibility of self-aggregation of the dyes to originate any new spectral characteristics (aggregation starts at a dye concentration above 10^{-4} M in aqueous solution).[33, 34, 35, 36]

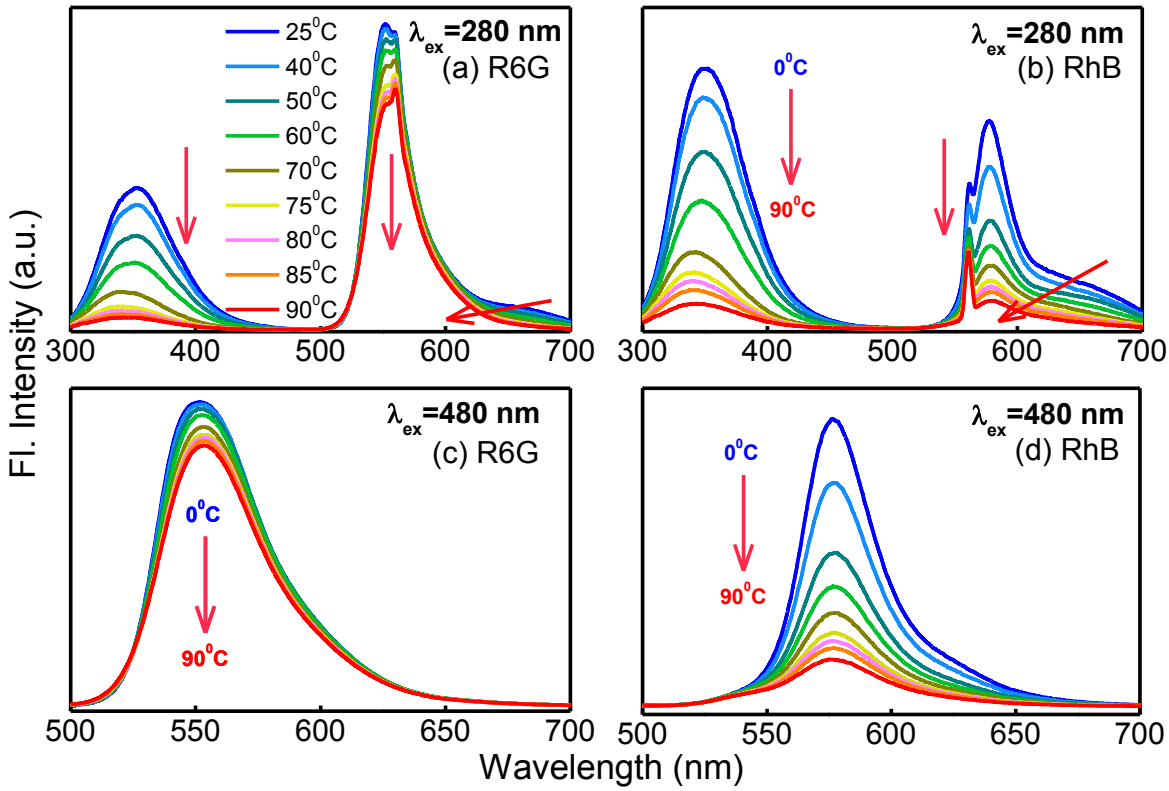

Figure 7.3.3: Temperature-dependent fluorescence study of rhodamine dyes as a function of increasing temperature with the excitation wavelength 280 nm for (a) R6G and (b) RhB and the excitation wavelength 480 nm for (c) R6G and (d) RhB respectively. The arrows indicate increasing temperature.

The appearance of the new peak renders support to the site-specific tight binding of the dye with the protein.[25] Temperature-dependent fluorescence study of R6G and RhB in buffer shows a noticeable reduction in the emission intensity at elevated temperatures (Figure 7.3.3).

For rhodamine dyes, such a decrease has been explained in terms of mobility change of the molecules' diethyl-amino groups.[37]

CD measurements:

The dyes are achiral, and therefore CD study of the dye-protein complex provides information on the protein structure only. We found that the addition of the dye does not noticeably perturb the native structure of the protein. An increase in temperature, however, affects the CD pattern as the protein structure modulates. It has been reported that BSA undergoes thermal denaturation beyond 60° C[38, 39], and accordingly, we notice a drastic change in the CD pattern at temperatures >60° C (Figure 7.3.4). CD measurements thus affirm a structural transition of the protein at a temperature beyond 60° C.

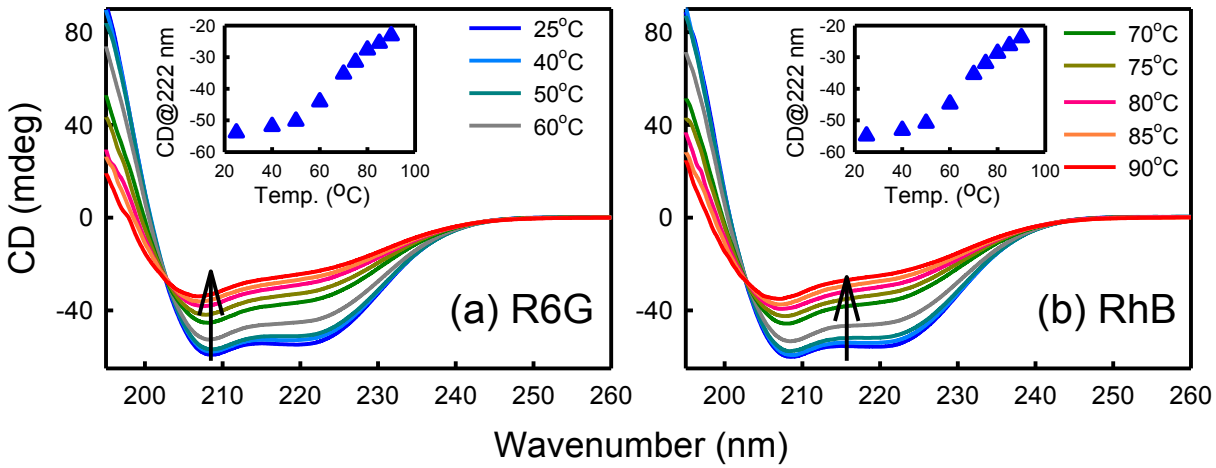

Figure 7.3.4: Temperature-dependent CD study of (a) R6G and (b) RhB in presence of 10 µM BSA. In all these cases we noticed an isodichroic point as a function of increasing temperature for both the dye.

Time-resolved fluorescence measurements:

Time-resolved emission spectra of R6G and RhB in presence of 10 µM BSA (excited at 299 nm) are shown in figures 7.3.5. Emission is collected at three different wavelengths, at 350 nm: corresponding to the emission from the protein itself (cyan), at ~550 nm: corresponding to the emission from the dye(s) (green) and at ~660 nm: corresponding to the dye-protein complex (red). We observe distinct dynamics at these three different wavelengths which strongly signifies the dye-protein binding. All the decays could only be fitted multi-exponentially and the fitting parameters are presented in table 7.3.1. The emission due to protein Trp (measured at 350 nm) shows two lifetimes of 1.8 and ~6 ns, which is in good agreement with earlier reports.[40] RhB emission in water (measured at ~550 nm) decays

mono-exponentially with a lifetime of ~4.5 ns.[26] In presence of BSA, however, the emission decay could not be fitted mono-exponentially, rather a bi-exponential decay model provides with a better fit with time constants of 0.94 ns (10%) and 5.5 ns (90%). The bi-exponential decay nature of RhB, site-specifically bound with BSA seems to vary with the increasing BSA concentrations as having been reported earlier.[26]

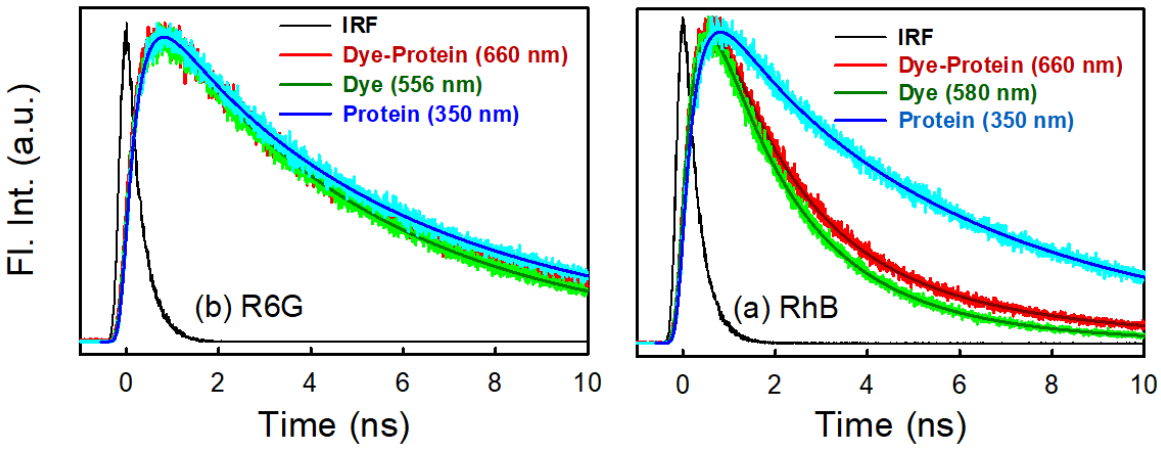

Figure 7.3.5: Time-resolved decay of rhodamine dyes in presence of 5 μM BSA excited at 299 nm measured at three different emission maximum for R6G (a) and RhB (b). The solid lines indicate bi-exponential fits.

Table 7.3.1: Decay time constants for R6G and RhB in presence of BSA with the excitation at 299 nm.

λ_{max} (nm)	a_1	τ_1 (ns)	a_2	τ_2 (ns)	χ^2
Rhodamine 6G					
660	0.09	1.60±0.11	0.91	5.51±0.02	1.02
350	0.18	1.79±0.13	0.82	6.31±0.05	0.99
555	0.09	0.94±0.23	0.91	5.05±0.02	0.97
Rhodamine B					
660	0.75	1.77±0.02	0.25	5.15±0.07	1.06
350	0.18	1.43±0.14	0.82	6.25±0.06	0.96
580	0.75	1.65±0.02	0.25	3.56±0.06	1.03

The observed quenching in emission lifetime can be correlated with the energy transfer as manifested in the steady-state measurements. For RhB the quenching has been more prominent and consequently, the dynamics also get faster (Table 7.3.1). The emission decay of the new peak (at ~660 nm) follows bimodal fits with time constants of 1.6 (10%) and 5.5 ns (90%) for R6G and 1.8 (75%) and 5.2 ns (25%) for RhB. The time constants of this new peak were thus found to be different in the two dyes which might be due to their difference in the structures and hence the consequent difference in their respective affinity of binding. We found that the lifetime of the dye-protein complex lies within those of the protein (blue) and the dye(s) (green) which corresponds to the allosteric binding of the dye with the protein as has been established in earlier studies.[41]

Two-photon imaging:

Representative two-photon images of R6G bound to BSA at different concentrations are shown in the insets of figure 7.3.6. It is observed that the contrast of the images decreases with increasing protein concentration which provides with direct evidence of the quenching of the dye fluorescence as a consequence of protein binding.

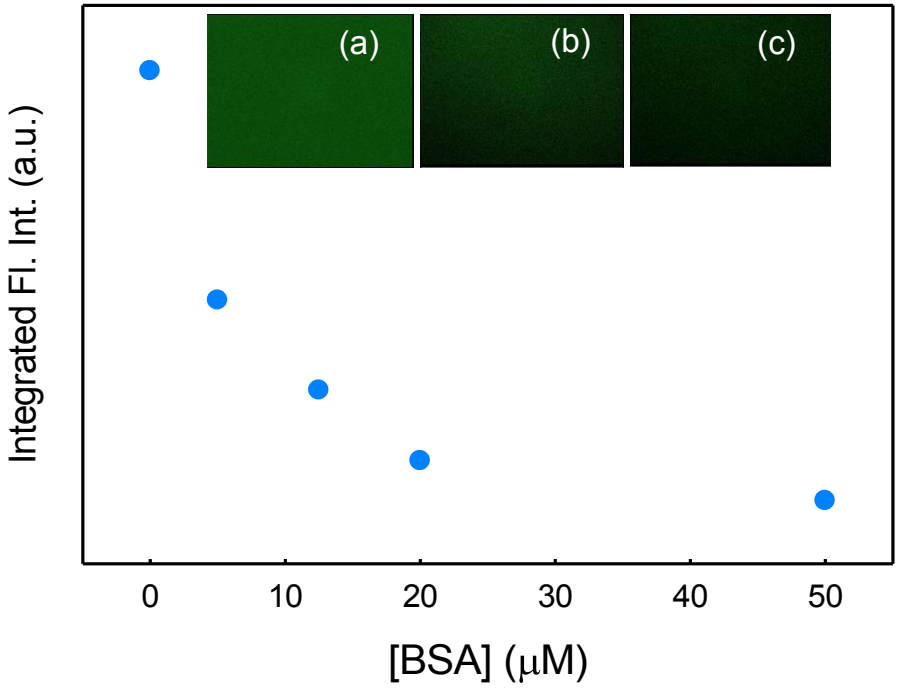

Figure 7.3.6: Integrated area ratio of R6G as a function of BSA concentration. The decrease in the area intensity ratio with the increasing of BSA concentrations indicates fluorescence quenching due to the formation of the R6G-BSA complex. The insets show two-photon fluorescence images of (a) R6G in buffer, (b) R6G in presence of 10 μM BSA, (c) R6G in presence of 50 μM BSA.

We plot the relative change in the integrated area intensity of R6G as a function of BSA concentration (Figure 7.3.6). We observe a non-linear decrease in the relative fluorescence intensity; initially, the quenching is rapid and beyond 20 μM of the protein concentration the changes are subtle.

Two-photon absorption cross-section measurements:

We measure the TPA cross-section (σ_2) of the dye(s) bound to the protein following the methodology described in the earlier sections 2.2.3 (chapter 2). Figure 7.3.7 (a, b) shows the changes in σ_2 of R6G and RhB dyes as a function of BSA concentration excited at the central wavelength of 800 nm. The σ_2 values obtained for both the dyes in water are in good agreement with previous results.[8] It is noticed that σ_2 decreases sharply with increasing BSA concentration for both the dyes which signify tight complex formation with a high association constant as has been reported in earlier studies.[26, 27, 30] It is known that heart-shaped BSA allows binding of the probe molecule(s) to its active sites (site I and site II, dual-mode binding).[26, 30, 42, 43]

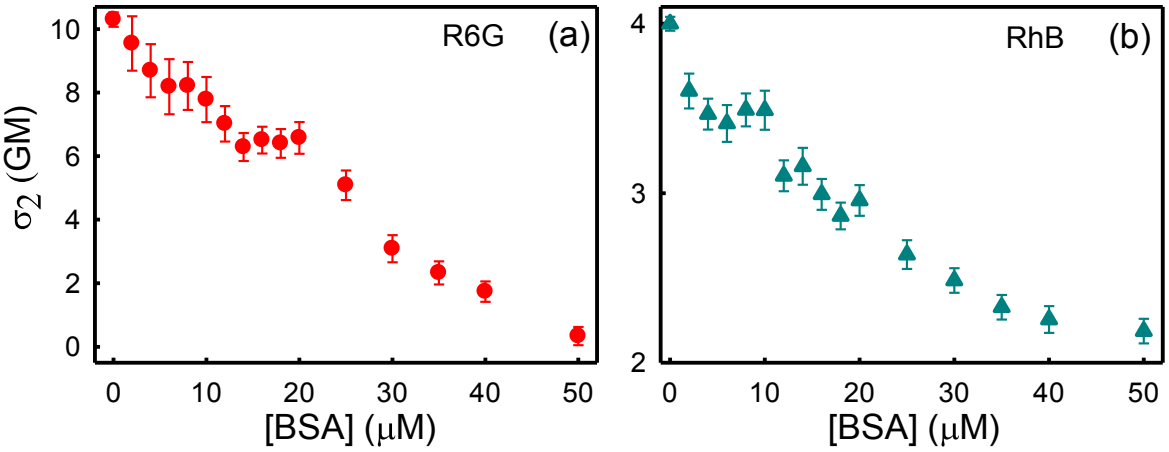

Figure 7.3.7: Two-photon absorption cross-section of R6G (a) and RhB (b) as a function of BSA concentration.

The sharp initial decrease in the σ_2 value up to 10 μM BSA concentration (corresponding to ~5 protein molecules per dye molecule) indicates progressive dye-binding with the protein. Further addition of the protein provides the only modest change in the σ_2 value. The next sharp change in the ≥20 μM protein concentration is perhaps caused by a prominent three-photon absorption process of the tryptophan and tyrosine amino acids present in BSA. It could be noted here that the three-photon absorption probability of the protein is relatively low[44], and in the low protein concentration regime, the TPA of the dye overwhelms it.

However, beyond a moderately high protein concentration (herein ≥20 μM), this process starts contributing a reasonable share towards the total σ_2 value and decreases it further.

Effect of temperature on two-photon absorption cross-section:

TPACS is known to sensitively depend on the temperature of the medium.[45,46] TPACS of RhB and R6G dyes in presence of 5 μM BSA as a function of temperature are shown in figure 7.3.8 (a & b). The protein concentration was kept fixed at 5 μM to avoid any possible interference from the three-photon absorption process. We found that σ_2 decreases with increasing temperature for both the dyes and that also in a non-monotonic fashion with a definite change in the slope at ~60º C. Previously Boni et al.[46] had shown that σ_2 decreases linearly with temperature in azo-aromatic compounds which has been explained on the basis of thermal-induced molecular conformation as a result of increasing temperature. Using femtosecond (fs) white-light-continuum Z-scan technique the same group[45] reported that σ_2 decreases quadratically with temperature for all-trans-β-carotene dyes which was related to the temperature-induced change in the dipole moment of the dyes. Our present data is intriguing in the sense that σ_2 of both the dyes decreases near-linearly in an aqueous medium (Figure 7.3.8, c & d) while in presence of the protein it deviates from linearity clearly being indicative of protein structural perturbation. The specific dye-protein binding thus gets influenced by the protein structural modification at elevated temperatures. It could be noted that BSA (in analogy to its structural analog HSA) undergoes a two-step denaturation process.[6] With initial increase in temperature a gradual native to molten globule state transition takes place up to 60º C in which the protein swells as the interaction between the various domains weakens and a marginal exposure of the otherwise buried hydrophobic residues of the protein takes place. On further increase in temperature the protein structure gets completely ruptured and it unfolds[6, 47] (see the representative CD profiles in figure 7.3.4). At elevated temperatures, the helical structure of the protein gets disrupted forming less structured secondary forms (mostly random coils)[38] and correspondingly its site-specific ligand binding ability also gets modified.[48] In the TPA study we observe a characteristic change in the σ_2 value near the protein unfolding temperature exactly following the protein denaturation pathway. The mode of binding of the dye with the protein changes as the protein unfolds and the change gets clearly manifested in the σ_2 vs. temperature profile.

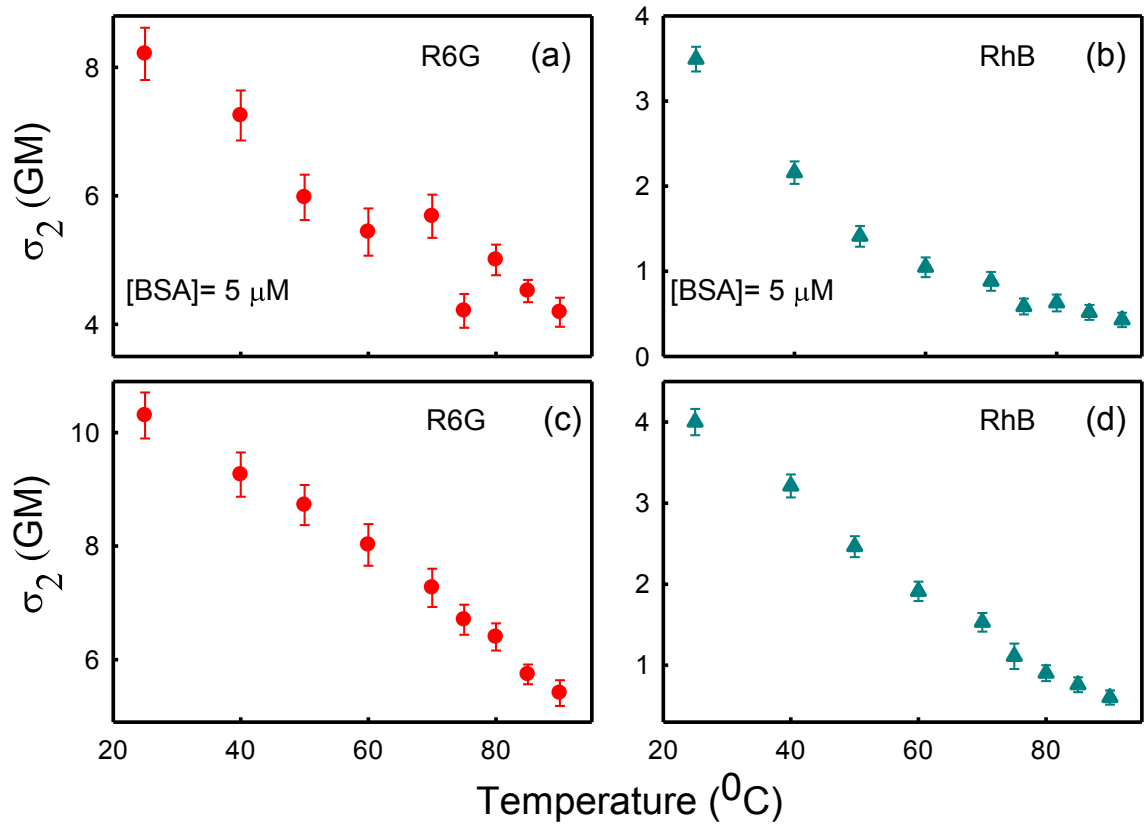

Figure 7.3.8: Temperature-dependent two-photon absorption cross-section (σ_2) of R6G (a) and RhB (b) in presence of 5 μM BSA solution. The plot of TPACS of the dyes as a function of different temperatures, R6G (c) and RhB (d) respectively, in buffer.

7.4. Conclusions

TPA has been a rather non-conventional process to investigating various biophysical processes, however, it has the advantages of possessing deep penetration depth, low excitation energy (in the near-IR region, which falls within the BTW), and small focal volume, which could approach to a few-molecule level excitation. We have studied the TPACS of rhodamine dyes, site selectively bound to a model protein BSA. TPA measurements and microscopy unambiguously confirms site-specific binding of the probes with the protein. We also found that this technique could also track the temperature-induced protein folding pathways as a sharp change in the σ_2 vs. temperature profile is observed, which perfectly resembles the protein unfolding temperature threshold that has previously been reported using various spectroscopic techniques. Our experimental results could open up a new avenue in bio-imaging in which exciting dyes in the BTW could extract information on the protein structural perturbation.

7.5. References

1. Hawe, A.; Sutter, M.; Jiskoot, W., Extrinsic Fluorescent Dyes as Tools for Protein Characterization. *Pharmaceutical Research* **2008,** *25* (7), 1487-1499.
2. Munishkina, L. A.; Fink, A. L., Fluorescence as a method to reveal structures and membrane-interactions of amyloidogenic proteins. *Biochimica et Biophysica Acta (BBA) - Biomembranes* **2007,** *1768* (8), 1862-1885.
3. Weissleder, R., A clearer vision for in vivo imaging. *Nature Biotechnology* **2001,** *19*, 316.
4. Frangioni, J. V., In vivo near-infrared fluorescence imaging. *Current Opinion in Chemical Biology* **2003,** *7* (5), 626-634.
5. Hemmer, E.; Benayas, A.; Legare, F.; Vetrone, F., Exploiting the biological windows: current perspectives on fluorescent bioprobes emitting above 1000 nm. *Nanoscale Horizons* **2016,** *1* (3), 168-184.
6. Samanta, N.; Mahanta, D. D.; Hazra, S.; Kumar, G. S.; Mitra, R. K., Short chain polyethylene glycols unusually assist thermal unfolding of human serum albumin. *Biochimie* **2014,** *104* (Supplement C), 81-89.
7. Yang, J.; Tian, Y.; Zhang, S.; Wu, J.; Jin, B., Two-photon absorption and sensitivity to DNA of dye molecule-driven CdSe quantum dots. *RSC Advances* **2014,** *4* (38), 19578-19583.
8. Xu, C.; Webb, W. W., Measurement of two-photon excitation cross sections of molecular fluorophores with data from 690 to 1050 nm. *J. Opt. Soc. Am. B* **1996,** *13* (3), 481-491.
9. Kim, S.; Ohulchanskyy, T. Y.; Pudavar, H. E.; Pandey, R. K.; Prasad, P. N., Organically Modified Silica Nanoparticles Co-encapsulating Photosensitizing Drug and Aggregation-Enhanced Two-Photon Absorbing Fluorescent Dye Aggregates for Two-Photon Photodynamic Therapy. *Journal of the American Chemical Society* **2007,** *129* (9), 2669-2675.
10. Fisher, W. G.; Partridge, W. P.; Dees, C.; Wachter, E. A., Simultaneous Two-Photon Activation of Type-I Photodynamic Therapy Agents. *Photochemistry and Photobiology* **1997,** *66* (2), 141-155.
11. Yao, S.; Belfield, K. D., Two-Photon Fluorescent Probes for Bioimaging. *European Journal of Organic Chemistry* **2012,** *2012* (17), 3199-3217.
12. Andrade, C. D.; Yanez, C. O.; Ahn, H.-Y.; Urakami, T.; Bondar, M. V.; Komatsu, M.; Belfield, K. D., Two-Photon Fluorescence Vascular Bioimaging with New Bioconjugate Probes Selective toward the Vascular Endothelial Growth Factor Receptor 2. *Bioconjugate Chemistry* **2011,** *22* (10), 2060-2071.
13. Weerasinghe, A. J.; Schmiesing, C.; Varaganti, S.; Ramakrishna, G.; Sinn, E., Single- and Multiphoton Turn-On Fluorescent Fe3+ Sensors Based on Bis(rhodamine). *The Journal of Physical Chemistry B* **2010,** *114* (29), 9413-9419.
14. Wang, L.; Zheng, J.; Yang, S.; Wu, C.; Liu, C.; Xiao, Y.; Li, Y.; Qing, Z.; Yang, R., Two-Photon Sensing and Imaging of Endogenous Biological Cyanide in Plant Tissues Using Graphene Quantum Dot/Gold Nanoparticle Conjugate. *ACS Applied Materials & Interfaces* **2015,** *7* (34), 19509-19515.
15. Wang, Y.; Goodson, T., Early aggregation in prion peptide nanostructures investigated by nonlinear and ultrafast time-resolved fluorescence spectroscopy. *The Journal of Physical Chemistry B* **2007,** *111* (2), 327-330.
16. Cotlet, M.; Goodwin, P. M.; Waldo, G. S.; Werner, J. H., A Comparison of the Fluorescence Dynamics of Single Molecules of a Green Fluorescent Protein: One- versus Two-Photon Excitation. *ChemPhysChem* **2006,** *7* (1), 250-260.

17. Nag, A.; Goswami, D., Solvent effect on two-photon absorption and fluorescence of rhodamine dyes. *Journal of Photochemistry and Photobiology A: Chemistry* **2009,** *206* (2–3), 188-197.
18. Doan, P. H.; Pitter, D. R. G.; Kocher, A.; Wilson, J. N.; Goodson, T., Two-Photon Spectroscopy as a New Sensitive Method for Determining the DNA Binding Mode of Fluorescent Nuclear Dyes. *Journal of the American Chemical Society* **2015,** *137* (29), 9198-9201.
19. Doan, P.; Pitter, D. R. G.; Kocher, A.; Wilson, J. N.; Goodson, T., A New Design Strategy and Diagnostic to Tailor the DNA-Binding Mechanism of Small Organic Molecules and Drugs. *ACS Chemical Biology* **2016,** *11* (11), 3202-3213.
20. Deiana, M.; Mettra, B.; Martinez-Fernandez, L.; Mazur, L. M.; Pawlik, K.; Andraud, C.; Samoc, M.; Improta, R.; Monnereau, C.; Matczyszyn, K., Specific Recognition of G-Quadruplexes Over Duplex-DNA by a Macromolecular NIR Two-Photon Fluorescent Probe. *The Journal of Physical Chemistry Letters* **2017**, 5915-5920.
21. Deiana, M.; Mettra, B.; Mazur, L. M.; Andraud, C.; Samoc, M.; Monnereau, C.; Matczyszyn, K., Two-Photon Macromolecular Probe Based on a Quadrupolar Anthracenyl Scaffold for Sensitive Recognition of Serum Proteins under Simulated Physiological Conditions. *ACS Omega* **2017,** *2* (9), 5715-5725.
22. McLean, A. M.; Socher, E.; Varnavski, O.; Clark, T. B.; Imperiali, B.; Goodson, T., Two-Photon Fluorescence Spectroscopy and Imaging of 4-Dimethylaminonaphthalimide Peptide and Protein Conjugates. *The Journal of Physical Chemistry B* **2013,** *117* (50), 15935-15942.
23. Kubin, R. F.; Fletcher, A. N., Fluorescence quantum yields of some rhodamine dyes. *Journal of Luminescence* **1982,** *27* (4), 455-462.
24. Langer, G.; Bouchal, K.-D.; Grün, H.; Burgholzer, P.; Berer, T., Two-photon absorption-induced photoacoustic imaging of Rhodamine B dyed polyethylene spheres using a femtosecond laser. *Opt. Express* **2013,** *21* (19), 22410-22422.
25. Zhu, J.; Li, J.-J.; Zhao, J.-W., Spectral characters of Rhodamine B as a multi-information fluorescence probe for bovine serum albumins. *Sensors and Actuators B: Chemical* **2009,** *138* (1), 9-13.
26. Cai, H.-H.; Zhong, X.; Yang, P.-H.; Wei, W.; Chen, J.; Cai, J., Probing site-selective binding of rhodamine B to bovine serum albumin. *Colloids and Surfaces A: Physicochemical and Engineering Aspects* **2010,** *372* (1), 35-40.
27. MA Yu-Xing, Z. R.-B., GUO Jun,LIU Yu-Shuang,YUAN Ming,BAI Zhi-Jun,LIU Tao-Tao,ZHAO Xin-Min,ZHANG Feng, A facile method for studying interaction of rhodamine B and bovine serum albumin: Towards physical-binding mediated fluorescence labeling of proteins. *Nuclear Science and Techniques* **2015,** *26* (6), 60502-060502.
28. Hermann, J. P.; Ducuing, J., Dispersion of the two-photon cross section in rhodamine dyes. *Optics Communications* **1972,** *6* (2), 101-105.
29. Jisha, V. S.; Arun, K. T.; Hariharan, M.; Ramaiah, D., Site-Selective Interactions: Squaraine Dye−Serum Albumin Complexes with Enhanced Fluorescence and Triplet Yields. *The Journal of Physical Chemistry B* **2010,** *114* (17), 5912-5919.
30. Jisha, V. S.; Arun, K. T.; Hariharan, M.; Ramaiah, D., Site-Selective Binding and Dual Mode Recognition of Serum Albumin by a Squaraine Dye. *Journal of the American Chemical Society* **2006,** *128* (18), 6024-6025.
31. Bolel, P.; Mahapatra, N.; Datta, S.; Halder, M., Modulation of Accessibility of Subdomain IB in the pH-Dependent Interaction of Bovine Serum Albumin with Cochineal Red A: A Combined View from Spectroscopy and Docking Simulations#. *Journal of Agricultural and Food Chemistry* **2013,** *61* (19), 4606-4613.

32. Magde, D.; Rojas, G. E.; Seybold, P. G., Solvent Dependence of the Fluorescence Lifetimes of Xanthene Dyes. *Photochemistry and Photobiology* **1999,** *70* (5), 737-744.
33. López Arbeloa, I.; Ruiz Ojeda, P., Dimeric states of rhodamine B. *Chemical Physics Letters* **1982,** *87* (6), 556-560.
34. Arbeloa, I. L.; Ojeda, P. R., Molecular forms of rhodamine B. *Chemical Physics Letters* **1981,** *79* (2), 347-350.
35. Terdale, S.; Tantray, A., Spectroscopic study of the dimerization of rhodamine 6G in water and different organic solvents. *Journal of Molecular Liquids* **2017,** *225*, 662-671.
36. Fischer, M.; Georges, J., Use of thermal lens spectrometry for the investigation of dimerization equilibria of rhodamine 6G in water and aqueous micellar solutions. *Spectrochimica Acta Part A: Molecular and Biomolecular Spectroscopy* **1997,** *53* (9), 1419-1430.
37. Kemnitz, K.; Yoshihara, K., Entropy-driven dimerization of xanthene dyes in nonpolar solution and temperature-dependent fluorescence decay of dimers. *The Journal of Physical Chemistry* **1991,** *95* (16), 6095-6104.
38. Takeda, K.; Wada, A.; Yamamoto, K.; Moriyama, Y.; Aoki, K., Conformational change of bovine serum albumin by heat treatment. *Journal of Protein Chemistry* **1989,** *8* (5), 653-659.
39. Moriyama, Y.; Watanabe, E.; Kobayashi, K.; Harano, H.; Inui, E.; Takeda, K., Secondary Structural Change of Bovine Serum Albumin in Thermal Denaturation up to 130 °C and Protective Effect of Sodium Dodecyl Sulfate on the Change. *The Journal of Physical Chemistry B* **2008,** *112* (51), 16585-16589.
40. Samanta, N.; Luong, T. Q.; Das Mahanta, D.; Mitra, R. K.; Havenith, M., Effect of Short Chain Poly(ethylene glycol)s on the Hydration Structure and Dynamics around Human Serum Albumin. *Langmuir* **2016,** *32* (3), 831-837.
41. Li, G.; Magana, D.; Dyer, R. B., Anisotropic energy flow and allosteric ligand binding in albumin. *Nature Communications* **2014,** *5*, 3100.
42. He, X. M.; Carter, D. C., Atomic structure and chemistry of human serum albumin. *Nature* **1992,** *358*, 209.
43. Ghosh, S.; Dey, J., Binding of Fatty Acid Amide Amphiphiles to Bovine Serum Albumin: Role of Amide Hydrogen Bonding. *The Journal of Physical Chemistry B* **2015,** *119* (25), 7804-7815.
44. Gryczynski, I.; Malak, H.; Lakowicz, J. R., Three-photon excitation of a tryptophan derivative using a fs-Ti : Sapphire laser. *Biospectroscopy* **1996,** *2* (1), 9-15.
45. Vivas, M. G.; Mendonca, C. R., Temperature Effect on the Two-Photon Absorption Spectrum of All-trans-β-carotene. *The Journal of Physical Chemistry A* **2012,** *116* (26), 7033-7038.
46. De Boni, L.; Piovesan, E.; Misoguti, L.; Zílio, S. C.; Mendonca, C. R., Two-Photon Absorption Dependence on the Temperature for Azoaromatic Compounds: Effect of Molecular Conformation. *The Journal of Physical Chemistry A* **2007,** *111* (28), 6222-6224.
47. Borzova, V. A.; Markossian, K. A.; Chebotareva, N. A.; Kleymenov, S. Y.; Poliansky, N. B.; Muranov, K. O.; Stein-Margolina, V. A.; Shubin, V. V.; Markov, D. I.; Kurganov, B. I., Kinetics of Thermal Denaturation and Aggregation of Bovine Serum Albumin. *PLOS ONE* **2016,** *11* (4), e0153495.
48. Sinha, S. S.; Mitra, R. K.; Pal, S. K., Temperature-Dependent Simultaneous Ligand Binding in Human Serum Albumin. *The Journal of Physical Chemistry B* **2008,** *112* (16), 4884-4891.

Chapter 8

8. Molecular Insight onto Dye-Surfactant Interaction at pre-micellar Concentrations: A Combined two-photon Absorption and MD Simulation Study

Both electrostatic as well as hydrophobic interactions play pivotal roles in ligand-surfactant interaction, especially for ionic surfactants. While much study have been reported in the micellar region, less attention has been paid on such interactions at a low (pre-micellar) surfactant concentration. We here study the interaction between a cationic dye Rhodamine 6G (R6G) with surfactants of different charge type: anionic SDS, cationic CTAB and non-ionic Tx 100 using absorption and emission spectroscopy. We identify that R6G forms dimeric (or higher order) aggregates at pre-micellar concentration of SDS. Formation of aggregates is also confirmed from classical simulation measurements. CTAB and Tx 100 do not form any such aggregate, presumably owing to unfavourable electrostatic interactions. For a molecular level understanding we perform two-photon absorption (TPA) spectroscopy for the same systems. TPA allows to calculate two photon absorption cross-section and the change in dipole moment ($\Delta\mu$) between ground and excited states of the dye. We calculate the $\Delta\mu$ and observe that it passes through a maximum at a surfactant concentration half of cmc of SDS. This observation imparts support to earlier quantum mechanical calculation which infers deviation from parallel orientation of dye during surfactant induced aggregation. We extended our measurements and varied the carbon chain length of the anionic surfactant and we found that all of them exhibit a maximum in $\Delta\mu$ while their relative magnitude is dependent on the surfactant carbon chain length.

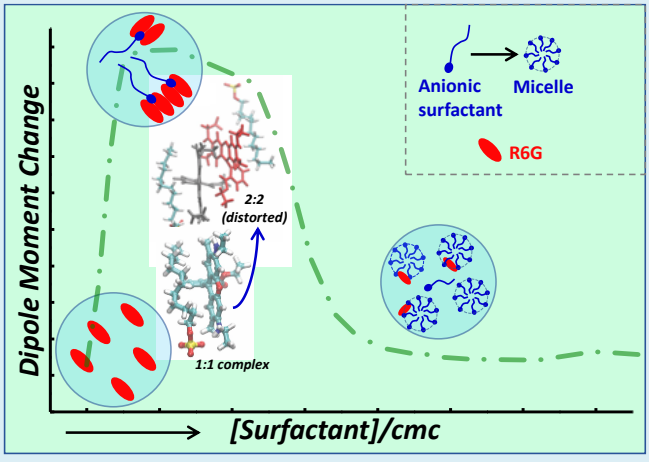

8.1. Introduction

Dye-surfactant interaction has great impact in dye industries as surfactants are widely used to wet and level dyes. Moreover, surfactants can disperse dyes of low solubility, especially which are less soluble in water.[1] Such interactions are complex in nature[2] and strongly depend on the chemical structures of both the dye and the surfactant.[3, 4] It is well accepted that charged dyes can form molecular complexes/aggregates with oppositely charged ionic surfactants through electrostatic interaction.[2, 5-7] These aggregates could be either of H type (sandwich type aggregation in which the dyes show a blue shift in the absorption spectrum with a concomitant weak fluorescence) or of J type (head to tail aggregation in which the dyes show a red shift in the absorption spectra).[8] As the surfactants start forming micelles such complexes are dissolved and the dyes accumulate into the micelles.[9] Different experimental as well as theoretical investigations have been carried out to investigate the spectral properties of dye-surfactant complexes at pre- and post- micellar concentrations.[6, 10-13] These studies have inferred a dramatic change in different spectral properties as well as physical parameters (e.g. ion pair formation rate, conductivity, thermodynamic parameters etc.) during the complex formation (either owing to dye aggregation or surfactant-dye complex formation). While these investigations have mostly been involved on the identification of the onset of such complex formation process, less attention has been paid on the molecular picture of such aggregates, especially in the pre-micellar region. We here attempt a combined experimental and molecular dynamics (MD) simulation study to elucidate the molecular picture of such complex formation. In order to do so we deploy a rather un-conventional spectroscopic technique, namely two-photon absorption (TPA) to intrude into the molecular mechanism of dye-surfactant complex formation.

TPA is a third-order ultrafast nonlinear process wherein a molecule, when irradiated with intense fs laser pulses, simultaneously absorbs two photons and promotes from a lower energy state to a higher one and the total transition energy equals to the sum of the two-photon energy.[14] As the laser beam is very tightly focused, the two-photon process is confined within a very small volume, and thereby making TPA a very sensitive and advantageous tool compared to conventional single photon measurements; moreover in this method biomolecules/ living cells are probed by exciting away from their intrinsic absorption range.[15, 16] Despite being an ultra-sensitive technique, reports using TPA as a probing

technique has mostly been sparse owing mostly to the experimental challenges.[17] TPA, in the recent past, has exclusively been used to address research problems related to polarity modification in neat solvents and their mixtures,[18, 19] in biomolecules[20-22] and in materials.[23, 24] However, their application in self-assembled aggregates remains rather limited. In an initial work Woo et al.[25] have used TPA measurements to investigate micelle formation in an aqueous solution of sodium dodecylsulfate (SDS) using chromophores with D-π-D type structures (where D is a donor group and π is a π-conjugated bridge). Tian et al.[26] studied the TPA properties of a series of multi-branched chromophores in an amphiphilic block copolymer micellar solutions. These previous studies were more focused on reporting the TPA ability of synthesized chromophores rather on the application of TPA technique to explore micellar properties. Bairu et al.[27] reported a TPA process of anionic Coumarin 519 ($C519^{-}$) in various micelles and they showed 2-3 times enhancement of $C519^{-}$ TPA in CTAB micelles. They also used the TPA parameters to measure the surface charge at the CTAB micellar surface (Stern layer). However, related studies are not very frequent in the literature.

In this chapter we choose rhodamine 6G (R6G), a cationic fluorone dye of xanthene family as the two-photon probe.[28] We select three surfactants of different charge types: sodium dodecylsulfate (SDS, negatively charged), cetyltrimethylammonium bromide (CTAB, cationic charged) and Titron X100 (Tx 100, uncharged) to observe the effect of charge on the dye-surfactant interaction. As intuited, negatively charged SDS is found to form complex with the dye, while the other two surfactants remain more or less indifferent. Formation of such pre-micellar complex has also been confirmed using atomistic MD simulation. We then extend our idea to investigate whether the surfactant hydrophobicity could modulate the complex formation, and therefore we systematically vary the chain length of the anionic surfactants: sodium octylsulfate (SOS), sodium decylsulfate (SDeS), sodium dodecylsulfate (SDS) and sodium tetradecylsulfate (TSDS) keeping the cation same. Both single-photon and two-photon measurements show the formation of complex at sub-*cmc* surfactant concentration, which eventually vanishes at and beyond the *cmc*'s. The TPA measurements provides with the unique advantage of calculating two-photon absorption cross section (σ_2) and using the quantum yield values obtained from single photon measurements, one can obtain the difference in the dipole moment ($\Delta\mu$) of R6G as it is excited with an ultrashort pulse. We found a marked change in the $\Delta\mu$ values in the pre-micellar solutions compared to that in bulk water, which unambiguously points towards a distorted orientation of the R6G dipoles in the dye-surfactant complex. Such a distortion has also been confirmed in the

simulation measurements which establish this technique as a powerful tool to investigated dye-surfactant interaction at the molecular level.

8.2. Materials and Methods

- **Experimental:**

All the chemicals, Rhodamine 6G (R6G), cetyltrimethylammonium bromide (CTAB), Triton X-100 (Tx-100), sodium octyl sulfate (SOS), sodium decyl sulfate (SDeS), sodium dodecyl sulfate (SDS) and sodium tetradecyl sulfate (TSDS) were procured from Sigma Aldrich (see chapter 2) and used as received. Millipore water was used as the solvent and all the experiments were performed at 25° C. The dye concentration was kept constant at 8 µM for all the measurements.

We have used the following instruments and methods (*for details see chapters 2, 3*). A *UV-Vis. spectrophotometer* was used for all the absorption spectrum measurements and to probe the local environment *fluorescence* measurements done by *steady-state spectroscopy*.

- **We calculated the corresponding oscillator strength[18] using the following relation:**

$$f_{osc} = 4.33 \times 10^{-9} \int \varepsilon(\bar{\nu}) d\bar{\nu} \qquad (8.2.1)$$

Where, $\varepsilon(\bar{\nu})$ signifies the molar extinction coefficient dispersion and $\bar{\nu}$ is in wavenumber.

- **Estimation of the number of dye molecules per micelle:**

Number of dye molecules in the solution, $N_d = N_A \times \text{concentration of dye}$

In our case, we have fixed the dye concentration at 12 µM

So the $N_d = 6.023 \times 10^{23} \times 12 \times 10^{-6}$ /lit

Now the number of surfactant molecules in the solution at the CMC,

$$N_s(/lit) = N_A \times \text{critical micellar concentration of surfactant}$$

If N_{Agg} is the aggregation number of the surfactant then the number of micelles, $N_m = \frac{N_s}{N_{Agg}}$

For the calculation of N_m, we used the recorded aggregation number of various surfactants, such as CTAB (N_{Agg}~91), Tx100 (N_{Agg}~142), TSDS (N_{Agg}~71), SDS (N_{Agg}~52), SDeS (N_{Agg}~44) and SOS (N_{Agg}~38).[29-31]

So the number of dye molecule per micelle, $N_{d/m} = \frac{N_d}{N_m}$

Two-photon induced fluorescence measurements were performed on a home-built *TPA spectroscopy* as described earlier[15] We use the reported σ_2 value of R6G (σ_{R6G} ~ 10.3 GM) in water as the standard.[19] All the analyses were performed in Mathematica 9.

- **Simulation details:**

All atomistic classical molecular dynamics (MD) simulations were carried out using the GROMACS software (version 2019.6).[32] Two separate systems were simulated containing (i) 1 R6G and 1 SDS molecule and (ii) 2 R6G and 2 SDS molecules in aqueous solution. Both systems were solvated in a cubic box of length 5 nm with periodic boundary conditions in all directions. GAFF force field was adopted for R6G and SDS molecules, and TIP3P model was used for water.[33, 34] The temperature and pressure were maintained at 300 K and 1 atm respectively using the velocity rescale thermostat and Parrinello-Rahman barostat.[35, 36] After an equilibration phase of 2 ns in the NPT ensemble, the production trajectory was continued for 20 ns and frames were saved every 10 ps.

8.3. Results and Discussion

Single-photon absorption spectroscopy (SPAS):

We measure the single photon absorption of R6G in water and in presence of different surfactants (Figures 8.3.4a and 8.3.1). We observe that the absorption maximum of R6G in pure water (blue broken line in figure 8.3.4a) appears at ~525 nm along with a faint shoulder band peaking at ~ 490 nm which perhaps appears due to the formation of dye-dimer or higher-order aggregates.[37] Upon the addition of SDS at very low concentration (0.25 mM) the absorption quenches substantially and two distinct peaks appear at ~510 nm and ~570 nm. Similar result was also observed previously and this phenomenon has been attributed due to the dimerization of R6G in presence of low concentration of SDS.[6, 13] Additionally, an isosbestic point (IBP) is also observed at ~555 nm (figure 8.3.4a) (in the pre-*cmc* to *cmc* concentrations). Appearance of such IBP further strengthens the co-existence of dimeric and monomer species of the dye in presence of pre-micellar SDS.[38] Absorption feature of R6G does not change appreciably upon further addition of SDS up to ~3 mM; beyond this concentration it increases with SDS addition up to 8 mM (*cmc* of SDS)[6, 39] and no further increase in absorption intensity is observed beyond the *cmc*. The same trend is observed for the other anionic surfactants (figure 8.3.1f). We also measure the absorbance of R6G in presence of a cationic CTAB (figure 8.3.1b) and non-ionic surfactant Tx 100 (figure 8.3.1a).

We do not observe any noticeable change in the absorption features upon the addition of these surfactants (figure 8.3.1e).

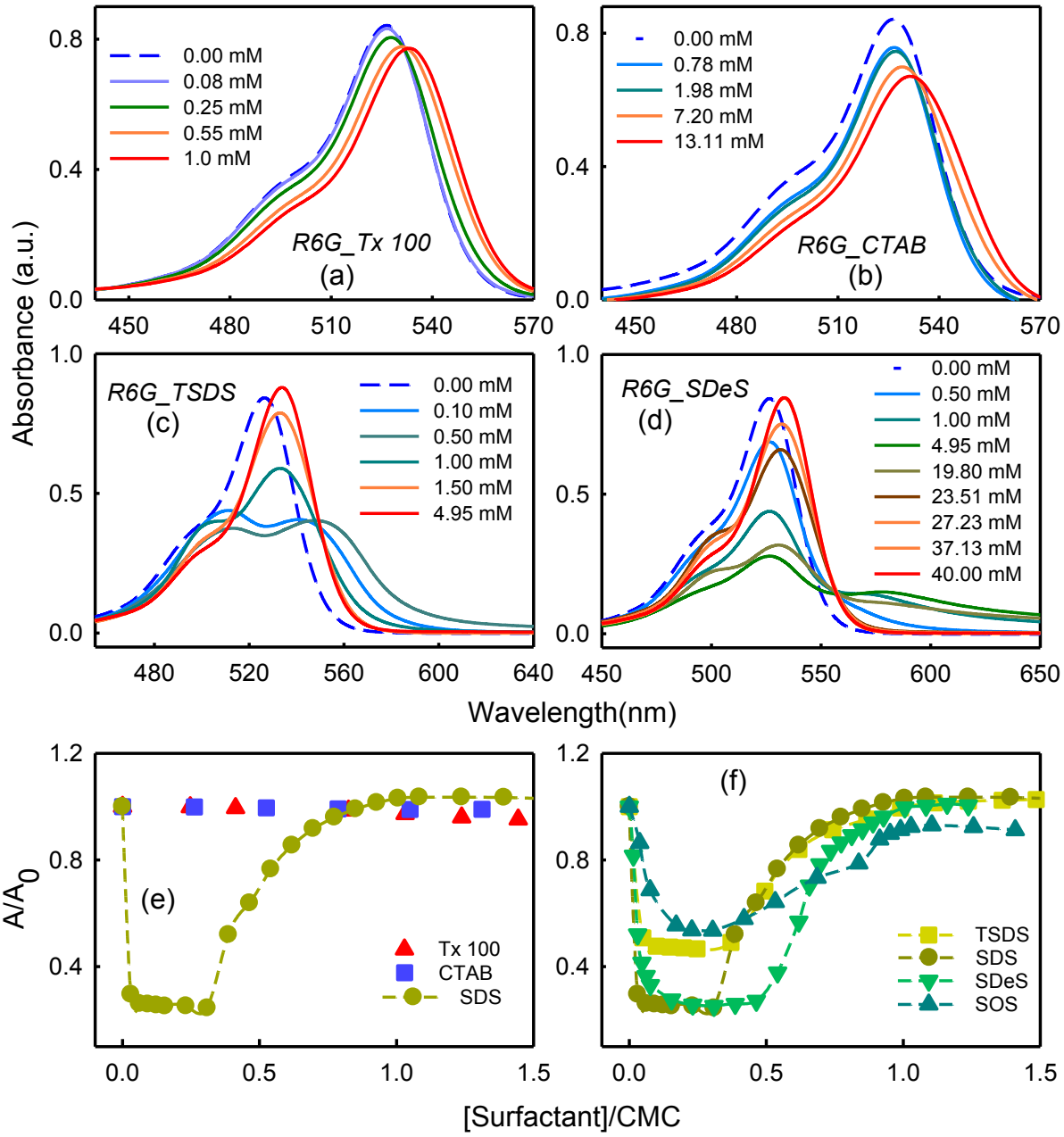

Figure 8.3.1: Steady-state (single photon) absorption spectra of R6G as a function of different surfactant concentration in (a) Tx 100 (b), CTAB (c), TSDS and (d) SDeS respectively. The plot of A/A_0 (where, A_0 and A are the maximum absorbance in the absence and in presence of different surfactant concentration) (e) in three different charge surfactants (Tx 100, CTAB, and SDS), (f) in different chain length of the alkyl group of anionic surfactants (TSDS, SDS, SDeS, and SOS) (normalized to the corresponding cmc).

We deconvolute all the absorption spectra to estimate the monomer-to-dimer ratio of R6G in presence of different surfactants. A representative deconvolution is shown in figure 8.3.2 for R6G in pure water and in SDS solution at C_s~0.38 (C_s =[surfactant]/*cmc*; we assume

that *cmc* of surfactants do not change appreciably in presence of the dye at low concentrations).[40] We plot the monomer to dimer ratio as a function of C_s in figure 8.3.4b. We observe that for all the anionic surfactants a maximum in dimerization is observed at C_s <0.5. The lowest surfactant concentration for the ratio maximum is registered in case of SOS (C_s~0.15), which has the lowest carbon chain length. The maximum extent of dimerization is observed in SDeS (figure 8.3.4b). We further calculate the ratio in presence of CTAB (figure 8.3.4b) and observe no change in it up to four times the C_s. In Tx 100 (figure 8.3.4b) the ratio does not change up to C_s=1 beyond which it increases linearly. It could be noted here that the pre-micellar dye-surfactant aggregates, formed in case of anionic surfactants, are non-existant in the (post)micellar region as those dissociate into monomeric dyes, and eventually get solubilized within the palisade layer of the micelles, thereby offering no further change in the relative absorbance (figure 8.3.4b).[11]

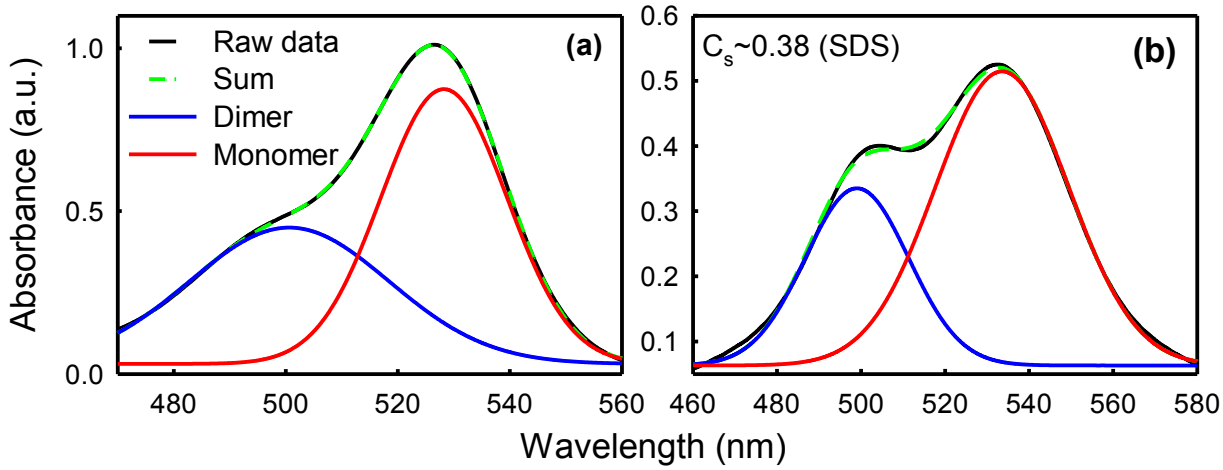

Figure 8.3.2: Representative deconvoluted curve of steady-state (single photon) absorption spectra of R6G (a) in pure water and (b) in c_s ~0.38 SDS surfactant respectively.

We then calculate and plot the oscillator strength, f_{osc} of R6G in presence of different surfactants as a function of C_s (figure 8.3.3). The f_{osc} value is indicative of solvent polarity as it increases with the solvent polarity.[18] f_{osc} of R6G in water is found to be ~1.75 which is consistent with earlier studies.[38] This value shows a non-linear dependence with anionic surfactant concentration (figure 8.3.3b); it passes through a minimum at a pre-micellar concentration; at and beyond *cmc* its value becomes comparable to that in bulk water. The calculated values of f_{osc} are used to estimating dipole moment from TPACS measurements as discussed in the subsequent sections.

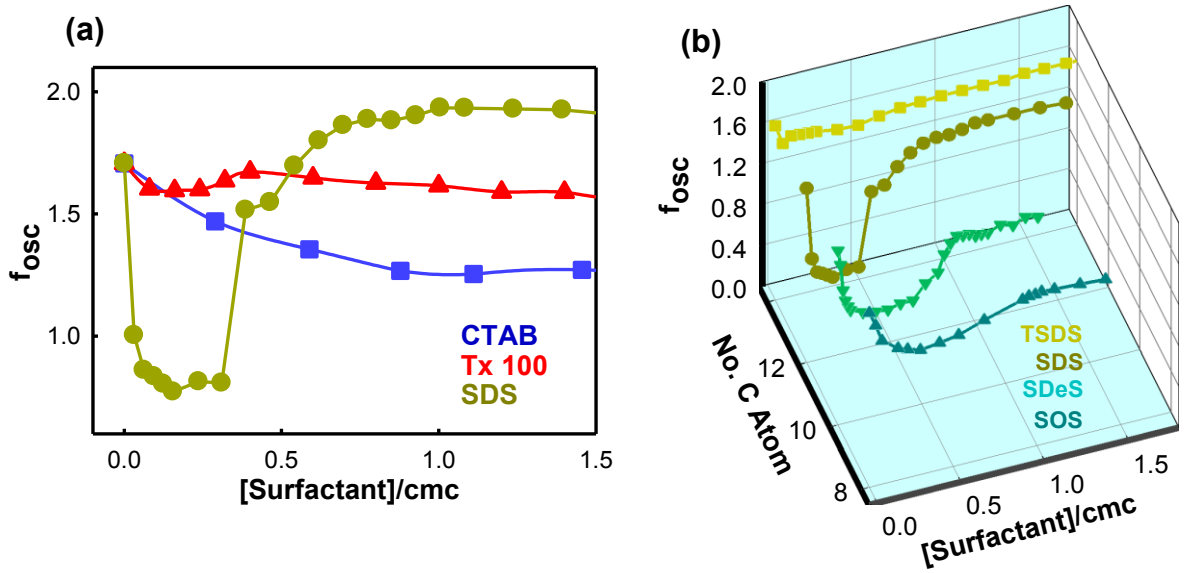

Figure 8.3.3: Oscillator strength of R6G (a) in different charge type surfactants (Tx 100, CTAB, and SDS) and (b) in different chain length of the alkyl group of anionic surfactants (TSDS, SDS, SDeS, and SOS) as a function of surfactant concentration (normalized to the corresponding cmc).

Single-photon fluorescence (SPF) spectroscopy measurements:

Emission profile of R6G in pure water is shown in figure 8.3.4c (blue broken line) having emission maximum at 556 nm.[6, 41] Some representative emission spectra of R6G at different SDS concentrations are also shown in the same figure. We also plot the relative fluorescence intensity of R6G in presence of different surfactants (figure 8.3.4d). Emission of R6G quenches severely upon the addition of small amount of SDS (c_s~0.03) (figure 8.3.4c) with a concomitant blue shift of ~6 nm. The observed quenching of R6G fluorescence intensity at low SDS concentration is attributed to the dimerization of the dye.[6] Maximum quenching is observed at ~0.5C_s. It is interesting to note that emission peak suffers a red shift (~9 nm) beyond c_s~0.5 which does not change further upon increasing the SDS concentration. Fluorescence intensity saturates in micellar environment (C_s>1) owing to complete dissolution of the aggregated R6G in the corresponding micelles. Emission intensity quenching follows the order: TSDS>SDS>SDeS>SOS (figure 8.3.4d) which infers that more hydrophobic environment leads to more dimerization or may be higher order aggregation of the dye. In contrast to anionic surfactants, we do not observe any significant change in the fluorescence intensity of R6G in presence of CTAB up-to C_s~1.5 (figure 8.3.4d, upper panel); at a higher CTAB concentration (C_s~3) fluorescence intensity quenches slightly with a bathochromic shift (~7 nm) due to the electrostatic repulsion between the dye and the surfactant head groups[5] (figure 8.3.5b). In case of Tx 100 the fluorescence intensity decreases

mildly with the surfactant concentration along with a ~7 nm bathochromic shift (figure 8.3.5a). Hydrophobic interaction between Tx 100 micelle and the hydrophobic part of the dye leads to dye penetration in micellar interior which results in the observed decrease in the fluorescence intensity with the bathochromic shift[42] as has previously been reported.[43]

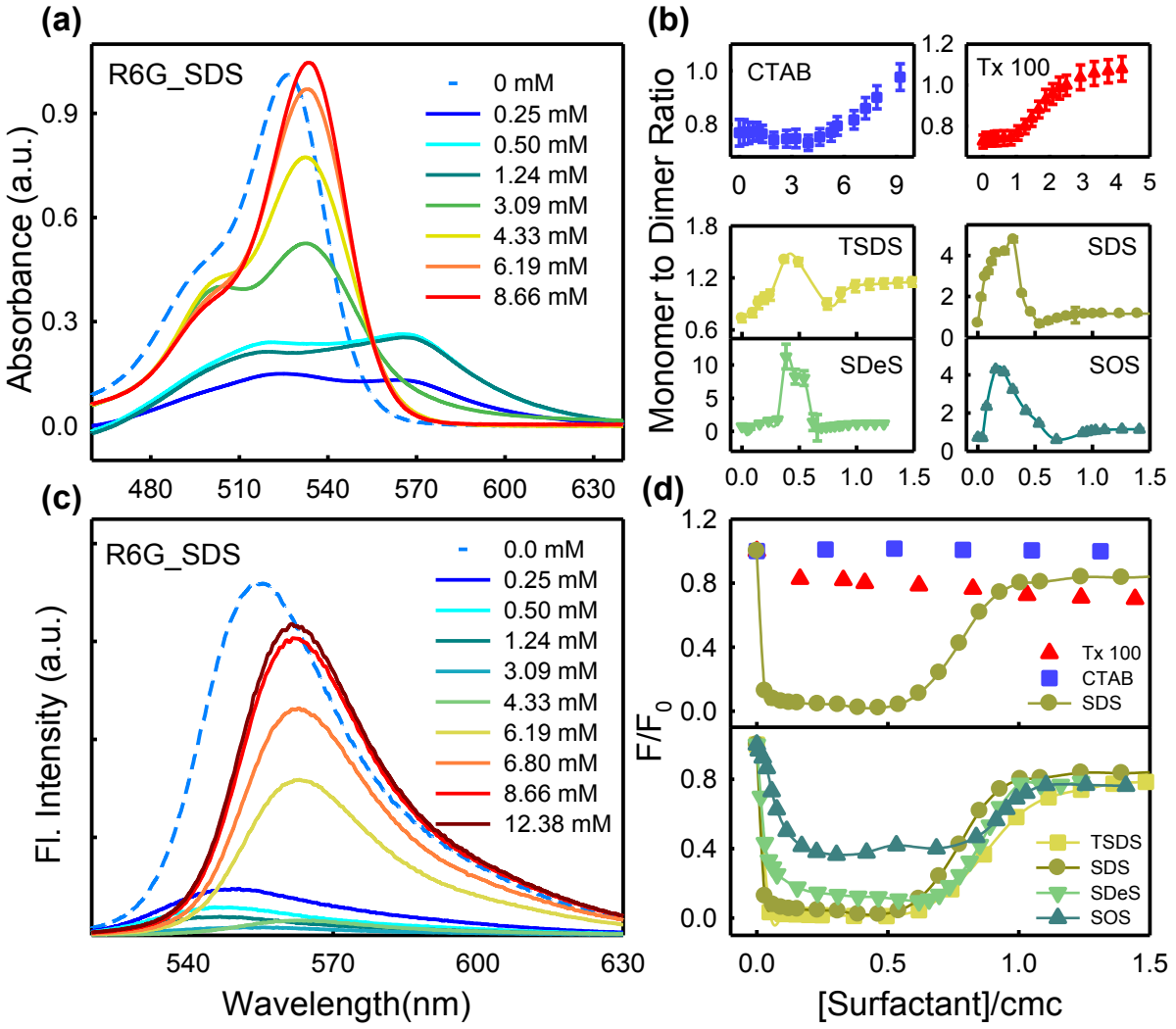

Figure 8.3.4: (a) Steady-state (single photon) absorption spectra of R6G in water and in presence of SDS at different concentrations. (b) Ratio of monomer to dimer population of R6G in presence of surfactant(s) as a function of surfactant concentration (normalized to the corresponding cmc). (c) Steady-state (single photon) emission spectra of R6G at different SDS concentrations. (d) Plot of F/F_0 (where, F_0 and F are the emission maxima in absence and in presence of surfactant) as a function of surfactant concentrations (normalized to the corresponding cmc).

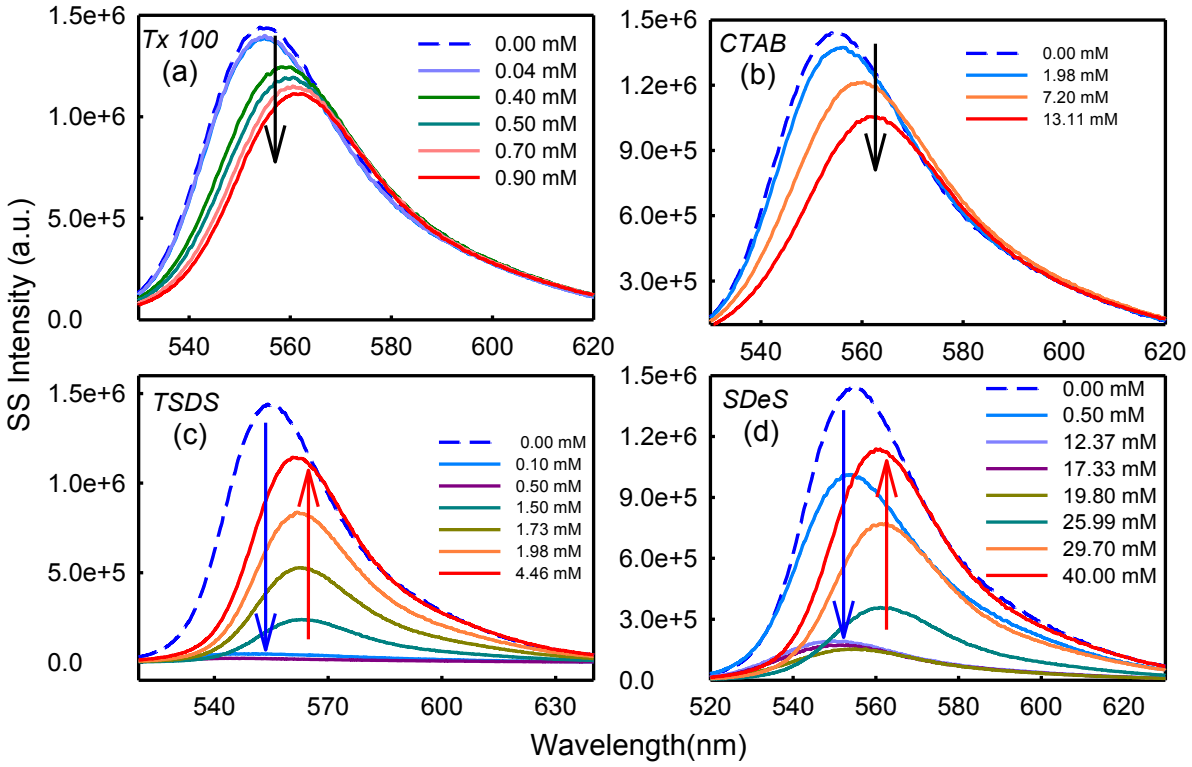

Figure 8.3.5: Steady-state (single-photon) emission profile of R6G as a function of different surfactant concentration in (a) Tx 100 (b), CTAB (c), TSDS and (d) SDeS respectively.

Single-photon quantum yield (QY) measurements:

We calculate the fluorescence quantum yield (*QY*) of R6G in presence of different surfactants and plot them as a function of c_s (figure 8.3.8a and table 8.3.1). *QY* value of R6G in water is found to be ~0.95, which is comparable to the previous reports.[44] *QY* does not change appreciably in CTAB throughout all the studied concentrations. Only a subtle change is observed in case of Tx 100 (figure 8.3.8a). In SDS, however, we observe a strikingly nonlinear behaviour as a function of surfactant concentration. We observe an initial substantial suppression of *QY* at low C_s (<0.03), which then remains almost unchanged up to C_s~ 0.4-0.6; *QY* value starts to increase beyond C_s~0.6 and in the micellar region it reaches a constant value. Similar behaviour is observed in all the other anionic surfactants and the QY_{min} follows the order QY_{SOS} (C_s~0.7)> QY_{SDeS} (C_s~0.6)> QY_{SDS} (C_s~0.55)> QY_{TSDS} (C_s~0.5) (figure 8.3.9a).

Two-photon measurements:

Two-photon induced fluorescence (*TPIF*) spectra of R6G (excited using 800 nm ultrafast laser) in absence and in presence at surfactants of different concentrations are shown

in figure 8.3.6. To verify that this fluorescence emanates solely from the *TPA* process we measure the fluorescence intensity of R6G (at 555 nm) in water at different laser powers. We observe a linear increase in the fluorescence intensity as a function of the laser power with a slope of 1.92 (Scheme 2.7, chapter 2), which is close to the ideal value of 2; this unambiguously confirms the TPA process responsible for the observed fluorescence.[19, 45]

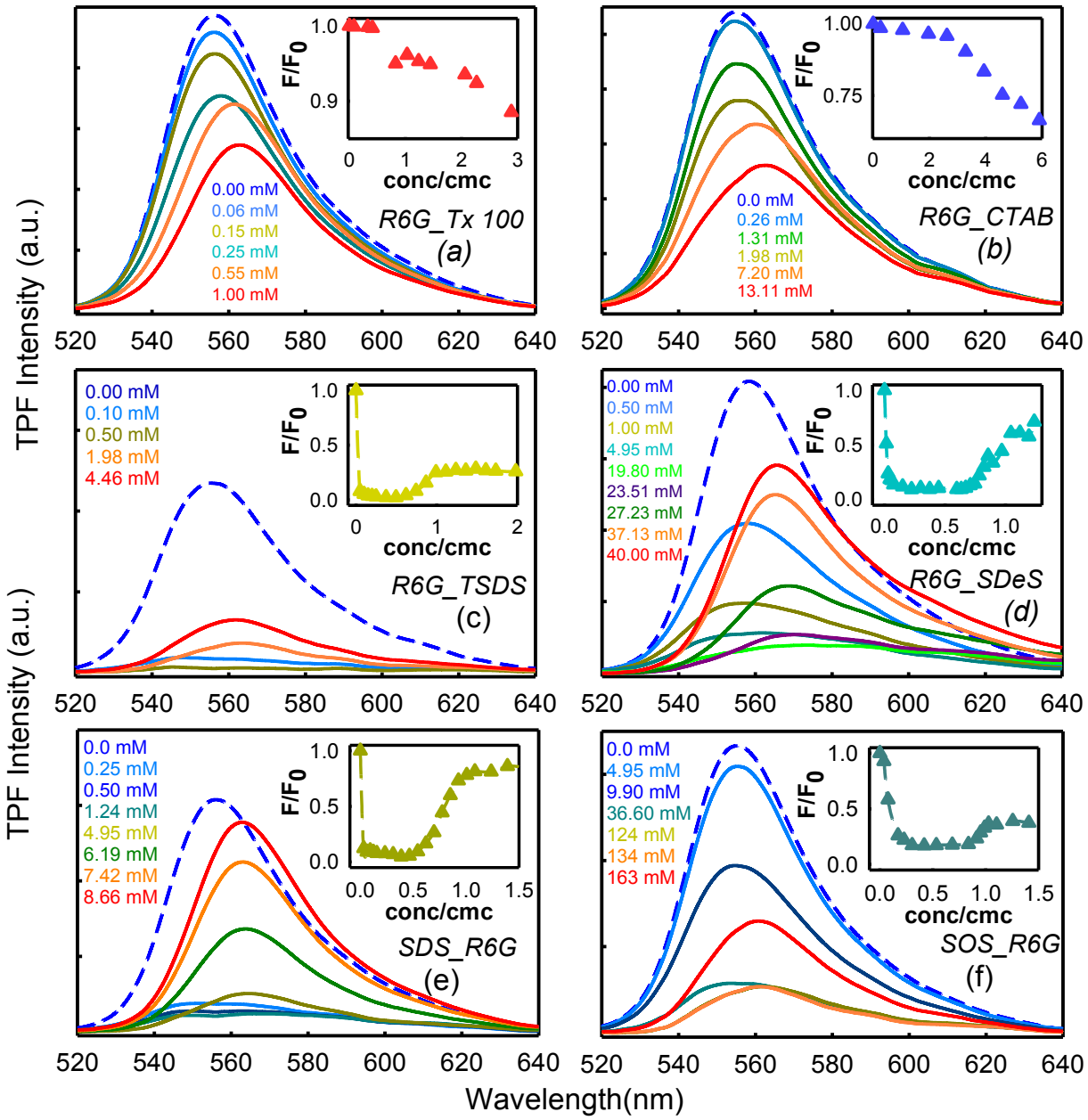

Figure 8.3.6: Two-photon induced fluorescence (TPIF) spectra of R6G as a function of different surfactant concentrations in presence of (a) Tx 100 (b), CTAB (c), TSDS (d) SDeS, (e) SDS and (f) SOS respectively. Inset plot represents F/F0 (where, F0 is TPE intensity in absence and F is in presence of a different concentration of surfactant) as a function of different surfactant cs (concentrations/cmc).

The *TPIF* of R6G in Tx 100 (figure 8.3.6a) and CTAB (figure 8.3.6b) shows a mild decrease in the TPIF emission intensity (at emission maximum ~ 555 nm) up-to the micellar

concentration beyond which it decreases regularly. Contrarily, in all the anionic surfactants we observe a drastic quenching of two photon emission intensity (*TFEI*) at low C_s which eventually is recovered at the cmc.

From the *TPIF* measurements one can calculate the two-photon absorption cross-section (σ_2) using the mathematical procedure described in the material and method section. We calculate and plot σ_2 of R6G in pure water and in different surfactant systems as a function of surfactant concentration (figure 8.3.8b and 8.3.9b). The observed value of σ_2 of R6G in pure water is ~10.4 GM which is in good agreement with the previous results.[19, 46] σ_2 is observed to decrease slightly with an increases in the CTAB concentration (figure 8.3.8b) while in Tx 100 it increases mildly (figure 8.3.8b). The trend in SDS is rather interesting as it increases sharply by 3.5-fold up to C_s~0.5; beyond which it decreases and at C_s~1.0 the value becomes equal to that in water. Further increase in the SDS concentration does not produce any noticeable change. Such a large enhancement in σ_2 has previously been observed in porphyrin-type molecule tetrakis(4-sulfonatophenyl) porphyrin diacid (H_4TPPS^{2-}), the enhancement being explained in terms of the formation of J-aggregates of the dye molecules[47]. In the present investigation we do observe changes in the single-photon absorption (figure 8.3.4a) and emission (8.3.4c) at low anionic surfactant concentrations as a consequence of dye aggregation, which is responsible for the observed change in σ_2 also. As $C_s \rightarrow cmc$ the the complexes disintegrate and σ_2 regain their value as that in their monomeric forms. For a more quantitative apprehension we estimate the number of dye molecules per micelle ($N_{d/m}$) (see materials and methods for details) and for SDS this value is ~0.08, while it is 0.43 for TSDS, 0.02 for SOS and 0.001 for SDeS, respectively. This estimation shows that the dye molecules are not aggregated in micelles. Previously Bairu et al.[27] have observed a 2.5 fold increase in σ_2 of anionic C519 dye in CTAB micelles while no such enhancement was observed in either SDS or Tx 100 micelles. The enhancement in σ_2 in CTAB micelles was due to the electrostatic fields appearing from the Stern layer of the CTAB where the C519 molecule gets solubilized. It is worth mentioning here that C519 molecules do not self-aggregate and no signature in the pre-micellar region was expected. We measure σ_2 of R6G in presence of different anionic surfactants (figure 8.3.9b) and observe identical σ_2 profiles in all surfactant solutions with a maximum ($\sigma_{2,max}$) occurring at C_s~0.5. The numerical value of $\sigma_{2,max}$ is found to be higher in SDS and TSDS compared to that in SOS and SDeS. In a previous study σ_2 has been reported to be dependent on the polarity (as estimated by the

dielectric constant) of common solvents ($CHCl_3$, DCM, DMF, MeOH) and it was observed that σ_2 value increases with the decreasing polarity of the solvents.[19] Our result suggests that it is the dimerization of R6G molecules followed by their interaction with surfactant monomers (due to opposite charge) that governs the σ_2 profile; also, the magnitude of σ_2 changes as the carbon chain length of the surfactant(s) changes.

Simulation results:

Both single and two-photon measurements have indicated towards the formation of SDS-R6G complex formation in the pre-micellar regions. In order to establish a molecular picture of the complexation process we have carried out atomistic MD simulations of several combinations of R6G and SDS mixture in the aqueous solution. It is expected that negatively charged SDS would offer a strong propensity to interact with the positively charged R6G. In our simulation setup of 1 R6G and 1 SDS molecule, they spontaneously form a complex and remains stable for the duration of 20 ns of simulation time. Figure 8.3.7a (inset) shows the temporal evolution of the non-bonded interaction energy between these two molecules. The dissection of Coulomb and Lennard Jones components clearly establishes that this interaction is primarily electrostatic in nature. Based on the wide distribution of the electrostatic interaction energy (figure 8.3.7a), we may speculate about the multiple modes of interactions and heterogeneity in the relative orientation of the SDS and R6G molecules. A representative structure of the complex is shown in figure 8.3.7b.

In order to investigate the mode of interaction of SDS with the R6G dimers, we perform a separate simulation containing two R6G and two SDS molecules. We observe the SDS molecules to be frequently interacting with the R6G dimer (figures 8.3.7c and 8.3.7d) as indicated by the spectroscopic measurements also. Interestingly, we observe quite a noticeable variation in the relative orientation and packing in the R6G dimer complex in the presence of SDS. The structure shown in figure 8.3.7c has a parallel packing of the monomers, whereas the structure shown in figure 8.3.7d has a distorted geometry. This observation is remarkable in the sense that such distorted orientation has previously been predicted in a quantum mechanical study[48] and is expected to impact the dipolar orientation of the R6G molecules in the complex. One, therefore, can expect a change in the dipole moment of the SDS-R6G complex at pre-micellar concentrations compared to that in the pure water. TPAS opens up with the unique opportunity to experimentally obtain the dipole

moment change as a dye molecule is excited with an ultrashort laser. We calculate the change in dipole moment in R6G in presence of water and pre-*cmc* surfactant solutions in the following section.

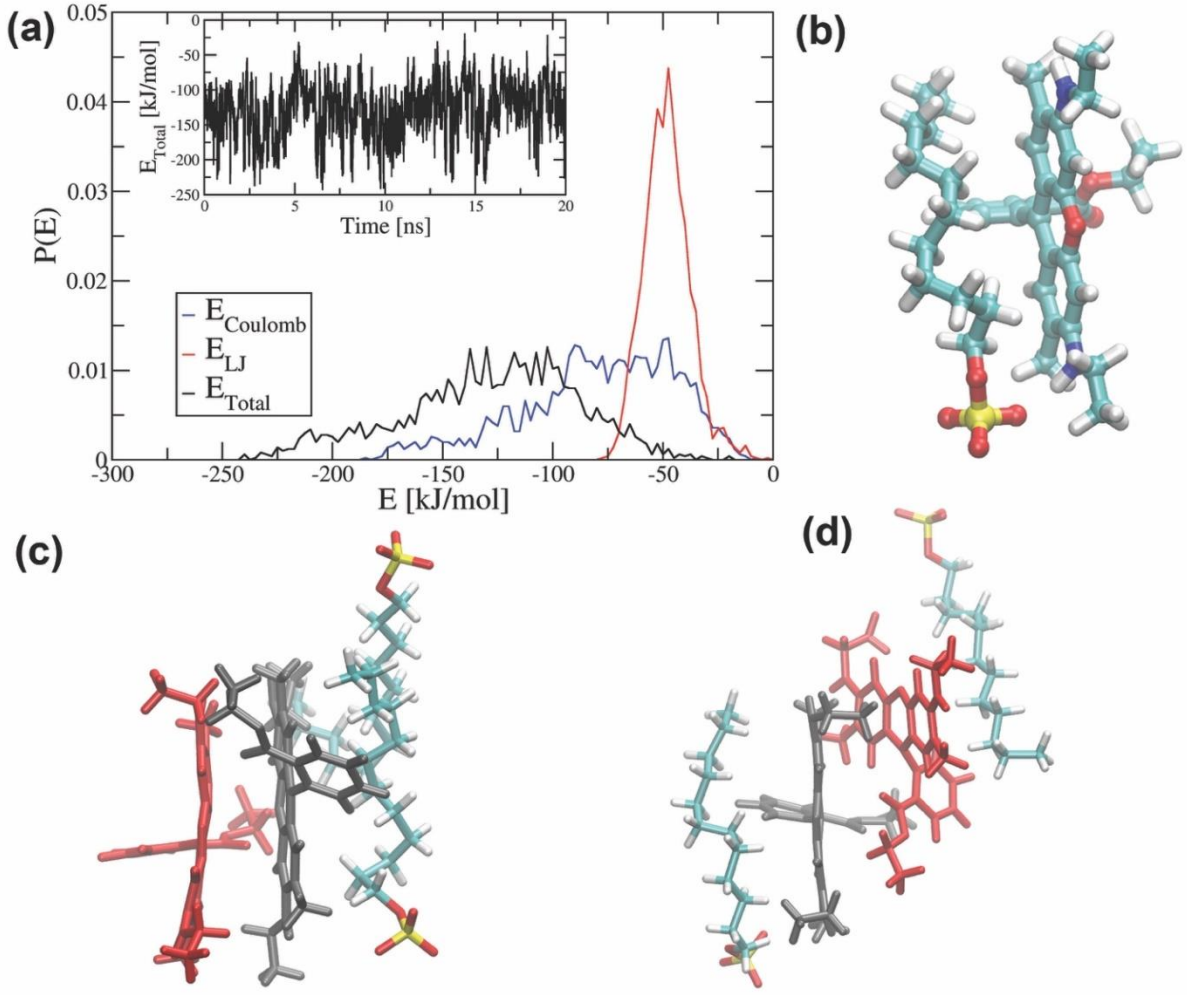

Figure 8.3.7: (a) Probability distribution of the non-bonded interaction energy terms (decomposed into Coulomb, Lennard-Jones and total) between R6G and SDS as computed from the 20 ns MD simulation trajectory (inset: time evolution of the total interaction energy), and representative snapshots of (b) 1:1 R6G-SDS complex, (c) 2:2 complex with parallel stacking of R6G dimer, and (d) 2:2 complex with distorted geometry of R6G dimer (R6G molecules are coloured in red and dark grey).

Dipole moment (Δμ) measurements:

As discussed, σ_2 is a function of solvent polarity[18, 19] and therefore measurement of this parameter could serve as a potential marker of the (micro)polarity of the immediate surroundings (in the present case the pre-micellar aggregate) of a dye. Assuming that laser induced transition in the dye takes place solely between the ground and the lowest electronic

excited state[49, 50] the corresponding change in the dipole moment of the fluorophore molecule can be correlated to the spectroscopic parameters as[18]:

$$\sigma_2 \sim \frac{(\Delta\mu)^2 f_{osc}}{\Gamma} \qquad (8.3.1)$$

where $\Delta\mu = \mu_e - \mu_g$, is the difference between the dipole moments of the fluorophore in the ground (μ_g) and in the lowest excited electronic states (μ_e), f_{osc} is the calculated oscillator strength (using equation 8.2.1) and Γ is the full width at half maximum (FWHM) of the single-photon absorption spectrum. It is to mention here that since we are interested in the change in the dipole moment of the individual R6G molecules, we deconvolute the absorption spectrum of R6G in presence of different surfactants and the Γ values are obtained accordingly (as mentioned in the single photon absorption section) (figure 8.3.2).

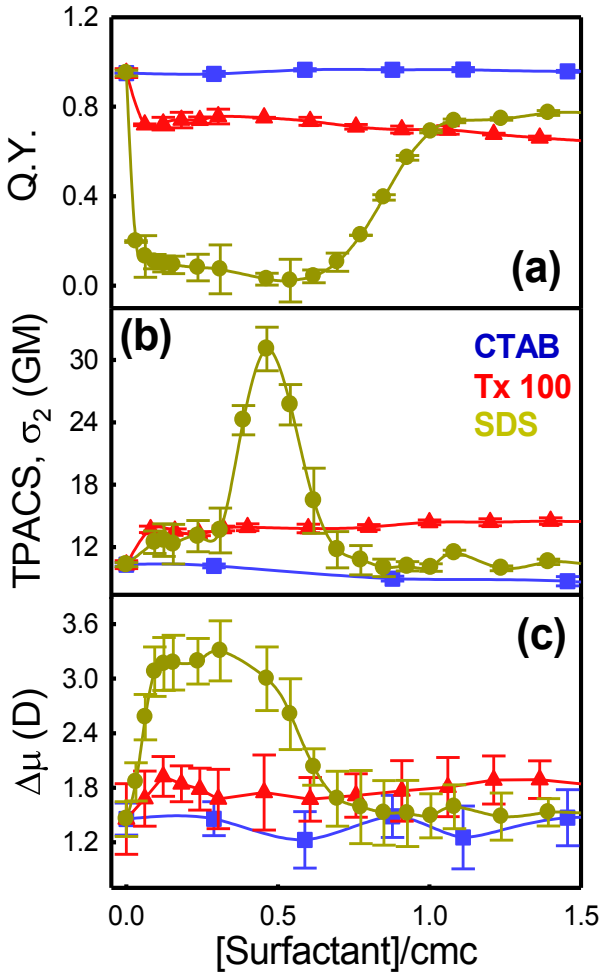

Figure 8.3.8: (a) Quantum yield, (b) two-photon absorption cross-section (σ_2) and (c) change of dipole moment ($\Delta\mu$) of R6G as a function of surfactant (Tx 100, CTAB, and SDS) concentration (normalized to the corresponding cmc).

The calculated value of $\Delta\mu$ of R6G in water is found to be ~1.45 D, which is a comparable to the earlier result obtained by using "Bakshiev and Kawski–Chamma–Viallet Polarity" approach.[44] This comparability validates the approximations we made in estimating $\Delta\mu$. We now calculate the $\Delta\mu$ values of R6G in all the surfactant solutions (table 8.3.2) and plot them as a function of C_s (figure 8.3.8c and 8.3.9c). In CTAB, $\Delta\mu$ does not change appreciably with C_s and the value remains the same as that in pure water. In Tx 100 the $\Delta\mu$ value does not show any marked trend up-to C_s=1 beyond which it remains almost constant at ~1.8 D. Interestingly, in SDS solutions $\Delta\mu$ initially increases markedly up to C_s ~0.3 to reach a maximum value of ~3.3 D at C_s~0.4; further increase in C_s decreases $\Delta\mu$ and at the *cmc* it reaches a value similar to that in water. It therefore seems evident that the change in the dipole moment occurs only in anionic surfactant solutions in which cationic R6G molecules aggregate with the surfactants. We next try to explore whether the chain length of surfactant could modulate the extent of change in the dipole moment. We measure and plot $\Delta\mu$ as a function of C_s in different anionic surfactants and we observe comparable trend (as SDS) as $\Delta\mu$ passes through a maximum (figure 8.3.9c). Importantly we found that $\Delta\mu$ profiles are indeed surfactant dependent as the maximum value follows the order: SOS< SDeS< SDS >TSDS.

While rationalizing the observation we need to understand that redistribution of the atomic charge in R6G molecule at the excited state causes the observed change in the dipole moment, specifically in the pre-micellar region. The single photon spectroscopic study has confirmed the formation of pre-micellar aggregates which is also supported by electrostatic and hydrophobic interactions between positively charged dye and anionic surfactant monomers.[51] A previous study[38] has revealed that electrostatic interactions between anionic azo dye and cationic CTAB surfactant, combined with hydrophobic effect and π-π interactions play a major role in aggregate formation, the size of which depends on surfactant alkyl group, loading ratio of dye to surfactant concentration. It was also been observed that the stability of aggregation enhances with the hydrophobic tail length of the surfactant.[52] This argument could also hold good for the present cationic dye-anionic surfactant aggregates. At a low SDS concentration, a strong electrostatic interaction between the two oppositely charged molecules (R6G and SDS) results in the formation of a sandwich type aggregation with a single SDS molecule neutralizing the coulombic repulsion between two R6G molecules. As a result the distance between dye monomers reduces inducing dimer or higher-

order aggregate formation.[6, 7] Our simulation results also support the aggregate formation in the pre-micellar region.

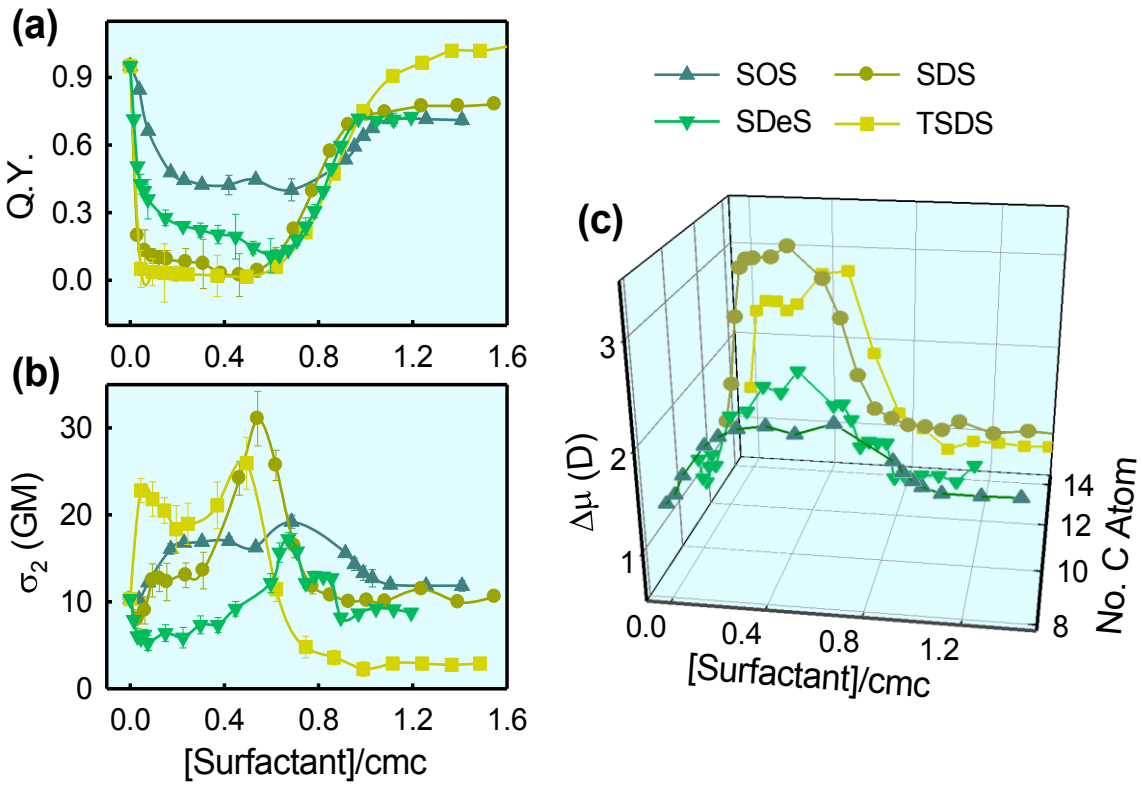

Figure 8.3.9: (a) the quantum yield, (b) the two-photon absorption cross-section (σ_2) and (c) change of dipole moment ($\Delta\mu$) of R6G as a function of surfactant (TSDS, SDS, SDeS, and SOS) concentration (normalized to the corresponding cmc).

Confirming the formation of such aggregation we now look for the possible rationale behind the observed change in $\Delta\mu$. As the definition stands, $\Delta\mu$ identifies a change in the ground-state vs. excited state electronic configuration of the dye molecules. Our observation leads to conclude that due to the dye aggregation in presence of anionic surfactants, the dipolar orientation of R6G changes in such a manner that its net magnitude decreases as compared to that in bulk water. An earlier quantum mechanical calculation[48] has identified that in such complexes the angular orientation of the phenyl substituents in R6G is asymmetric as they deviate from the parallel arrangement resulting in an oblique orientation in the transition dipole moment, which results in the quenching of R6G fluorescence. This theoretical model is therefore being validated in the present experimentation. Noteworthy is that $\Delta\mu$ reaches to a maximum (figure 8.3.9c) where the dye aggregation is the maximum (figure 8.3.4c), beyond that the dye starts to disaggregate and hence the decrease of $\Delta\mu$. After micellization, the aggregated species are dissolved in the micelle, wherein each micelle

contain a single dye only and consequently the $\Delta\mu$ value returns to the value similar to that in water (figure 8.3.9c). As the figure also suggests the maximum change in $\Delta\mu$ is also dependent on the surfactant carbon chain length. The dipolar orientation between the two dipoles of R6G deviates from being parallel and perhaps such deviation is also dependent on the hydrophobic interaction between the surfactant and R6G.

8.4. Conclusions

In this chapter, investigation unambiguously establishes TPAS as a potential tool to investigate the molecular mechanism of the ever-important dye-surfactant interaction. We identify that at pre-micellar concentrations monomeric anionic surfactants get solubilized in cationic dye dimers, which in turn, distorts the parallel orientation of the dyes. More importantly, such distortion has been found to be dependent on the surfactant hydrophobicity also, which is intriguing keeping in mind that the interaction is predominantly electrostatic in nature. A more detailed and systematic experimental and simulation investigation is needed to explore the interaction pattern.

Table 8.3.1: Single-photon quantum yield of different charge types of the surfactant inside R6G dye in different concentrations of surfactants.

Single-photon quantum yield (ϕ) measurements							
Tx 100		**CTAB**		**SOS**		**SDeS**	
C_s	ϕ	C_s	ϕ	C_s	ϕ	C_s	ϕ
0.00	0.950±0.020	0.00	0.950±0.001	0.00	0.950±0.009	0.00	0.950±0.023
0.08	0.719±0.004	0.29	0.946±0.011	0.04	0.846±0.016	0.02	0.715±0.000
0.16	0.724±0.028	0.59	0.965±0.005	0.08	0.663±0.001	0.03	0.506±0.010
0.24	0.740±0.035	0.88	0.965±0.010	0.17	0.478±0.004	0.04	0.427±0.044
0.32	0.739±0.015	1.11	0.965±0.009	0.23	0.444±0.014	0.06	0.397±0.029
0.40	0.756±0.033	1.46	0.958±0.004	0.30	0.424±0.002	0.07	0.360±0.088
0.60	0.750±0.002	2.19	0.958±0.004	0.42	0.423±0.044	0.15	0.277±0.035
0.80	0.734±0.018	3.00	0.940±0.000	0.53	0.446±0.006	0.22	0.241±0.015
1.00	0.709±0.010	3.59	0.925±0.001	0.69	0.401±0.049	0.30	0.223±0.031
1.20	0.697±0.016	4.38	0.931±0.003	0.91	0.536±0.019	0.37	0.203±0.041
1.40	0.696±0.019	5.11	0.936±0.008	0.95	0.593±0.013	0.45	0.193±0.060
1.60	0.677±0.004	5.83	0.923±0.006	0.99	0.640±0.005	0.52	0.145±0.028
1.80	0.660±0.008	6.22	0.954±0.006	1.03	0.675±0.004	0.60	0.109±0.076
2.00	0.647±0.014	7.29	0.934±0.015	1.10	0.714±0.003	0.63	0.112±0.006
2.20	0.637±0.020	8.02	0.932±0.004	1.26	0.715±0.009	0.67	0.135±0.016
2.40	0.628±0.013	8.67	0.920±0.006	1.41	0.711±0.022	0.71	0.178±0.023
						0.75	0.239±0.037
SDS		**TSDS**				0.78	0.307±0.029
0.00	0.950±0.013	0.00	0.950±0.001			0.82	0.397±0.017
0.03	0.197±0.004	0.05	0.050±0.002			0.86	0.499±0.008
0.06	0.131±0.094	0.10	0.036±0.001			0.89	0.597±0.006
0.09	0.107±0.022	0.15	0.033±0.002			0.97	0.718±0.007
0.12	0.097±0.036	0.20	0.029±0.002			1.04	0.708±0.010
0.16	0.093±0.039	0.25	0.026±0.005			1.12	0.713±0.029
0.24	0.081±0.039	0.37	0.020±0.000			1.19	0.725±0.016
0.39	0.029±0.002	0.62	0.059±0.028				
0.46	0.023±0.003	0.75	0.213±0.007				
0.54	0.042±0.019	0.87	0.473±0.006				
0.62	0.105±0.041	0.99	0.750±0.001				
0.70	0.226±0.001	1.12	0.907±0.003				
0.77	0.395±0.012	1.24	0.966±0.004				
0.85	0.571±0.011						
0.93	0.689±0.006						
1.01	0.736±0.008						
1.08	0.745±0.006						
1.24	0.772±0.011						
1.39	0.773±0.012						
1.55	0.781±0.004						

Table 8.3.2: Dipole moment measurements of various surfactant charge forms within R6G dye at various surfactant concentrations.

Dipole moment (Δμ, Debye) estimation							
Tx 100		**CTAB**		**SOS**		**SDeS**	
C_s	Δμ (Debye)	C_s	Δμ (Debye)	C_s	Δμ (Debye)	C_s	Δμ (Debye)
0.00	1.455±0.388	0.00	1.455±0.171	0.00	1.454±0.135	0.00	1.455±0.178
0.08	1.680±0.303	0.29	1.459±0.186	0.04	1.550±0.120	0.02	1.258±0.353
0.16	1.924±0.218	0.59	1.227±0.31	0.08	1.742±0.169	0.03	1.221±0.487
0.24	1.843±0.197	0.88	1.486±0.231	0.17	2.038±0.393	0.04	1.385±0.293
0.32	1.784±0.229	1.11	1.254±0.345	0.23	2.129±0.427	0.06	1.511±0.500
0.40	1.676±0.326	1.46	1.471±0.308	0.30	2.211±0.473	0.07	1.399±0.449
0.60	1.748±0.413	2.19	1.409±0.363	0.42	2.253±0.393	0.15	1.919±0.469
0.80	1.674±0.240	3.00	1.564±0.204	0.53	2.193±0.401	0.22	1.977±0.186
1.00	1.715±0.239	3.59	1.608±0.280	0.69	2.311±0.350	0.30	2.232±0.343
1.20	1.766±0.333	4.38	1.615±0.284	0.91	2.000±0.366	0.37	2.181±0.596
1.40	1.807±0.324	5.11	1.538±0.339	0.95	1.899±0.317	0.45	2.400±0.457
1.60	1.886±0.264	5.83	1.584±0.227	0.99	1.825±0.291	0.60	2.082±0.497
1.80	1.890±0.207	6.22	1.495±0.251	1.03	1.774±0.372	0.63	2.100±0.361
2.00	1.837±0.362	7.29	1.506±0.398	1.10	1.724±0.412	0.67	1.949±0.523
2.20	1.835±0.301	8.02	1.498±0.263	1.26	1.723±0.392	0.71	1.681±0.469
2.40	1.967±0.363	8.67	1.523±0.347	1.41	1.730±0.432	0.75	1.742±0.562
						0.78	1.734±0.530
SDS		**TSDS**				0.82	1.736±0.305
0.00	1.455±0.191	0.00	1.455±0.141			0.86	1.385±0.345
0.03	1.865±0.210	0.05	2.335±0.407			0.89	1.420±0.350
0.06	2.576±0.250	0.10	2.448±0.485			0.97	1.432±0.303
0.09	3.076±0.272	0.15	2.447±0.474			1.04	1.437±0.217
0.12	3.163±.291	0.20	2.352±0.229			1.12	1.383±0.202
0.16	3.176±0.301	0.25	2.426±0.390			1.19	1.562±0.296
0.24	3.192±0.250	0.37	2.765±0.481				
0.39	3.306±0.331	0.50	2.807±0.402				
0.46	2.999±0.350	0.62	1.917±0.412				
0.54	2.609±0.390	0.75	1.248±0.241				
0.62	2.028±0.201	0.87	1.080±0.331				
0.70	1.679±0.301	0.99	0.853±0.431				
0.77	1.587±0.402	1.12	0.964±0.466				
0.85	1.524±0.356	1.24	0.962±0.542				
0.93	1.517±0.364	1.37	0.941±0.266				
1.01	1.491±0.242	1.49	0.950±0.489				
1.08	1.591±0.241						
1.24	1.483±0.259						
1.39	1.530±0.150						
1.55	1.510±0.245						

8.5. References

1. Shah, S. S.; Shah, S. W. H.; Naeem, K., Surfactants-Dye Aggregates. In *Encyclopaedia of Surface and Colloid Science*, Hubbard, P. S. a. A., Ed. Marcel Dekker: 2002; p 5207.
2. Sarkar, M.; Poddar, S., Studies on the interaction of surfactants with cationic dye by absorption spectroscopy. *J. Colloid Interface Sci.* **2000,** *221*, 181-185.
3. Barni, E.; Savarino, P.; Viscardi, G., Dye-surfactant interactions and their applications. *Acc. Chem. Res.* **1991,** *24*, 98-103.
4. Bielska, M.; Sobczyńska, A.; Prochaska, K., Dye–surfactant interaction in aqueous solutions. *Dyes Pigm.* **2009,** *80*, 201-205.
5. Freire, S.; Bordello, J.; Granadero, D.; Al-Soufi, W.; Novo, M., Role of electrostatic and hydrophobic forces in the interaction of ionic dyes with charged micelles. *Photochem. Photobiol. Sci.* **2010,** *9*, 687-696.
6. Macedo, E. R.; De Boni, L.; Misoguti, L.; Mendonça, C. R.; De Oliveira, H. P., Dye aggregation and influence of pre-micelles on heterogeneous catalysis: A photophysical approach. *Colloids Surf. A* **2011,** *392*, 76-82.
7. Moulik, S. P.; Ghosh, S.; Das, A. R., Interaction of acridine orange monohydrochloride dye with sodiumdodecylsulfate,(SDS) cetyltrimethylammoniumbromide (CTAB) and p-tert-octylphenoxypolyoxy ethanol (Triton X 100) surfactants. *Colloid Polym. Sci.* **1979,** *257*, 645-655.
8. Hestand, N. J.; Spano, F. C., Expanded theory of H-and J-molecular aggregates: the effects of vibronic coupling and intermolecular charge transfer. *Chem. Rev.* **2018,** *118*, 7069-7163.
9. Gohain, B.; Dutta, R. K., Premicellar and micelle formation behavior of dye surfactant ion pairs in aqueous solutions: deprotonation of dye in ion pair micelles. *J. Colloid Interface Sci.* **2008,** *323*, 395-402.
10. Neumann, M. G.; Gehlen, M. H., The interaction of cationic dyes with anionic surfactants in the premicellar region. *J. Colloid Interface Sci.* **1990,** *135*, 209-217.
11. Sharma, R.; Kamal, A.; Mahajan, R. K., Detailed study of interactions between eosin yellow and gemini pyridinium surfactants. *RSC Adv.* **2016,** *6*, 71692-71704.
12. Terdale, S.; Tantray, A., Spectroscopic study of the dimerization of rhodamine 6G in water and different organic solvents. *J. Mol. Liq.* **2017,** *225*, 662-671.
13. Micheau, J.; Zakharova, G.; Chibisov, A., Reversible aggregation, precipitation and re-dissolution of rhodamine 6G in aqueous sodium dodecyl sulfate. *Phys. Chem. Chem. Phys.* **2004,** *6*, 2420-2425.
14. Rumi, M.; Perry, J. W., Two-photon absorption: an overview of measurements and principles. *Adv. Opt. Photonics* **2010,** *2*, 451-518.
15. Das, D. K.; Islam, S. I.; Samanta, N.; Yadav, Y.; Goswami, D.; Mitra, R. K., Two Photon Spectroscopy Can Serve as a Marker of Protein Denaturation Pathway. *J. Fluoresc* **2018,** *28*, 855-862.
16. Drobizhev, M.; Tillo, S.; Makarov, N. S.; Hughes, T. E.; Rebane, A., Absolute two-photon absorption spectra and two-photon brightness of orange and red fluorescent proteins. *J. Phys. Chem. B* **2009,** *113*, 855-859.
17. Pawlicki, M.; Collins, H. A.; Denning, R. G.; Anderson, H. L., Two-Photon Absorption and the Design of Two-Photon Dyes. *Angew. Chem. Int. Ed.* **2009,** *48*, 3244 – 3266.
18. Wielgus, M.; Michalska, J.; Samoc, M.; Bartkowiak, W., Two-photon solvatochromism III: Experimental study of the solvent effects on two-photon absorption spectrum of p-nitroaniline. *Dyes Pigm.* **2015,** *113*, 426-434.

19. Nag, A.; Goswami, D., Solvent effect on two-photon absorption and fluorescence of rhodamine dyes. *J. Photochem. Photobiol. A* **2009,** *206*, 188-197.
20. Hanczyc, P.; Samoc, M.; Norden, B., Multiphoton absorption in amyloid protein fibres. *Nat. Photonics* **2013,** *7*, 969-972.
21. Doan, P. H.; Pitter, D. R. G.; Kocher, A.; Wilson, J. N.; Goodson, I., T., Two-Photon Spectroscopy as a New Sensitive Method for Determining the DNA Binding Mode of Fluorescent Nuclear Dyes. *J. Am. Chem. Soc.* **2015,** *137*, 9198−9201.
22. Chen, C.; Zhou, L.; Liu, W.; Liu, W., Coumarinocoumarin-Based Two-Photon Fluorescent Cysteine Biosensor for Targeting Lysosome *Anal. Chem.* **2018,** *90*, 6138−6143.
23. Olesiak-Banska, J.; Waszkielewicz, M.; Obstarczyka, P.; Samoc, M., Two-photon absorption and photoluminescence of colloidal gold nanoparticles and nanoclusters. *Chem. Soc. Rev.* **2019,** *48*, 4087-4117.
24. Gonçalves, E. S.; Cocca, L. H. Z.; Araujo, W. E. R.; Parekh, K.; Oliveira, C. L. P.; Siqueira, J. R.; Mendonça, C. R.; De Boni, L.; Neto, A. M. F., Influence of Magnetic Field on the Two-Photon Absorption and Hyper-Rayleigh Scattering of Manganese–Zinc Ferrite Nanoparticles. *J. Phys. Chem. C* **2020,** *124*, 6784–6795.
25. Woo, H. Y.; Korystov, D.; Mikhailovsky, A.; Nguyen, T.-Q.; Bazan, G. C., Two-Photon Absorption in Aqueous Micellar Solutions. *J. Am. Chem. Soc.* **2005,** *127*, 13794-13795.
26. Tian, Y.; Chen, C.-Y.; Cheng, Y.-J.; Young, A. C.; Tucker, N. M.; Jen, A. K.-Y., Hydrophobic Chromophores in Aqueous Micellar Solution Showing Large Two-Photon Absorption Cross Sections†. *Adv. Funct. Mat.* **2007,** *17*, 1691-1697.
27. Bairu, S.; Ramakrishna, G., Two-Photon Absorption Properties of Chromophores in Micelles: Electrostatic Interactions. *J. Phys. Chem. B* **2013,** *117*, 10484-10491.
28. Gupta, R. K.; Kant, S.; Rawat, A. K.; Goswami, D., Two-Photon-Induced Fluorescence Study of Rhodamine-6G Dye in Different Sets of Binary Solvents. *J. Fluoresc* **2020,** *30*, 1043-1048.
29. Ranganathan, R.; Tran, L.; Bales, B. L., Surfactant-and salt-induced growth of normal sodium alkyl sulfate micelles well above their critical micelle concentrations. *The journal of physical chemistry. B* **2000,** (10), 2260-2264.
30. Acosta, E.; Bisceglia, M.; Kurlat, D. H., Self-aggregation in aqueous TRITON X-100 solutionsnear CMC. *Phys. Chem. Liq.* **2005,** (3), 269-275.
31. Imae, T.; Kamiya, R.; Ikeda, S., Formation of spherical and rod-like micelles of cetyltrimethylammonium bromide in aqueous NaBr solutions. *J. Colloid Interface Sci.* **1985,** (1), 215-225.
32. Abraham, M. J.; Murtolad, T.; Schulz, R.; Páll, S.; Smith, J. C.; Hess, B.; Lindahl, R., GROMACS: High performance molecular simulations through multi-level parallelism from laptops to supercomputers. *SoftwareX* **2015,** *1–2*, 19-25.
33. Wang, J.; Wolf, R. M.; Caldwell, J. W.; Kollman, P. A.; Case, D. A., Development and testing of a general amber force field. *J. Comput. Chem.* **2004,** *25*, 1157-1174.
34. Berendsen, H. J. C.; Grigera, J. R.; Straatsma, T. P., The missing term in effective pair potentials. *J. Phys. Chem.* **1987,** *91*, 6269–6271.
35. Bussia, G.; Donadio, D.; Parrinello, M., Canonical sampling through velocity rescaling. *J. Chem. Phys.* **2007,** *126*, 014101.
36. Parrinello, M., Polymorphic transitions in single crystals: A new molecular dynamics method. *J. App. Phys.* **1981,** *52*, 7182.
37. Tajalli, H.; Gilani, A. G.; Zakerhamidi, M.; Moghadam, M., Effects of surfactants on the molecular aggregation of rhodamine dyes in aqueous solutions. *Spectrochim. Acta A* **2009,** (4), 697-702.

38. Martínez Martínez, V.; López Arbeloa, F.; Bañuelos Prieto, J.; Arbeloa López, T.; López Arbeloa, I., Characterization of Rhodamine 6G Aggregates Intercalated in Solid Thin Films of Laponite Clay. 1. Absorption Spectroscopy. *J. Phys. Chem. B* **2004,** *108*, 20030-20037.
39. Tadros, T. F., Physical chemistry of surfactant solutions. *J. Colloid Interface Sci.* **2005,** *5*, 19-40.
40. De Vendittis, E.; Palumbo, G.; Parlato, G.; Bocchini, V., A fluorimetric method for the estimation of the critical micelle concentration of surfactants. *Anal. Biochem.* **1981,** *115*, 278-286.
41. Tajalli, H.; Ghanadzadeh Gilani, A.; Zakerhamidi, M. S.; Moghadam, M., Effects of surfactants on the molecular aggregation of rhodamine dyes in aqueous solutions. *Spectrochim. Acta A* **2009,** *72*, 697-702.
42. Maiti, N. C.; Krishna, M.; Britto, P.; Periasamy, N., Fluorescence dynamics of dye probes in micelles. *J. Phys. Chem. B* **1997,** *101*, 11051-11060.
43. Vinogradov, A. M.; Tatikolov, A. S.; Costa, S. M., The effect of anionic, cationic and neutral surfactants on the photophysics and isomerization of 3, 3′-diethylthiacarbocyanine. *Phys. Chem. Chem. Phys.* **2001,** *3*, 4325-4332.
44. Ogunsipe, A., Solvent Effects on the Spectral Properties of Rhodamine 6G: Estimation of Ground and Excited State Dipole Moments. *J Solution Chem* **2018,** *47*, 203-219.
45. Nag, A.; De, A. K.; Goswami, D., Two-photon cross-section measurements using an optical chopper: z-scan and two-photon fluorescence schemes. *J. Phys. B* **2009,** *42*, 065103.
46. Xu, C.; Webb, W. W., Measurement of two-photon excitation cross sections of molecular fluorophores with data from 690 to 1050 nm. *J. Opt. Soc. Am. B* **1996,** *13*, 481-491.
47. Collini, E.; Ferrante, C.; Bozio, R., Strong enhancement of the two-photon absorption of tetrakis (4-sulfonatophenyl) porphyrin diacid in water upon aggregation. *J. Phys. Chem. B* **2005,** *109*, 2-5.
48. Chambers, R. W.; Kajiwara, T.; Kearns, D. R., Effect of Dimer Formation of the Electronic Absorption and Emission Spectra of Ionic Dyes. Rhodamines and Other Common Dyes. *J. Phys. Chem.* **1974,** *78*, 380-387.
49. Murugan, N. A.; Kongsted, J.; Rinkevicius, Z.; Aidas, K.; Mikkelsen, K. V.; Ågren, H., Hybrid density functional theory/molecular mechanics calculations of two-photon absorption of dimethylamino nitro stilbene in solution. *Phys. Chem. Chem. Phys.* **2011,** *13*, 12506-12516.
50. Drobizhev, M.; Makarov, N. S.; Tillo, S. E.; Hughes, T. E.; Rebane, A., Two-photon absorption properties of fluorescent proteins. *Nat. Methods* **2011,** *8*, 393-399.
51. Sen, P. K.; Talukder, S.; Pal, B., Specific interactions of anions and pre-micelles in the alkaline fading of crystal violet carbocation. *Colloids Surf. A* **2015,** *467*, 259-269.
52. Kutz, A.; Mariani, G.; Gröhn, F., Ionic dye–surfactant nanoassemblies: interplay of electrostatics, hydrophobic effect, and π–π stacking. *Colloid Polym. Sci.* **2016,** *294*, 591-606.

Chapter 9

9. Overview and Future Perspective

9. 1: Overview

In this dissertation, we have actively investigated excited-state photophysical processes in different bimolecular and biomimetic recognition processes, as well as to understand ultra-fast dynamics of different constrained environments (e.g. RMs, mixed RMs, etc.) using spectroscopic techniques. Compared to single ones, surfactant blend systems (mixed RMs) often provide more advantageous properties. The oil-water interface, which is more versatile and capable of taking up more water to improve solubilization ability, is adjusted by a mixture of surfactants. Therefore, the primary aim of this thesis was to research the modulation (both increase and decrease) of the ESPT rate by changing surfactant blend interfaces of RM systems. We have also used two-photon spectroscopy to analyze the local atmospheric of aggregate structures.

Chapter 1 offers a general introduction to the overall thesis work and aims to answer some questions, such as: *why do biomolecular systems require ultrafast spectroscopy? Why is the use of fluorescent probes necessary? How to get information about the local environment of the system (e.g. specific location of protein-like biomolecules, aggregate properties, etc) by NIR radiation?* This chapter also discusses the potential applications of surfactants, micelles, RM, binary mixes, and ESPT in a variety of sectors, as well as the assessment of physical parameters such as water structure and dynamics in such confined systems using various techniques.

Chapter 2 provides a brief description (theory and experimental methods) of the basic theory of photophysics, quantum yield, fluorescence quenching, solvent dynamics, anisotropy, ESPT, and two-photon absorption analysis using two-photon absorption

spectroscopy. A general description of the processes, surfactants, solvents, molecular probes, biomolecules used in this dissertation has been given and sample preparation techniques were also discussed.

Chapter 3 describes the general background of spectroscopic techniques used in this dissertation.

Chapter 4 to **Chapter 8** is based on the experimental work I did during my Ph.D. tenure. It covers two broad categories which have already been mentioned in the introduction Part (see chapter 1).

Overview of the dissertation from the ESPT studies

In this dissertation, we initially investigated the ESPT reaction of D-luciferin in mixed RM systems composed of non-ionic (Ig-520) with cationic (DDAB) and anionic (AOT) in cyclohexane (Cy) at different mole fractions of Ig (X_{Ig}) and fixed hydration (w_0=10). In AOT RM, we observed that ESPT is feeble, while in the other two RMs, it is favourable. We introduced a new parameter in the form of charge type at the interface of RM systems to modulate (both increase and decrease) the ESPT rate by only mixing surfactants of different charge types, keeping all other parameters unchanged. In addition to Ig, we also observed that it facilitates ESPT in AOT RM linearly, whereas, in DDAB, it shows a synergistic effect.

Our next study was aimed to understand the ESPT mechanism of a photo-acid at various temperatures at a fixed hydration w_0=10, in different charge types of RMs. *We have tried to address a debatable query, which process precedes: ESPT dynamics or solvation?* ESPT was found to be the most prominent in DDAB, followed by Ig, while the formation of deprotonated species in AOT was heavily restricted. We observed that in the charged RMs solvation precedes ESPT; however, in Ig they co-occur. Both k_{PT} and k_{solv} increased near-linearly with temperature; however, it was found that the increase in k_{solv} did assist ESPT in Ig while it actually was disfavoured in DDAB. Our study has established the pivotal role of solvation to explain the ESPT process, especially in constrained environments like in RMs.

Next, to identify how micro-heterogeneity in aqueous environments affects ESPT process, we investigated the ESPT of D-luciferin in aqueous mixtures of H_2O-EtOH (water-ethanol) and H_2O-TFE (water-trifluoroethanol). It is interesting to compare the H-bonding interactions between these two aqueous solutions. In EtOH-water, the ESPT kinetics

of D-luciferin is faster and increases near-linearly with X_w (water mole fraction), whereas, in TFE-water, the improvement is not linear and is slower. We discovered an isoemissive point in the TFE-water system due to accelerated solvation dynamics which is otherwise unaffected by the ESPT kinetics. We noted very low ESPT in TFE-water mixture (up to X_w~0.6) because of the electronegative nature of fluorine atoms leading to a higher degree of hydrophobicity in the solutions, whereas, in the EtOH-water system, solvation and ESPT occur simultaneously in the entire X_w region.

Overview of the dissertation from the two-photon spectroscopy studies

In this section of the dissertation, we have used a unique spectroscopic technique, 2PA spectroscopy (see chapter 3), which can probe the specific binding of probes with proteins, and we have investigated whether this could be exploited to understand site-specific binding as well as conformational changes of proteins during thermal/chemical denaturation. In order to verify this, we investigated TPACS (σ_2) of two rhodamine dyes: R6G and RhB, site selectively bound to a model protein (BSA, for more details see chapter 2), by excitation at 800 nm at various concentrations and temperatures. The identified similarity in the trends of TPACS and CD measurements strongly affirmed the suitability of the TPA method in protein imaging and as an alternative marker for monitoring its conformational transformations using NIR radiation and confirms the site-specific binding of the protein probes and can monitor the protein (un) folding pathways induced by temperature.

Finally, we have shown that (NIR radiation) TPA spectroscopy could be used to investigate the molecular basis of cationic dye (R6G)-surfactant (anionic) interactions, and that these interactions have been corroborated by classical simulation studies. We then changed the chain length of anionic surfactants while keeping the cationic dye constant to determine if the hydrophobicity of the surfactant influences the complex formation. We found that, the electrostatic attraction (between R6G and SDS) enhances the $\Delta\mu$ whereas electrostatic repulsion (between CTAB and R6G) did resist to redistribute the charge of R6G and hence no change in $\Delta\mu$ is observed. Moreover, we observed that monomeric anionic surfactants are solubilized in cationic dye dimers at pre-micellar concentrations, distorting the dyes' parallel orientation. Such distortion has been found to be influenced by the hydrophobicity of the surfactant, which is intriguing given that the interaction is predominantly electrostatic in nature.

In essence, this thesis is to understand the changes in the photophysical processes/properties of fluorescence/laser dyes in the excited-state in the presence of various biological and biomimetic systems (e.g. model proteins, micelles, reverse micelles, mixtures of RM, pure solvents, binary mixtures, etc.) using different experimental techniques in the presence of different environments (temperature, pH, concentration, etc.).

9.2: Future Perspective

Reverse micelles (RMs) are interesting entities that have recently received a lot of recognition, and their usefulness has been demonstrated in a variety of chemical systems.[1] Because the dimensions and shapes of reverse micelles, as well as their bulk equivalents, are easily tunable[2], they have long been a topic of interest. A spherical cavity of water (or another polar protic and aprotic solvent) is surrounded by a shell of surfactant molecules that serves as an interface between the polar cavity and the nonpolar medium in which they are isolated. With this in mind, we plan to expand our research by investigating the ESPT rate of photoacid at different mole fractions of water using other essential amphiphilic molecules in binary mixtures (such as N, N-Dimethylformamide (DMF) and water, Dimethyl sulfoxide (DMSO) and water, and so on) within different charge forms RMs (such as DDAB, AOT, Ig-520, etc.). It is well known that the surfactant molecules position themselves with their head group directed inward and make the polar core by the interaction between water and surfactant head groups. That is a suitable combination between water and surfactant that can be solubilized in a nonpolar organic solvent, forming "reverse micelles" or "micro-emulsions.[3] In recent years, RMs have been prepared without water, where water has been replaced by polar aprotic or non-aqueous solvents, which are otherwise immiscible in hydrocarbon solvents with high dielectric constants. [4, 5] These non-aqueous RM systems are of better usage to the aqueous ones predominantly because they can be used as good reaction media. Some non-aqueous, highly polar solvents commonly used in chemistry include dimethylformamide (DMF), dimethylacetamide (DMA), formamide (FA), ethylene glycol (EG), propylene glycol (PG), and glycerol (GY).[4, 5] A common anionic surfactant AOT reverse micelles in nonpolar or non-aqueous solvents has been the focus of many studies because this surfactant can solubilize a large quantity of water in a nonpolar solvent.[4, 6] Previously, it was reported that changing solvents from polar protic water to polar aprotic DMF, DMSO and also the number of solvents inside the polar core changed the structural alternation of RMs.[7]

The main goal of this future proposal is to expose the photophysical properties of D-luciferin in an atmosphere with unique polarity, rigidity, and other properties. Apart from that, we've tried to figure out what happens to the excited-state proton transfer mechanism in pure solvent or binary compositions. According to our findings the ESPT process of D-luciferin from the polar protic core to the polar aprotic core is better regulated by a more rigid and confined environment within the reverse micelle.

Our future research would focus on the structure and relaxation dynamics of polar protic or aprotic molecules encapsulated in the solvent pool of differently charged RM systems. Then, using photoacid or fluorescence probes and various spectroscopic techniques (*see below the experimental scheme*), I intend to characterize the RMs interfaces in the presence of various organic polar solvents (such as DMF, DMA, FA, PG, EG, GY, and so on). In addition, we plan to investigate the THz dielectric relaxation of polar protic or aprotic solvents in RM systems with hydrogen bond stretching and libration band in the far-IR region (with a time resolution of a few ps to sub-ps). THz spectroscopy (1 THz=10^{12} Hz =1ps^{-1}) has proven to be a useful tool for obtaining information about the solvation layers, especially the libration and collective hydrogen bond stretching vibration bands.[8-11] Previously, mid-infrared (MIR) and far-infrared (FIR) FTIR techniques were used to examine the hydrogen-bonded network structure and dynamics of water molecules in RM systems.[12]

The following is the experimental scheme:

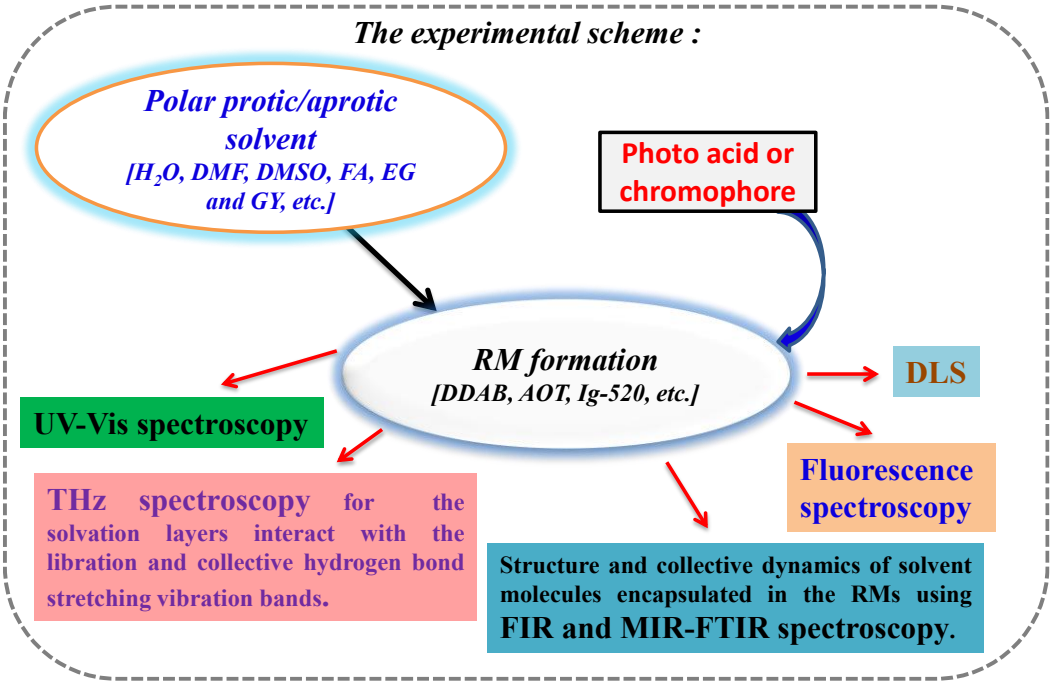

9.3: References

1. Pileni, M.-P.; Zemb, T.; Petit, C., Solubilization by reverse micelles: Solute localization and structure perturbation. *Chemical Physics Letters* **1985,** *118* (4), 414-420.
2. Pileni, M., Reverse micelles as microreactors. *The Journal of physical chemistry* **1993,** *97* (27), 6961-6973.
3. Cohen, B.; Huppert, D.; Solntsev, K. M.; Tsfadia, Y.; Nachliel, E.; Gutman, M., Excited State Proton Transfer in Reverse Micelles. *J. Am. Chem. Soc.* **2002,** *124*, 7539-7547.
4. Riter, R. E.; Kimmel, J. R.; Undiks, E. P.; Levinger, N. E., Novel Reverse Micelles Partitioning Nonaqueous Polar Solvents in a Hydrocarbon Continuous Phase. *The Journal of Physical Chemistry B* **1997,** *101* (41), 8292-8297.
5. Falcone, R. D.; Silber, J. J.; Correa, N. M., What are the factors that control non-aqueous/AOT/n-heptane reverse micelle sizes? A dynamic light scattering study. *Physical Chemistry Chemical Physics* **2009,** *11* (47), 11096-11100.
6. De, T. K.; Maitra, A., Solution behaviour of Aerosol OT in non-polar solvents. *Advances in colloid and interface science* **1995,** *59*, 95-193.
7. Kuchlyan, J.; Banik, D.; Kundu, N.; Ghosh, S.; Banerjee, C.; Sarkar, N., Effect of Confinement on Excited-State Proton Transfer of Firefly's Chromophore d-Luciferin in AOT Reverse Micelles. *J. Phys Chem. B* **2014,** *118*, 3401-3408.
8. Ebbinghaus, S.; Kim, S. J.; Heyden, M.; Yu, X.; Heugen, U.; Gruebele, M.; Leitner, D. M.; Havenith, M., An extended dynamical hydration shell around proteins. *Proceedings of the National Academy of Sciences USA* **2007,** *104* (52), 20749-20752.
9. Born, B.; Weingärtner, H.; Bründermann, E.; Havenith, M., Solvation Dynamics of Model Peptides Probed by Terahertz Spectroscopy. Observation of the Onset of Collective Network Motions. *Journal of the American Chemical Society* **2009,** *131* (10), 3752-3755.
10. Meister, K.; Ebbinghaus, S.; Xu, Y.; Duman, J. G.; DeVries, A.; Gruebele, M.; Leitner, D. M.; Havenith, M., Long-range protein–water dynamics in hyperactive insect antifreeze proteins. *Proceedings of the National Academy of Sciences* **2013,** *110* (5), 1617-1622.
11. Heyden, M.; Sun, J.; Funkner, S.; Mathias, G.; Forbert, H.; Havenith, M.; Marx, D., Dissecting the THz spectrum of liquid water from first principles via correlations in time and space *Proceedings of the National Academy of Sciences USA* **2010,** *107*, 12068-12073.
12. Patra, A.; Luong, T. Q.; Mitra, R. K.; Havenith, M., Solvent dynamics in a reverse micellar water-pool: a spectroscopic investigation of DDAB–cyclohexane–water systems. *Physical Chemistry Chemical Physics* **2013,** *15* (3), 930-939.

Appendices

➢ *Preparation of buffer of a particular pH*

Buffer is termed as an aqueous system that tends to resist changes in pH when a small amount of acid or base is added. It can be prepared by mixing an aqueous solution of the weak acid and its conjugate base.

The acid (*HA*) dissociation equilibrium in water is as follows,

$$HA(aq) + H_2O(aq) \leftrightarrows H_3O^+(aq) + A^-(aq)$$

The dissociation constant (K_a) is related to pH by the Henderson-Hasselbalch Equation given below,

$$pH = pK_a + \log\frac{[A^-(aq)]}{[HA(aq)]}$$

The buffer capacity range is $pK_a \pm 1$ and maximum capacity at pK_a.

In our experiment, we have generally used sodium phosphate buffer (pH 7.4) or sometimes called **phosphate buffer saline (PBS)** which is isotonic with physiological fluid. Na_2HPO_4 and NaH_2PO_4 are mixed in a particular ratio to prepare the buffer solution.

Calculation:

$$pH = pK_a + \log\frac{[Na_2HPO_4]}{[NaH_2PO_4]}$$

or, $$\log\frac{[Na_2HPO_4]}{[NaH_2PO_4]} = pH - pK_a = 7.4 - 7.2 = 0.2$$

or, $$\frac{[Na_2HPO_4]}{[NaH_2PO_4]} = 10^{0.2}$$

If we take an equimolar mixture (say 50 mM) of both the solution in a total volume of 100 ml then we can write the equation in terms of volume,

$$\frac{V_{Na_2HPO_4}}{V_{NaH_2PO_4}} = 10^{0.2}$$

or, $$\frac{V_{Na_2HPO_4}}{100 - V_{Na_2HPO_4}} = 10^{0.2}$$

or, $$V_{Na_2HPO_4} = \frac{100 \times 10^{0.2}}{1 + 10^{0.2}} = 61.34\ ml$$

Therefore, 61.34 ml Na_2HPO_4 (50 mM) and 38.66 ml NaH_2PO_4 (50 mM) are mixed to make a 100 ml 50 mM buffer of pH 7.4.

Index